Thèse n° 10 408

Vapor Deposition of Perovskite Solar Cells

Présentée le 15 décembre 2023

Faculté des sciences et techniques de l'ingénieur
Laboratoire de photovoltaïque et couches minces électroniques
Programme doctoral en énergie

pour l'obtention du grade de Docteur ès Sciences

par

Quentin Jean-Marie Armand GUESNAY

Acceptée sur proposition du jury

Dr S. R. Cherkaoui, président du jury
Prof. C. Ballif, Dr C. M. Wolff, directeurs de thèse
Prof. M. Morales Masis, rapporteuse
Dr P. Schulze, rapporteuse
Prof. G. Tagliabue, rapporteuse

École
polytechnique
fédérale
de Lausanne

2023

'Le sens de la vie supprimé,
il reste encore la vie.'
— Albert Camus

Acknowledgements

I, logically, would like to thank first Prof. Christophe Ballif who believed in me four years ago. This generic sentence common to all ackowledgements sections feels especially true in this case, I'm still amazed how he kept renewing this trust through the long months of trials and errors in this early PhD journey. Passionate, he is, for sure, but I would like to thank him for his pragmatic approach of science and research. Not every single thing tried in this lab will save the world, for sure, but at the very least I think that each one of us can say 'it's worth trying'. This feeling, priceless to me, would not be possible without this pertinent vision of Christophe and the team leaders.
I also thank Dr. Quentin Jeangros and Dr. Christian M. Wolff, respectively co-supervising the first and second half of this thesis. Their different and complementary backgrounds have been useful to construct myself as a scientist. The backing, supporting and allowing me to express myself, has been continuous and seamless over the four years.
I warmly thank my jury members : Dr. Rachid Cherkaoui, Prof. Giulia Tagliabue, Prof. Monica Morales Masis and Dr. Patricia Schulze for giving their (precious) time to the evaluation of this work.
Special thanks go to now Dr. Florent Sahli, which initiated the organohalide vapor deposition activities in the lab, this thesis would have been very different without his preliminary work, sympathy and good spirits.
Special thanks also to the charitable souls who helped me one way or another during the last weeks of rush to try to get the most out of my project : Kerem, Deniz, Austin, Florent (the same) and Noémie.
A such exploratory topic would be nothing without the support of a good technical team, that's why we are lucky to have a very good technical team at PV-lab and I deeply thank all of its members : Cédric, Aymeric, Nicolas, Nathanaël et Joël. I also thank in general all the people who passed by PV-lab over the last four years for the good time spent.
Je tiens également à exprimer mon infinie gratitude envers tous ceux qui, loin des solvants et des expériences douteuses (quoi que, pas tous ...), donnent un sens à la vie en la vivant : la mif' FMA et la team BJJ IA, l'équipe INSAR/BNS3 (étendue) ainsi que mon inconditionnellement soutenante famille. Les derniers remerciements spéciaux vont au bipède et au quadrupède qui égayent mon quotidien depuis presque 10 et 3 ans, respectivement.

Neuchâtel, Septembre 2023 Q. G.

Abstract

Thanks to the continuous improvement of crystalline silicon (c-Si) solar cells, largely dominating the market, photovoltaic electricity is nowadays the cheapest source of energy on the market. Yet, solar energy is far from being completely harvested, as there is a fundamental limit to how much a single absorber can generate electrical power with solar irradiation. This conversion efficiency limit for one absorber is around 30%. One of the most promising ways to overcome this theoretical limit is to combine two light-absorbing materials, fabricating so-called 'tandem' solar cells.

The most realistic entry on the highly competitive photovoltaic market for a new technology is to take advantage of the already existing c-Si production lines and upgrade them to produce tandem devices. Among the best candidates to be paired with c-Si solar cells are halide perovskites, referring to the general ABX_3 crystal structure (with A an organic cation, B a bivalent metal and X a halide). Hybrid organic/inorganic lead halide perovskites are extremely attractive thanks to bandgap tunability, exceptional optoelectronic properties and potential to be processed at low costs.

The objective of this work is to develop a vapor deposition process of perovskite thin films. Vapor based processes allow upscalable deposition in a controlled and solvent-free environment of thin films in a conformal manner. However, most existing vapor deposition processes are not well adapted to the organic precursors of perovskites, resulting in unreliable depositions with standard vapor processes.

After an introduction to perovskite vapor deposition, the first part of this thesis covers the basics of perovskite photovoltaics theory. The following chapter is composed of an analytical review of the existing perovskite vapor phase processes, deepened by a discussion of the linkage between theoretical considerations of thin film growth and experimental observations. The last chapter presents the experimental work achieved during this thesis.

The first part of this chapter discusses a study on the single source evaporation of metal halide precursors. Co-evaporated $CsBr/PbI_2$ (1 : 6 molar ratio) metal halide films are compared to ball milled powders with varying relative ratios ($CsBr/PbI_2$) (1 : 8 - 1 : 4). The powders are studied before and during the evaporation process via in situ GIWAXS, revealing no new phases in the powder mixes and thermally assisted halide exchange during the evaporation process. All deposited thin films exhibit stoichiometries different from the evaporated reference films. Yet, the 1 : 5 films enable 15% efficient solar cells, with 1.7eV perovskite absorbers.

The second part of this chapter demonstrates a simple, versatile organohalide vapor deposition process that is flexible, robust, low cost, upscalable and easy to reproduce. The growth of perovskite films based on $CsBr/PbI_2$ templates is followed for different conditions using in situ photoluminescence and GIWAXS, revealing four distinct phases (initialization, nucleation, grain growth, and saturation). Critical process parameters, as well as the chemical environment and mechanical designs for optimal thin film growth are discussed. The flexibility is demonstrated by tuning the composition of the final perovskite thin films via halide exchange (affecting the bandgap) or additive addition to the vapor process and culminates in 17% efficient perovskite solar cells.

Key words: Photovoltaics, perovskite, thin films, vapor deposition, metal halide, perovskite growth, in situ monitoring, grazing-incidence wide-angle X-ray, photoluminescence quantum yield, nuclear magnetic resonance.

Résumé

Grâce aux progrès continus des cellules solaires en silicium cristallin, dominant largement le marché, l'électricité solaire est désormais l'une des moins chères. Il y a cependant une limite intrinsèque à la quantité d'énergie que peut produire un seul matériau absorbant. L'un des moyens les plus prometteurs pour dépasser cette limite consiste à combiner deux matériaux, absorbant différentes portions du spectre solaire, pour former des cellules photovoltaïques dites 'tandems'.

L'entrée la plus réaliste pour une nouvelle technologie tandem sur un marché du photovoltaïque devenu extrêmement compétitif est de tirer parti des lignes de production déjà existantes, en modifiant ces dernières afin de produire des cellules tandems. Les pérovskites, désignant une structure cristalline ABX_3 (avec A un cation organique, B un métal bivalent et X un halogène) sont particulièrement adaptées à une combinaison avec des cellules en silicium. Plus particulièrement, les compositions de pérovskites hybrides organiques/inorganiques sont très attractives en raison de leurs propriétés optoélectroniques exceptionnelles et modifiables, ainsi que de leur potentiel bas coût de production.

L'objectif de cette thèse est de développer un procédé de dépôt en phase vapeur de couches minces de pérovskite. Les procédés basés sur la vapeur permettent un dépôt homogène sur de grandes surfaces dans un environnement contrôlé et sans solvant. Cependant, les procédés déjà existants sont peu adaptés aux précurseurs organiques des pérovskites, rendant leur dépôt peu fiable avec les procédés conventionnels.

Après une introduction générale du sujet, la première partie de cette thèse aborde les bases théoriques du photovoltaïque, ainsi que les spécificités des pérovskites. Le chapitre suivant est constitué d'une analyse approfondie des procédés d'évaporation existants, tissant des liens entre observations expérimentales et considérations théoriques. Le dernier chapitre présente le travail expérimental réalisé au cours de cette thèse.

Dans un premier temps, un travail préliminaire sur le mélange et l'évaporation de poudres d'halogènures métalliques est présenté. L'évaporation de plusieurs mélanges de poudres de $CsBr/PbI_2$ avec différents ratios (1 : 8 - 1 : 4, ratio atomique) est comparée à la co-évaporation du ratio standard ($CsBr/PbI_2$ 1 : 6) utilisé au PV-lab. Les poudres sont étudiées avant et pendant

l'évaporation par diffraction de rayons X en incidence rasante in situ, révélant l'absence de nouvelles phases dans les mélanges sous stoechiométriques. Un échange d'halogènes durant l'évaporation est également découvert et étudié. Le mélange 1 : 5 permet d'obtenir des cellules solaires avec un rendement de 15% pour des couches de pérovskites à 1.7eV.
La seconde partie traite du développement d'un nouveau procédé d'évaporation d'halogènures organiques. Ce nouveau procédé est rapide, flexible, facile à reproduire et réalisable à bas coût, par conséquent prometteur pour une potentielle industrialisation. La croissance de pérovskite basée sur un template $CsBr/PbI_2$ est étudiée in situ par photoluminescence et diffraction de rayons X en incidence rasante. Différentes phases sont ainsi observées et analysées : initialisation, nucléation, croissance et saturation. L'influence des paramètres d'évaporation, de l'environnement chimique ainsi que de la conception mécanique sur le procédé est discutée en détail. La flexibilité du procédé est démontrée en modifiant la composition finale de la pérovskite par échange d'halogènes (affectant donc son absorption de la lumière) ou par l'incorporation d'additifs en phase vapeur. Le procédé ainsi développé est robuste, répétable, maitrisé et permet d'obtenir des cellules solaires pérovskites avec un rendement de 17% pour une bande interdite à 1.63eV.

Mots clés : Photovoltaïque, pérovskite, couches minces, déposition phase vapeur, halogénure de métal, croissance de pérovskite, mesure in situ, diffraction rayons X en incidence rasante, rendement quantique de photoluminescence, résonance magnétique nucléaire.

Contents

Acknowledgements **i**

Abstract (English/Français) **iii**

List of figures **ix**

1 Introduction **1**
1.1 General context 1
1.2 Objectives and structure of the thesis 4
1.3 Contribution to the field 5

2 Basics of photovoltaics and perovskite peculiarities **7**
2.1 Physics of Photovoltaics : General Considerations 7
2.1.1 Origins of voltage 7
2.1.2 Origins of current 9
2.1.3 Fundamental losses 10
2.2 Perovskite peculiarities 12
2.3 Characterization : how to analyse photovoltaic perovskite thin films ? 13
2.3.1 X-ray diffraction 13
2.3.2 Spectroscopy 13
2.3.3 Nuclear magnetic resonance 14
2.3.4 Time of flight secondary ion mass spectrometry 14
2.3.5 Electron microscopy 14
2.3.6 Photoluminescence 14
2.3.7 Photovoltaic device characterization : current-voltage characteristic and external quantum efficiency 15

3 State of the art and theory of perovskite vapor deposition **17**
3.1 Introduction 18
3.2 Vapor deposition of metal halide perovskite solar cells 18
3.2.1 “Line-of-sight” vapor deposition processes 18
3.2.2 Vapor transport deposition 26
3.2.3 Hybrid vapor deposition processes 29
3.3 On the understanding of perovskite vapor deposition processes 33

3.3.1 Layer nucleation and growth: some theoretical considerations 34
3.3.2 Linking theory to experiments 37
3.4 Conclusion 44

4 Vapor Deposition of Perovskite Thin Films 47
4.1 Sub-stoichiometric mixing of metal halide powders and their single source evaporation for perovskite photovoltaics 48
4.1.1 Introduction 48
4.1.2 Results and discussion 49
4.1.3 Conclusion 58
4.2 Pizza Oven Processing of Organohalide Perovskites (POPOP) : a simple, versatile and efficient vapor deposition method 59
4.2.1 Introduction 59
4.2.2 Presentation of the process 60
4.2.3 In situ study of thin film growth 66
4.2.4 Conversion regimes 71
4.2.5 Influence of chemical environment 73
4.2.6 Bandgap tuning and additive engineering 80
4.2.7 Photovoltaic devices 83
4.2.8 Conclusion 84

5 Conclusion and perspectives 85

A Appendix A : experimental details 87
A.1 Processing of thin films and photovoltaic devices 87
A.1.1 Single source evaporation of metal halide powders 87
A.1.2 Vapor deposition of organohalides 88
A.2 Characterization 89
A.2.1 Single source evaporation of metal halide powders 89
A.2.2 Vapor deposition of organohalides 89

B Appendix B : Supporting Information (SI) 93
B.1 SI : single source evaporation of metal halide powders 94
B.2 SI : vapor deposition of organohalides 102

Bibliography 132

Acronyms and abbreviations 133

Contributions and Curriculum Vitae 137

List of Figures

1.1 Different morphologies of c-Si bottom cells when coupled to perovskite solar cells in tandem devices . . . 2

2.1 Absorption, transmission of light by semiconductor . . . 8
2.2 5800K blackbody, AM1.5G irradiance and photon flux . . . 9
2.3 Recombination mechanisms in a semiconductor . . . 11

3.1 Examples of line-of-sight vapor depositions . . . 20
3.2 Flash evaporation, ball milling principle and flash laser printing. . . . 23
3.3 Examples of vapor transport deposition systems. . . . 27
3.4 Hybrid vapor deposition processes . . . 30
3.5 Nucleation theory . . . 35
3.6 First stages of MAPI vapor growth observed via in situ XPS . . . 39
3.7 Schematic of perovskite vapor growth . . . 41
3.8 Influence of process conditions on layer morphology . . . 43
3.9 Summary of the influence of process parameters on perovskite growth . . . 45

4.1 XRD of ball milled powders . . . 49
4.2 Schematics of the measurement configuration . . . 50
4.3 In situ synchrotron GIWAXS monitoring of powder evaporation . . . 51
4.4 GIWAXS in situ monitoring of an evaporation. . . . 52
4.5 Arrhenius plot of the $PbBr_2$ peak evolution with temperature for all powder mixes 53
4.6 GIWAXS and SEM of single source evaporated template . . . 54
4.7 EDX of single source evaporated thin films . . . 55
4.8 GIWAXS and SEM of a converted perovskite thin film . . . 57
4.9 Photovoltaic device parameters . . . 57
4.10 First iteration of CVD setup and preliminary work . . . 61
4.11 Pipe shortening leading to perovskite formation in CVD chamber . . . 62
4.12 Schematic of the process. 1) Vacuum chamber 2) To pump 3) Holder 4) Organohalide source (powder, pellet, dried solution etc) 5) Substrate facing down 6) Heating stage 7) Forming perovskite 8) Metal halide template 9) Organohalide vapors. . 63
4.13 Holder prototype, POPOP repeatability . . . 64
4.14 NMR and SEM of POPOP repeatability study . . . 65
4.15 POPOP in situ GIWAXS & PL monitoring . . . 67

4.16 Disambiguation of two 0.7 $Å^{-1}$ GIWAXS signals 69
4.17 GIWAXS azimuthal intensity profiles of all phases during growth 70
4.18 Conversion regimes study 71
4.19 SEM, XRD and NMR of conversion study 72
4.20 PLQY, XRD and PL of POPOP in different chemical environments 74
4.21 NMR of thin films grown in different environments and solar cells confirming poor optoelectronic properties of samples obtained with 304 stainless steel holder 75
4.22 Comparison of in situ GIWAXS and NMR of films obtained with PTFE and 306 stainless steel holders 76
4.23 Comparison of in situ PL of films obtained with PTFE and 306 stainless steel holders 77
4.24 Baseline drift due to chamber contamination 79
4.25 Bandgap tuning 81
4.26 Additive incorporation 83
4.27 Proof of concept photovoltaic devices 84

B.1 Powder diffractograms of the mixtures obtained by ball milling. Full range . . . 94
B.2 Temperature evolution of integrated GIWAXS profile for all powder mixes . . . 95
B.3 Diffraction as a function of azimuthal angle of evaporated films. All compositions 96
B.4 EDX of pure precursors 97
B.5 Top view SEM of all evaporated compositions 98
B.6 Diffraction as a function of azimuthal angle of converted films. All compositions 99
B.7 Stacked 1D XRD of all compositions 100
B.8 Photovoltaic devices statistics 101
B.9 In situ GIWAXS & PL setup 102
B.10 Comparison of different heating profiles 103
B.11 Comparing continuous/discontinuous PL illumination influence 104
B.12 Comparative analysis of the 0.7 $Å^{-1}$ peak 105
B.13 Holder of the baseline and thoughts on mechanical design 106
B.14 Broader range data of bandgap tuning and characterization of the baseline . . 107
B.15 MACl as vapor additive 108
B.16 NMR and ToF SIMS study of FASCN additive strategy 109
B.17 Statistics of photovoltaic devices 110
B.18 EQE measurements 111
B.19 Losses study of the different interfaces 112

1 Introduction

1.1 General context

[I] The development of efficient but low cost renewable electricity sources is essential to sustain the momentum towards a carbon-free society and achieve the objectives of the 2015 World Climate Conference agreement. Photovoltaics (PV) is driving the progression of renewable electricity generation technologies, with more than 623 gigawatts (GW) installed worldwide at the beginning of 2020 [1], and surpassing the symbolic terawatt installed capacity early 2022. However, realizing these climate goals will require these numbers to quickly increase: terawatts of renewable electricity generation capacity will soon have to be installed every year [2]. Even though the market-dominating crystalline silicon (c-Si) photovoltaic technology can sustain a large shift of energy systems alone, it will remain limited in its efficiency. The key issue is that c-Si solar cells, or any single-junction technology, do not fully exploits the sun's energy. A 3 eV blue photon absorbed by a c-Si solar cell will thermalize to the band edge and contribute to around 0.6 eV in electrical energy, hence limiting with other processes the efficiency of c-Si to a theoretical maximum of 29.5% [3]. Striving for higher solar cell efficiency is of paramount importance for different reasons. First, for the same amount of produced energy, a more efficient system uses less space, which in itself is already a non-negligible benefit, but it also substantially lowers the cost of solar electricity (through reduction of balance of system costs). Higher efficiency also means that less materials (polymers, metals, glass) are required per given amount of energy produced, thus reducing the environmental impact of the system.

As previously demonstrated with III-V materials [4], the most promising option to reduce transparency and thermalization losses and surpass the 30% efficiency mark relies on stacking at least 2 semiconductors with different bandgaps on top of each other in a multi-junction cell [5]. III-V multi-junction designs can surpass this efficiency value but the scarcity of their

[I] This chapter is partially based on the publication: Guesnay Q., Sahli F., Jeangros Q. and Ballif C., 'Vapor deposition of metal halide perovskite thin films: Process control strategies to shape layer properties' *APL Materials*, (**2021**), with the permission of AIP Publishing. Guesnay Q. did the literature review and analysis, wrote the article and made the figures not adapted from literature. Jeangros Q. did Figure 1.1 and participated to elaboration of manuscript, along with Sahli F. by proposing relevant sources and ideas to enrich the article.

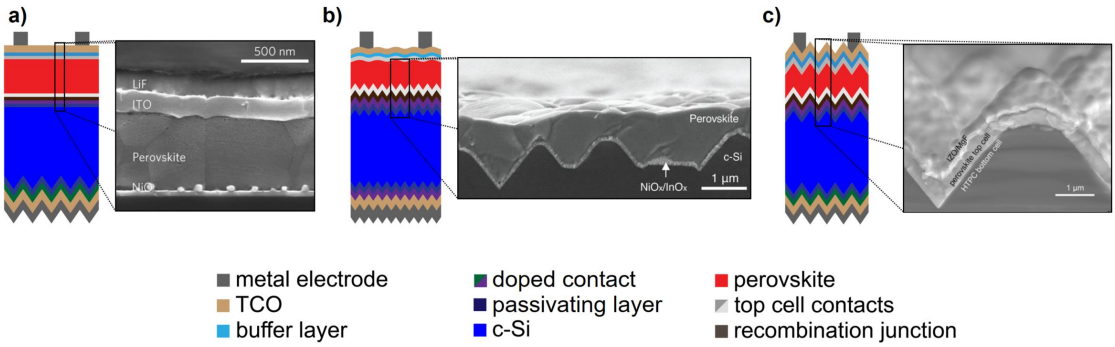

Figure 1.1: Schematics and scanning electron microscopy (SEM) cross sections of silicon heterojunction/perovskite tandem solar cells featuring : a) a solution-processed perovskite cell on a front side-polished structure [16], b) solution-processed perovskite covering a downsized c-Si texture [17], and c) a perovskite solar cell deposited by a hybrid vapor/solution process to conformally coat the texture of the c-Si cell. TCO stands for transparent conductive oxide. Reprinted with permission from [18]. Copyright 2019 American Chemical Society.

constituent materials and their high cost do not allow this technology to achieve a competitive levelized cost of electricity (LCOE), restricting their use to niche markets such as space or military applications. They could possibly be used with concentrated photovoltaics. However, this approach did not succeed to take a significant market share of terrestrial PV. The recent emergence of organic-inorganic metal halide perovskite solar cells may change this situation: this material has the potential to yield cost-competitive highly efficient multi-junction solar modules.

Perovskite semiconductors crystallize in the ABX_3 lattice structure, where A is usually an organic cation such as methylammonium and/or formamidinium, sometimes mixed with Cs, B a bivalent metal such as lead and/or tin, and X a halide such as iodide, bromide and/or chloride. This composition can be adapted to produce materials with bandgaps from 1.2 to >3 eV [6, 7]. In addition to this bandgap tunability, perovskite materials can be processed at low temperatures and still exhibit excellent optoelectronic properties [8], have the potential to be produced at low-costs [9, 10], and exhibit a high power conversion efficiency of currently up to 26% for small area single-junction level [4]. These characteristics make perovskite solar cells the ideal building block of multi-junction solar cells, e.g. with other perovskite cells or on top of a c-Si cell. With c-Si solar cells dominating more than 95% of the market, the latter approach is particularly attractive as it has the potential to upgrade c-Si technologies to efficiencies above 30% [11–15] without impacting the c-Si process flow. Perovskite multi-junction solar cells hence appear as a promising option to continue the learning curve of PV efficiency. At constant $/W, stacking solar cells on top of each other to form a higher efficiency device is the most efficient approach to reduce the cost of a PV system. This is due to the large portion taken by area-related expenses in the total cost of a system.

The direct deposition of a perovskite top cell onto a c-Si solar cell to form a 2-terminal monolithic tandem induces certain constraints on the processing methods that can be used for the top cell. All monocrystalline c-Si technologies commercialized today are based on 6" wafers (or even larger). The front-side is textured by KOH etching to reduce reflection losses and promote light trapping of infrared light. The challenge is that this pyramidal texture complicates the coating of the c-Si cell with conventional perovskite deposition methods, which are based on solution processing [19]. The perovskite layer is about one order of magnitude thinner than the height of the pyramids, typically a few micrometer, it has to cover. Depositing the perovskite absorber from a solution directly on top of this texture results in a discontinuous film, with shunts forming at the position of the summits of the pyramids [20]. To circumvent that issue and still benefit from the global expertise in solution processing, most perovskite/c-Si tandem solar cell reported to date have instead employed a bottom c-Si cell mechanically polished on its front side [10, 16, 21–31] or that features pyramids downsized to a height in the hundreds of nanometer range to enable their coverage by a solution-processed perovskite [17, 32, 33] (Figure 1.1a-b). In both cases, the top surface of the device is flat, leading to lower photocurrents due to an absence of double bounce effects. This optical loss can be only partially mitigated by additional light management schemes (additional antireflective layers, rear-side texturization, front glass texture), which complicate the final product design and manufacturing [26, 28]. Based on these considerations, conformal layers on top of large Si pyramids would be the ideal optical system (Figure 1.1c). Vapor-based deposition methods hence appear particularly suited to achieve this feat. Conformally covering the pyramids of the c-Si cell with a perovskite front cell should eventually facilitate the achievement of tandem efficiencies beyond 30% thanks to short-circuit current densities surpassing 20 mA/cm^2 [12].

Vapor deposition processes have been employed with success to deposit metal halide perovskite materials. Perovskite single-junctions deposited with these approaches reach efficiencies now surpassing 20% [34] and demonstrate a good uniformity when deposited over larger areas (e.g. 100 cm^2 [35–37]). In addition to the conformal nature of the deposited layers [38], another advantage of these methods over solution-based routes include an absence of solvents (which need to be managed at the industrial level). Moreover, sublimating the lead precursors in a dedicated vapor deposition chamber in vacuum greatly reduces contamination risks. Vapor deposition processes also benefit from a strong industrial know-how as physical and chemical vapor deposition techniques are widely applied in industrially mature fields: flat panels, photovoltaic thin films, silicon industry etc. Vapor-based processes hence appear particularly promising to accelerate the transfer of perovskite technologies from the laboratory to industry.

Hybrid vapor deposition processes, defined by sequential usage of vapor depositions of perovskite precursors (inorganic then organic) are especially appealing by the flexibility they provide. Using vapor processes tailored to the inorganic and organic precursors peculiarities is a promising path to a robust and reliable process. Vapor deposition of metal halides (inorganic frame of perovskite structure) is straightforward with already existing and mastered processes such as thermal evaporation or magnetron sputtering. Conversely, organohalide (the organic

core of the perovskite structure) are more delicate to process in vapor phase because of a high vapor pressure and a tendency to decompose upon both transport and evaporation [39, 40]. In a previous work [41], a homemade vapor transport deposition chamber has been developed in-house. The partially achieved ambition was to demonstrate an industrially compatible system for the deposition of organohalides, to convert metal halide template into perovskite. While demonstrating homogeneous coating of a textured wafer on large area (239 cm^2) and decent proof of concept devices, the process was still long (hour scale), and turned out to be unable to deposit the high performing formamidinium organic cation. The motivation of this thesis is to follow on from this pioneering work.

1.2 Objectives and structure of the thesis

The main objective of this thesis is to study, understand and circumvent the limitations faced by the initial vapor deposition system developed in-house [41]. The final goal is to develop a perovskite vapor deposition process industrially relevant in terms of homogeneity, robustness and flexibility.

The first chapter following this introduction reviews the basics of photovoltaic principles and specificities of perovskite semiconductors. A short overview of the characterization techniques used in this thesis is also provided.

The following chapter is a critical review of the state of the art of perovskite vapor deposition. This analysis is deepened by a discussion of the theories of thin film growth in light of experimental observations. The assessment of the flaws and limitations of existing systems is used as a basis for the development of a new deposition process in the next chapter.

The last chapter of this manuscript presents the experimental results obtained during the thesis. The first section of that chapter lays the first stone of a potential evolution of the current co-evaporation process of the metal halide template. The single source evaporation of pre-mixed metal halide precursors is studied. Finally, the second part of that chapter presents the main objective of this thesis : the development of an industrially relevant vapor deposition process of organohalides. After a presentation of the experiments-based principles that led to the development of the new process, a complete picture of the process is portrayed, by an identification of the growth regimes, influence studies of process parameters, chemical environment and mechanical design. Solar cell devices of high quality and a robust baseline are also demonstrated.

1.3 Contribution to the field

This work contributed to the field of perovskite vapor deposition in different ways. First of all, the published literature review analysis [42] is a unique and exhaustive critical breakdown proposing models explaining perovskite precursors evaporation and perovskite thin films growth, based on experimental facts and theoretical considerations.

The single source evaporation of mechanically mixed metal halide precursors [43], is to our knowledge the first report of its kind in literature, showing the absence of phase formation after ball milling, highlighting necessity of future work studying the formation conditions of such phases. Moreover, the in situ GIWAXS study of the evaporation combined to EDX analysis of deposited thin films reveals that a halide exchange is happening during the process. Proof of concept devices of photovoltaic solar cells are demonstrated, with a satisfying 15% efficiency with a bandgap of 1.7eV.

As discussed earlier, vapor deposition of organohalides for perovskite thin films often met various limitations when practical applications were proposed. Based on our lab's experience and literature analysis, an evolution of the existing processes is proposed, resulting in a fast, flexible, robust, low cost and simple process. Moreover, in depth characterization of the process provides new insights on the perovskite conversion and on the influence of the chemical environment and mechanical design on the process. Often overlooked in literature, the latter two topics are demonstrated to have a significant impact. A robust and flexible baseline of photovoltaic devices yielding up to 17% efficiency with 1.63eV bandgap is demonstrated as proof of concept. The results described in the current paragraph are summarized in a manuscript to be submitted for publication and were in part presented in international conferences (EU PVSEC 2021, WCPEC 2022).

2 Basics of photovoltaics and perovskite peculiarities

This chapter introduces the basics of photovoltaics, including perovskite specificities, and the methods used to analyse perovskite thin films. Deliberately using as little equations as possible, it is by no mean an exhaustive course on these topics, and readers interested in may want to consult, for example, the following references [44–46].

2.1 Physics of Photovoltaics : General Considerations

Photovoltaic devices convert solar irradiation into electrical power. This transformation is quantified by the power conversion efficiency (PCE), the ratio of the produced electrical power divided by the incoming power of sun's irradiation. Directly driving the cost of produced electricity, the output power of photovoltaic devices logically gathers most of the research and development efforts. This section introduces how the two components of electrical power, voltage and current, spring up in a photovoltaic solar cell. Sources of fundamental losses, charge recombinations, are also introduced.

2.1.1 Origins of voltage

The photovoltaic effect arises from a particularity of semiconductors, the bandgap (E_g). From the interaction between the outmost electrons of atoms in molecules, continuum bands of allowed energy values (taken by electrons) emerge in semiconductor solids. The bandgap can be simply described as the energy difference between the top of the farthest band mostly full of electrons (valence band) and the bottom of the next energy band, mostly empty (conduction band).

If this range where no electronic state exists is sufficiently small, external stimulus (heat, light) can provide enough energy to an electron in the valence band to reach the conduction band, leaving a 'hole' behind. In the case of the photovoltaic materials considered in this thesis, the charges generated this way can then be considered as 'free' carriers, moving in the conduction band until extraction from the semiconductor or deexcitation.

In the practical case of photovoltaic devices, it means that only photons with an energy higher than the bandgap (E_1, E_2 in Figure 2.1) will have enough energy to raise an electron from the valence to the conduction band, and thus contribute to the produced electrical power. Photons with an energy lower than the bandgap (E_3) cannot raise an electron from one band to the other and thus cannot be absorbed: they are transmitted through the material. Photons with an energy much higher than the bandgap (E_1) raise the electron in a corresponding high energy state. However, due to the pace at which intraband relaxation happens, the excess energy above the bandgap is dissipated (via so called thermalization) too fast to be extracted in conventional solar cells. The potential difference, or voltage, that a photovoltaic material can deliver is thus dictated by its bandgap, irrespective of the energy of absorbed photons.

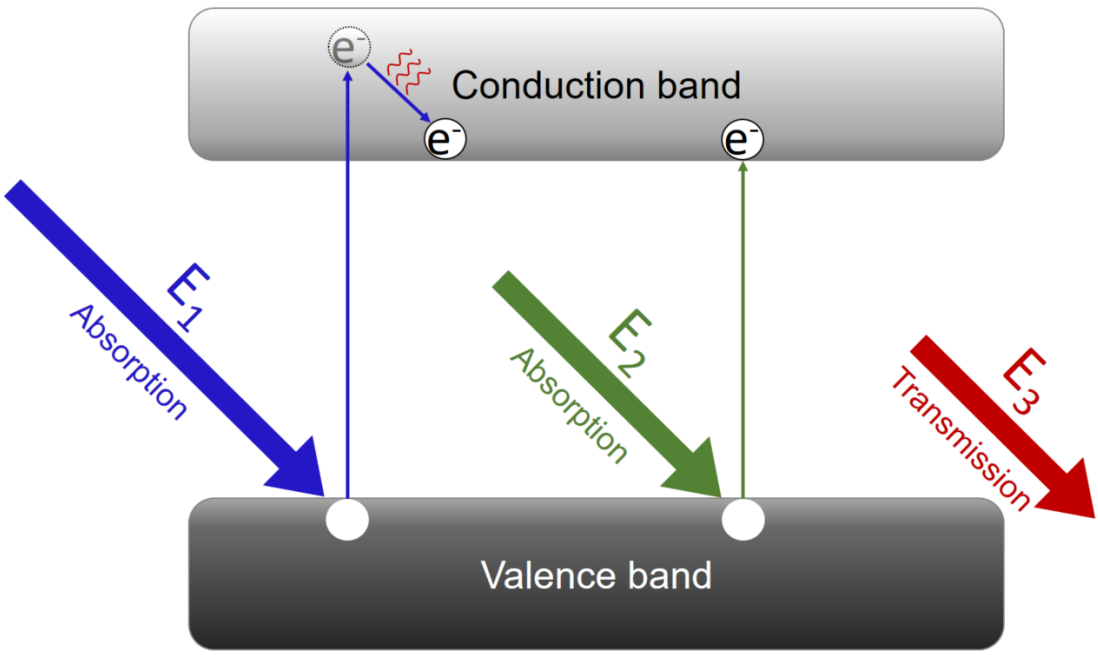

Figure 2.1: Absorption and transmission of light by a semiconductor. Photons with energy higher or equal to the bandgap (E_1, E_2, resp.) are absorbed and generates hole-electron pairs. Electrons with excess energy then thermalize (energy dispersion via heat exchange with lattice), to the band edge. Electrons remain at that energy level before recombining or being extracted. Photons with energy lower than the bandgap (E_3) are transmitted through the semiconductor.

The usable (entropy free) part of this potential energy is described by the quasi-Fermi level splitting (QFLS), also called electrochemical potential. Divided by the elementary charge e, it gives the maximum voltage achievable by the considered semiconductor.

$$QFLS = E_g - k_B T ln\left(\frac{N_c N_v}{np}\right) \tag{2.1}$$

With k_B the Boltzmann constant, T the temperature, N_c and N_v effective density of states in conduction and valence band respectively and n, p the electron and hole densities respectively. The prefactors N_c and N_v are proportional to $T^{\frac{3}{2}}$.

This expression points out that high bandgap material, lower temperatures and high charge concentrations promote high voltage in a photovoltaic device.

2.1.2 Origins of current

The AM1.5G standard solar spectrum considered when developing solar cells is depicted Figure 2.2. It was chosen as being representative of the average irradiance throughout the year in temperate latitudes. The result can be expressed as the emission of a 5800K blackbody (effective temperature of the photosphere of our sun) minus absorption throughout the corresponding portion of atmosphere crossed.

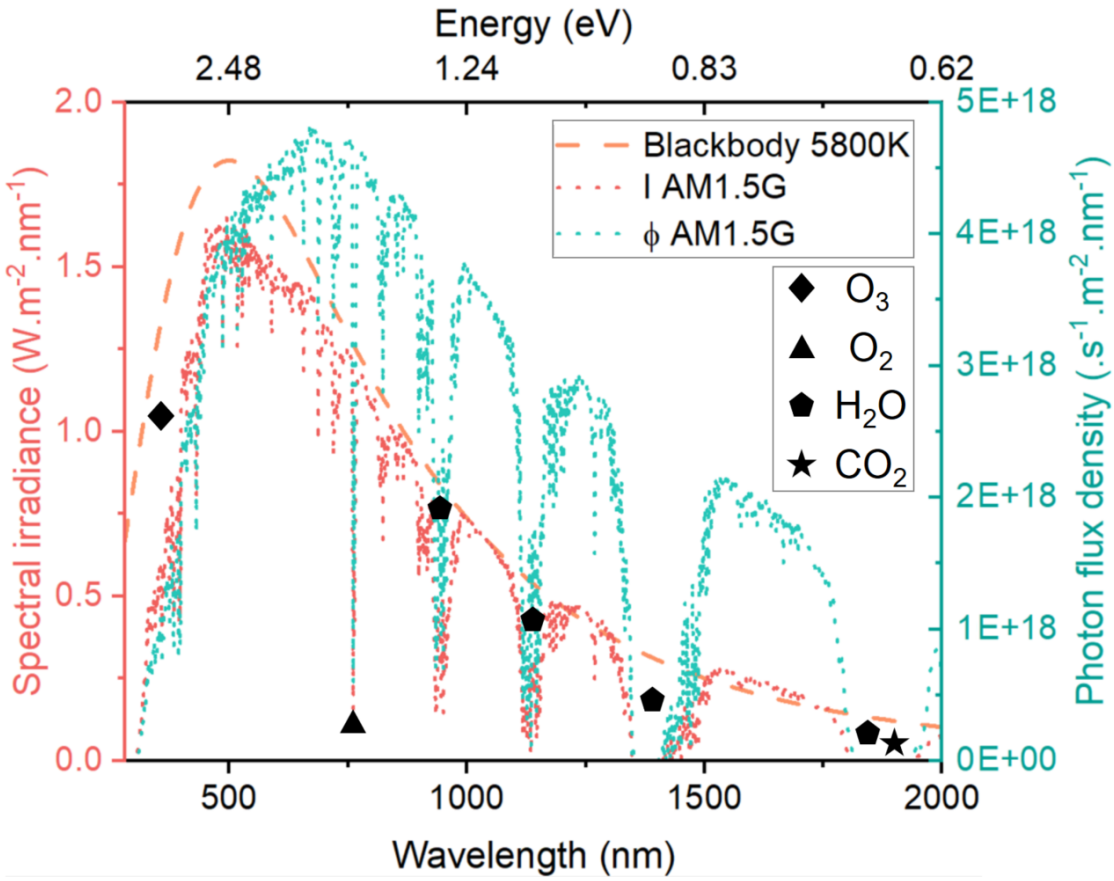

Figure 2.2: Blackbody radiation at 5800K, standard AM1.5G spectral irradiance and corresponding photon flux density. Differences between blackbody radiation and AM1.5G spectral irradiance is due to absorption by atmosphere's molecules.

Dividing the spectral solar irradiance by the energy of photons, the photon flux density ϕ (incoming photons per second per area for each wavelength/energy) is deduced and plotted on the right axis of Figure 2.2. As described in the previous section, in an ideal case, any photon with an energy higher than the bandgap is absorbed by the semiconductor and generates an electron assumed to be mobile and participating to generated photocurrent. Consequently, the maximum current density (current produced per area) can be expressed as follow :

$$J_{max} = e \int_{E_g}^{\infty} \phi(E)\, dE \tag{2.2}$$

This expression suggests that the bandgap of a semiconductor should be minimized to maximize the output current of the photovoltaic device. However, previous section showed that the voltage is maximized when increasing the bandgap. This interplay, with other minor phenomena (namely Boltzmann, Carnot and emission losses), greatly reduces the maximum electrical power that can be generated with a single material. Multijunctions solar cells overcome this limit by associating semiconductors with different bandgaps for a more optimized absorption of the solar spectral irradiance.

2.1.3 Fundamental losses

After photon absorption, the generated charge carriers have to be extracted from the semiconductor to participate to the generated electrical power. Before extraction, generated free carriers can deexcitate through different mechanisms and thus, not participate to the generated power. These fundamental losses are called recombination. Reducing the amount of circulating electrons, they lower the current; and reducing the population of free carriers they also reduce the voltage (cf. equation 2.1). It is thus the highest priority to reduce as much as possible these losses happening after photon absorption and before charge extraction.

Due to the finitude of real semiconductors used in photovoltaics, the periodicity of the crystalline materials used is broken at the external surfaces of the films. This discontinuity generates defects at the surfaces acting as intermediate energy states, dramatically facilitating the recombination of charges. Strategies called 'surface passivation' are used to prevent this harmful phenomenon.

Impurities and structure defects, if electronically active, can create energy states within the bandgap. Close enough to the conduction or valence band, these traps are benign to solar cell operation : although they may capture free carriers, thermal excitation will allow the carriers to rejoin their respective bands. However, close to the middle of the bandgap, thermal excitation

is not enough to rejoin the bands, and recombination by capturing a carrier of opposite charge is much more probable. This trap-assisted recombination, or Schokley-Read-Hall recombination, can drastically reduce free carrier populations. A lot of efforts is dedicated to obtain the purest and defectless possible semiconductors to reduce this type of recombination.

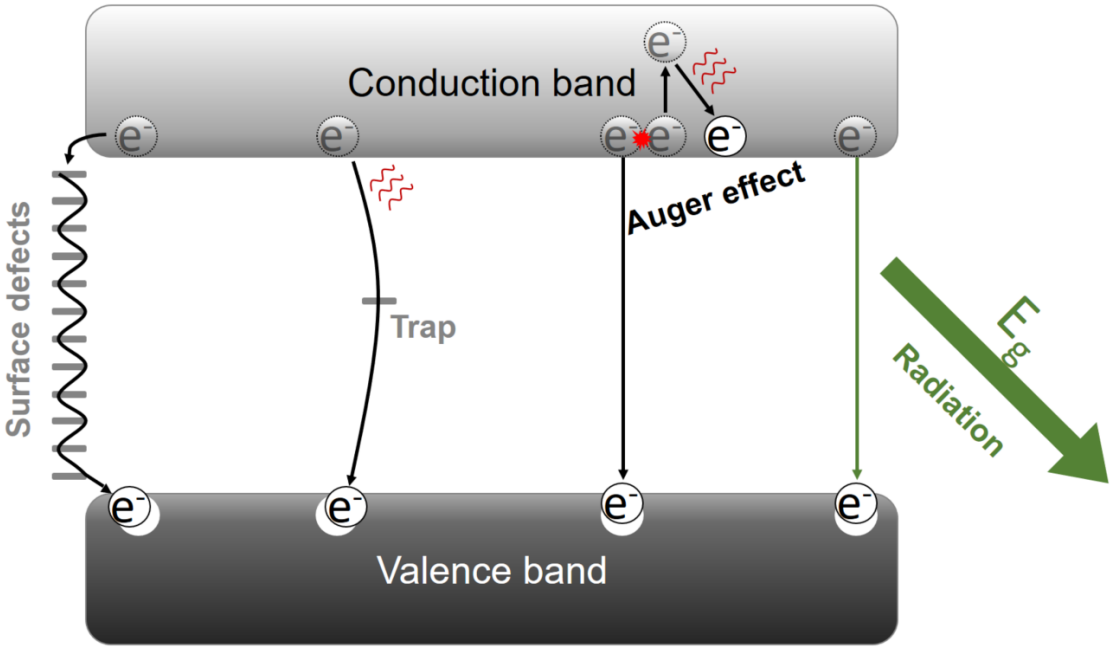

Figure 2.3: Recombination mechanisms in a semiconductor : surface, Schockley-Read-Hall or trap-assisted, Auger and radiative recombinations. In non-concentrated perovskite photovoltaics Auger recombination is negligible, and radiative recombination is by definition unavoidable. Efforts are focused on reducing surface and trap-assisted recombinations.

Auger recombination happens when two excited electrons interact together, one transmitting its excitation to the other. The electron loosing energy goes back to the valence band, while the extra-excited electron goes to higher energy state in the conduction band. However, given the timescales of charge extraction and thermalization in a solar cell, this extra energy is lost before being useful to power generation. This type of recombination becomes predominent in cases of very high carrier concentration (highly doped layers, concentrated photovoltaics) and thus has minor impact in the photovoltaic materials considered in this thesis.

Recombination by emission of a photon, or radiative recombination, is the reciprocal process of absorption and unavoidable by definition (cf. Kirchhoff's law of thermal radiation). This emission close the bandgap of the material is used in photoluminescence to deduce the preponderance of the other recombination mechanisms, and thus, thin film quality.

2.2 Perovskite peculiarities

Contrary to most conventional semiconductors used in photovoltaics, halide perovskites are ionic crystals. With the general structure ABX_3, with A an organic cation (formamidinium, methylammonium) sometimes alloyed (caesium, guanidinium etc), B a bivalent metal (lead or tin) and X a halide. From this ionic characteristic arises parasitic ionic losses when operating as solar cell and an acute sensitivity to moisture or any kind of polar solvent.

One of the most appealing feature of perovskites for photovoltaic is the ability to tune the semiconductor properties by changing, alloying the different ions of this ABX_3 structure. Absorption, stability or crystalline phase can be precisely designed this way, but bandgap tunability is a major motivation for perovskite development. As detailed previously, increasing further the electricity produced by photovoltaic cells will have to rely at some point on multijunction solar cells. The list of eligible candidates for high efficiency and low cost photovoltaic electricity being small (and so the list of usable bandgaps), the advent of the low-cost and bandgap tunable perovskites offers a very attractive possibility for the next evolution of photovoltaics.

Besides, perovskites also feature high electrons and holes mobilities, promoting good charge extraction, essential for high solar cell efficiency. The direct bandgap provides a very high absorption coefficient, allowing thin films to fully harvest solar energy. Interestingly, perovskite compositions used for photovoltaics present some structural defect tolerance. This particularity comes from the fact that the potential vacancies in the perovskite lattice produce trap states either lying close to or within the bands (conduction or valence), making them benign for photovoltaic power production, as explained in previous section.

The consensus on perovskite solar cell operation is similar to working principle of n-i-p or p-i-n thin film solar cell : the perovskite thin film behaves as an intrinsic layer generating free carriers (electrons and holes) upon light absorption. The as-generated charges are then screened/collected by contacts depending on their polarity, establishing a current flow with the corresponding electrodes and external circuit. Charge transport layers are chosen to have a good selectivity (i.e. allowing transfer of charges with a certain polarity and repelling the charges of opposite polarity) based on their energy levels. They must also ensure a good mobility of the charges and good transparency to prevent parasitic absorption of light. The interfaces between charge transport layers and the perovskite (whether it is the layer on which perovskite is grown, thus influencing the whole perovskite growth, or the charge transport layer deposited on the formed perovskite) have to be carefully design to avoid formation of interface states that would drastically reduce the performances of the solar cell through surface recombination. This simplistic model can be complexified in practice by adding passivating, buffer or antireflective layers to the stack and taking into account ionic effects due to the relatively high ionic mobility in the perovskites [47].

2.3 Characterization : how to analyse photovoltaic perovskite thin films ?

2.3.1 X-ray diffraction

Diffraction happens when radiation with a given wavelength meets an object with a dimension close to its wavelength. Taking the range of possible distances between the planes of crystals, the corresponding wavelength is in X-ray range. From constructive interferences between the incoming X-rays and the crystal lattice, diffraction only happens at characteristic angles. Thus, measuring then studying the diffraction pattern of a fabricated thin film indicates what crystalline species are present in the film and predominance of each crystalline phase. Playing with angle of incidence gives access to different penetration depths and allows studying different regions of the sample.

Synchrotron X-ray diffraction (SXRD), used in this thesis, uses a particle accelerator as X-ray source instead of the traditional Cu-K α lab sources. Thanks to a much higher intensity and brilliance, SXRD provides diffraction patterns with a much better resolution, and guarantees an acquisition time small enough to comfortably run in-situ experiments.

In grazing incidence wide-angle X-ray scattering (GIWAXS), also used in this thesis, a large two dimensionnal detector is positioned close to the sample. The projection of the diffraction patterns on a wide 2D detector allows to determine the orientation of the crystalline phase with respect to the substrate. Insights on thin film growth or structure rearrangement can be deduced from this information.

2.3.2 Spectroscopy

Ultraviolet-visible-near infrared (UV-Vis-NIR) spectroscopy examines the interaction of light with matter across the cited ranges of electromagnetic spectrum. It relies on the principle of absorption spectroscopy, where molecules selectively absorb light at specific wavelengths, leading to distinct absorption patterns. Insights on absorption coefficient or optical bandgap can be obtained quickly and without damaging sample. UV-Vis-NIR can also be used to monitor perovskite degradation.

Fourier-transform infrared spectroscopy (FTIR) probes the full infrared spectrum at once, shining different infrared wavelengths at different frequencies. Fourier transform is performed to disentangle raw data and obtain absorption spectrum on the full range. Compared to a scan wavelength by wavelength with a monochromator, this approach highly accelerates measurement. The probed range corresponds to the fundamental vibrations of molecular bonds, allowing non-destructive and swift chemical analysis of samples.

2.3.3 Nuclear magnetic resonance

Nuclear magnetic resonance (NMR) is based on the intrinsic magnetic moment of some atomic nuclei (hydrogen, carbon 13 etc) due to nuclear spin. Exposed to a strong magnetic field, the nuclear spin preferentially aligns itself with the external field. Radiofrequency pulses are then applied at given frequencies, perpendicular to the magnetic field to excite nuclei. Characteristic relaxation is recorded with detection coils. NMR provides precise quantitative insights on chemical bonds, as well as info on how these different bonds, atoms interact together (with the proper pulse sequence).

2.3.4 Time of flight secondary ion mass spectrometry

In time of flight secondary ion mass spectrometry (ToF SIMS), a high-energy beam of primary ions, typically gallium, is directed onto the surface of a sample. This bombardment induces the release of secondary ions from the sample's surface, then analyzed by a mass spectrometer. ToF SIMS allows precise detection and quantification of atoms or molecules, as well as depth profiling.

2.3.5 Electron microscopy

Scanning electron microscopy (SEM) uses electrons, instead of photons in conventional optical microscopes, to probe surface of samples with a high resolution. Dedicated detectors analyze the different interactions of the primary electron beam and the sample. Low energy 'secondary' electrons are kicked out of the sample, giving images with a topographic contrast. Electrons of the primary beam backscattered by the sample produces images with an atomic number (Z) contrast. In the sample, some electrons are excited to higher energy levels of inner shells; upon deexcitation they emit characteristic X-rays. With a dedicated detector (energy dispersive X-ray spectroscopy or EDX), element identification with corresponding SEM imaging can be performed.

2.3.6 Photoluminescence

Photoluminescence (PL) designates the emission of light following photon absorption. In practice, a monochromatic laser irradiates a semiconductor with an energy much higher than its bandgap. As described previously, the semiconductor then emits light around its bandgap via radiative recombination. By precisely quantifying the photoluminescence quantum yield (PLQY, how much photons are emitted per photons absorbed), one is able to directly obtain the quasi-Fermi level splitting (QFLS) of a semiconductor. PLQY provides a fast and non-destructive estimation of the maximum voltage attainable by a solar cell featuring the measured semiconductor. It is used to evaluate intrinsic thin film quality but also losses (non radiative recombinations) induced by contact with other layers.

2.3.7 Photovoltaic device characterization : current-voltage characteristic and external quantum efficiency

The current density - voltage (JV) curve is a fundamental characteristic of solar cells, displaying the current flowing per illuminated area under different applied voltages. By definition, power conversion efficiency is defined with the standard AM1.5G spectrum with a 1000W per m^2 intensity. The point by point multiplication of current and voltage gives the power output of the photovoltaic device. However, much more can be inferred from JV curves. When the device is maintained in open circuit condition, charges are not extracted anymore from the cell, so the current is null and voltage is at its maximum value. The corresponding open circuit voltage is then directly related to the bulk lifetime of the charge carriers and the different recombination mechanisms. Conversely, when the solar cell in is short circuit, the voltage is null and the extracted current is at its maximum. This short circuit current can give hints on optical or collection losses. From the shape and the slopes of the JV curve itself, several other loss sources can be detected : shunts, potential barriers, high series resistance etc.

External quantum efficiency (EQE) is a measurement complementary with JV, giving how much electrons are produced per incident photon. Varying photon's energy illuminating the solar cell with a monochromator, the EQE spectrum depicts the cell's efficiency across the entire solar spectrum. Dividing EQE by one minus the reflection losses, internal quantum efficiency (IQE) is obtained, giving how much the absorbed photons contribute to the produced current. Combining both EQE and IQE helps to distinguish among the different possible losses in a photovoltaic device. Besides, their spectral dependency allow to probe different parts of devices : while high energy photons are absorbed in the first few dozens of nanometers in the cell, low energy photons of the solar spectrum travel across the full thickness of the cell.

3 State of the art and theory of perovskite vapor deposition

Vapor-based processes are particularly promising to deposit the perovskite thin film absorber of solar cells. These deposition methods are up-scalable, involve a controlled solvent-free environment, have the ability to conformally coat rough substrates, involve soft, low-energy deposition conditions, are compatible with shadow masks for patterning, and are already widely deployed at the industrial level. Still, solar cells featuring layers processed with these methods have not yet reached the same performance as their solution-processed counterparts, in part, due the complexity of controlling the sublimation of the organic precursors.

This chapter[I] will discuss the different vapor-based deposition processes that have been reported to deposit perovskite thin films and will discuss reaction chamber designs that provide an enhanced control over the deposition process.

The second part of this chapter will then link experimental observations, regarding layer properties depending on process conditions, to theoretical concepts describing the sublimation and condensation of precursors and the growth of the perovskite thin film.

[I]This chapter is based on the publication: Guesnay Q., Sahli F., Jeangros Q. and Ballif C., 'Vapor deposition of metal halide perovskite thin films: Process control strategies to shape layer properties' *APL Materials*, (**2021**), with the permission of AIP Publishing. Guesnay Q. did the literature review and analysis, wrote the article and made the figures not adapted from literature. Jeangros Q. and Sahli F. participated to elaboration of manuscript by proposing relevant sources and ideas to enrich the article. Louis Rotrou is also thanked for his time saving advice with software Blender.

3.1 Introduction

In this chapter, we will discuss the different vapor deposition processes that have been used to deposit organic-inorganic lead-halide perovskite materials. A classification of the different methods is done considering whether the sublimed vapors are brought to the substrates without or with a carrier gas, a classification that we label here "line-of-sight" and "vapor transport deposition" techniques, respectively. Processes relying on the sequential use of techniques belonging to both categories are defined in this state of the art as hybrid vapor deposition processes. This categorization was preferred to the classical chemical vapor deposition (CVD) versus physical vapor deposition (PVD) one, since processes labelled PVD may also involve a decomposition of precursors and chemical reactions in the case of perovskite processing. We would like to mention here that the techniques presented below are often unequally investigated, meaning that device properties (active area, efficiency, stability) scatter significantly but not necessarily as a result of inherent weaknesses of certain methods.

After reviewing the wide variety of methods used to deposit perovskite thin films from vapors, we will aim to link experimental observations regarding layer chemistry and morphology to theoretical concepts describing the evaporation of precursors, their condensation on substrates, and the perovskite growth mechanisms.

3.2 Vapor deposition of metal halide perovskite solar cells

3.2.1 "Line-of-sight" vapor deposition processes

Methods labelled here "line-of-sight" vapor deposition regroup techniques in which precursors are sublimated directly towards the substrates without the intervention of a carrier gas. These evaporations are usually performed in high vacuum conditions to increase the mean free path of the evaporated species, lower sublimation temperatures, and improve the purity of the as-deposited layers.

Co-evaporation from multiple precursors

Thermal co-evaporation in high-vacuum

Co-evaporation consists in simultaneously sublimating multiple precursors in a chamber maintained in high vacuum (around 1.10^{-3} Pa). Loaded in crucibles facing a rotating substrate holder, precursors are brought to their respective sublimation point. A schematic of the technique is presented in Figure 3.1a. In 1997, Era *et al.* [48] reported the first co-evaporation of two and three dimensional perovskites, including of cubic methylammonium lead triiodide ($CH_3NH_3PbI_3$, or MAPI). A few years later, Matsushima *et al.* successfully fabricated field effect transistors by co-evaporating a tin halide perovskite [49, 50]. The first co-evaporation of a perovskite layer included in a solar cell was reported in 2013 by Liu *et al.* [51]. In this pioneering

work, solar cells were produced by co-evaporating methylammonium iodide (CH_3NH_3I, or MAI) and lead chloride ($PbCl_2$). The fabricated solar cells achieved a power conversion efficiency of 15%. These vapor-deposited layers exhibited a uniform microstructure as well as a homogeneous thickness. These thermal co-evaporation processes did not require any post annealing step [52–54], a potentially important aspect regarding a potential industrialization of the process.

One issue became however rapidly evident with thermal co-evaporation: the high vapor pressure of organohalides. Indeed, the evaporation rate of a precursor is usually controlled by a quartz crystal microbalance (QCM). Due to their poor sticking on surfaces, organohalides may re-evaporate from chamber surfaces and from the QCM supposed to monitor their evaporation rate, leading to severe reproducibility issues. In addition, these organic precursors usually evaporate following a multidirectional flow, leading to their deposition on QCMs dedicated to other precursors as depicted in Figure 3.1a. Furthermore, the calibration of the QCM monitoring the organohalide sublimation rate is made complex by their tendency to grow under Volmer-Weber or Stranski-Krastanov modes [55], leading to layers with inhomogeneous thicknesses when deposited on their own. Additionally, Borchert *et al.* [56] demonstrated that QCMs used to monitor evaporation rates are very sensitive to the organohalide impurities typically found in commercially available powders. Originating from the synthesis process of MAI, these impurities usually have a higher sticking coefficient on the gold surface of QCMs than pure MAI.

Different approaches have been explored to facilitate process control, notably by controlling the vapor pressure during deposition [57], the composition of the evaporated compounds [58], or the substrate temperature to tune the perovskite growth [55]. Researchers have proposed to circumvent cross-talk and cross-contamination issues by either using a Knudsen cell evaporator and a QCM facing the opposite direction of the substrates [59], or by adding a shield between the inorganic and the organohalide sources [55]. In addition, cooling the evaporation chamber down to -25°C as demonstrated by Roß *et al.* prevents the re-evaporation of organics from chamber walls and QCMs [60]. Other research groups calibrated the organohalide evaporation rate off-line by analyzing the perovskite layers with different MAI:PbI_2 ratios by X-ray diffraction (keeping the evaporation temperature of MAI constant) [61]. This approach resulted in 20%-efficient perovskite solar cells. An interesting outcome of this work is that high efficiency cells were obtained with an absorber featuring relatively small grains. The trend in the field is usually to promote films with large grains spanning across the full perovskite absorber thickness. An alternative control strategy was recently proposed by Lohmann *et al.* [62]: the PbI_2 deposition rate was kept constant while the MAI sublimation rate was varied. The MAI evaporation rate was then deduced from the difference between the thickness measured at a QCM located close to the substrates and that from a QCM close to the PbI_2 crucible. This method presents the advantage that MAI will stick more easily on the PbI_2-coated QCM.

Figure 3.1: a) Thermal co-evaporation b) Laser co-evaporation c) Close space vapor transport system. [63]

Despite the general issue of precisely controlling composition, proof of concept solar cells produced by co-evaporation and featuring different cations and halides have been demonstrated [52, 64, 65]. This evolution from depositing MAPI to mixed perovskites is especially important for perovskite/silicon tandem solar cells, where a fine control of the perovskite top cell bandgap and thickness is necessary to ensure maximum performance [11, 66]. In addition, replacing MA with formamidinium ($(HC(NH_2)_2$ or FA) and Cs yields layers that are thermally more stable [67–69]. Recently published studies report vapor-deposited devices exhibiting a stability comparable to the state-of-the-art. In Ref. [38], 99% of the initial power conversion efficiency (PCE) was retained after 1000h at maximum power point under a 1-sun illumination, in nitrogen atmosphere. Cells deposited via vapor-based processes were also subjected to thermal stresses, with some devices keeping 80% of their initial PCE after 3600h at 85°C in 10% relative humidity (RH) [70]. Promising efficiency and stability were also reported with mini-modules [71]: 18% on an active area of 21 cm^2 with good stability in various conditions (>85% of initial PCE after 8000s at maximum power point (MPP) in 70% RH, 80% after 100h at 65°C, 95% after 60 days on a shelf in 35% RH).

Compared to solution-processing, one limitation of thermal evaporation is the need to reach a high vacuum and the high source temperatures that are needed (several hundreds of °C depending on the precursor). Pumping down to such pressure and the delay induced by the need to warm/cool sources add to the process time, generally comprised between 30 minutes and 2 hours. It indicates that dedicated production tools with load-lock and linear sources would be required to achieve reasonable throughputs.

Laser-induced co-evaporation

Miyadera *et al.* introduced in 2016 [72] a co-evaporation process in which the precursors are not sublimed by conventional resistive heating but by a continuous laser exposure, leading to a local heating of the MAI and PbI_2 precursors. A schematic of the setup is presented in Figure 3.1b. Compared to the usual resistive heating of the entire crucible plus the quantity of precursor necessary for a full evaporation, this method greatly reduces the thermal response

of the sublimated material and should provide a more precise control over the evaporation rate. The best performing solar cell processed with this route achieved an efficiency of 15.4%. Still, it should be mentioned that this method has remained largely unexplored, likely due to the complexity and cost of such an evaporation system.

Sequential evaporation routes

As a response to the cross contamination and cross-talk issues occurring during co-evaporation, sequential evaporation processes have been developed. Instead of sublimating the precursors simultaneously, metal halide salts are evaporated first, followed by the organohalide salts.

Sequential thermal evaporation in high vacuum

Sequential evaporation in high vacuum is usually performed using the same chamber [73–76], except in the notable work of Hsiao *et al.* [77]. There, two vacuum chambers were used, one for the lead halide precursor, transport layers and electrodes and another one specifically dedicated for the sublimation of organohalides. The evaporation of the latter was monitored by controlling the partial pressure of the methylammonium iodide (MAI) vapor. The authors achieved a complete conversion of the lead iodide into a perovskite phase by fine tuning the partial pressure of MAI. The duration of the process is one weakness of such sequential approaches. In this case, the MAI deposition step took two hours to reach optimal results, in part due to the density and thickness (240 nm)of the PbI_2 layer that needed to be converted.

Chen *et al.* [75] highlighted the tradeoff that must be reached regarding substrate temperature when depositing MAI. As the penetration of MAI in the lead halide template is diffusion-limited, there is an incentive to increase the substrate temperature to promote conversion. However, doing so also decreases the sticking coefficient of the organohalide vapors on the substrate. In this work, the difficulty of controlling the MAI evaporation rate with a QCM also led the authors to evaporate the organic precursor at a constant temperature. Another way of producing a perovskite absorber with suitable thickness and complete conversion is to perform alternated depositions [78, 79]. Successive layers of PbI_2 and MAI are sublimated one by one in the vacuum chamber, with varying thicknesses and number of pairs of layers. Meant to facilitate the conversion, this layer-by-layer technique still requires, in the presented cases, a post-annealing step to complete the conversion (typically from one to two hours). Another alternated deposition scheme was demonstrated by Feng *et al.* [34], who produced cells with an impressive efficiency of 21.3%. Their vacuum deposition setup features three sources: PbI_2, FAI and CsI. These sources vaporize one at a time their respective species, following which the samples stay in the vacuum chamber for a post annealing to completely form the perovskite. Each deposition is monitored with a dedicated QCM. With this setup, a 10 cm^2 module with an efficiency of 14.6% PCE was also demonstrated, as well as large area (400 cm^2) perovskite films with high crystalline quality.

Close-space sublimation of organohalides

In high-vacuum line-of-sight evaporation processes, having a certain distance between the sources and the substrates improves the homogeneity of the deposition of precursors, as some have a ballistic behavior during sublimation. This distance, generally a few tens of centimeters, must be adapted to the size of the substrate to coat, as longer distances lead to a loss of material. Things however differ for organohalides as they tend to deposit everywhere in the chamber, even on surfaces not directly in the line-of-sight of the crucible [59]. In that regard, close-space sublimation methods employ a chamber with a small gap between substrates and source [36, 63, 80–83]. Substrates can be exposed to a MAI vapor by enclosing substrates and the MAI powder in a closed and heated vessel [84–86], or even by heating substrates directly in contact with the organohalide powder [87]. Despite their relative simplicity, these processes have resulted in high efficiencies in the range of 15-20%. Various compositions, from simple MAPI to mixed cations perovskites, were demonstrated. Layers were included in mini-modules, which exhibited an efficiency of 12% for an active area of 41.25 cm^2. The PCE of these devices remained above 80% after 200h of storage in ambient conditions (RH = 30%, 25°C) and when heated to 60°C (nitrogen atmosphere) [36].

In addition to powders, the organohalide precursor used in close space evaporation can be made by solution processing (e.g. spin or spray coating) or dry alternatives such as pressed powder in the form of pellets [63]. Most close space evaporation studies report long vapor exposure and/or post annealing steps, and sometimes a washing of the excess of MAI by isopropyl alcohol before annealing. Still the process flow can be accelerated, as demonstrated by Li *et al.* [63] who presented a process taking about 10 minutes for the evaporation, washing and annealing.

Overall, dissociating the evaporation of the inorganic and organic perovskite precursors enables an easier process control. One issue however is that the already long processing time tends to be exacerbated by the addition of extra steps.

Single source vapor deposition processes

Another way of facilitating process control is to place all the precursors in a single source. This group of methods evaporate precursors pre-mixed in various forms, namely thin films, powders or targets.

Flash evaporation routes

Mitzi *et al.* introduced the concept in 1999 with the so-called thermal ablation technique [88]. One of the initial purpose of the method was to uniformly coat irregular surfaces with a perovskite for light emitting applications. To circumvent issues linked to controlling the sublimation rate of each precursor separately, both the organic and inorganic precursors were dissolved in a solvent (anhydrous N,N-dimethylformamide, or DMF), before dispersing

the resulting solution on a tantalum sheet (chosen for its high melting point and chemical resistance). The tantalum sheet was then connected to two electrodes inside a vacuum chamber, before passing a large current through it to rapidly sublime the precursors. The deposited perovskite layers did not require any post-deposition treatment.

The first application of perovskite thermal ablation for photovoltaics comes under the denomination "flash evaporation", which was introduced in 2015 by Longo *et al.* [89]. The precursor employed were MAI and PbI_2 dissolved in DMF deposited by meniscus coating on a tantalum sheet and annealed to form MAPI. The tantalum sheet was then loaded in a high vacuum chamber, which was quickly heated to sublimate the film after reaching a pressure of 10 Pa. The setup is presented in Figure 3.2a. The deposited thickness was controlled by the amount of material on the tantalum sheet. Solar cells made with this approach reached an efficiency of 12.2%. Xu *et al.* [90] investigated the perovskite formation and highlighted the importance of performing the flash evaporation in high vacuum to form dense MAPI films. Pressures higher than 10 Pa led to perovskite films with irregular grains and voids.

In 2016, Fan and co-workers [91] reported a single source evaporation method midway between flash evaporation and classical thermal evaporation. A pure MAPI powder synthesized in-house was loaded in a high vacuum thermal evaporation chamber, before rapidly heating the crucible to evaporate the powder. The evaporation lasted three minutes, longer than flash evaporation but much faster than conventional thermal deposition processes. The thin film deposited on the substrates did not require any post treatment annealing and displayed a good uniformity and phase purity. Solar cells reached an efficiency of 10.9%. In 2018, Lan *et al.* [92] used the same process to deposit formamidinium lead triiodide perovskites ($FAPbI_3$ or FAPI).

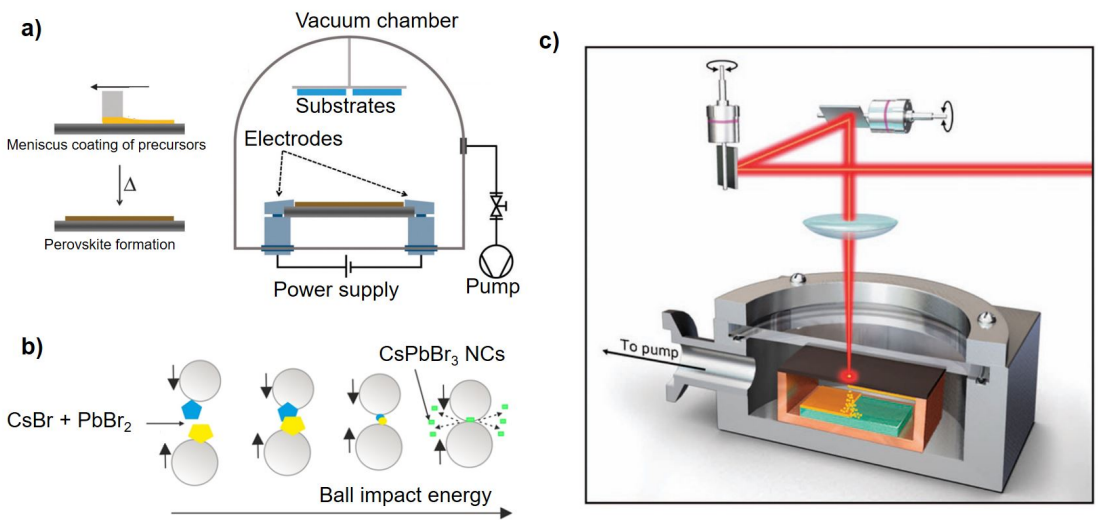

Figure 3.2: a) Flash evaporation setup. Reproduced from Ref. [89] with permission from the Royal Society of Chemistry, b) Working principle of ball milling [93], c) Flash laser printing [94]

Ball milling of perovskite precursors for evaporation

Despite reducing the processing time and avoiding control issues, single source processes still require the production of a mixture of the perovskite precursors prior to the deposition process. In that regard, ball milling appears especially promising as it is a solvent-free, simple, low cost and continuous process to synthesize phase pure perovskite powders. During the rotation of a cylinder shell, the friction between grinding balls causes the loaded precursors to be downsized, mixed, which eventually leads to their chemical transformation. The working principle is schematically illustrated in Figure 3.2b. A direct synthesis of perovskites precursors by ball milling has been the focus of a number of publications [93, 95, 96]. Moreover, in a recent work by López *et al.* [96], the long-term stability of a MAPI powder obtained by such a mechano-synthesis approach was inferred to be superior compared to a solution-processed powder. This was explained by the absence of solvents and impurities and the high yield of the synthesis.

Single source evaporation employing ball milled precursors was demonstrated in 2018 by El Ajjouri *et al.* [97], who deposited inorganic perovskite layers. In 2019, Crane *et al.* [98] presented a proof of concept $(FA_{0.81}MA_{0.14}Cs_{0.05})Pb(Cl_{0.02}Br_{0.14}I_{0.84})_3$ perovskite thin film evaporated by combining ball milling and single source flash evaporation. While the material performance in solar cells remain to be demonstrated with this approach, the ability of ball milling to synthesize mixed cation/halide perovskite powders that can then be evaporated at once is particularly interesting given the complexity of evaporating each precursor independently in a controlled way.

Sputtering

The development of simple, low-cost processing techniques of pure perovskite powder could benefit another vapor deposition technique: sputtering. This process, widely used in industry, is known for its fast and (relatively) conformal coatings on large surfaces, as well as for the good film properties achievable. With respect to perovskite research, two interesting proof of concept process flows were published in 2018 by Bonomi *et al.* [99] and in 2019 by Borri *et al.* [100]. In the first reference, MAPI thin films were produced in a single step by radiofrequency magnetron sputtering. The target was made by pressing together MAI and PbI_2 powders. The second study reports the use of ball milling to manufacture an inorganic perovskite $CsPbBr_3$ from $PbBr_2$ and CsBr precursors. The resulting perovskite powder was pressed to form a target, which was then sputtered.

Laser-based single-step evaporation processes

Laser-induced evaporation is another method that will certainly benefit from the advent of organic-inorganic perovskite targets. The one-step laser evaporation of perovskites, similarly to sputtering or even flash evaporation, is another under-investigated yet promising approach. In 2017, Bansode *et al.* [101] demonstrated the pulsed laser deposition of MAPI and $MAPbBr_3$ The evaporation was performed by shining a laser on a target which was made by pressing MAI

(or MABr) and PbI_2 (or $PbBr_2$) powders together and annealing them for one hour at 100°C. Solar cells featuring an absorber processed with this approach achieved an efficiency of 10.9%. In 2020 [102], Kiyek *et al.* presented the pulse laser deposition of a $CsSnI_3$ perovskite. The target was made by compressing a pure $CsSnI_3$ powder obtained by ball milling from CsI and SnI_2 powders. While no solar cell was demonstrated, this work further highlights the potential of ball milled precursors. Overall, high deposition rates were achieved as the evaporation process lasted between 5 and 10 minutes for a 200 nm-thick perovskite films. In a recent work, Soto-Montero *et al.* [103] applied the same technique to demonstrate organic perovskite thin films with $MA_{1-x}FA_xPbI_3$ compositions. Solar cell devices fabricated with this industrially relevant process achieved 14% PCE.

Another single source laser evaporation process is the so-called resonant infrared, matrix-assisted pulsed laser evaporation (RIR-MAPLE) reported by Dunlap-Shohl *et al.* [104]. A pulsed laser ablates a cryogenically frozen solvent matrix containing the already formed perovskite. The energy of the laser is chosen to resonate with vibrational modes specific to the solvent to trigger the evaporation. With this approach, the risk of damaging the perovskite itself is negligible compared to other techniques directly heating the perovskite through heat conduction or laser absorption. A solar cell processed with this approach exhibited an efficiency of 12%. While promising, the process needs to be optimized further as it lasts several hours and a post-deposition annealing is required.

Laser evaporation was combined with flash evaporation in what is called laser printing. In 2017, Wei *et al.* [94] presented an evaporation setup composed of a laser illuminating a sheet of carbon nanotubes on which a lead iodide solution was dropped and dried, as presented in Figure 3.2c. An interesting characteristic of the carbon nanotube sheet is its low heat capacity per unit area (several orders of magnitude lower than metal heaters), resulting in an extremely fast temperature increase when illuminated by the laser. In this work, it took four seconds to print a PbI_2 layer of 300 nm on a 20 x 20 mm^2 surface. The lead iodide film was then converted to the perovskite phase by dipping it in a MAI solution. In 2019, Tai *et al.* [105] pushed the concept further by demonstrating inorganic perovskite layers deposited solely with the laser printing part of the process. To do so, the carbon nanotube sheet was coated with a $CsPbI_2Br$ solution. The evaporation process took only a few seconds and the resulting layer was then annealed at 280°C during one minute. Perovskite layers printed with this technique were incorporated in solar cells that reached an efficiency of 12.2%. Despite requiring heavy solvents to dissolve the metal halide, the high speed of this method makes it compatible with roll-to-roll processing.

To conclude on this part, single source vapor deposition methods include a broad range of promising techniques addressing process control issues faced by standard co-evaporation processes. By evaporating the perovskite in a single-step, the deposition process is simplified and accelerated. One issue is that these methods require a pre-existing perovskite precursor of the targeted composition, an aspect mitigated by the advent of ball milling techniques for

perovskite processing. While solar cells featuring an absorber processed with these techniques do not exhibit the same efficiency as solution-processed cells, this difference is more likely a result of the smaller research community working on these techniques rather than of an intrinsic limitation.

3.2.2 Vapor transport deposition

A recurrent feature of "line-of-sight" vapor deposition routes is the high vacuum maintained during the evaporation to ensure a high mean free path and purity of the condensed compounds. However, as discussed above, the high vapor pressure and low sticking coefficient of organohalides makes such processes sometimes difficult to control.

In vapor transport deposition processes, the evaporated vapors of the precursors are transported from the sources to the substrates with a carrier gas. Compared to most "line-of-sight" vapor deposition processes, the operating pressure is orders of magnitude higher with vapor transport deposition (in the hundreds of Pa range), which hence requires a simpler pumping system. Physically separating the evaporation from the deposition also provides some additional process flexibility. In addition to providing a control over the temperature of the source, substrates and sometimes chamber walls, the composition, temperature and flow rate of the carrier gas can also be tuned. Outside of the fields of perovskites, vapor transport deposition are particularly well-suited to process CdTe thin films [106, 107] or layers for organic electronics [108].

In this section, the focus is on processes using solely vapor transport deposition to grow perovskite thin films. Processes featuring a combination of "line-of-sight" vapor deposition and vapor transport deposition are designated here as "hybrid" processes and will be treated in the next section.

Tubular furnace deposition

Tube furnaces are amongst the simplest chambers used for vapor transport deposition. The first perovskite solar cell entirely processed by vapor transport deposition, in a tube furnace, was presented in 2015 by Takavoli *et al.* [109]. The setup features a two-zones tube furnace with different temperatures, one for the substrates and another one for the precursors (lead halide and organohalide salts). An argon carrier gas transports the vapors of the sublimated precursors from the higher temperature zone to the lower temperature zone where the substrates were positioned. The two precursors are placed in a way so that they reach their respective sublimation temperature. While this approach is simple and inexpensive to setup, one major issue is the complexity of controlling individually the evaporation rate of each material, a complexity that increases drastically with the number of precursors present along the tube furnace length, as is the risk of cross-contamination of precursors.

In an attempt to decorrelate the sublimation of different precursors, sequential depositions of perovskites were also demonstrated [110, 111]. However, sequentially sublimating the organic and inorganic precursors in the same tube furnace may led to cross-contamination and long cooling times between process steps.

Upgrades to tubular furnaces

Issues related to cross-contamination and individual control of sources was addressed for tin halide perovskites by Clark *et al.* [112]. Their experimental setup is an evolution of a tubular furnace and is inspired by advances in the field of organic vapor phase deposition [113]. The system, detailed in Figure 3.3a, is made of a three zones tube furnace containing a set of sources and an axisymmetrically positioned substrate holder cooled by water. Each tube source contains a porous frit of a given material attached to a linear actuator with a thermocouple. Sources can be translated along the tube to vary their temperatures thanks to a thermal gradient within the furnace. The carrier gas, nitrogen, is independently fed through each tube and the surrounding volume. The influence of each of the many process parameters on stoichiometry, morphology and electrical properties was thoroughly studied, highlighting the robustness of the process. Another upgrade to tubular furnace systems was presented by Hoerantner *et al.* in 2019 [114] and is depicted in Figure 3.3b. The main tube contains the temperature-controlled substrate holder and is connected on one side to three separate tubes, one containing MAI, one PbI_2 and one used as N_2 inlet for pressure control. N_2 flows through each precursor tube to bring their vapors to the substrates.

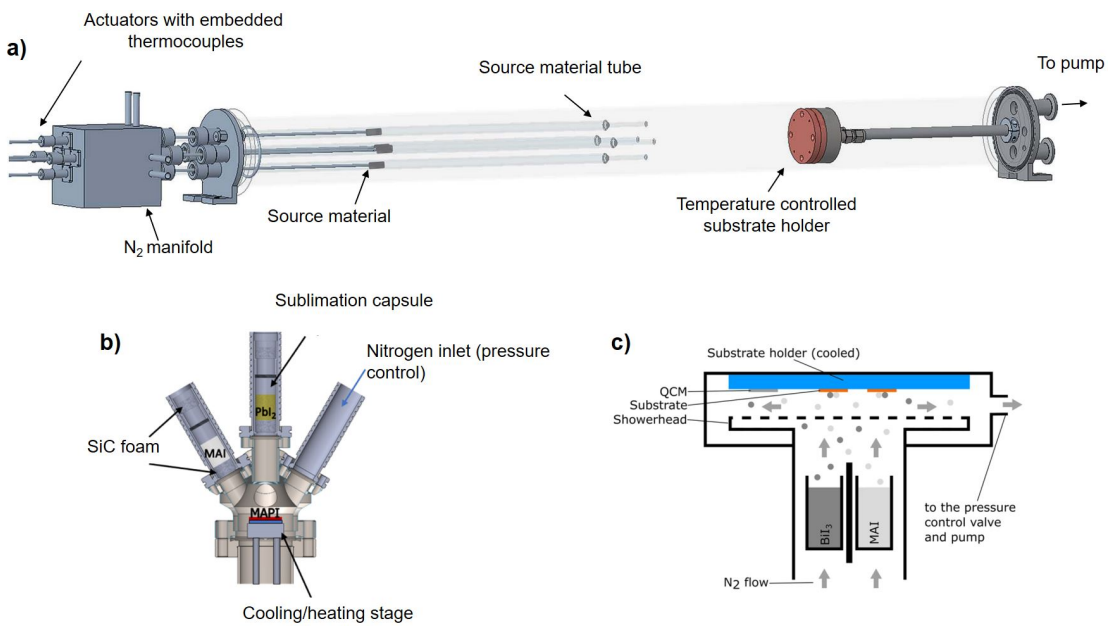

Figure 3.3: a) Tubular furnace setup with independent tubes for each precursor [112] b) Cross section views of the trident-shaped reactor presented by Hoerantner *et al.* [114] c) Schematic of the showerhead-based reaction chamber reported in Ref. [115]

A silicon carbide foam is used to keep the solid precursors in the capsule and homogenize the flow. The deposition is performed sequentially by forming three thin pairs of PbI_2/MAI layer stacks on the substrate holder heated at 100°C, a strategy that favors the perovskite formation. The as-deposited layers do not require any post-deposition annealing to complete the conversion. Considering the deposition of all the layers and the time required to alternate between PbI_2 and MAI, the process takes only a few minutes, with deposition rates reaching more than one nanometer per second. The study underlined the need to precisely control several parameters (chamber pressure, temperatures of walls, tubes, substrate holder) to produce a high-quality perovskite. A first solar cell made with this approach reached an efficiency of 6.9%. This modest result was partly attributed to unoptimized charge collection layers and a probably suboptimal perovskite composition. A generalization of this approach is presented in a patent filed by the authors [116] : the process is upscaled and features a vaporizer, a precursor mixing zone and a larger reaction chamber.

Showerhead-based reaction chambers

The last systems discussed are promising to produce perovskite layers in low vacuum with enhanced process control compared to standard "line-of-sight" vapor deposition routes. However, while upscaling these systems is feasible, the homogeneity of the deposited layer may suffer. This issue can be mitigated when forcing the precursor vapors and carrier gas through a showerhead, as used in industry in chemical vapor deposition (CVD) systems or in some plasma-enhanced CVD processes [117, 118].

A showerhead-based vapor transport deposition system for perovskites was reported in 2019 by Sanders *et al.* [115]. Methylammonium bismuth iodide layers were deposited on substrates facing a showerhead located below. Vapors of MAI and BiI_3 were carried by nitrogen from sources separated by a shield to avoid cross contamination. A schematic of the setup is presented in Figure 3.3c. Incorporating such thin films in a solar cell led to low efficiencies, in part due to the nature of the absorber but also due to the low penetration of the perovskite in the mesoporous TiO_2 electron selective layer. Still, a stoichiometric bismuth-based perovskite could be deposited and links between precursor evaporation rates, substrate temperature, morphology, optical and crystallographic properties of the resulting layers could be established. Later on, the same group presented a similar setup for MAPI deposition from MAI and PbI_2 sources [119]. While the system enables the growth of stoichiometric MAPI, first implementations in solar cells led to low efficiencies due to the porosity of the perovskite layer and a high series resistance. An important requirement of the system is that the walls must be heated above the highest vaporization temperature of the precursors, here that of metal halides. A probable consequence of such high temperatures is the thermal decomposition of the organic vapors, as discussed in the second part of this state of the art.

In conclusion, vapor transport deposition as a standalone way of fabricating perovskite thin films is still an under-investigated field. However, the proof of concept systems reported to date appear promising due to the enhanced process control they provide and in some cases, the speed of deposition that can be achieved compared to standard thermal evaporation process.

3.2.3 Hybrid vapor deposition processes

Metal halide and organohalide salts, the main perovskite precursors, exhibit opposed behaviors during vapor deposition. Metal halide salts are well suited for "line-of-sight" vapor deposition processes thanks to high sublimation temperatures and low volatility. On the other hand, vapor transport deposition processes appear more suited to deposit the volatile organohalides. This difference has encouraged the development of hybrid sequential processes, where each step is tailored to the properties of the species to evaporate.

Thermal evaporation followed by vapor transport deposition

In most hybrid processes, the metal halide precursor is first thermally evaporated with a precise control over its thickness (by a QCM). Its conversion to a perovskite phase is then performed by exposing it to organohalide vapors brought by a carrier gas. Leyden *et al.* [120] presented one of the first hybrid vapor deposition process for perovskite solar cells in 2014. A $PbCl_2$ template was thermally evaporated in a high vacuum chamber, before depositing MAI by vapor transport deposition in a two-zones tubular furnace. A typical setup is presented in Figure 3.4a.

The choice of substrate temperature is a subtle tradeoff between different phenomena: increasing the temperature promotes the diffusion of the adsorbed species on the template, but it lowers the sticking coefficient of the MAI vapors and, if too high, it may lead to a degradation of the just-formed perovskite. While in an ideal case a high wall temperature would be beneficial to prevent unwanted condensation, in a tube furnace, the wall temperature determines that of the substrates. This compromise of temperature was thoroughly investigated by Moser *et al.* [121], who studied the vapor transport deposition of FAI on thermally evaporated caesium lead halide templates. They presented an isochronal map featuring source and substrate temperatures, highlighting the different regimes of vapor transport deposition: overconversion, underconversion, perovskite growth and degradation. In another work [122], Leyden *et al.* demonstrated that, when depositing FAI on substrates placed at temperatures higher than 145°C, a perovskite phase formed directly without the need for a post annealing and without significant organohalide oversaturation. They also highlighted a limitation of tubular furnaces: the high concentration gradient of vapors. Lead halide templates placed along the tube length reached different levels of conversion, as highlighted by X-Ray Diffraction (XRD) diffractograms.

In 2016, Ng *et al.* [123] investigated the impact of the post-deposition cooling rate. Solar cells fabricated with an absorber cooled faster displayed pinholes and a lower shunt resistance, leading to poorer performances. The authors also studied the impact of the composition of the carrier gas and found that mixing nitrogen with oxygen led to a passivation effect resulting in a higher power conversion efficiency. Other studies reported the use of air as carrier gas with similar benefits [37, 124]. It is also worth mentioning that the carrier gas flow rate is another parameter that must be optimized.

Mixed cation/halide compositions can also be deposited with hybrid processes [37], an important aspect in view of a multijunction integration. Bandgap tuning can be achieved by co-evaporating different metal halide compounds (PbI_2 and CsBr for example), before depositing the organohalide (MAI, FAI) via vapor transport deposition [125].

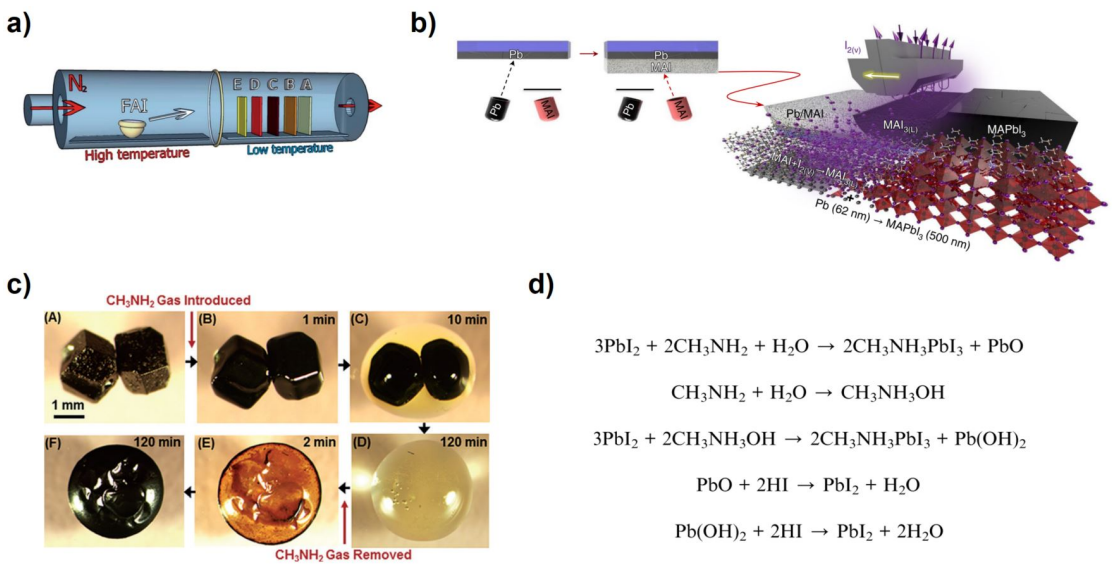

Figure 3.4: a) Typical tubular furnace setup used to bring organohalide vapors to metal halide templates. Reproduced from Ref. [122] with permission from the Royal Society of Chemistry. b) Reactive polyiodide melts process [126]. c) Recrystallisation of MAPI upon MA exposure [127]. d) Subsequent reactions of lead halide upon exposure to MA and HI vapors in ambient air [128].

The up-scalability of the technique was also investigated in different studies [37, 122], with recent results demonstrating modules reaching dimensions of up to 100 cm^2 and an efficiency on the order of 10%. In the same study, a mini-module with an active area of 22.4 cm^2 and an initial efficiency of 10% was reported to degrade linearly at a rate of -0.04abs%/hour after an initial burn-in loss (test conditions of 25°C under one sun illumination at MPP during a 250 hours experiment). Regarding up-scalability, Sahli *et al.* [41] recently presented a vapor transport deposition system for organohalide deposition. Following the thermal evaporation of a metal halide template, the substrates were placed in a reaction chamber. MAI sublimation

products were transported from a distant evaporator by a carrier gas and brought to the substrates through a showerhead. The walls, evaporator and substrate temperatures were independently controlled, which enabled the authors to produce conformal and homogeneous perovskite layers on a textured 6 in. silicon wafer (239 cm^2).

Reactive polyiodide melts

An inherent weakness of vapor transport deposition in tubular furnace is the appearance of a gradient in precursor concentration along the flow path. Experimental conditions and substrate positioning are known to affect this gradient [122, 124]. Uniformity can be enhanced by increasing the tube furnace temperature to reduce the deposition of the precursors on the tube walls [122]. However, the temperature of the walls directly determines that of the substrates: the two cannot be tuned independently, hence limiting the processing window. The use of reactive polyiodide (MAI_3, FAI_3) melts relaxes some of these constraints. The different steps of the process are presented in Figure 3.4b. This hybrid deposition method was demonstrated in 2019 by Turkevych and co-workers [126] and involves the thermal evaporation of a metallic lead layer, before thermally evaporating MAI and exposing the layer stack to I_2 vapors. This exposure triggers the formation of a liquid polyiodide melt, MAI_3, which reacts with the lead layer to form the perovskite through a fast redox reaction. The reaction driving force and large volume expansion ensure the absence of intermediate phases and/or pinholes. Uniform perovskite layers could be deposited onto substrate areas up to 600 cm^2. The method is flexible as MAI can be replaced with CsI/MAI/FAI mixtures. Best cells on the mm^2 scale achieved conversion efficiencies of about 16-17% depending on composition and contact architecture.

Atomic layer deposition of the lead template

While thermal evaporation is well suited to deposit the metal halide template, alternatives have also been explored such as atomic layer deposition. The substrates are sequentially exposed to different gas precursors that react in a self-limiting way. This results in a conformal and precisely controlled deposition. The deposition occurs at low temperature and the working pressure is orders of magnitude higher than in the case of thermal evaporation. In a first attempt, Sutherland *et al.* [129] proposed in 2015 a three steps method to grow a perovskite layer. An atomic layer deposited PbS template was exposed to I_2 to trigger its conversion to PbI_2. This lead halide template was then converted to a perovskite by dipping it in a MAI solution. In 2019, Popov *et al.* [130] reported another Atomic Layer Deposition (ALD) process to deposit directly PbI_2, yet without converting it in a perovskite thin film.

Sputtering of lead-based templates

Radio frequency magnetron sputtering is another interesting way of depositing metal halide template. As presented in a previous section, sputtering is a conformal, low temperature and fast process that is already widespread in industry. Nonetheless, sputtering is a high kinetic energy deposition, capable of damaging soft layers such as the organic charge transport layers commonly used in perovskite solar cells [131]. Similarly to the approach of Sutherland *et al.* [129] with atomic layer deposition, da Silva Filho *et al.* [132] presented in 2018 a three step process that involves sputtering PbS, its conversion to PbI_2 by an exposure to I_2, before dipping this template into a MAI solution to trigger the perovskite formation.

Hwang *et al.* [133] proposed in 2019 an evolution of this method by sputtering a PbO layer and then directly converting it into perovskite through a MAI vapor exposure in a two-zones tube furnace. In the furnace, the perovskite formation was found to occur in two steps: MAI decomposed notably into HI and CH_3I, reacting with PbO to form PbI_2, and finally to MAPI. A 10.2%-efficient cell was demonstrated, and the method produced a conformal perovskite coating on textured silicon over 100 cm^2. The vapor exposure of the Pb-based sputtered template resulted in oversaturation, requiring an annealing step to remove the $(MA)_4(PbI_6).2H_2O$ dihydrate that formed on the surface. Most importantly, a complete conversion of the PbO layer was also difficult to achieve. To mitigate the issue, a gas treatment was performed by exposing the layer to methylamine (CH_3NH_2 or MA), leading to a recrystallization of the perovskite. This effect was first demonstrated by Zhou *et al.* in 2015 [127]: in a MA vapor, MAPI single crystals were shown to form a metastable $MAPbI_3 \cdot x\ CH_3NH_2$ liquid phase. Removing the MA partial pressure led to a recrystallization of MAPI into a single crystal without any intermediate phase. Figure 3.4c features optical microscopy images demonstrating each step of this recrystallization.

Vapor treatments of perovskite thin films

Methylamine has been used as a post-deposition treatment to passivate defects and modify the layer microstructure but also to produce perovskite absorbers from lead halide templates [127, 134–139]. Notably, the reaction between methylamine and presumably $HPbI_3(Cl)$, or more likely $DMAPbI_3(Cl)$ based on recent evidence [140], enabled the crystallization of thick perovskite absorbers (1.1 μm). When included in small devices of 0.1 cm^2 and 5 x 5 cm^2 mini-modules (active area of 12 cm^2 [141]), solar cells reached efficiencies of 19.1% and 15.3%, respectively. The ability of this approach to crystallize thick absorbers with a high optoelectronic quality is particularly attractive for monolithic tandems. Indeed, it should widen the range of bandgap/thickness combinations that can be used to achieve current-matching conditions, with each subcell delivering the highest voltage possible [66].

In 2016, Raga *et al.* [128] used a MA vapor treatment to directly convert PbI_2 into MAPI in ambient air. The presence of water vapor generates a significant amount of lead oxide byproducts, and the authors obtained films of higher quality by exposing simultaneously the lead halide films to MA and hydroiodic acid (HI) vapors. As presented in Figure 3.4d, HI vapors are used to convert the lead oxide byproducts back to lead iodide. Best solar cells using a MAPI absorber processed with this gas treatment method displayed an efficiency of 15.3%. In 2020, Mortan *et al.* [142] presented a setup based on the same working principle: a tubular furnace fed with gaseous HI and MA to convert lead halide templates. In their case, they obtained better results by alternatively exposing the lead iodide template to each vapor. They emphasized the importance of using a drying agent between the tube furnace and the homemade HI gas source. On average, cells made with a drying step exhibited a 2% absolute higher power conversion efficiency (12.9%).

Another type of vapor treatments involves the use of formamidine ($CH(NH_2)_2$ or FA), in a vapor phase, to displace to the MA cations of $MAPbI_3$. Resulting $FA_xMA_{1-x}PbI_3$ cells produced with this method reached an efficiency of 18% [143]. Advantageously, the method was found to maintain the smooth microstructure of the initial $MAPbI_3$ layer. Moreover, ion exchange via a vapor phase was also shown to modify the halide anion of MAPI in 2015 by Li *et al.* [144]. Using MABr and MAI vapors, they demonstrated a reversible transformation between $MAPbI_3$ and $MAPbBr_3$. A vapor treatment was recently used to stabilize at room temperature FAPI perovskite in the photo-active α phase. Pristine FAPI may crystallize in a photo-inactive δ phase below 150°C. So far, this phase change has often been circumvented by alloying the perovskite with MA, Br or Cs ions. Lu *et al.* [145] proposed an organic thiocyanate (SCN) vapor exposure at moderate temperature (100°C) to convert FAPI films from the δ to α phase (the treatment works with both MASCN and FASCN). The short exposure (one minute) produced a stable photoactive layers and high-efficiency devices (>23%).

The possibilities offered by vapor treatments are numerous and particularly interesting for device processing. Ion exchange, bandgap tuning or stabilization via such versatile processes may be combined advantageously with the vapor-based deposition techniques mentioned above.

3.3 On the understanding of perovskite vapor deposition processes

The second part of this state of the art discusses the underlying mechanisms of perovskite deposition from vapors. The growth of thin films from vapors is a succession of steps, from the sublimation of precursors, the adsorption of precursor adatoms/molecules, their surface migration, the formation of the first stable nuclei, their (sometimes preferential) growth, their impingement and possibly their coarsening at the expense of smaller grains. Each of these steps may limit the growth process, an aspect that the final layer morphology may reflect. In

this section, we will review simple theoretical concepts describing the main steps of the growth process and attempt to tie these concepts to experimental observations. Readers interested in the mathematical formalism of heterogeneous nucleation, atomistic considerations or simulations are referred to dedicated work [146–152].

3.3.1 Layer nucleation and growth: some theoretical considerations

When particles from sublimated vapors are brought in the vicinity of substrates, either by their own ballistic motion or by a carrier gas, they may eventually be adsorbed on the surface. The adsorbed molecules or atoms (adatoms) diffuse on the surface until meeting other adatoms/-molecules or re-evaporate from the substrate. The adatom density, $\rho(x,t)$, can be described using the diffusion equation based on Fick's second law [153]:

$$\frac{\partial \rho(x,t)}{\partial t} = D_s \frac{\partial^2}{\partial x^2}\rho(x,t) - \frac{1}{\tau_v}\rho(x,t) + F \tag{3.1}$$

Where D_s is the surface diffusion coefficient of adatoms, τ_v the residence time of an adatom before evaporating from the surface, and F the incoming flux of atoms on the substrate from the vapor phase. This diffusion equation is solved by assuming that the diffusion rate is much slower than the rate of attachment and detachment of adatoms, leading to an equilibrium value of adatom density ρ_0 at a given location. When surface diffusion is assumed to be much faster than the motion of already bonded adatom clusters, $\frac{\partial \rho(x,t)}{\partial t} = 0$. In the case of an isolated cluster at $x = 0$, the following boundary conditions are used : $\rho(0) = \rho_0$, $\rho(\infty) = F\tau_v$. The following solution is then obtained:

$$\rho(x) = \rho_0 + \left(F\tau_v - \rho_0\right)\left[1 - e^{-\frac{|x|}{\lambda_s}}\right] \tag{3.2}$$

Where $\lambda_s = \sqrt{D_s \tau_v}$ is the surface diffusion length of adatoms. This means that only adatoms condensing on the surface within λ_s from an isolated cluster will contribute to the growth of the cluster, while others will re-evaporate.

The complex influence of the substrate temperature on the deposition process is already highlighted by the equation presented above, which only describes the adatom density at the first steps of the process. Indeed, the arriving flux of atoms on the substrate F is proportional to $\frac{p}{\sqrt{mT}}$, with p the partial pressure, m the mass of the adatoms/molecules and T the absolute temperature in the vicinity of the substrate. In addition, both the diffusion coefficient D_s and adatom residence time τ_v follow an Arrhenius dependence to temperature, meaning that both can be expressed as follows : $k = Ae^{\frac{-E_a}{k_B T}}$, with A the pre-exponential factor, E_a the activation energy and k_B the Boltzmann constant. At the experimental level, the influence of the substrate temperature on the process is made even more complex due to the need to consider the temperature-dependent intercalation of organohalides into metal halide clusters, a key step of the perovskite growth process.

These adatoms condensed on the surface may then coalesce into stable nuclei. The nucleation step is most commonly described by the classical nucleation theory (CNT). This theory is based on the so-called capillarity approximation describing the embryonic clusters as spherical drops of an incompressible fluid. The free energy of formation is split into volume and surface components, the latter taken equal to the macroscopic surface energy. The reversible work, or free energy, necessary to obtain a cluster of n adatoms is described by the following expression:

$$\Delta G(n) = -nk_B T ln\frac{p}{p_s} + 4\pi\sigma\left(\frac{3v}{4\pi}\right)^{\frac{2}{3}} n^{\frac{2}{3}} \tag{3.3}$$

With p_s the saturation vapor pressure, σ the surface energy per unit area and v the volume per atom in the cluster.

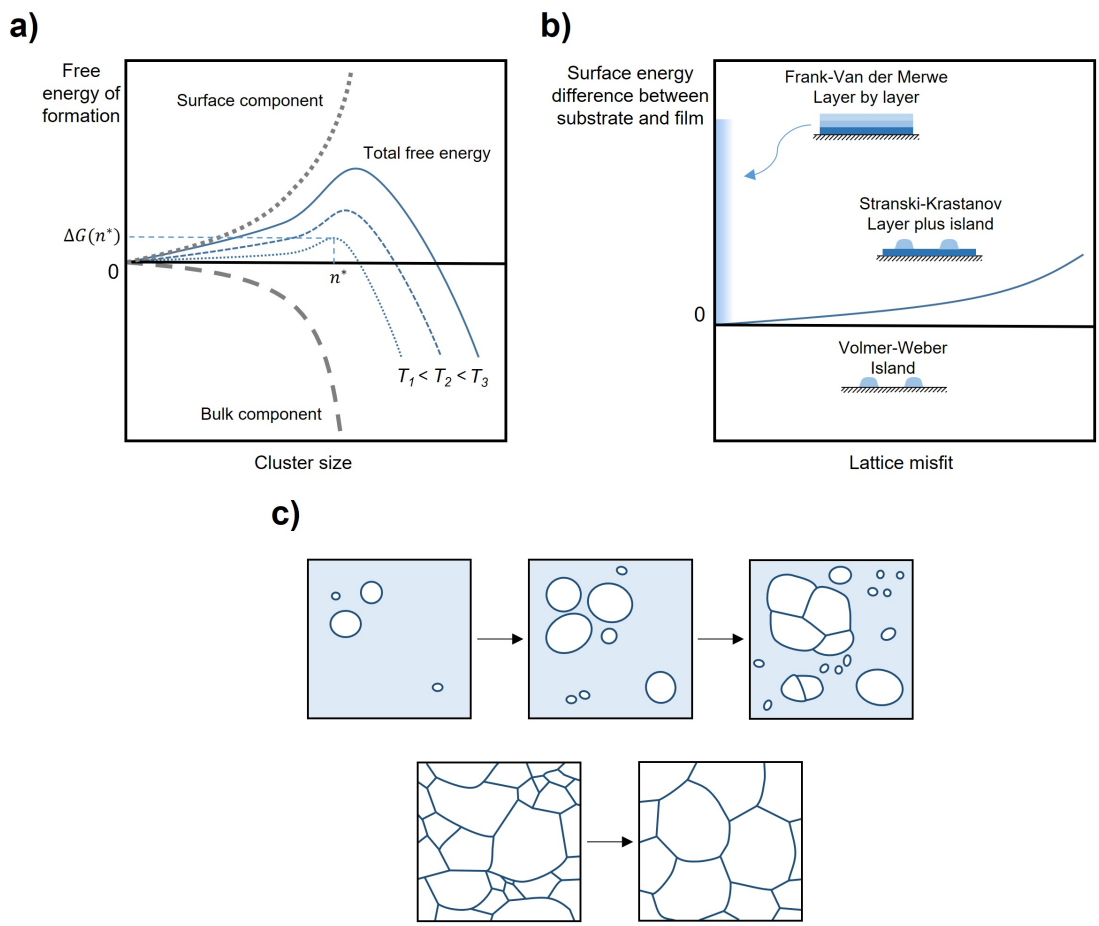

Figure 3.5: a) Free energy of formation as a function of the cluster size. Effect of an increasing temperature on the free energy of formation, with $T_1<T_2<T_3$ b) Film growth modes c) Nucleation, grain growth, coalescence and coarsening

The influences of the bulk and surface contributions are illustrated in Figure 3.5a, where one can notice that the positive surface component induce an energy barrier impeding nucleation. Finding the solution to $\frac{\partial \Delta_{G(n)}}{\partial n} = 0$ and injecting the resulting critical cluster size n^* (the size below which the cluster is unstable) in the equation gives the corresponding energy barrier $\Delta G(n^*)$ for the nucleation process:

$$n^* = \frac{32\pi\sigma^3 v^2}{3\left(k_B T ln \frac{p}{p_s}\right)^3}; \; \Delta G\left(n^*\right) = \frac{16\pi\sigma^3 v^2}{3\left(k_B T ln \frac{p}{p_s}\right)^2} \tag{3.4}$$

For values above unity, increasing the vapor supersaturation $\frac{p}{p_s}$ tends to decrease the energy barrier and the critical cluster size. The influence of temperature in the vicinity of the substrate has various effects on the critical cluster size and barrier height: supersaturation and surface energy decrease with an increasing temperature, while the critical cluster size increases (Figure 3.5a). Adding the influence of kinetics, the nucleation rate R can be expressed by:

$$R = Ke^{\frac{-\Delta_{G(n^*)}}{k_B T}} \tag{3.5}$$

Where K is a factor proportional to temperature representing the departure of the cluster distribution from equilibrium and the collision rate between clusters and atoms. These competing influences of temperature lead the nucleation rate to behave as a nonlinear function with a global maximum.

The CNT has been successfully applied to understand and predict simple homogeneous and heterogeneous nucleation cases since decades. However, the capillary approximation is invalid at low cluster sizes. To describe the nucleation of small clusters, extensions to CNT have been developed using statistical mechanics. Instead of relying on macroscopic quantities such as surface energy, atomistic models introduce the energy of adsorption between a single atom and the substrate or the binding energy between two adatoms, for example. However, the difficulty of obtaining precise values of these microscopic parameters coupled to the exponential nature of these atomistic functions hinder the prediction capacity of atomistic models. This means that the extended nucleation model is often used for theoretical interpretation of experimental results while the CNT is favored to evaluate qualitatively the impact of process parameters on nucleation rates, as discussed in the next section.

The overall layer morphology can then follow one of the three thin-film growth modes: layer by layer, layer plus island or island (Frank-Van der Merwe, Stranski-Krastanov and Volmer-Weber modes, respectively) depending on the surface energy difference and lattice misfit with the substrate (Figure 3.5b). Organohalides typically grow according to Stranski-Krastanov or Volmer-Weber modes when deposited on their own [55], while co-evaporation processes yield perovskite layers with morphologies closer to the Frank-Van der Merwe mode with a smooth topography. A more detailed description of the thin films grown from vapors can be achieved with structure-zone models, which qualitatively predict the grain structure of films as function of a reduced set of parameters: the substrate temperature, the melting point of the material

and the deposition pressure [154, 155]. These structure-zone models reflect how each of the three main steps of the growth of a thin film are affected by these process parameters: the transport of species to the substrate in the vapor phase, their adsorption and surface diffusion, and finally their reaction or uptake with/by the thin film. The final layer morphology may also be dominated by the preferential growth of grains with a specific crystallographic orientation (competitive growth models) [156, 157]. Finally, depending on the substrate temperature or whether a post-deposition annealing step is applied, a coarsening of the grain structure may occur as the system minimizes its surface energy, as highlighted in Figure 3.5c [158].

Regarding specifically perovskite materials, computational fluid dynamics studies and approaches using heat and mass transfer equations have been used to investigate their vapor deposition [112, 114, 159–162]. Although some of the hypotheses adopted do not fit with experimental results (*e.g.* the laminarity of the flow or the implicit absence of thermal degradation of organohalides into byproducts), these approaches may help in the design of evaporation setups and in the search for process parameters. The main particularity of perovskite vapor deposition lies in how the layers grow: metal halides follow a classic ballistic motion common in physical vapor depositions, while some of the organohalide thermal byproducts are adsorbed by the deposited metal halide clusters. Once adsorbed, the organohalide molecules diffuse through the metal halide to start the perovskite formation [62, 76, 162]. This two-step growth model has been adopted by Kim et al. [162] in their development of a kinetic model of the film growth during MAPI co-evaporation. Based on a sticking probability following an Arrhenius law and Fick's first law of diffusion, their model gave coherent values when fitting experimental data of adsorption.

The theoretical considerations presented in this section highlight how common process characteristics (temperature and surface energy of the substrate, partial pressure, etc.) alter the different steps of a thin film growth. A peculiarity of perovskites vapor growth is the interdiffusion and subsequent reaction of organohalides vapors and metal halides. The next section will treat how this chemical reaction is influenced by the evaporation setup and the process parameters.

3.3.2 Linking theory to experiments

The structure of the perovskite layer is often determined by one step of the growth process, either the interdiffusion and chemical reaction between precursors to form the perovskite, the nucleation of the first perovskite crystalline seeds, their growth until impingement, or their coarsening during the layer growth or a subsequent annealing step. In the next paragraphs, we will discuss how process parameters impact each of these steps of the growth of the perovskite thin films and in turn the layer structure.

Sublimation, adsorption, nucleation: first stages of the growth

Before condensing on substrates from a vapor phase, perovskite precursors must be sublimed. Apart from inducing a process control challenge as discussed beforehand, organohalides tend to decompose into different byproducts upon sublimation. As underlined by different reports [163–165], the main products of MAI evaporation are methyl iodide (CH_3I), hydrogen iodide (HI), ammonia (NH_3), methylamine (CH_3NH_2) and, in smaller quantities, its dimer form $(CH_3NH_2)_2$ [163]. Experiments and first-principles density functional theory (DFT) calculations [165] suggest that the kinetically favored degradation pathway is the reaction leading to the thermal decomposition of the parent molecule into CH_3I and NH_3. The degradation upon sublimation depends on the type of organohalide precursor as demonstrated by Williams *et al.* [166]. The thermal decomposition of MAI at high temperature (>170°C) mainly results in methyl iodide and ammonia, while traces of methylammonium (CH_3NH_3, or MA) can be detected at lower temperatures [163, 164]. On the other hand, MACl thermally degrades into MA and HCl. The evaporation of the other organohalide precursor, e.g. FAI, also results in the fragmentation of the parent molecule. In this case, the main decomposition byproducts are hydrogen cyanide (CHN), ammonia (NH_3), sym-triazine ($C_3H_3N_3$) and formamidine ($CH(NH_2)_2$) [167]. The formation of a perovskite thin film from these different byproducts seems to mostly result from an acid/base reaction between organic cations and hydrogen halides in the presence of a metal halide [128, 163, 165, 167, 168]. In Ref. [163], it was also hypothesized that the small amount of MAI dimer detected by mass spectrometry could participate in the perovskite formation process.

The decomposition of organic precursors upon sublimation has consequences on the layer nucleation and layer growth process. Indeed, the growth of the perovskite layer can be slowed down if one byproduct does not reach the reaction site, e.g. as a result of a lower residence time or low diffusion length on the substrate surface. In 2015, Liu *et al.* tracked the thermal evaporation of MAI on an already formed PbI_2 layer and the resulting MAPI formation with X-ray photoelectron spectroscopy (XPS) [169]. From the XPS spectra, a carbon containing species was detected from the very beginning of the evaporation of MAI, while nitrogen was only detected after a certain incubation period. This carbon signal likely originated from methyl iodide, a known decomposition byproduct of MAI. This result would imply that methyl iodide is present in the bulk of their perovskite, as also inferred by data retrieved from solution-processed layers [170]. Olthof and Meerholz performed in 2017 in situ XPS and ultraviolet photoelectron spectroscopy (UPS) at different steps of the growth of co-evaporated MAPI [171]. One of the main finding of their XPS experiments is that the evaporation is characterized by a substrate-dependent induction period. Figure 3.6 displays the XPS spectra measured after 0.5 and 10 nanometers of deposition on PEDOT:PSS, PEIE, MoOx and indium tin oxide (ITO). While organic substrates such as PEDOT:PSS and PEIE are covered by a perovskite from the first nanometers, early stages of the growth on MoOx and ITO are characterized by lead or nitrogen signals, respectively. The catalytic nature of metal oxides was presented as the main factor explaining the difference with organic substrates. XPS data taken from layers thicker than 10 nm displays a strong MAPI signal on all substrates.

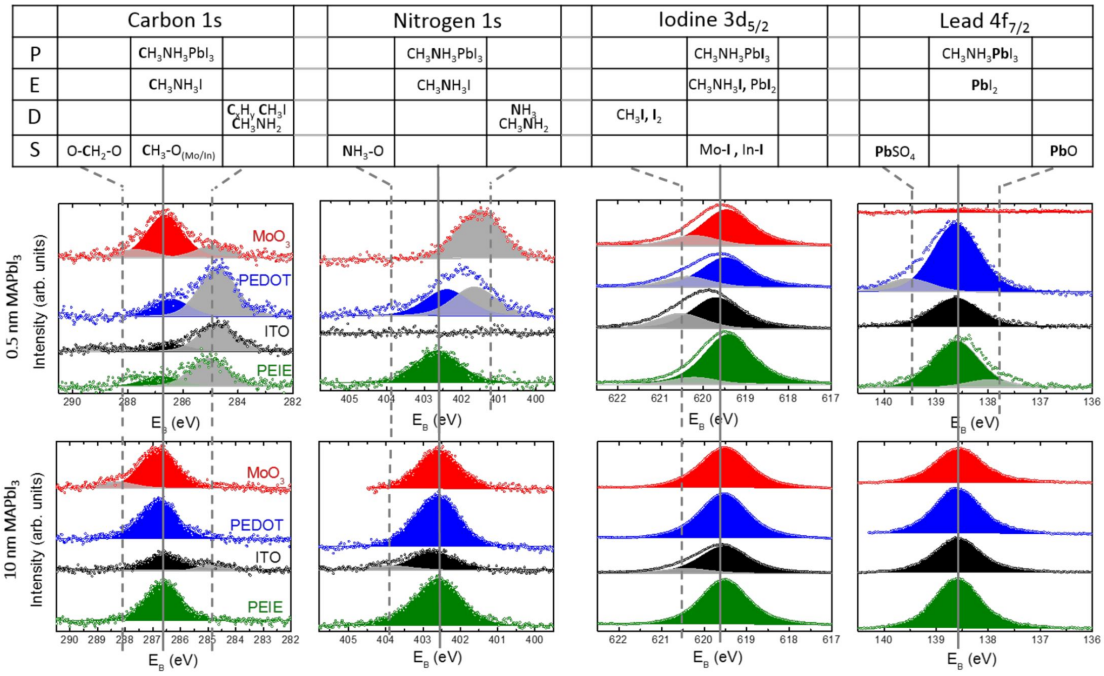

Figure 3.6: Carbon, nitrogen, iodine and lead XPS spectra of co-evaporated MAPI on 4 different substrates measured after 0.5 and 10 nm of deposition. Solid and dashed vertical lines show expected binding energies characteristic of the perovskite and other molecules, respectively. The table lists possible reaction products responsible for the additional peaks, divided into products (P), educts (E), decomposition products (D), and surface bonds (S). Adapted from [171].

Moreover, the authors mentioned that surface reactions occurring during the first few nanometers of the growth could be triggered by surface hydroxyl (-OH) groups. This means that, at least with co-evaporation, decomposition byproducts may preferentially deposit during the very first steps of the growth depending on the nature of the substrate. In [172], Thampy *et al.* demonstrated that these decomposition byproducts impact the long-term stability of the layer. A solution to mitigate this byproducts incubation layer was presented by Moser *et al.* with a custom-made vapor transport deposition system [121]. They reversed the carrier gas flow (from substrates to source to the pump) during the heating phase of the crucible in tubular furnace to ensure that fragments sublimating at lower temperatures do not reach the substrate. When the evaporator reached its temperature setpoint, they switched the flow direction from source to substrate to trigger the deposition process.

Experiments show that, during both co-evaporation and sequential deposition processes, the final perovskite thickness is proportional to the evaporation rate of the metal halide or the thickness of the metal halide template, respectively [75, 169, 173]. During co-evaporation, it appears that organohalide vapors preferentially adsorb on metal halides to form a perovskite [48, 62, 162]. In their study on co-evaporation, Roß *et al.* [60] reported that the adhesion of PbI_2 on substrates is constant for substrate temperatures between -30 and 60°C, while that of MAI decreases by 70% when increasing temperature in this range.

To summarize, apart from the notable exception of the first nanometers of growth on metal oxides as reported by Olthof and Meerholz [171], the general trend is that perovskite growth during co-evaporation occurs through a two-stage process, at least on a local scale. This behavior is depicted in Figure 3.7a, which illustrates how metal halides preferentially stick onto the substrate. Some of the organohalide degradation byproducts then react with these metal halides to form the perovskite phase. Similarly, Figure 3.7b shows the growth sequence for sequential processes, where a metal halide film is first grown and then exposed to the organohalide vapors to eventually form a perovskite layer (Figure 3.7c).

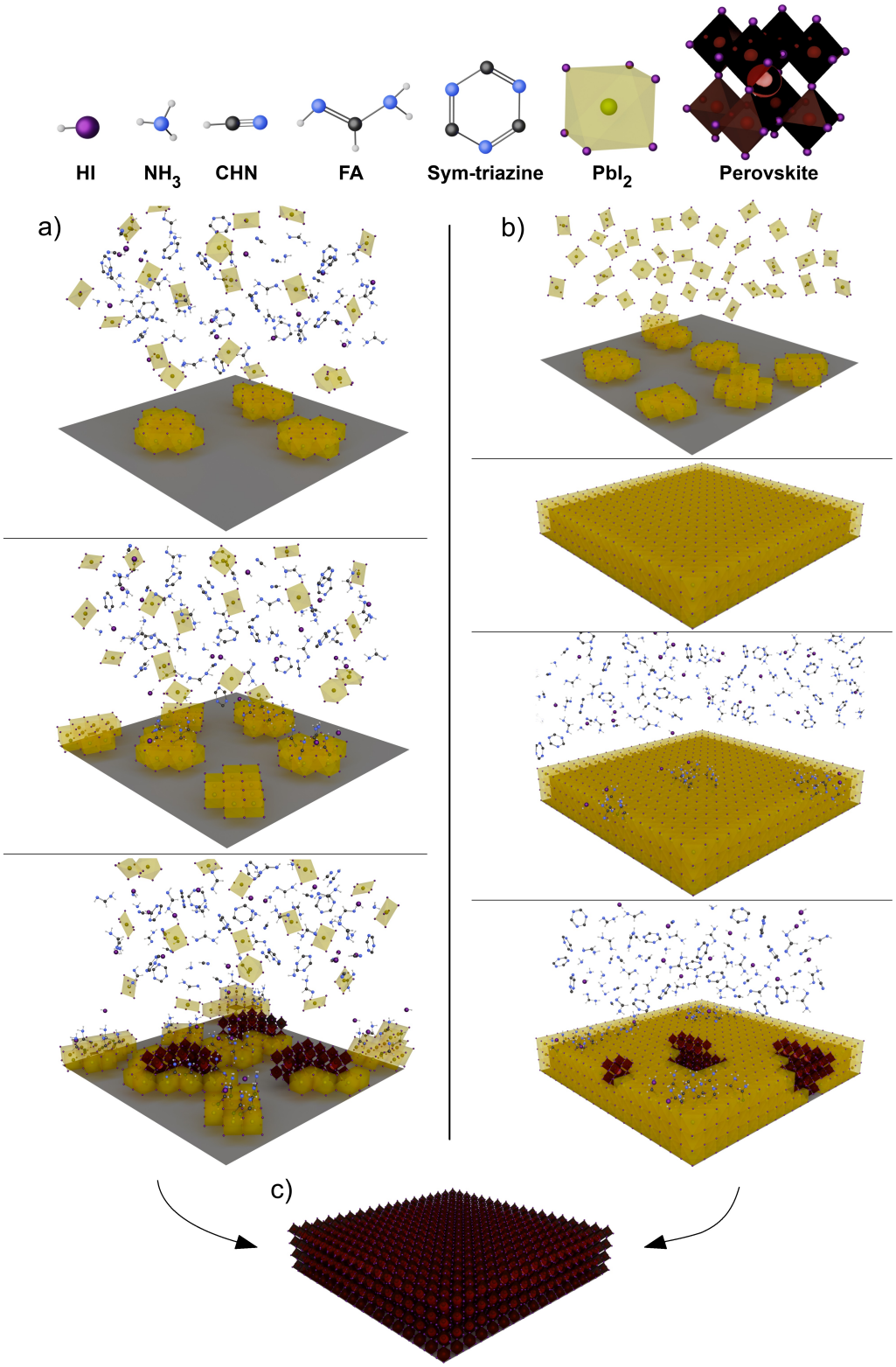

Figure 3.7: Schematic description of the perovskite growth process from vapors. The metal halide preferentially sticks onto the substrate and some of the organohalide byproducts react with it to form a perovskite. Sequences describing a) co-evaporation b) sequential evaporation processes. The resulting perovskite seed is shown in c).

Layer growth and resulting thin film structure

Various types of perovskite layer morphologies can be obtained with vapor-based processes: perovskite thin films featuring small grains stacked on top of each other [61], duplex microstructures with small equiaxed grains covered by larger columnar ones [62], narrow columnar grains [60], large grains spanning across the full layer thickness [62, 77], etc. Depending on processing conditions, one step of the growth often dominates the process and dictates the final layer morphology as discussed below.

Substrate temperature is one key parameter that may lead to significant changes in growth regime. Lohmann *et al.* [62] presented perovskite films exhibiting large grains films without unconverted lead iodide when co-evaporating MAI and PbI_2 on substrates kept at -2°C, a morphology counterintuitive with respect to structure-zone models [156]. As grain coarsening was likely limited in these low temperature conditions, such a morphology would be indicative of a low density of nuclei on the substrate and an impeded nucleation of new grains (Figure 3.8a). When increasing the substrate temperature or applying specific temperature profiles, films with equiaxed or duplex grain structures could be observed as the nucleation of new grains, and in some cases their growth, became facilitated. The growth rate was also reduced when increasing the substrate temperature, highlighting the critical impact of the adsorption/desorption of the organohalide fragments (factor τ_v in Eq. 3.2). Roß *et al.* [60] cooled the substrates to even lower temperatures (-25°C), which resulted in amorphous and non-photoactive co-evaporated films. While the desorption of precursors was made less likely, the interdiffusion of species and their reaction to trigger the formation of the perovskite phase became the limiting factor. After a post-deposition annealing step at a moderate temperature (40°C), XRD diffractograms demonstrated the presence of a mixture of crystalline lead iodide and perovskite phases. The authors mentioned that a substrate temperature close to room temperature is typically an optimal trade-off between increased adatoms mobility and diffusion length (higher temperatures) and higher organohalide fragment residence time (lower temperatures).

The deposition pressure also influences the growth process. Hsiao *et al.* noticed that increasing the partial pressure of organohalides during a sequential deposition process (from 1.3 10^{-2} to 1.3 10^{-1} Pa) multiplied the number of grain nucleation sites in these deposition conditions (with the substrates and walls heated at 75°C), producing perovskite layers with smaller grains. Clark *et al.* [112] studied the impact of varying substrate temperature (30 – 70°C) and pressure (40 – 1333 Pa) during the vapor transport deposition of $MASnBr_xI_{3-x}$. It should be noted that, in this case, a higher pressure corresponds to an increased carrier gas/evaporated precursor ratio and thus a decrease in reactant concentration. Their experiments showed an increase in grain size with increasing pressure and substrate temperature, in line with trends given by structure-zone models (regarding the impact of the substrate temperature). On the other hand, morphological changes differ when performing co-evaporation at lower pressures. In these conditions, increasing the substrate temperature leads to a decrease in grain size. Figure 3.8b-c shows top-view images of co-evaporated FAPI [174] and MAPI [61] perovskite films,

respectively. In both cases, the substrates were at room temperature and the total pressure is below 10^{-3} Pa. Films grown in these conditions typically display smaller grains than films co-evaporated under high vacuum but at lower substrate temperatures, as shown in Figure 3.8a and by Roß *et al.* [60].

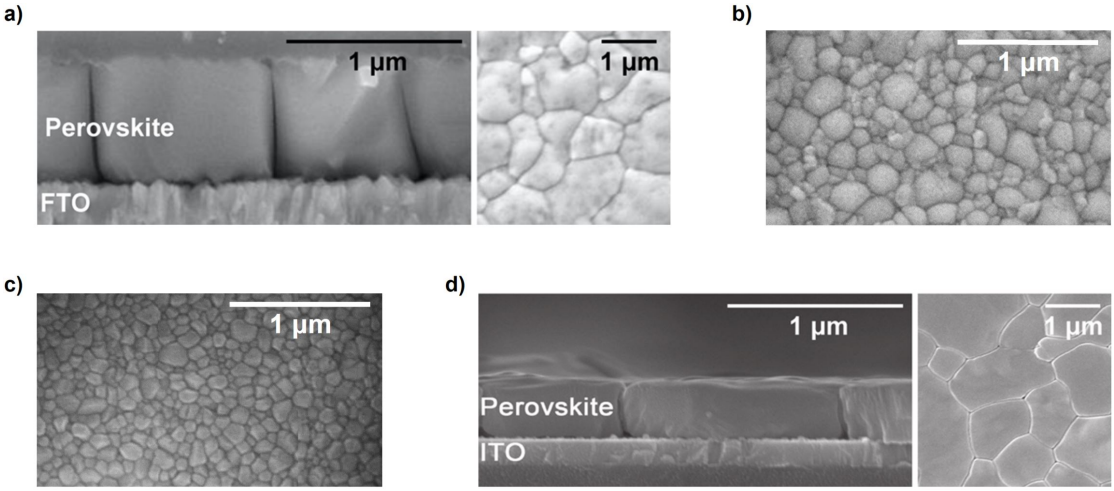

Figure 3.8: a) Cross-sectional and top-view scanning electron microscopy image of a perovskite film obtained by co-evaporation with substrates kept at -2°C and 10^{-3} Pa, adapted from [62], b) Co-evaporated $FAPbI_3$ film at room temperature and 10^{-3} Pa. Reprinted with permission from [174]. Copyright 2020 American Chemical Society. c) Co-evaporated $MAPbI_3$ film at room temperature and 10^{-3} Pa, adapted from [61]. d) Cross-sectional and top-view scanning electron microscopy image a perovskite thin films fabricated by exposing a 240 nm-thick template of PbI_2 to a MAI vapor at a partial pressure of 10^{-2} Pa, adapted from [77]

The film morphology is also severely impacted by the substrate itself as it directly impacts parameters such as surface energy, surface diffusion length of precursors adatoms and molecules λ_s, and their residence time τ_v. Lohmann *et al.* [62] showed that distinct morphologies could be produced when co-evaporating in the same conditions on various substrates at low substrate temperatures. The large grains presented in Figure 3.8a were grown on Fluorine-doped Tin Oxide (FTO)/C_{60}. Layers grown on ITO/C_{60} and crystalline silicon exhibited smaller columnar grains, while growth on FTO alone results in small and compact grains. Roß and co-workers also observed a difference in layer morphology depending on the contact below the perovskite [60]. For sequential processes, the morphology of the lead halide template also influences the perovskite process: the use of a porous template can facilitate the perovskite crystallization process [124, 175, 176].

Another way to influence the growth and the final layer is to change the environment in which the layer is grown or treated after its deposition. Several reports tend to show that the presence of oxygen may passivate perovskite trap states [120, 123, 177]. Humid air has a large impact on the perovskite conversion process as it favors interdiffusion and the subsequent crystallization process by making MAI more mobile within the perovskite [76]. Still, exposure to moisture

must be controlled to avoid any formation of hydrates and/or a degradation of the perovskite [178–180]. Hydrates or excess organohalide can be removed from the layers to some extent by a washing step using solvents [76, 181, 182]. In general, the presence of a metal halide excess in the final layer may accelerate the degradation of the perovskite layer in operational conditions [183].

Among the different post-deposition treatments, annealing in a moderate temperature range (100-150°C) is known to promote a better interdiffusion of the remaining unreacted species. It may also lead to a coarsening of the perovskite grains depending on the annealing temperature [184]. However, post-annealing treatments must be compatible with the different layers of the solar cell stack to avoid detrimental effects. As already presented earlier in this state of the art, the post-deposition cooling rate of the substrate also has a significant impact on the final film morphology: Ng *et al.* [123] reported that films cooled faster displayed pinholes and a lower shunt resistance.

In the end, numerous parameters may be adapted to tune layer properties. This flexibility also means that a similar film structure can be obtained with different processing routes. Figure 3.8a and d shows top-view and cross-section scanning electron microscopy (SEM) images of layers obtained by co-evaporation [62] and sequential evaporation [77], respectively. Both images display a similar fully converted perovskite morphology with smooth and micrometer-sized grains. The first example was obtained by co-evaporating precursors at low substrate temperatures (-2°C) without any post-deposition annealing, while the second one resulted from the sequential deposition of MAI on PbI_2 templates kept at 75°C.

Overall, the competing influences of the different process parameters offer numerous pathways to tune the microstructure of the perovskite layer and hence its optoelectronic properties. The critical step determining the perovskite layer morphology may quickly change from one set of process parameter to another one.

3.4 Conclusion

Vapor-deposited perovskite layers have shown good performance when included in single-junction solar cells, also when up-scaled to larger area active areas a few tens of cm^2. While solution-processing perovskite solar cells have so far exhibited a higher efficiency at the single-junction level, this difference results mostly from the fact that a smaller community is exploring vapor-phase routes rather than from any fundamental aspect. Still, the volatile behavior of organohalides and their tendency to decompose into several compounds upon sublimation complicates the deposition of high quality layers by evaporation processes. As discussed in the first part of this state of the art, innovative deposition chambers have been developed to improve the control over the deposition process and to account for the peculiarities of

organohalides. Notable examples include cooled shields in multi-source thermal evaporators, vapor transport systems decorrelating evaporation and deposition conditions, showerheads to improve deposition homogeneity, tube furnaces with variable flow directions to coat substrates when reaching steady state sublimation conditions, etc.

Process parameters		**Impact on the deposition process**	
Chamber Wall temperature		Less cross contamination, reduced thermal degradation of organohalides	Higher material yield
Source temperature		Easier control	Higher evaporation rate
Partial pressure of organohalides		Higher mean free path	Higher concentration of reactants
Substrate temperature		Higher adsorption of organohalides, lower free energy barrier, increase of surface energy (amorphous growth if too low)	Higher diffusion and mobility of reacting species
VTD	Carrier gas flow rate	Higher concentration of reactants, lower risk of turbulent flow	Better vapor transport
	Carrier gas temperature	Reduced thermal degradation of organohalides	Less parasitic condensation

Figure 3.9: Influence of process parameters on a vapor deposition of perovskites. Note that we refer here to the partial pressure of organohalides and not the one of the system (with or without carrier gas). In the latter case, the advantage of a lower system pressure is a higher homogeneity of vapors thanks to a higher diffusivity (cf Chapman-Enskog theory).

In the second part of this state of the art, we discussed the growth mechanisms of perovskite thin films grown from vapors and detailed the critical steps of the process which may impact the final layer structure. Experimental observations were related to theoretical concepts in an attempt to understand the impact on the layer properties of the process parameters accessible to the operator. Figure 3.9 summarizes the impact of key process parameters on the deposition process. Overall, one should keep in mind that small changes to a specific process condition can lead to significant differences in the layer properties, hence complicating the identification of clear process-property links. Still, the impact of certain process parameters is rather straightforward to establish, e.g., the usage of precursors increases with chamber wall temperature, or the evaporation rate increases with source temperature, two temperature settings that nonetheless should be selected to avoid/minimize the degradation of the organic precursors. Low deposition pressures increase the mean free path of the precursors, impacting how precursors reach the surface and possibly the microstructure. The impact of other process parameters is more difficult to predict. For example, the substrate temperature will impact the adsorption of the precursor species, their surface diffusion, interdiffusion and reaction to nucleate the first perovskite domains, grain coarsening, and a trade-off condition between these processes will need to be selected. In the case of vapor transport deposition, the carrier gas flow rate and its temperature may also impact the final layer properties. In the end, different processing routes may lead to similar layer properties if precisely adjusted, e.g. large columnar grains of high optoelectronic quality spanning across the full layer thickness.

This critical review of literature nourished the experimental results of this thesis presented in the next chapter. New discoveries, updating the understanding of organohalide vapor deposition and perovskite formation, are presented here and assembled in a manuscript to be submitted.

4 Vapor Deposition of Perovskite Thin Films

Historically, EPFL PV-lab's Perovskite group relies on a so called 'hybrid vapor-solution' process. It consists in a sequential process where a thermally co-evaporated metal halide template is converted into perovskite by spin-coating. This approach gave good results in the past, even on textured substrates [20], but usage of spin-coating on rough substrates is limited to small areas.

Consequently, Sahli *et al.* [41] started organohalide vapor deposition activities in order to replace this spin-coating step. The main objectives of this thesis are to analyze and understand the limitations of this first iteration, and continue the development of the vapor deposition activities.

The first section of this chapter is dedicated to experimental investigations on the first step of the process. Single source evaporation of pre-ball milled powders is studied as a potential replacement of co-evaporation, in the view of simplifying and accelerating the deposition of organohalides. Unlike most reports in literature, ball milling of substoichiometric mixes did not lead to new phase apparition. The in situ study via GIWAXS of the evaporation and EDX analysis reveal halide exchange during the phenomenon and changes in stoichiometry. Proof of concept devices reaching 15% efficiency for 1.7eV are demonstrated.

The second section of this chapter presents the development of a new vapor deposition process of organohalides. In situ GIWAXS & PL unveils different stages of perovskite conversion of a metal halide template via organohalide vapor deposition. Influence of process parameters is studied, providing insights on the different conversion regimes achievable. The influence of chemical environment and mechanical design is also studied, showing that for example, the commonly used materials for deposition chambers significantly impact the process. The presented process is proven to be flexible and compatible with bandgap tunability (via halide exchange) and additive strategies. Once applied to proof of concept devices, a robust and repeatable baseline of up to 17% perovskite solar cells (with 1.63eV bandgap) is obtained.

4.1 Sub-stoichiometric mixing of metal halide powders and their single source evaporation for perovskite photovoltaics[I]

4.1.1 Introduction

Vapor deposition processes are excellent candidates for photovoltaic device fabrication. A wide range of these techniques has been developed and mastered through decades of industrial development in numerous fields, e.g., in the semiconductor industry for light-emitting diodes, thin film processing, etc. Applied to perovskite thin films, evaporation processing demonstrated its capability to coat large areas with highly homogeneous and conformal films [35–38]. Photovoltaic devices with high power conversion efficiencies above 20% were also demonstrated [34, 38], albeit for comparably small devices areas (0.09 - 0.16 cm^2).

One of the most widely used vapor deposition techniques is high vacuum thermal evaporation. The evaporation of precursors in one or multiple crucibles in a high vacuum chamber involves different advantages: high purity growth, precise rate and thickness control, or low risks of lead contamination. This evaporation technique is particularly well-suited for depositing the metal halide backbone of hybrid organic-inorganic halide perovskites. It is however more delicate to employ when organic precursors are used, resulting in the development of sequential processes of perovskite thin films [42]. They comprise the thermal evaporation of a metal halide template, followed by its conversion into the perovskite phase by deposition of organohalides. This conversion can be obtained by any solution or vapor deposition technique.

Co-evaporation of multiple precursors allows alloying, therefore fine-tuning the resulting thin film's characteristics. However, increasing the number of sources increases the overall complexity of the process: more signals to stabilise and control, cross-talking concerns or sensitivity to single-signal fluctuations. In an attempt to simplify this process, we present here the mixing of metal halide precursors (lead iodide (PbI_2) and caesium bromide (CsBr)) and subsequent single source evaporation of the resulting mixture. The mixture, its evaporation and deposition are studied via synchrotron grazing incidence wide-angle X-ray scattering (GIWAXS). In situ GIWAXS allows tracking of the formation, fluctuation and disappearance of every crystalline phase, as well as its orientation with respect to the substrate. Readers

[I]This section is based on the publication: Guesnay Q., McMonagle C.J., Chernyshov D., Zia W., Wieczorek A., Siol S., Saliba M., Ballif C. and Wolff C.M., 'Sub-stoichiometric mixing of metal halide powders and their single source evaporation for perovskite photovoltaics' *ACS Photonics* with permission. Copyright (**2023**), American Chemical Society. Guesnay Q. did the experiments and measurements presented in the article, wrote the article and made the figures. McMonagle C.J. and Chernyshov D. provided training and assistance with the synchrotron XRD experiments. Zia W. and Saliba M. provided the ball milled powders. Wieczorek A. and Siol S. provided XPS data for reviewing stage of the article. Wolff C.M. initiated the project and provided guidance and suggestions for writing and revision of the manuscript.

interested in this technique are referred to the work of Held *et al.* [185] or the review of Qin *et al.* [186]. Energy-dispersive X-ray spectroscopy (EDX) complements this structural information with chemical insights. The resulting metal halide templates are then converted into perovskite thin films and implemented in photovoltaic devices.

4.1.2 Results and discussion

Powder mixing and evaporation

Lead iodide (PbI_2) and caesium bromide (CsBr) powders were mixed by ball milling at different molar ratios (0.125, 0.156, 0.2, and 0.25 CsBr for 1 PbI_2). These compositions will be referred to as 0.125, 0.156, 0.20 and 0.25 powder mixes, respectively. The objective was to find a mixture that, once thermally evaporated in a single crucible, results in a thin film with a composition similar to our co-evaporated template baseline [187]. The chemical composition of the latter corresponds to an approximate $Cs_{0.24}PbI_{2.2}Br_{0.25}$ in the resulting thin film, as measured with a self-consistent Energy-dispersive X-ray spectroscopy (EDX) procedure detailed in the Method section. The theoretical value expected from the evaporation rates forming compact films (0.1 Å/s CsBr : 1 Å/s PbI_2) is 0.156 CsBr : 1 PbI_2. This difference suggests a rearrangement during the evaporation and growth of the film.

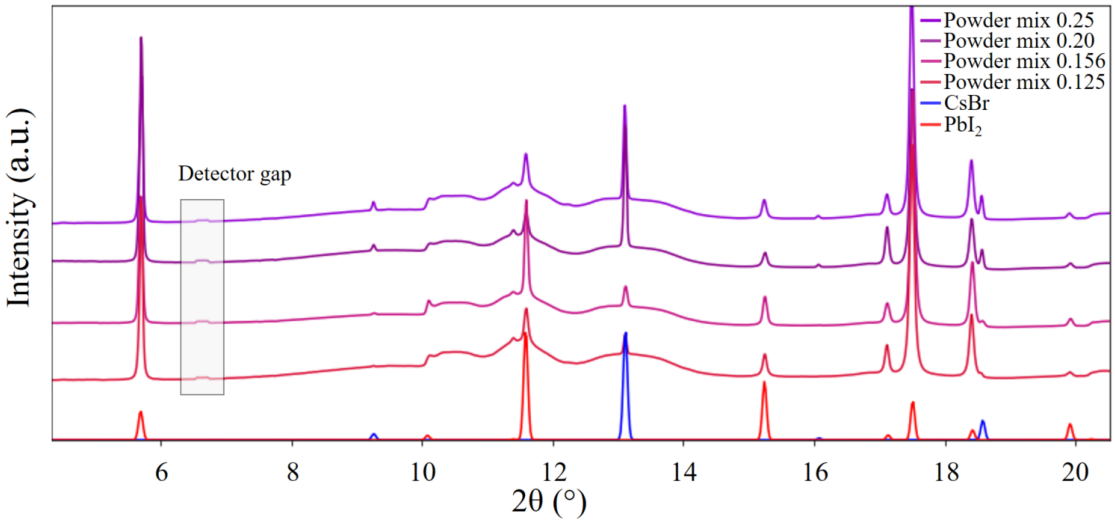

Figure 4.1: Powder diffractograms of the mixtures obtained by ball milling. All the powder mixes diffractograms can be expressed as a linear combination of the diffractograms of CsBr and PbI_2, without the appearance of any third crystalline compound. Note : the patterns were collected via synchrotron X-ray diffraction with a beamline wavelength of 0.694 Å.

The powder diffraction patterns of different CsBr:PbI_2 mixtures obtained by ball milling are shown in Figure 4.1. The patterns with an extended range of angles (2θ = 2.5-36.5°) are available in the supporting information (Figure B.1). Importantly, we did not observe a third crystalline phase in any of the different mixtures. This is a notable difference from other

ball milling reports in perovskite literature featuring the appearance of new phases [188–194]. For all diffractograms and the probed range of diffraction angles, all the diffraction peaks can be ascribed to either PbI_2 or to CsBr. Here, the CsBr-associated signal appears increasingly pronounced corresponding to the precursor fraction. The diffractograms can be expressed as linear combinations of the reference diffractograms of CsBr and PbI_2, except for two prominent features: 1. The shoulder next to the PbI_2 (1 0 0) peak at 10° that is very likely caused by a stacking fault of the PbI_2 structure [195], explained by the well-known polytypism nature of PbI_2 [196, 197], accentuated by the attempt to intermix the CsBr, and 2. Three broad features (8-12°, 12-14° and 17-18.5°) that can be associated with the glass capillary.

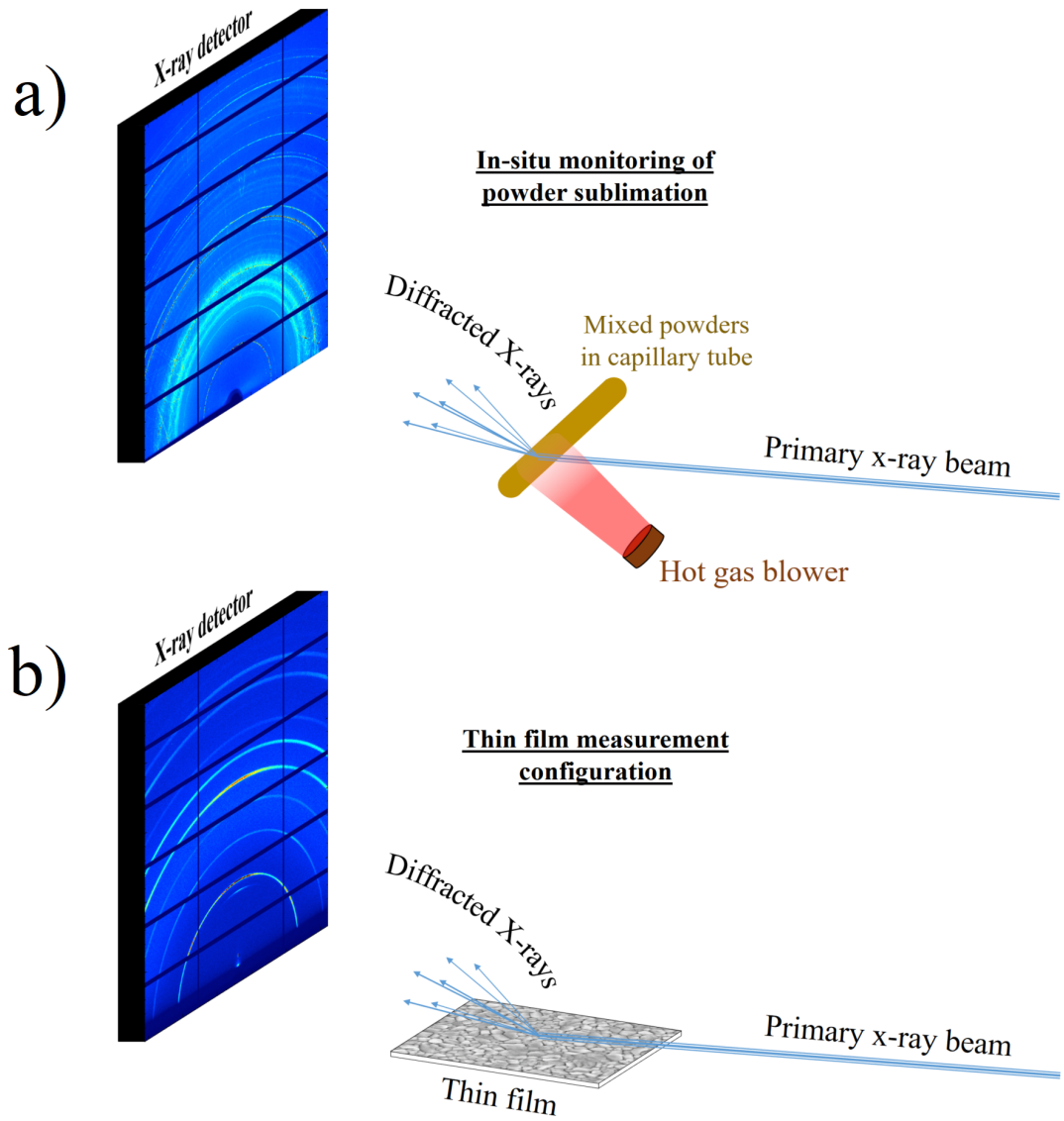

Figure 4.2: Schematic of the measurement configuration when measuring a) powder x-ray diffraction and b) thin films.

In the literature, Igual-Muñoz *et al.* [188] were reporting signs of a third perovskite phase after ball milling the same precursors, albeit with a stoichiometric ratio of 1 CsBr : 1 PbI_2. Rodkey *et al.* [189] documented the mass fractions evolution as a function of ball milling time with AgBr, CsBr and $BiBr_3$ as precursors. After a few minutes, a decrease of the precursors' fractions and an increase in intermediate phases (Cs_3BiBr_6, $Cs_3Bi_2Br_9$) was observed. Eventually, when approaching a hour of mixing, the only contribution came from the desired $Cs_2AgBiBr_6$ perovskite phase. Li *et al.* [198] adjoined a salt melting step after the mechanical mixing of the powders (CsI + PbI_2, CsI + PbI_2 + $PbCl_2$, CsI + PbI_2 + $PbCl_2$+ $PbBr_2$) and were, according to their differential scanning calorimetry (DSC) measurements, able to obtain new phases distinct from the precursors, albeit without diffraction measurements to confirm the presence of a new crystallographic phase. All the compositions investigated in this study feature low caesium content (in the 0.1 Cs : 1 Pb range).

After mixing, we studied the evaporation of the powder mixes via in situ synchrotron X-ray diffraction. A hot gas blower heated the glass capillary tube containing the powder mixes while acquiring the GIWAXS patterns. A schematic of the experiment is available in Figure 4.2. The capillary tube was furthermore connected to a turbo pump which established a pressure in the 10^{-6} mbar range, conventional values for thermal evaporation. In the following, the 0.2 mix is shown, as the behavior is qualitatively similar for all mixtures. The data of the other mixes are available as supporting information (Figure B.2).

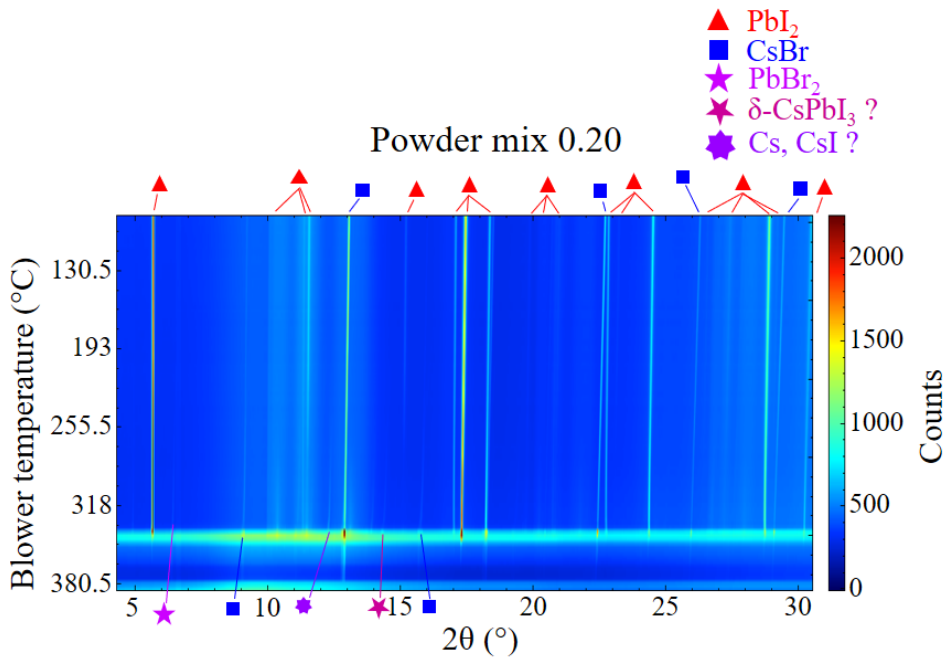

Figure 4.3: Temperature evolution of the integrated 2D GIWAXS map from 0.2 powder mix. Note : the patterns were collected via synchrotron X-ray diffraction with a beamline wavelength of 0.694 Å.

Figure 4.3 shows the in situ monitoring of the powder evaporation for the 0.2 CsBr : 1 PbI_2 case. In the first part of the measurement, from ambient temperature to 330°C, a general shift of the diffraction peaks toward lower angles can be observed. It is caused by heating resulting in a lattice expansion, as expected from materials with a positive thermal expansion coefficient. A phase rearrangement can be deduced from orientations increasing or decreasing in intensity, like the CsBr (100) close to 9° or the PbI_2 (102) peak close to 15°, respectively (with a beamline wavelength of 0.694 Å). Between 330°C and 370°C, a horizontal band can be observed. As displayed in Figure 4.4, in this temperature range the maps feature needle-like shapes with orientations that are quickly changing. This is due to the coalescence of powder particles forming crystallites with defects and rapidly changing orientations. This rearrangement of matter continues until the temperature is high enough for evaporation. At this point, only the background from the glass capillary is detected.

Interestingly, some new species can be detected close to the evaporation temperature. Prominently, a newly formed $PbBr_2$ phase is clearly distinguishable from the peak positions and the diffraction multiplicity, well below the evaporation temperature. Just above the transition to the evaporation regime, which results in a significant reduction in the signal-to-noise ratio, several other species appear.

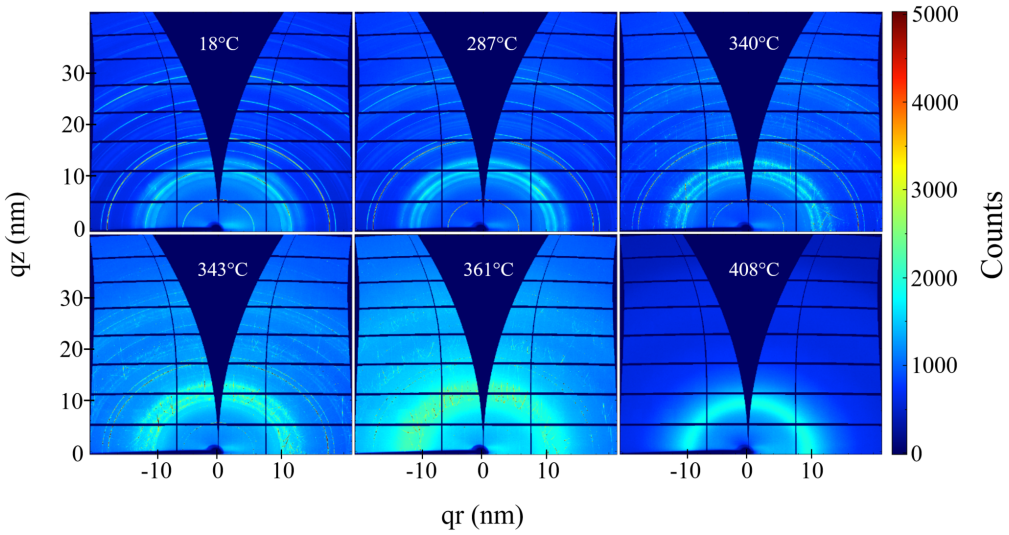

Figure 4.4: 2D GIWAXS in situ monitoring of the evaporation of a powder mix, in this case the 0.2 composition. All compositions follow the exact same trend. From ambient temperature to approximately 300°C the rings contract because of the thermal expansion. Then above, the patterns start to feature fireworks shapes. This is due to a sintering-like effect : when heated the powders particles start to coalesce when temperature is high enough and then form crystallites with defects and preferential orientation. These crystallites continue to coalesce as the temperature increases then everything is vaporised around 400°C, leaving only the background signal from the glass capillary.

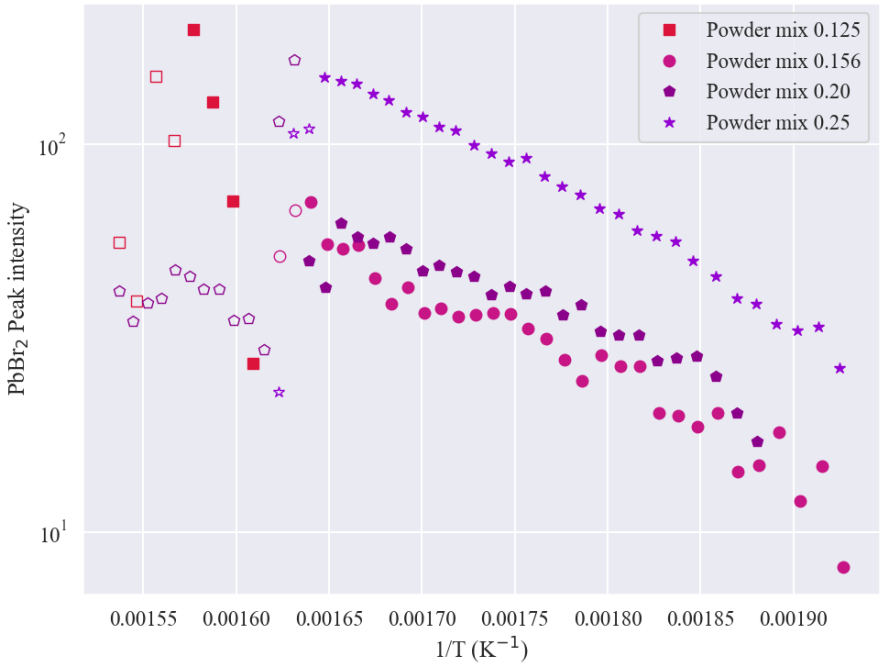

Figure 4.5: Arrhenius plot of the $PbBr_2$ peak evolution with temperature for all powder mixes. Plain markers denote pre-sublimation data; empty markers show data during sublimation.

This is possibly pointing toward other (mixed/halide exchange) species such as $CsPbI_3$, Cs or CsI, as indicated by the different symbols. However, given the signal-to-noise ratio for these peaks and the overlap of possible phases, their presence cannot be assessed with certainty. The halide substitution in the powder mixes follows a thermally activated, single-rate process, as can be seen in the Arrhenius plot of the clearly identified $PbBr_2$ peak close to evaporation, available in Figure 4.5.

This demonstrates that halide exchange between the precursors takes place close to and during evaporation and points towards the possibility of actively tuning halide exchange and pre-melted mixes in the future. This calls to mind the molten salt approach of Li *et al.* [198] previously discussed in this manuscript, where they melted the mixed salts before usage. Rapid interfacial halide diffusion has also been studied in the case of stacked metal halide perovskite thin films by Hautzinger *et al.* [199]. They show that spin-coating $CsPbI_3$ nanocrystals on top of a formed $CsPbBr_3$ nanocrystal thin film (then annealing at 50°C to remove the solvent) results in considerable halide interdiffusion, which can be prevented with single-layer graphene between the two inorganic perovskites. Single source evaporation of mixed precursors is a very attractive technique by its simplicity and rapidity, but the halide exchanges that may occur during the process must be taken into account. Future work would investigate a detailed description of this aspect of the process and the potential tuning leverage that it provides for compositional engineering.

$Cs_xPbI_yBr_z$ metal halide template thin films

The different powder mixtures were evaporated from a single source with our in-house thermal evaporator. For each single source evaporation, 1 gram of each mix was loaded into a pre-cleaned and pre-baked ceramic crucible and evaporated at a set, constant temperature (325, 350 and 375 °C). The evaporation temperatures were chosen based on our experience with the single powders, in order to satisfy the following compromise: the temperature has to be high enough to allow evaporation of both PbI_2 and CsBr and sufficiently low to ensure that the evaporation rate profile is controlled and repeatable. All powder mixes were evaporated targeting a 200 nanometers thin film, analogous to the co-evaporated metal halide template used in our baseline. The pressure in the chamber was in the 10^{-6} mbar range.

Figure 4.6a shows the two-dimensional diffraction pattern of a metal halide template obtained by evaporating the 0.2 powder mix as a function of the azimuthal angle. The measurement only shows the presence of PbI_2, with the (001) plane and its higher order reflections detected with a strong preferential orientation at 90 ± 10°. The latter result agrees with the nanoplatelets' arrangement predominantly oriented face up (with respect to the substrate) that is typically obtained when thermally evaporating PbI_2 [73, 200, 201] and visible in the scanning electron microscope (SEM) image of the corresponding film in 4.6b. The two diffraction wings on the sides stem from the substrate background.

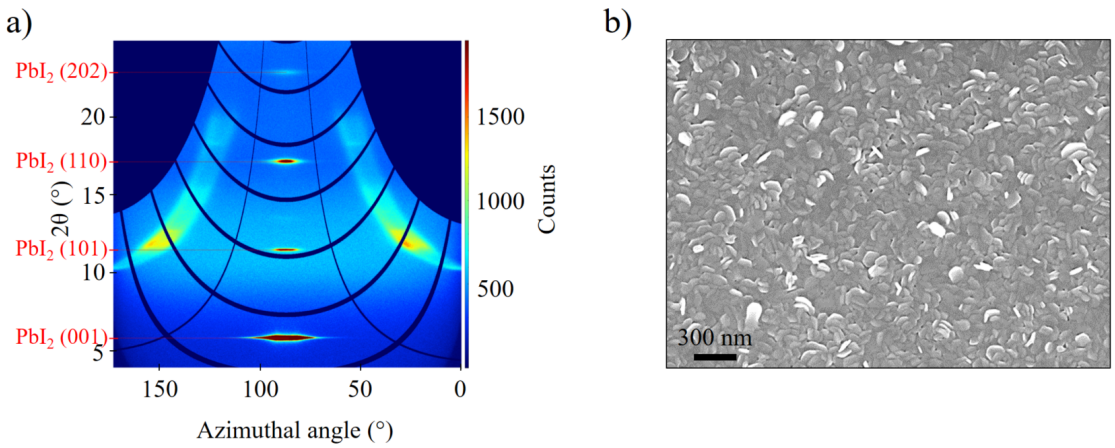

Figure 4.6: (a) Diffraction pattern as a function of the azimuthal angle of the metal halide thin film obtained by single source evaporation of the 0.2 powder mix and (b) corresponding SEM top-view of the film.

Measurement data of the other powder mixes and a co-evaporated template are provided as supporting information (Figure B.3) and all feature the exact same characteristics: we observe no clearly distinguishable crystalline CsBr nor any other phase, but within the measured range only a strong PbI_2 signal, oriented perpendicular to the substrate.

As a complement to this structural information, quantification of the chemical composition was done using EDX, with the protocol described in the Method section. Figure 4.7 compares the obtained Cs/Pb, Br/Pb, and Cs/Br ratios for thin films evaporated from different ball milled powders and at different evaporation temperatures. The target ratios of 0.2414 Cs/Pb, 0.2476 Br/Pb and 0.975 Cs/Br are defined by the values obtained in our co-evaporated template baseline (see pure precursor materials before and after evaporation in the supporting information, Figure B.4). Thus, when depositing Cs and Br in the targeted stochiometry (i.e., co-evaporating CsBr and PbI_2 powders in dedicated crucibles) it results in a relatively identical atomic ratio in the grown thin film.

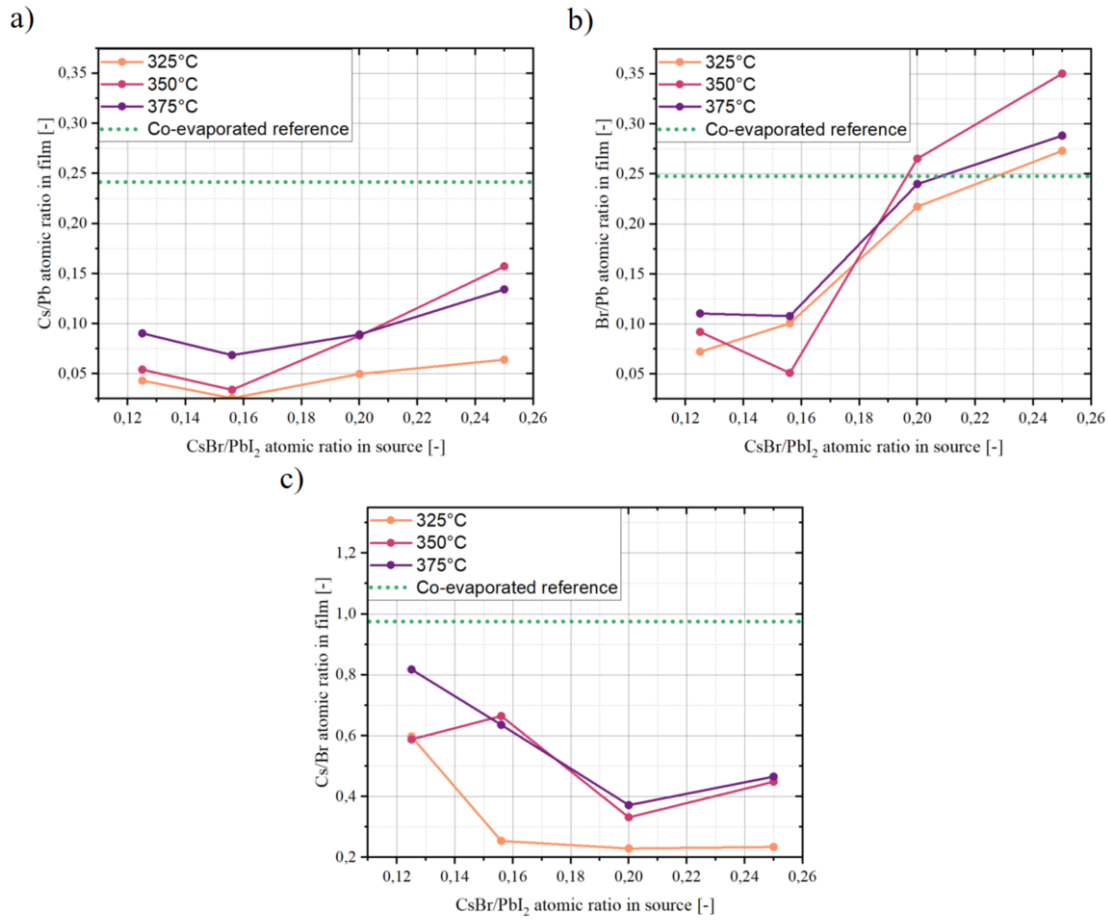

Figure 4.7: Chemical quantification of (a) Cs and (b) Br content with respect to Pb in the single source-evaporated thin films. (c) Corresponding Cs/Br ratios. Data obtained by EDX.

However, Figure 4.7 demonstrates that evaporating the mixed powders does not allow us to achieve the intended atomic ratios within the chosen experimental parameters (the Cs/Br ratios are comprised between 0.23 and 0.82 with a median value of 0.46, far from the 0.975 of the co-evaporated reference). This in turn suggests a species dissociation/halide exchange during the heating and single source evaporation phase, in line with the in situ observed

appearance of e.g., $PbBr_2$. Different phenomena are happening at the same time. First, an increase in CsBr/PbI_2 atomic ratio in the source increases the likeliness of a halide exchange. The latter, as discussed previously, follows a behavior described by the Arrhenius equation and is thus favored at higher temperatures. Higher temperatures also mean more caesium halides are evaporated, because of their higher sublimation point, but also increases further the evaporation rate of lead halides. Figure 4.7c shows the intricacy of this interplay.

This halide exchange may be resolved by evaporating at a higher temperature and heating rate, or flash-evaporation. We chose not to seek this path due to setup limitations (insufficient heating capacity, i.e., evaporating substantial amounts of PbI_2 before reaching the setpoint) and deemed the approach less desirable since we expect the ensuing vast evaporation rates would bring controllability/repeatability issues. Alternatively, we speculate that a more promising approach could be a partial replacement of CsBr by CsI in the powder mix. This would allow for increasing the amount of caesium in the resulting film while moderating the bromine content to reach the targeted relative amounts while ensuring repeatability. Since these template films are converted into mixed organic-inorganic perovskite layers in a subsequent step, an alternative could be to accept an increased Br content in the template and tune the final iodine/bromine content with the organohalide deposition used for the conversion into a perovskite in the second step. Investigating the spatial distribution of chemical species after single source evaporation is out of the scope of this study. However, the work of Moser *et al.* [202] shows that upon conversion into perovskite of a metal halide template, compositional gradients are homogenized. In their case, the initial template consisted of a bilayer of a pure PbI_2 layer on top of a pure CsI layer and after conversion into perovskite Cs and Pb are homogeneously spread along the perovskite layer.

Template conversion into perovskite

The metal halide templates obtained by co- or single source evaporation were converted into perovskite thin films by spin coating a formamidinium halide solution (1 FAI : 2 FABr in ethanol, 0.46M). The thin films were then annealed at 150°C for 20 minutes in air with controlled humidity (30% RH). Figure 4.8a shows the diffraction pattern as a function of the azimuthal angle of a converted template, obtained by evaporation of the 0.2 powder mix. Note, that we observed residual PbI_2, indicative of a mild under-conversion. The identified phases demonstrate the presence of PbI_2, as well as cubic and hexagonal formamidinium-based perovskites. The perovskite phases show a certain preferential orientation with the faces of the cubic structure mostly centered around three azimuthal angles : 37, 90 and 143°. This is the result of perovskite crystals dominantly oriented face and corner up, perpendicular to the substrate [203, 204]. When the conversion into perovskite is completed, this translates into small and randomly oriented domains as displayed in Figure 4.8b. The other converted perovskite film diffraction maps are provided in supporting information (Figures B.6 and B.7) and they all display the same features.

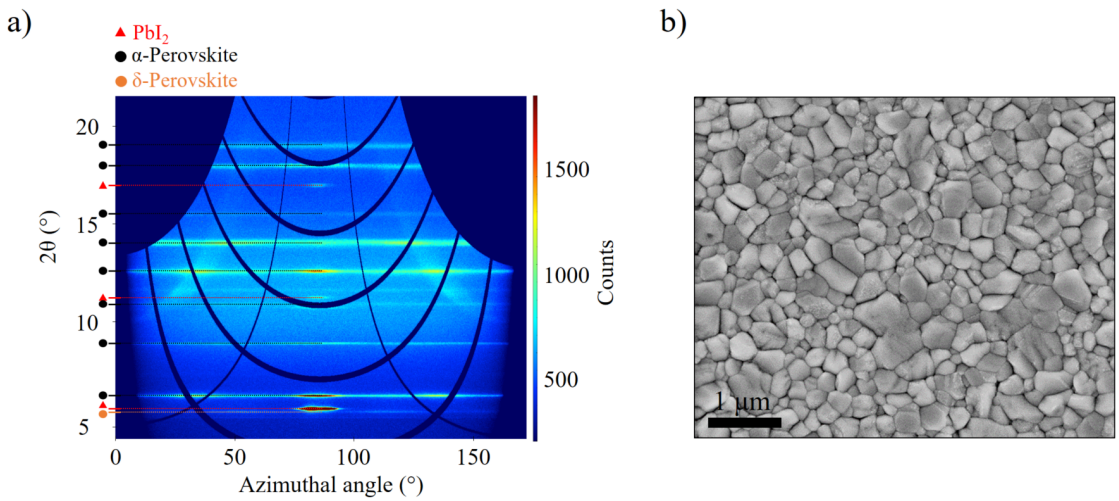

Figure 4.8: (a) Diffraction pattern as a function of the azimuthal angle of a partially converted metal halide template (from 0.2 powder mix evaporation) and (b) SEM top-view of a randomly oriented perovskite obtained by evaporation of metal halide then spin coating of organohalide.

A notable exception are films arising from the 0.25 powder mix templates, featuring a more pronounced presence of impurities such as hexagonal formamidinium perovskite and also a weak but distinguishable signal from the orthorhombic non-photoactive phase of $CsPbI_3$. Groeneveld *et al.* [205] observed the same non-photoactive impurities in their solution-processed thin films. Similarly, a small increase in bromine content ($Cs_{0.1}FA_{0.9}PbI_{3-x}Br_x$ with x increased from 0.45 to 0.6) was enough to have a detrimental effect on the purity and photoluminescence lifetime of the film. The appearance of such defects sets boundaries for the experimental space to be explored by the compositional engineering approach mentioned in previous sections.

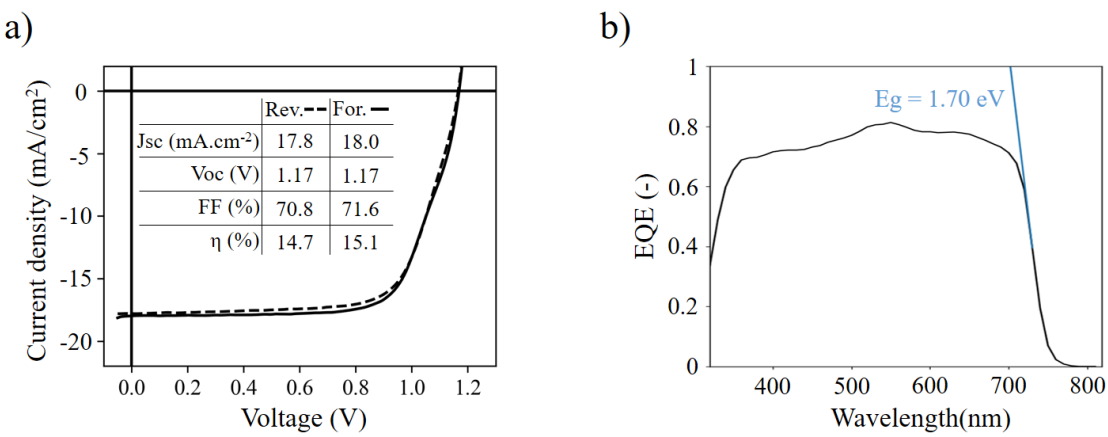

Figure 4.9: (a) Current density - voltage curve and parameters of the best proof of concept device and (b) corresponding external quantum efficiency.

Proof of concept photovoltaic devices were realised with the following architecture: Glass/Indium Tin Oxide/MeO-2PACz/Perovskite/C_{60}/Bathocuproine/Silver. The metal halide templates obtained by single source evaporation of the 0.20 and 0.25 powder mixes at 350°C were chosen. This choice was motivated by the fact that these conditions represent the best compromise between the Cs/Pb and Pb/Br ratio relative to the co-evaporated baseline, (cf. Figure 4.7). Fortunately, these conditions also exhibited the most repeatable and controllable evaporation. The organohalide solution concentration has been increased to maximize the conversion into perovskite and the performance. Figure 4.9 exhibits the main characteristics of the best proof of concept device. It reaches 15% efficiency with an optical bandgap of 1.70 eV and is obtained with a 0.20 powder mix template converted by a 0.51M organohalide solution. Devices fabricated with the 0.25 powder mix exhibit a much narrower range of "optimal performance" and are even in the best case less efficient (best device at 12%, statistics provided in supporting information, Figure B.8). This can be explained by the increased amount of impurities in the film, as discussed previously, and a higher optical bandgap of 1.72 eV, further away from the Shockley-Queisser optimum.

4.1.3 Conclusion

We investigated the mixing, single source evaporation and conversion into perovskite of non-stochiometric PbI_2 and CsBr mixes. Although no new phase could be formed during the ball milling of the precursors, new phases created by halide exchange were observed close to evaporation via in situ GIWAXS. This species rearrangement was confirmed by chemical analysis of the as-deposited thin films with EDX, and shown to be favored by lower temperatures of evaporation. Consequently, we chose to compromise between a high evaporation rate and controllable/reproducible evaporation profiles. The conversion of the metal halide templates into formamidinium-based perovskite reveals a face and corner up, perpendicular to the substrate, favored orientation. It is found that films with an initially higher amount of CsBr promote the growth of non-photoactive phases and thus lessen the photovoltaic device performances. In a future study it would be interesting to study under which conditions mechanosynthesis techniques such as ball milling can favor, or not, the appearance of new phases when mixing metal halides. In the case of strict mixing, without new phases, fine-tuning the final film composition by introducing new metal halides appears as an engaging path to follow.

Various benefits could be gained adopting single source evaporation of the metal halide template, the most significant being the time saved compared to co-evaporation. However, this is a matter of optimising the process flow for potential industrialisation, the thermal evaporation of metal halides is nowadays very well understood and controlled. This is not the case of organohalide vapor deposition: its understanding is still rudimentary. Moreover, efficient and industrially meaningful processes are yet to be presented. The next section of this chapter brings suggestions to tackle these challenges.

4.2 Pizza Oven Processing of Organohalide Perovskites (POPOP) : a simple, versatile and efficient vapor deposition method[II]

4.2.1 Introduction

As detailed in previous chapters, vapor deposition is a promising path for perovskite fabrication. However, hybrid organic-inorganic lead halide perovskites, demonstrating the highest performances, are delicate to evaporate. Complexity arises from the different behaviors of inorganic and organic precursors upon evaporation. While vapor deposition of inorganic halide precursors is relatively straightforward, vapor deposition of organohalides is more challenging because of their high vapor pressure and an inclination to degradation [39, 40, 163–165].

Hybrid vapor deposition processes are defined by combining two different vapor techniques: one adapted to metal halide deposition and another designed to best cope with the peculiarities of organohalides. Whereas already existing vapor processes (such as thermal evaporation or magnetron sputtering) are well adapted to metal halides, there is a need for the development of a vapor deposition process of organohalides, capable of converting metal halide templates into large-scale, uniform and high-quality perovskite thin films with process durations of industrial relevance. [42].

To tackle these challenges, Sahli *et al.* presented a vapor transport deposition system featuring a separated evaporator and deposition chamber [41]. The generated organohalide vapors are transported from the evaporator to the deposition chamber by a carrier gas through a network of pipes and dispensed on the samples via a showerhead. All process parameters (different temperatures, pressure, carrier gas flux etc.) are decorrelated and independently controlled. The setup's capabilities were demonstrated by homogeneously coating an industrially standard 6-inch (239 cm^2) textured silicon wafer with a methylammonium lead tri-iodide ($MAPbI_3$) perovskite layer. Still, the transition to depositing formamidinium (FA) as the organic cation for the high-performing perovskites is more complicated because of the degradation of the

[II]This section is based on a manuscript under preparation: Guesnay Q., Sahli F., Artuk K., Turkay D., Kuba A.G., Mrkývková N., Végsö K., Šiffalovič P., Schreiber F., Ledinský M., Lai H., Fu F., Fürst N., Schafflützel A., Bucher C., Jeangros Q., Ballif C. and Wolff C.M. 'Pizza Oven Processing of Organohalide Perovskites (POPOP) : a simple, versatile and efficient vapor deposition method.'. Guesnay Q. did the experiments and measurements presented (if not stated otherwise), wrote the article and made the figures. Sahli F. started the vapor deposition activities as described in the manuscript. Artuk K., Turkay D. and Kuba A.G. provided support with development of proofs of concept tandems and large area deposition unfortunately not ready for the manuscript due to machine failures. Mrkývková N., Végsö K., Šiffalovič P. and Schreiber F. provided training and access to their unique setup of combined in situ PL and GIWAXS. Ledinský M. initiated this collaboration. Lai H. and Fu F. did ToF-SIMS measurements. N. Fürst, A. Schafflützel and C. Bucher provided technical support throughout the years. Jeangros Q. provided guidance the first months of the project as thesis co-director, replaced by Wolff C.M for the following years. Wolff C.M. also provided help by suggesting improvements of the manuscript.

organohalide vapors both during evaporation [39] and transport [40]. Here, replacing the inert nitrogen carrier gas with ammonia to mitigate the degradation of FA vapors was proposed, enabling the formation of FA-based halide perovskites, albeit only after several hours of vapor exposure [40].

This section presents a fast, low-cost, simple, and easy-to-reproduce advancement over the previous processes (Pizza Oven Processing of Organohalide Perovskites, POPOP). We study the perovskite formation in this process from structural (in situ Grazing Incidence Wide Angle X-ray Scattering, GIWAXS), optoelectronic (in situ PhotoLuminescence, PL; PhotoLuminescence Quantum Yield, PLQY) and chemical (Nuclear Magnetic Resonance, NMR; Fourier-Transform InfraRed spectroscopy, FTIR) perspectives. We elucidate the influence of deposition parameters, mechanical design and chemical environment within the reaction chamber on thin film growth. Bandgap tuning and growth modulation via additive incorporation is demonstrated before implementing the developed thin films into perovskite solar cells.

4.2.2 Presentation of the process

The first iteration of the in-house developed vapor deposition chamber [41] was designed with the objective of decoupling the evaporation and the deposition of the organohalides as much as possible. This entails a physical separation of the two processes. Consequently, evaporation was performed outside of the deposition chamber, and a nitrogen carrier gas guided the as-generated vapors through a pipe network to the chamber. This design choice is prevalent among industrially mature chemical vapor deposition processes [106, 107, 206], as it offers a straightforward approach for upscaling.

In the case of perovskite vapor deposition, this approach is accompanied by limitations to the process development. While working reasonably well with methylammonium (MA) based perovskites, formamidinium (FA) based perovskite cannot be deposited with the original process. As demonstrated in Figure 4.10, the thermally evaporated metal halide template (200nm of PbI_2 : CsBr co-evaporated at 1 Å/s and 0.1 Å/s respectively) cannot be converted into FA perovskite, under a wide variety of process parameters. The only change detected in the thin films after the process is a strong presence of NH_4I. Suspecting the transport pipes as the origin of the lack of conversion, we reduced the pipe path from the evaporator to the reaction chamber (cf. Figure 4.11). This approach enabled the formation of FA-perovskites, albeit still limited by a long process duration and residual presence of NH_4I. We also observed that a complete template conversion into perovskite could be achieved if the substrate is directly positioned in the evaporator.

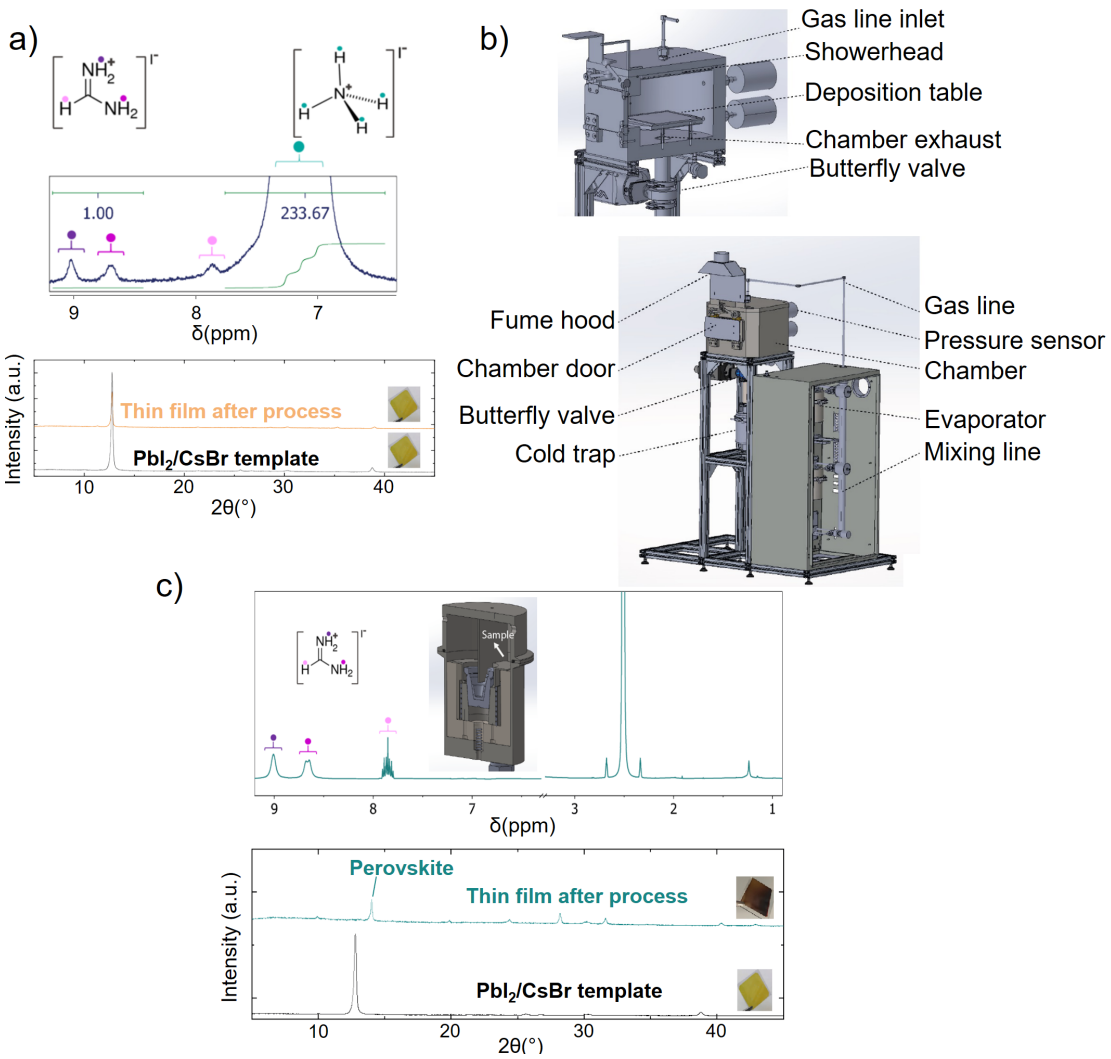

Figure 4.10: a) Nuclear magnetic resonance (NMR) and X-ray diffraction (XRD) of a thin film located on the deposition table before and after an attempt to deposit FAI. With the powder burnt from the evaporator and the vapors pushed in the chamber with a nitrogen carrier gas, only an overwhelming presence of NH_4I is detected in the resulting layer. The temperature of the pipes is maintained at 200°C, maximum setpoint. Lowering it only results in a gradual condensation of any gaseous specie in the pipes. b) Schematic of the setup: cross section of the deposition chamber and complete view of the setup. c) NMR and XRD of a sample that stayed in the evaporator, close to the crucible during the process. In this case, when the vapors were not carried through the pipes and the showerhead but directly generated close to the substrate, a complete (no remaining PbI_2) and clean (no parasitic NH_4I) conversion of the template into perovskite was observed. The 'default' process parameters (crucible temperature 200°C, 800 sccm of nitrogen carrier gas, deposition table at 140°C, gas line at 200°C, duration of 2h etc) were all varied in order to obtain perovskite conversion, with no different results that the one presented in this figure.

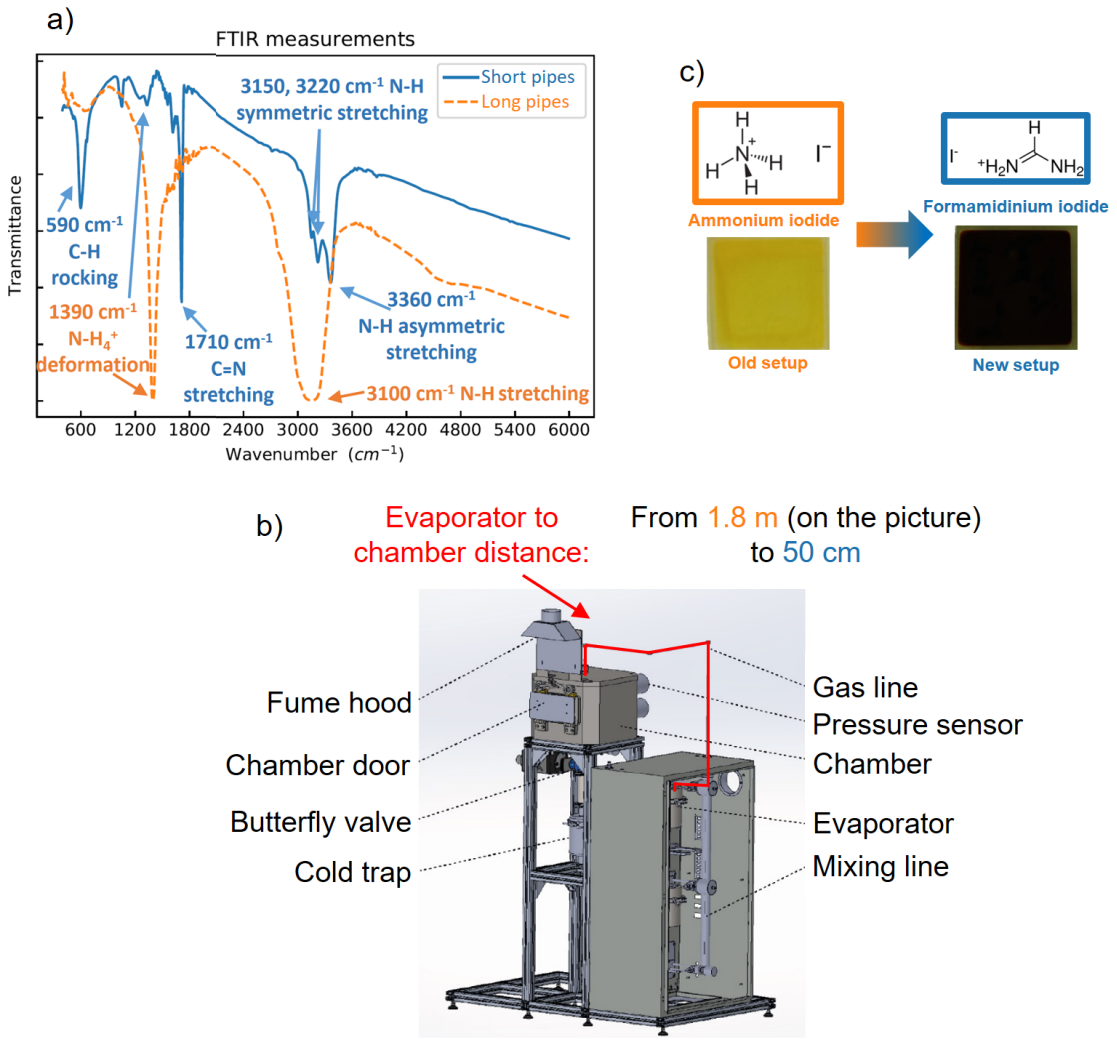

Figure 4.11: a) Fourier Transform InfraRed (FTIR) spectra of thin films positioned on the deposition table in the chamber, before and after shortening the pipes path between the evaporator and the chamber. This greatly reduces the quantity of NH_4I and allows FAI incorporation in the resulting thin film. As described in Figure 4.10, temperature of the tubes between the evaporator and the chamber is in all cases maintained at 200°C, to avoid parasitic condensation. From these results, we can conclude that the degradation of the FAI vapors generated in the evaporator is proportional to the path length crossed by the vapors. With long pipes, the thin films always show NH_4I traces whatever the duration of the process, while with the short tubes it takes up to 6 hours to have a complete conversion of the 200nm metal halide template into perovskite (with NH_4I traces).

We conclude that the formamidinium vapors degrade along the path through the pipes, scaling with the path length. This could be provoked by the high temperatures of the pipes (heated at 200°C after process optimisation to prevent direct condensation of organohalide salts in the pipes) or FA degrading into several byproducts upon heating [39, 40]. We consequently

designed a setup with minimal substrate to organohalide distance and designed a microreactor based on polytetrafluoroethylene (PTFE) for its chemical inertness after carrying out a detailed study (cf 4.2.5, Figures 4.20-4.24) showing the effect of different materials in the vicinity of the reaction volume (two grades of stainless steel, PTFE, polyimide, aluminum foil). Moreover, short distances and small reaction volumes promote faster reactions, a critical parameter to reduce takt time for perovskite vapor deposition processes in an envisaged production line[42].

In a last design modification, we aimed to remove the heating phase and start the reaction by placing precursors and substrate in a reaction chamber maintained at a temperature setpoint. A constant temperature without complicated heating/cooling profiles simplifies the process, making it less error-prone and easier to reproduce. Lastly, loading the precursors at a given temperature setpoint, if high enough, allows to mix precursors with different boiling points and expose substrates almost simultaneously to all species. For example, a vapor additive could be provided to the growing thin film all along the process, whereas a heating profile starting from room temperature would unevenly disperse chemical species following their different phase transitions at a given temperature/pressure.

To combine all these advantages, i.e., initiating the reaction without delay due to transfer or pre-heating, reducing the vapor transport path length to a minimum, and ease of handling, we developed a method in which the reaction enclosure - constituting the lead halide template on a substrate, the holder made from PTFE and the organohalide powder delivery system - is pre-mounted and subsequently transferred as one unit into a vacuum oven at a temperature setpoint that reaches its vacuum state ($p \approx 10^{-1}$ mbar) within seconds.

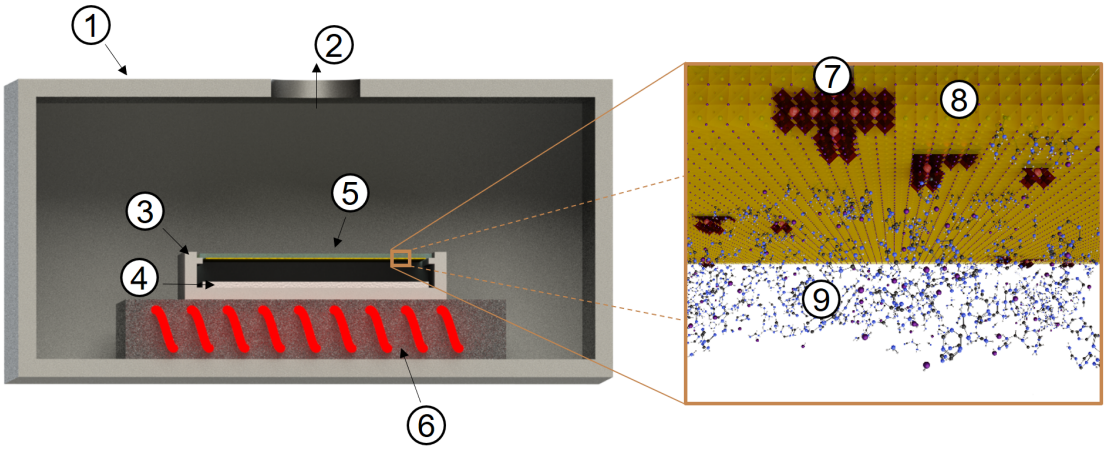

Figure 4.12: Schematic of the process. 1) Vacuum chamber 2) To pump 3) Holder 4) Organohalide source (powder, pellet, dried solution etc) 5) Substrate facing down 6) Heating stage 7) Forming perovskite 8) Metal halide template 9) Organohalide vapors.

All these principles together lead to a concept reminiscent of the craftsmanship of a pizzaiolo, coining the name of the process: *Pizza Oven Processing of Organohalide Perovskites (POPOP)*. A mild vacuum environment is an attractive compromise between high vacuum and ambient. Unlike the latter, it provides control of the atmosphere and promotes the diffusion of the vapors, promising enhanced homogeneity. However, pumping time is only in the range of seconds, while reaching high vacuum in a chamber large enough for vapor deposition takes dozens of minutes. A proof of concept prototype is developed and consists of a hollow PTFE cube, with formamidinium iodide (FAI) powder dispersed in it and holding a substrate covered with a metal halide template (PbI_2 alloyed with CsBr, details in Methods) facing downwards. A schematic of the process is shown in Figure 4.12, drawing of the holder prototype available in Figure 4.13a.

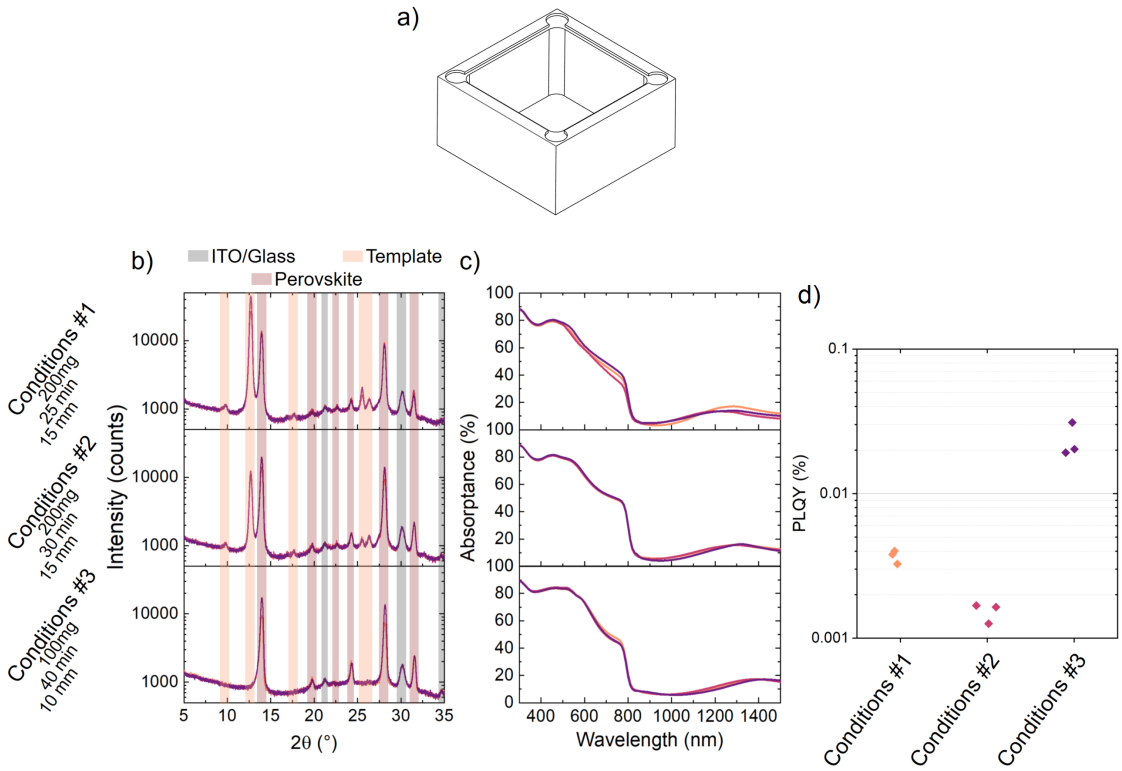

Figure 4.13: a) Schematic of the prototype holder. b) Investigation of the process repeatability. Process is run at the same conditions three times for three different sets of process parameters (9 separate runs), and XRD, c) Absorptance and d) PLQY are measured.

Several process conditions were varied and repeated (mass of loaded FAI, duration of the process and substrate to precursor distance) to assess the repeatability and controllability of the approach. The produced thin films were then analyzed by X-ray diffraction (XRD), Ultraviolet to Visible Absorption Spectroscopy (UV-Vis) and PhotoLuminescence Quantum

Yield measurements (PLQY), with the results presented in Figure 4.13. The simple prototype allows for the repeatable and controllable fabrication of perovskite films, albeit with low throughput (one 2.5 x 2.5 cm^2 sample for any given condition). We showcase three different conditions representative of a larger set of conditions tested. In particular, from condition no. 1-3 we see a reduction in XRD signals assigned to the template (10° & 13°) coinciding with an increase in perovskite signal (14°). At the same time we observe significant differences in the PLQY (ca. one order of magnitude higher PLQY for condition no. 3 vs condition no. 2) of the films converted under these different conditions. The absorptance, however, appears nearly identical for the different conditions. Scanning Electron Microscope (SEM) images and Nuclear Magnetic Resonance (NMR) spectra (Figure 4.14), show no apparent differences in the film morphology, and the NMR spectra show no additional signal except FA signal without any other undesired species, irrespective of the process conditions.

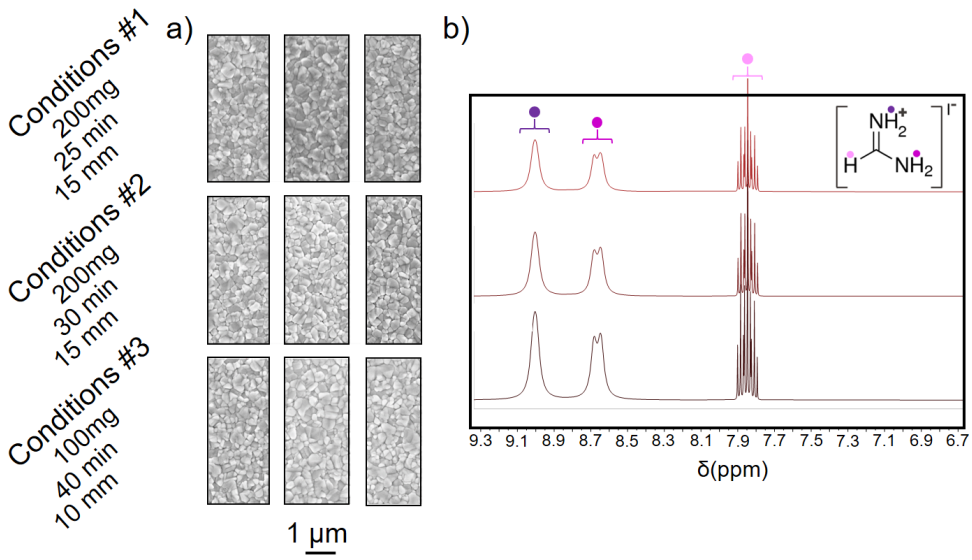

Figure 4.14: Complement to Figure 4.13 : a) Scanning Electron Microscope (SEM) images and b) NMR spectra of the thin films (1 randomly selected substrate for each condition).

4.2.3 In situ study of thin film growth

The abovementioned ex situ measurements after the conversion process suggest different conversion stages depending on the process conditions (temperature, duration, mass of organohalides, etc.) reflected in differences in the crystallographic and optoelectronic properties. We sought to follow the evolution from template to perovskite by measuring the photoluminescence and X-ray diffraction (via GIWAXS) in situ during the reaction as proposed by Mrkyvkova and Held *et al.*[185, 207][III].

The reaction chamber for the in situ setup is designed to mimic the reference chamber closely, yet one notable difference between the setups is the temperature profile. To exclude artefacts introduced hereby, we compared films reacted with different temperature profiles, either with a progressive heating profile or the reference flat temperature profile in Figure B.10 after the same reaction times. From a structural (XRD), optoelectronic (PLQY) and chemical (NMR) point of view, the thin films produced with these two temperature profiles exhibit nearly identical results for all probed stages of conversion. Furthermore, intensity tests of the X-ray beam and laser excitation were made to exclude any detrimental influence on the in situ monitoring. The X-ray fluence was 10^8 photons/cm^2/s, two orders of magnitude below 10^{10} suggested by Held *et al.* [185] to prevent degradation and well below the 10^{16} decomposition threshold reported by Svanström *et al.* [208]. We did not observe a degradation by illumination either, by comparing the evolution under continuous and discontinuous (30s off, 5s on) light illumination, Figure B.11. Note, the in situ experiments were conducted with a temperature setpoint at 170°C, enabling a slightly decelerated reaction, allowing for more precise tracking and a faster heating to setpoint, despite the smaller heating capacity [IV].

[III] A few adjustments to the sample holder were made. The main change consists of two lateral X-ray transparent windows in polyimide (PI), to allow the primary X-ray beam to reach the forming perovskite layer facing down, and let the diffracted beams to reach the X-ray detector. The holder is also slightly higher (2 cm substrate to precursor distance) to grant a sufficient solid angle for X-ray collection. A schematic of the holder, as well as pictures describing the experimental setup, are available in Figure B.9. The process parameters were chosen to mimic conditions in the original reaction chamber: layer stack, pressure, temperature, geometry, materials used etc. Experimental details are available in the Methods section of the supporting information

[IV] reaching 190°C would have taken ca. 45 min.

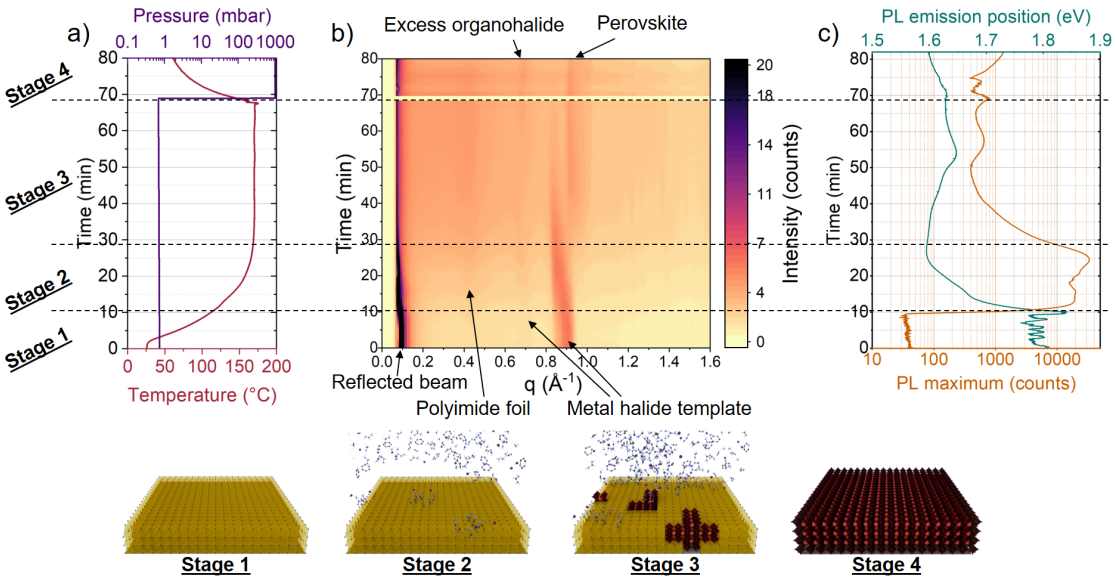

Figure 4.15: In situ GIWAXS & PL monitoring of the metal halide template converting into perovskite upon reacting with FAI. a) Pressure and temperature profiles, b) azimuthally integrated GIWAXS profiles and c) evolution of PL emission intensity and peak energy position. Four different stages are identified : 1) Heating up, template luminescence 2) Thermal expansion of the holder (cf. reflected beam shift) and formation of highly emissive perovskite clusters undetected via GIWAXS 3) bulk formation of perovskite and consumption of metal halide template and 4) interruption of heating and exposure to ambient air.

An exemplary in situ run is displayed in Figure 4.15. The reaction process can be divided into four stages. The first stage (0-10 min) is the initialization stage: the temperature reaches ca. 75% of its target (125°C vs 170°C). The GIWAXS signal stemming from the metal halide template does not show major changes and only a weak luminescent signal from the inorganic template [69] is detected. The thermal expansion of the system marks the second stage (10-30 min), evident from the shift of all the reflected and diffracted X-rays to lower q. The expansion invokes a slight deviation from initial grazing conditions, affecting the signals, and limiting the information drawn from GIWAXS here. On the other hand, the photoluminescence signal displays a significant increase in intensity after ~10 minutes with an emission peak emerging at a photon energy of ~1.8 eV that then gradually shifts to lower energies. This marks the perovskite nucleation featuring highly emissive perovskite clusters.[185, 209–211].

In stage three, the clusters coalesce and the main perovskite formation occurs. The metal halide template signal gradually decreases, while the perovskite signal progressively increases (GIWAXS data, blends over after ~35 min). The PL peak energy drops to ~1.6 eV and the signal drops by one order of magnitude. This can be explained by the fact that as the conversion progresses, the initially isolated perovskite crystallites, passivated by surrounding lead iodide, spread and merge. The as-formed domain boundaries embody non-radiative recombination centers [212], hence decreasing the luminescence. Two factors influence the position

of the photoluminescence emission: changes in perovskite cluster size (with an inversely proportional relationship, cf. quantum confinement)[185, 210, 211, 213] and halide exchange (more iodine incorporation decreases the bandgap in terms of energy). The metal halide template (containing CsBr) constitutes a finite bromine source, promoting a mild blueshift of the bandgap. This phenomenon is visible between 30 and 55 minutes. Meanwhile, the continuous exposure to FAI vapors encourages a redshift via halide exchange [144, 214], visible from 55 to 70 minutes through a shift back from 1.65 eV to 1.6 eV.

After 69 minutes, the GIWAXS signal from the metal halide template has vanished and the conversion is considered as completed. Entering stage 4, heating is stopped, and the chamber is opened to ambient air. This stage mimics the condition when the substrate is removed from the POPOP deposition chamber. We observe that the PL peak emission energy decreases and that the intensity increases. A possible explanation of the PL emission position redshifts could be the cooling of the substrate [215], while the increased PL intensity can be ascribed to a lower degree of electron-phonon scattering as the temperature decreases [216].

Towards the end of stage 3, we observe an additional signal at 0.7 $Å^{-1}$, arising from an excess organohalide phase [122], not to be confused with the metal halide template. The latter, already visible in underconverted perovskite films as presented in Figure 4.13, stems from clusters of δ-$CsPbI_2Br$ [217, 218] created during the co-evaporation of PbI_2 and CsBr. A comparison is shown in Figure 4.16.

Beyond tracking the growth, the orientation relative to the substrate - and how it evolves during conversion - can be inferred from the GIWAXS data, displayed in Figure 4.17. The template signal at 0.7 $Å^{-1}$ and the signal at 0.7 $Å^{-1}$ in stage 4 (overconverted) follow the orientation of the lead iodide and perovskite phases, respectively.

The two template-related signals indicate a preferential orientation facing up with respect to the substrate, typical of the nanoplatelets obtained when evaporating metal halides [73, 200, 201]. The cubic perovskite phase, dominantly oriented face up at the start of the growth, transforms into a preferential face and corner-up orientation during the conversion [203, 204]. The fact that the excess organohalide signal follows the perovskite's orientation suggests that it's behaving as a 2D-like phase growing on the perovskite facets likely forming a structure close to FA_2PbI_4 [219].

As detailed in Figure B.12, this low angle excess perovskite phase appears to be correlated with NH_4I content in the thin films, as determined by FTIR and NMR. A notable exception is observed with the PTFE hollow cube introduced as proof of concept in the last section. Overconverted films obtained with this holder and the presented process do not show NH_4I in the thin films.

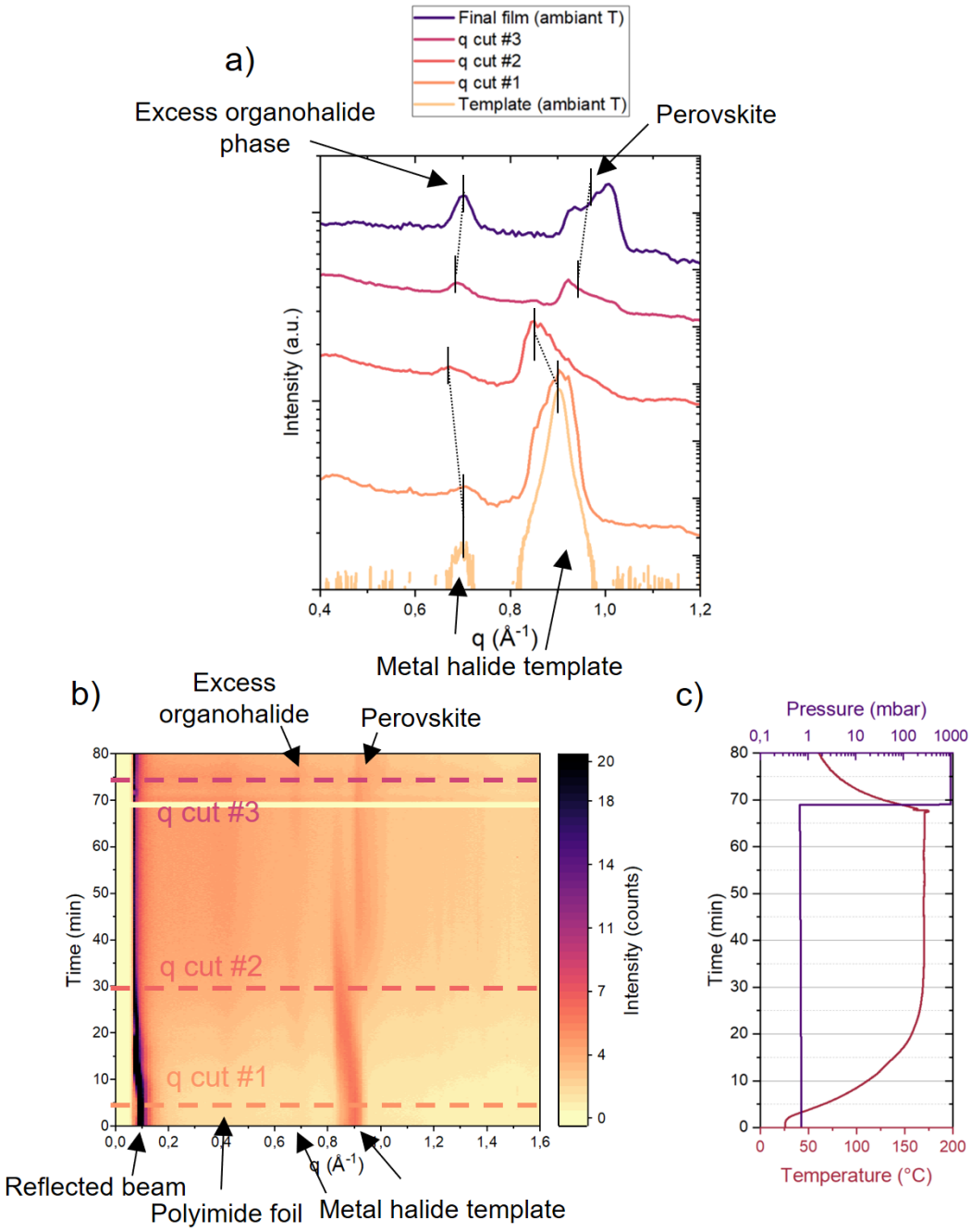

Figure 4.16: a) q cuts of the in situ GIWAXS data. The #1 and #2 cuts correspond to the initial metal halide template before and after a shift due to thermal expansion, respectively. The #3 cut shows the film once fully converted into perovskite, with an excess organohalide phase appearing. b) Integrated GIWAXS profiles with corresponding cuts and c) pressure and temperature profiles. The visible alignment of the metal halide template and excess organohalide peaks is due to their initial closeness and this confusion is amplified by the shift of the signals provoked by the thermal expansion of the holder (cf. the reflected beam shift).

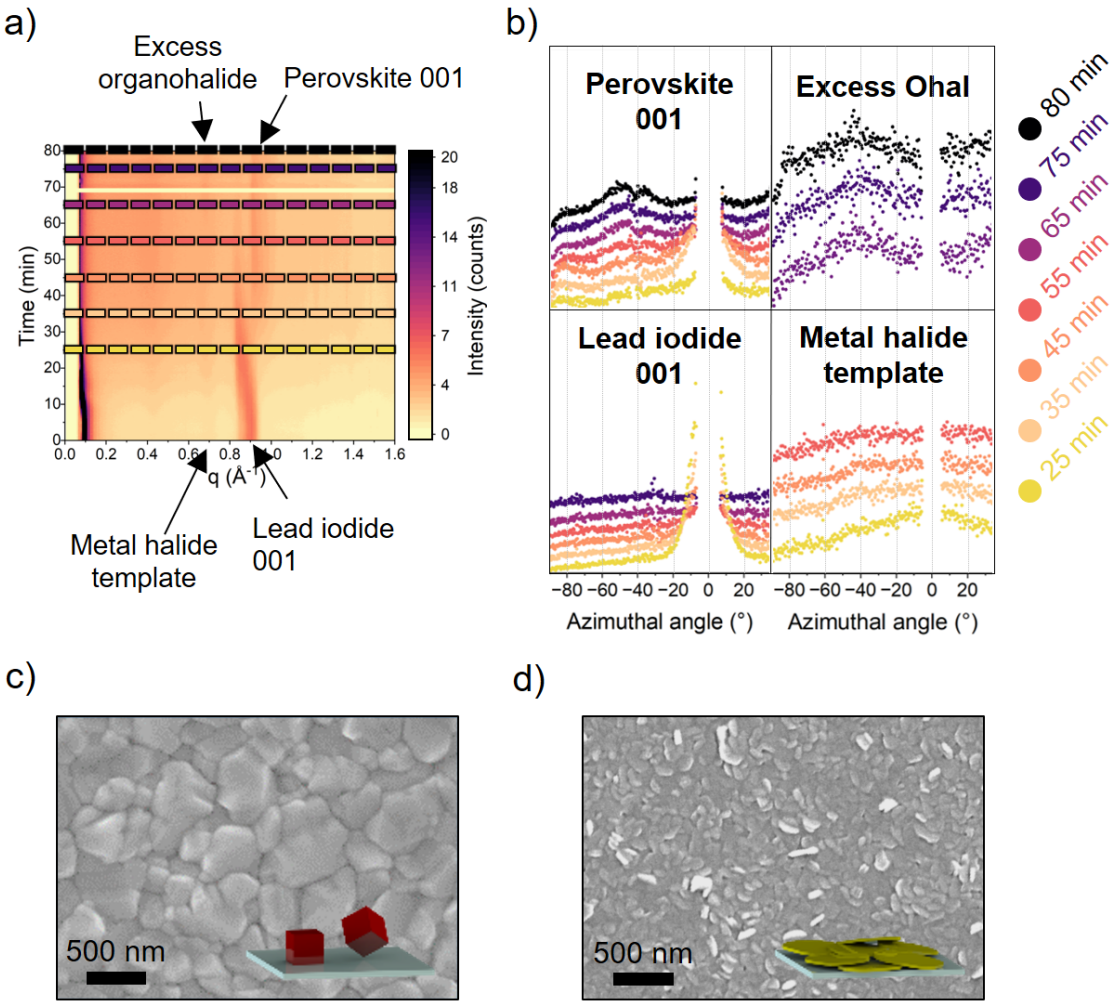

Figure 4.17: Evolution of the orientation of different phases of interest. a) Integrated GIWAXS profiles, with dashed lines marking the corresponding timecodes of the b) azimuthal intensity profiles of different phases. 0° corresponds to the normal to the substrate. Out of plane data close to 0° azimuthal angle are lost due to the missing wedge correction. c) Scanning Electron Microscope (SEM) image of a fully converted perovskite thin film, corresponding to this face and corner-up orientation of the perovskite phase. d) SEM image of the thermally co-evaporated metal halide template, composed of nano-platelets mainly oriented perpendicular to the substrate.

Having identified the four conversion stages, where the last stage presents the transition into an overconverted film, we further investigated how different process parameters impact the different conversion regimes.

4.2.4 Conversion regimes

We created a process condition matrix in which we varied the precursor quantity (FAI powder mass), the process duration, and substrate to precursor distance (height of the hollow cube), displayed in Figure 4.18. Importantly, the substrate to precursor distance (between 5 and 15 mm) did not result in temperature changes at the substrate level, measured as ca. 150°C when the heated table is set to 191°C, irrespective of the substrate to precursor distance. To compare the different conversion regimes, we define a conversion ratio (CR) as:

$$CR = \begin{cases} \frac{\int_{OHal}\phi(i,j)\ d\theta}{\int_{Pk}\phi(i,j)\ d\theta} \cdot \frac{max_{j,\forall i}(\int_{Pk}\phi(i,j)\ d\theta)}{max_{j,\forall i}(\int_{OHal}\phi(i,j)\ d\theta)} > 0, & \text{if overconverted} \\ 0, & \text{if perfectly converted} \\ -\frac{\int_{Template}\phi(i,j)\ d\theta}{\int_{Pk}\phi(i,j)\ d\theta} \cdot \frac{max_{j,\forall i}(\int_{Pk}\phi(i,j)\ d\theta)}{max_{j,\forall i}(\int_{Template}\phi(i,j)\ d\theta)} < 0, & \text{if underconverted} \end{cases}$$

With $\phi(i,j)$ the background-removed XRD signal for given process duration i and substrate to precursor distance j. Signals are normalised with respect to their maximum values (selected in dataset with same powder mass) to account for the fact that diffraction signal from template is orders of magnitude higher than signal from excess organohalide, and thus give a proper feeling of severe overconversion cases.

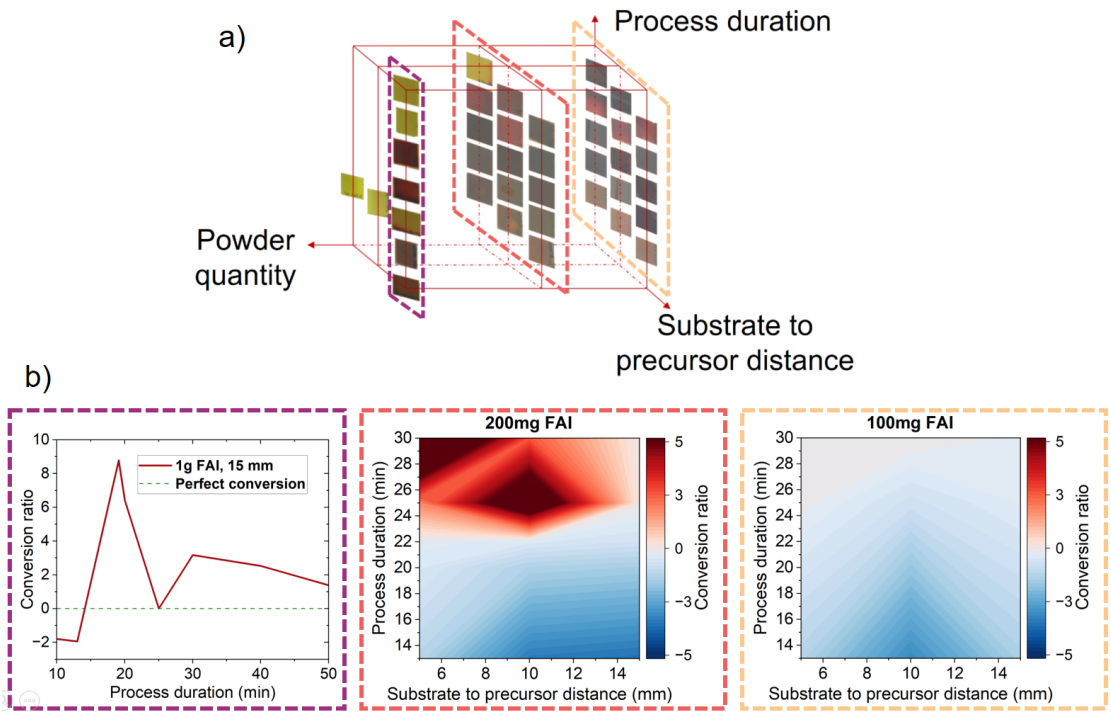

Figure 4.18: a) Experimental space explored. b) Evolution of the conversion ratio along the experimental space.

The precursor quantity is the dominant driver of all changes and allows tuning the reaction kinetics in order to obtain different conversion regimes. While higher quantities of FAI (1g, 200mg) favour a monotonous evolution of the conversion ratio, with signs of overconversion promptly visible after complete conversion, lesser FAI quantity (100mg) provides a more converging evolution of the conversion ratio (Figure 4.18b). With less precursors, the substrate balances the transport of material partially through re-evaporation, enabling more control, albeit at the cost of speed. Morphologically, the domains first form small rough domains in underconverted films that then transform into medium-sized flatter domains in perfectly converted films followed by a further growth into large flat grains in overconverted films (Figure 4.19a). At the same time, the XRD patterns show the presence of the metal halide template (underconverted), a clean perovskite (optimum) to additional signals from the excess organohalides (overconverted), 4.19b. Despite these differences in morphology and crystallography, we did not observe signs of NH_4I in the NMR spectra, cf. Figure 4.19b.

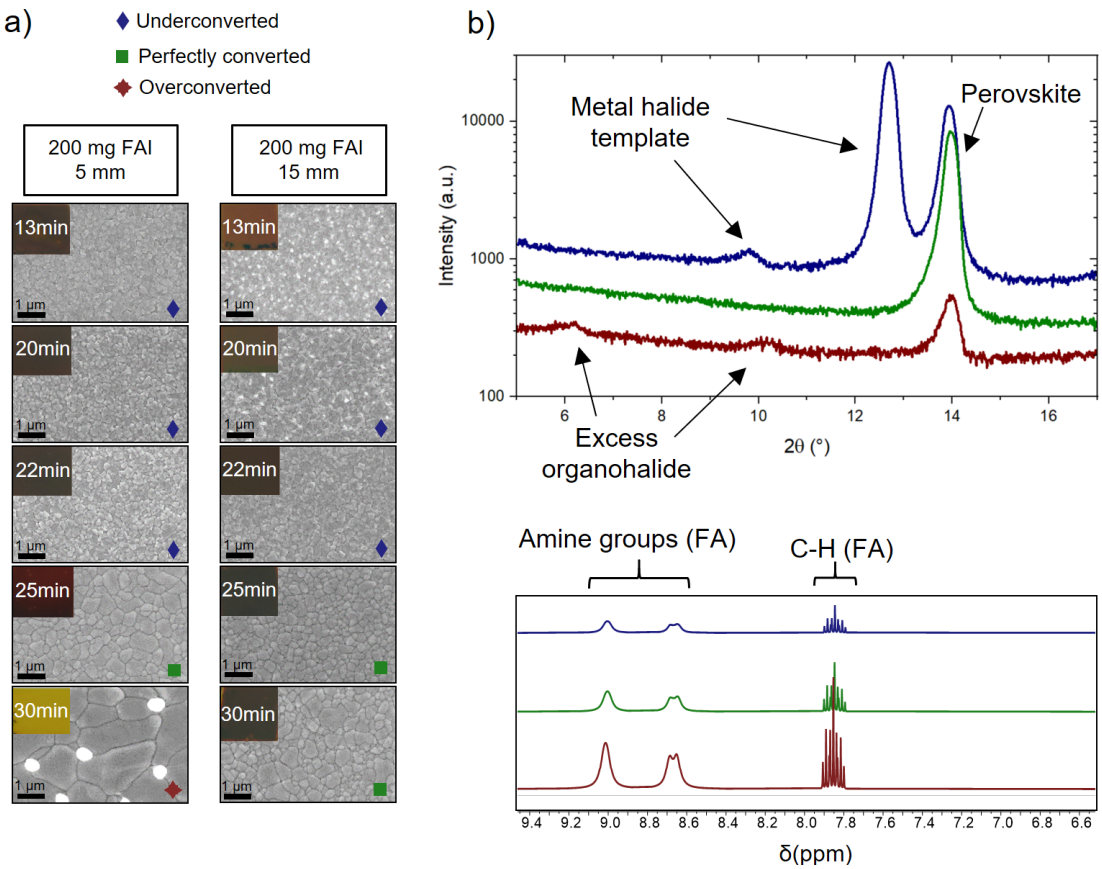

Figure 4.19: a) SEM images of different films of the experimental space presented Figure 4.18. Increasing the process duration increases the domain size. Going in overconversion, some bright domains will appear, rich in caesium from the Energy Dispersive X-ray (EDX) spectroscopy. b) XRD and NMR of thin films under, perfectly and overconverted, showing that in all cases only pure FAI is detected in the films by proton NMR.

The in situ study of the previous section was realised with 300mg of FAI per run. The aforementioned results are coherent with the saturating conversion regime identified in this section. Obvious process parameters, such as precursors quantity or duration of the process are demonstrated to have a significant impact on perovskite growth. The next section aims to investigate a hidden variable easily overlooked, the influence of the chemical environment on the growth.

4.2.5 Influence of chemical environment

How the deposition systems material choice influences perovskite vapor deposition is an underinvestigated matter. We sought to demonstrate the differences depending on different material (combinations), in Figure 4.20a. Starting from hollow PTFE cubes and fixing all other experimental conditions we investigate the impact of different materials in the surrounding of the PTFE reaction holder (see insets in 4.20a.: PTFE holder alone, PTFE holder + aluminium foil around, PTFE holder + PI foil in the vicinity of the powder, PTFE + aluminium + PI), in our homemade evaporation system. These different materials correspond to the chemical environment of the chamber used for in situ monitoring: the inner walls of the beryllium chamber are covered with an aluminium foil at each deposition, and the custom made in situ holder features polyimide windows for live GIWAXS monitoring.

We observed no presence of NH_4I irrespective of the different chemical environments, Figure 4.21, but a difference in conversion speed and a mild change in optoelectronic quality, cf. PLQY. Interestingly, despite not being in the direct vicinity of the powders, the aluminium foil substantially slows down the perovskite conversion (lead iodide peak is one order of magnitude higher than reference). On the other hand, PI foils accelerate the conversion. As the PLQY is influenced by the degree of conversion (cf. Figure 4.13), and the variations being small, one cannot draw definitive conclusions on relationships between film quality and the presence of PI or aluminium.

Another commonly used type of material for CVD chambers is stainless steel. 316L grade is one of the most widespread types of stainless steel, used in various industries for its extra corrosion resistance compared to the more standard 304 grade. The initial setup was built in 316L (deposition chamber, heated table, pipes etc). After the initial reduction of path length (Figure 4.11), we sought to study the implications of a standard 304 stainless steel on the film. The short-distance sample holders result in rapid conversion, however the stainless steel holder takes ca. 2x longer (relative to PTFE) to obtain the same conversion level. We did not observe NH_4I in either films (Figure 4.21). Importantly, in this case the environment still impacts the optoelectronic quality substantially (Figure 4.20b, Figure 4.21c). No emission is detected in PLQY measurements (one sun, resolution limit is ca. 10^{-7}). These highly defective films result in very poor efficiency of photovoltaic devices fabricated (Figure 4.21c).

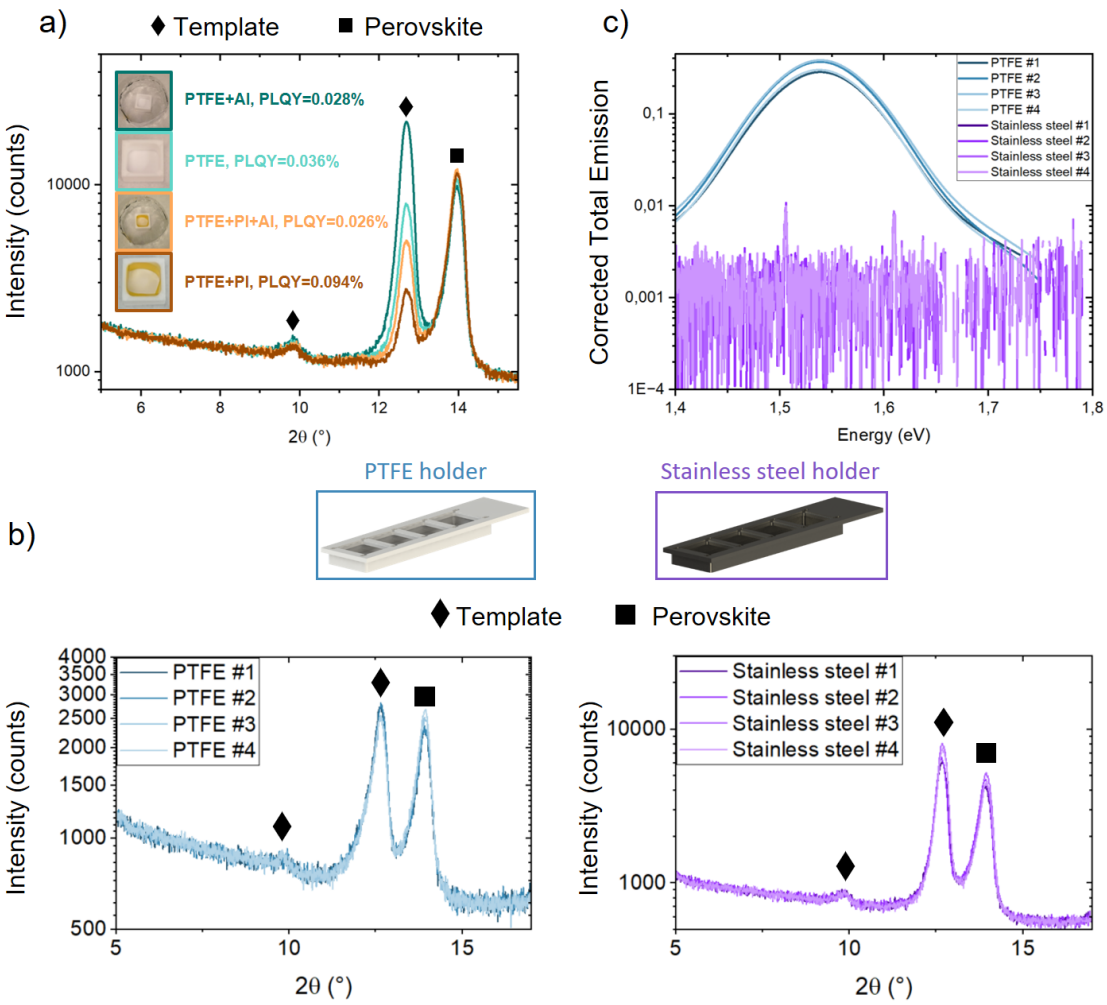

Figure 4.20: a) Influence of the chemical environment on thin film growth : for the same conditions (same holder, 200 mg FAI, constant temperature of 191°C, 25 min duration), adding polyimide (PI) close to the powder or aluminium foil around the holder changes the growth. The aluminium foil tends to decrease conversion speed, while PI accelerates the conversion. When combined, the resulting film has a PLQY lower and a conversion accelerated compared to the reference sample. b) Influence of the holder material itself. For both cases, 50 mg of FAI was evaporated at a constant temperature of 191°C. Both holders are geometrically identical. For the 304 stainless steel holder, the partial conversion is obtained in 23 minutes, while it takes 11 minutes for the PTFE holder. Whereas both films show similar conversion from their X-ray diffractograms, the films obtained with the stainless steel holder do not show signs of c) photoluminescence. This suggests high rates of non-radiative recombination and thus, a very poor film quality. This is confirmed by the very low efficiencies of solar cell devices realised with this holder, displayed in Figure 4.21.

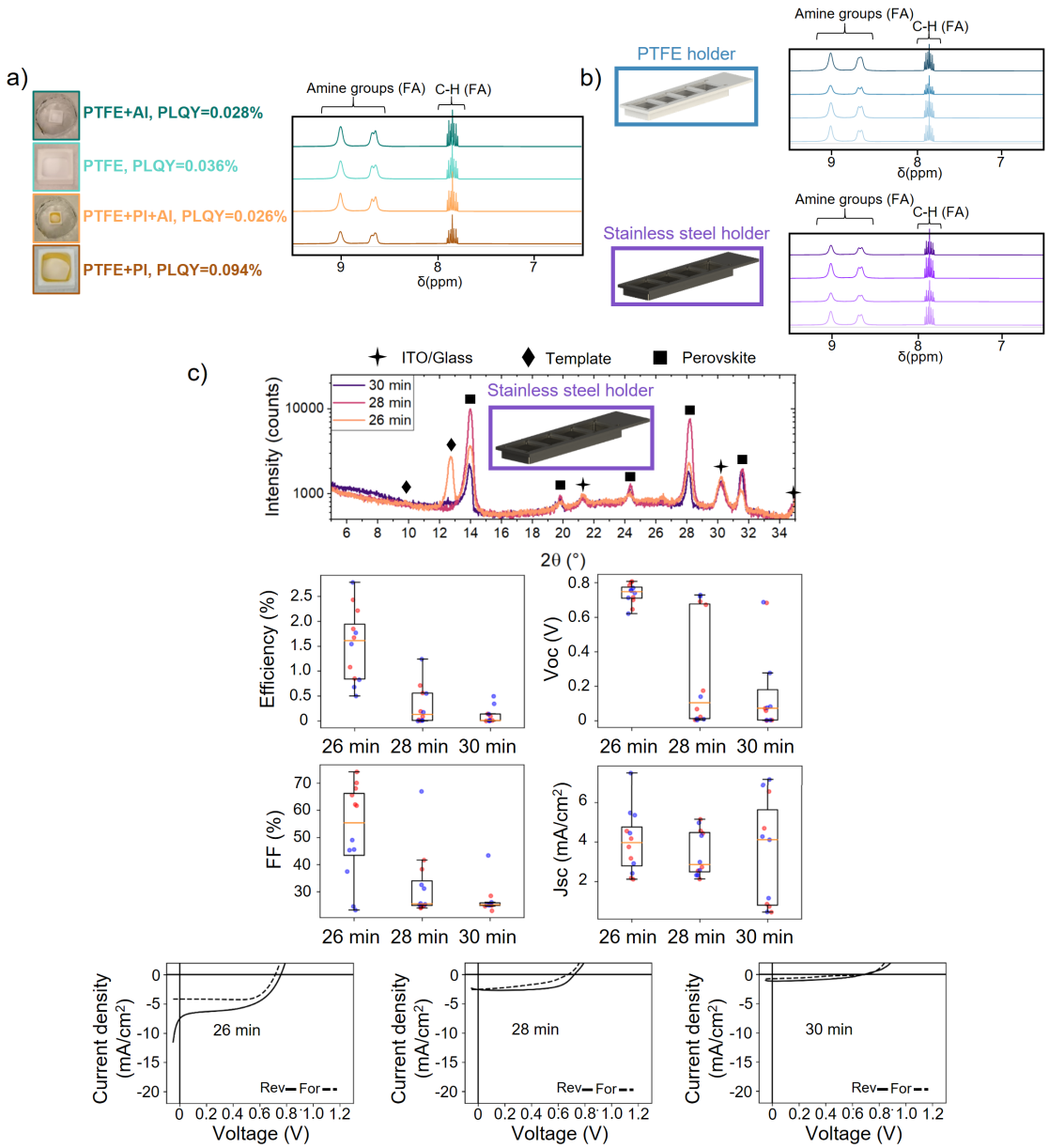

Figure 4.21: a) and b) NMR spectra of the thin films presented Figure 4.20. c) Attempt of photovoltaic devices fabrication with the stainless steel holder, for three different conditions: underconverted template (26 min), perfectly converted template (28 min) and slightly overconverted film (30 min), as evaluated by XRD (up). For all cases, the very poor devices performances (middle) confirms the highly defective characteristic of the thin films obtained with this stainless steel holder, as displayed by the flat emission spectra Figure 4.20b. Only the process duration is changed from the experimental conditions described Figure 4.20b. Current density – Voltage (JV) curves of the devices with the least worst performances of each condition are displayed (down). Device structure is: Glass/ITO/MeO-2PACz/Perovskite/C_{60}/SnO_2/Ag

We furthermore looked at a different stainless steel grade: 316L. An in situ stainless steel (316L) holder is used to reproduce the aforementioned in situ monitoring of perovskite conversion. It is geometrically identical to the in situ PTFE holder. The difference of temperature as seen by the powders at the bottom of the holder is less than a few degrees, thanks to a thin (2mm) wall.

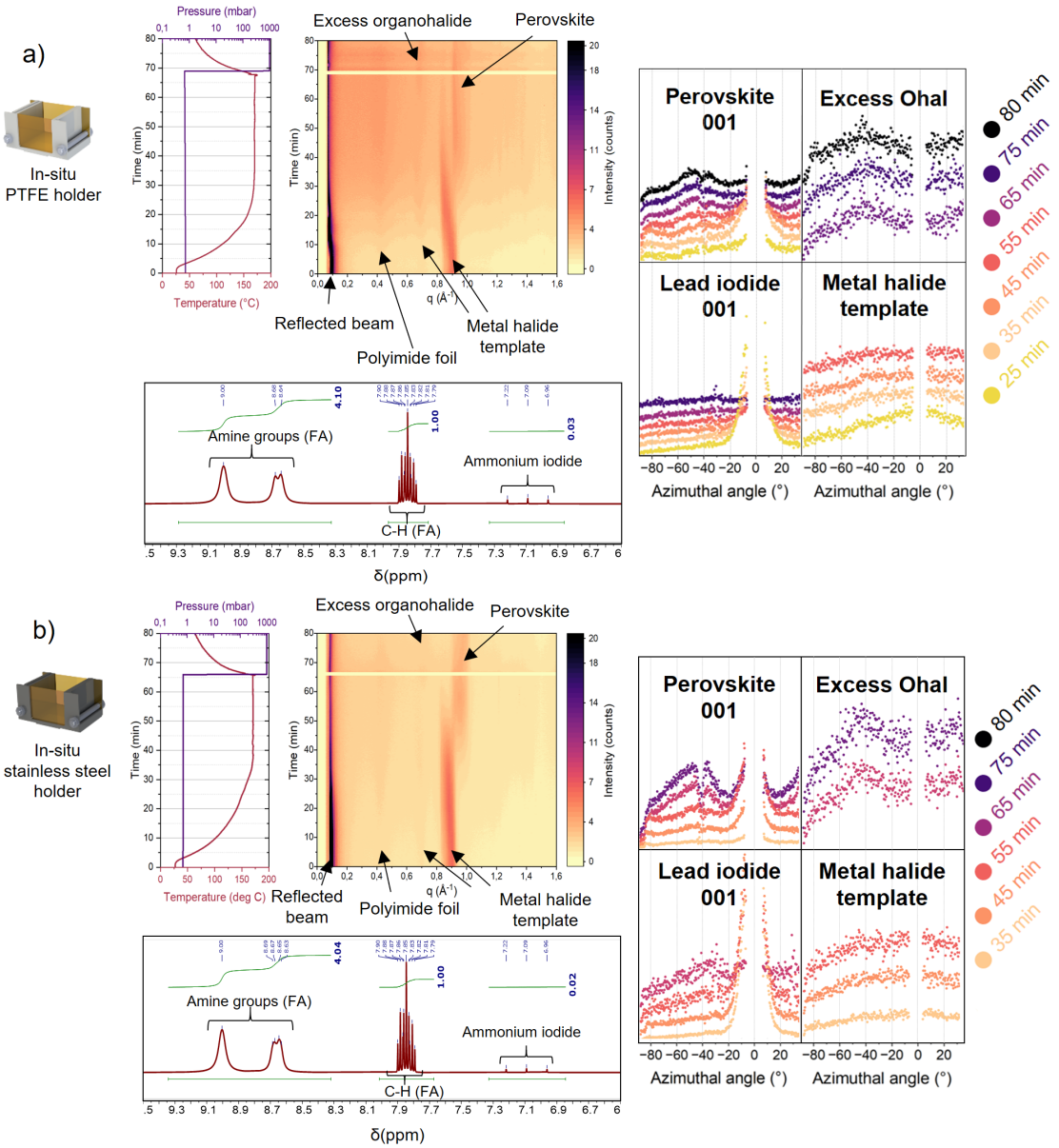

Figure 4.22: Temperature and pressure profiles, integrated GIWAXS and azimuthal intensity profiles and NMR of thin films fabricated with a) the PTFE holder and b) the stainless steel holder. From the structural and chemical point of view, both holders deliver thin films with identical characteristics. All other NMR sequences (13C, COSY, HMBC, HSQC) are also identical for both cases.

Nonetheless, due to the low heat capacity of the heating stage and the different thermal properties of PTFE and 316L, the stainless steel holder slightly behaves as a heat sink and marginally delays the temperature profile.

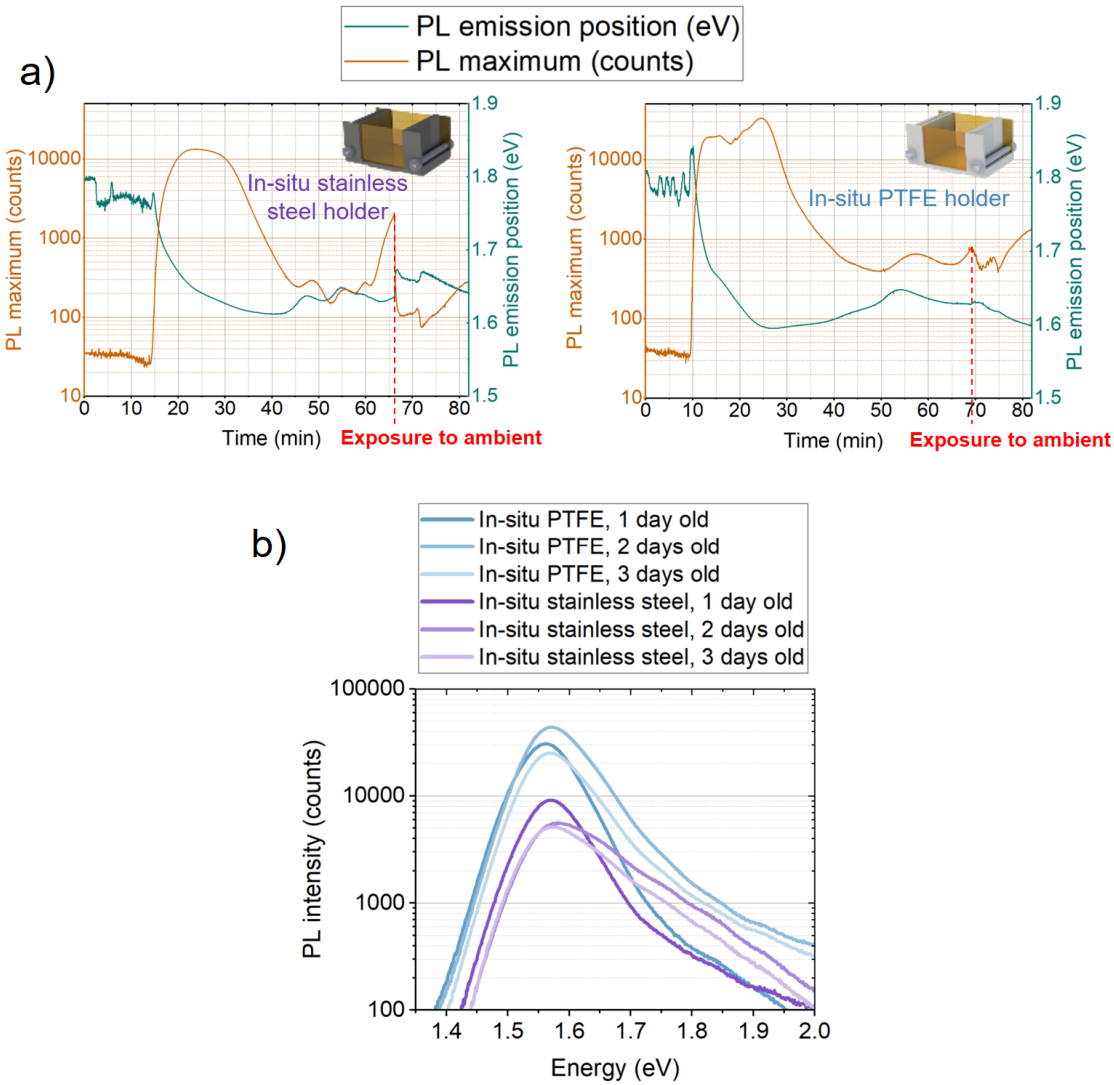

Figure 4.23: a) PL in situ monitoring of perovskite conversion during the organohalide vapor deposition, comparing experiment with the stainless steel (316L) holder (left) versus PTFE holder (right). GIWAXS in situ monitoring and NMR analysis are identical in both cases and displayed in Figure 4.22. Both in situ experiments were stopped when metal halide template was considered fully consumed from in situ GIWAXS. b) PL remeasurements of the same films the next days. The order of magnitude difference between the films obtained with the two different holders is stable in time. Films were stored in a nitrogen glovebox overnight and taken out in ambient air for measurement.

In Figure 4.22, results show that from structural (integrated GIWAXS and azimuthal intensity profiles) and chemical (NMR) point of views, the thin films produces by both holders (PTFE and 316L) are identical, yet, the PL intensity is still lower, both during the conversion, but also after several days of storage (Figure 4.23). These results show that the holder's material must be carefully chosen.

All other parameters being equal, the two comparisons of PTFE vs 316L and PTFE vs 304 show that the choice of stainless steel is by far not benign and that PTFE beats both stainless steel grades, where 316L is still much superior to 304 and should be used to fabricate reaction chambers in conjunction with PTFE. The results indicate that not all stainless steel deposition chambers (probably still the vast majority) should be avoided. In the case of the 316L deposition chamber and the in-house process of this manuscript, good quality thin films and well-performing photovoltaic devices are demonstrated when PTFE is used as holder material. However, the 'far environment' represented by the chamber inner walls should not be considered as insignificant.

In the case of the main deposition chamber used for this study (not the in situ setup), the inner surface of the chamber is a cylinder of 29cm diameter and 20cm height. The substrate and precursor, distant from 5 to 15mm, are located right in the middle of the chamber. Chamber walls are kept at 150°C to allow the heated table to reach high temperatures and to prevent parasitic condensation of the walls. Experiments showed that sudden baseline drifts could only be rectified if the internal surfaces are thoroughly cleaned, especially with deionized water. Attempts to clean the inside chamber walls with common solvents (isopropanol, acetone, ethanol) were ineffective for retrieving the baseline process. After cleaning, the inside of the chamber is kept at 150°C, pumped and continuously flushed with nitrogen to remove potential traces of water.

These baseline drifts are characterised by an abrupt increase in the time required for full perovskite conversion (process time almost doubled), a reduction in layer quality (order of magnitude difference in PLQY), and sometimes appearance of ammonium iodide in the films. Details are displayed in Figure 4.24. The example here is obtained with the hollow PTFE cube and the POPOP process. These drifts happen regularly in time and do not seem to be related to a specific usage (precursor quantity, holder, additives, specific organic molecule etc). This means that from evaporation to evaporation, and despite the distance and the temperature, a 'contamination layer' is building on the inside surfaces of the reactor, and will drastically affect the process above a certain threshold. This assessment is in agreement with the similar experience of Thierry Moser with deposition of FAI in a tube furnace [220].

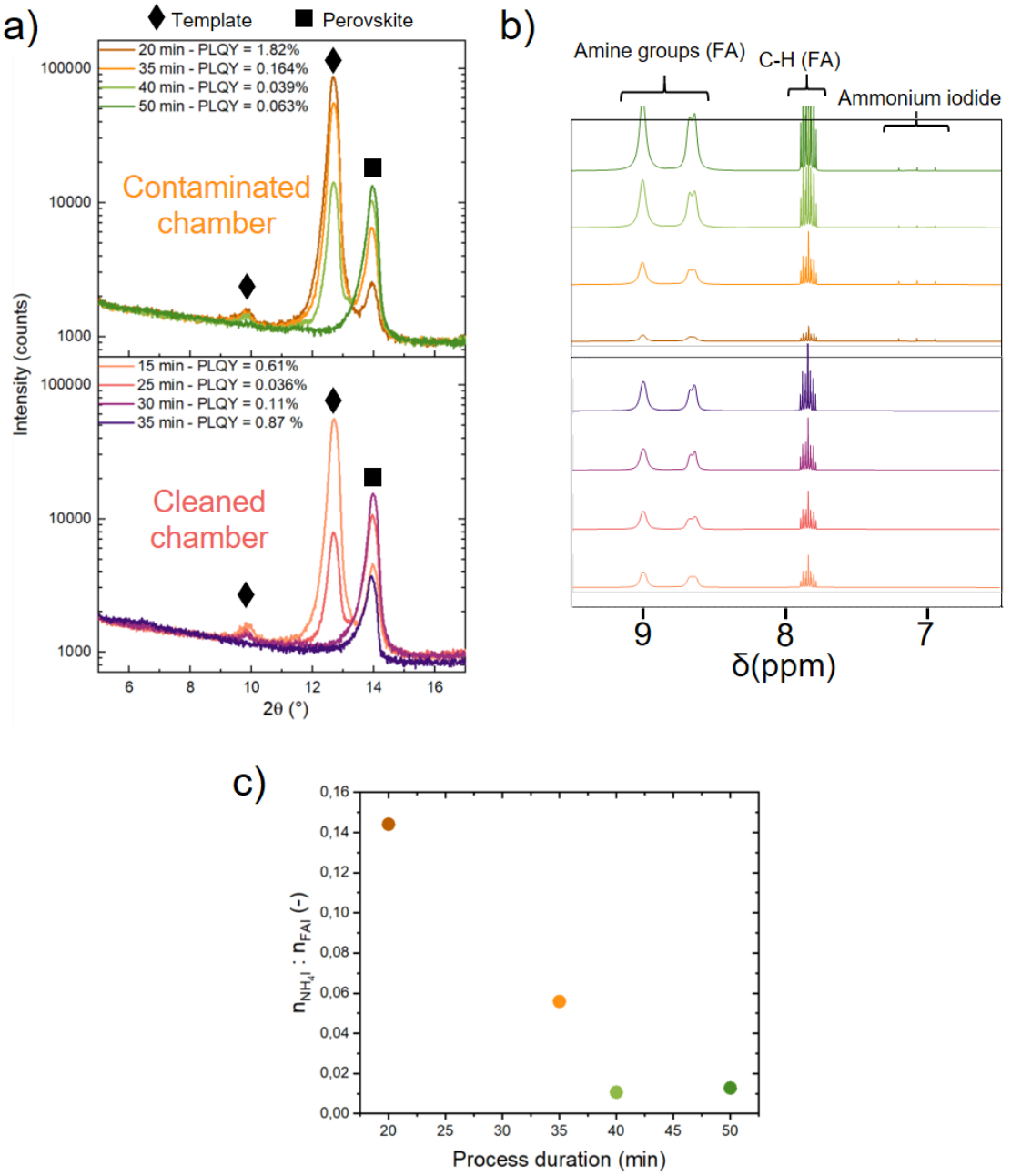

Figure 4.24: Drift of the process baseline, illustrated with thin films fabricated with the cubic PTFE holder presented Figure 4.14. a) XRD and PLQY, b) NMR and c) evolution of the ammonium iodide to formamidinium iodide ratio during the process in the case of a contaminated chamber. A contaminated chamber slows down the conversion and reduces the quality of the films. Data obtained with the PTFE hollow cube holder.

This explains the differences of PLQY between almost identical conditions (30 minutes 200mg FAI Figure 4.13 and 25 minutes 200 mg FAI Figure 4.20a), and may also points out why films of apparent similar state (for ex. overconverted) may have different NMR spectra. In this case, experiments of Figure 4.20a were obtained after a chamber cleaning, while Figure 4.13 films were obtained a long time ago during preliminary tests of this new process. NH_4I is always generated when heating FAI salts [39, 40].

However, numerous examples of perovskite films without NH_4I in all states of conversion are presented in this manuscript. So this implies that an external factor in the chemical environment, even far from the small, 'pseudoconfined' reaction volume, can either favor degradation of the vapors/powder into NH_4I or make its inclusion in the growing films more likely to happen. In literature, a small amount of NH_4I as additive seems to have positive impact on layer quality [221]. However during the vapor deposition of formamidinium salts, from our observations, its appearance in thin films is correlated to a chemical environment hindering perovskite conversion and/or altering thin film quality.

Further investigations are needed to describe more precisely factors hindering the process and examine more materials. From these preliminary results, it can still be concluded that the chemical environment in the direct vicinity of perovskite vapor deposition but also far away from it must be carefully considered when elaborating a process.

With the different conversion regimes identified and more insights on the influence of the chemical environment, we sought to expand the toolset by exploring the possibility of tuning the composition of the final perovskite through the addition of mixed organohalide powders or alternative additives.

4.2.6 Bandgap tuning and additive engineering

One of the properties that makes halide perovskites interesting for photovoltaic applications in (multijunction) solar cells is their tunable bandgap. We explore the possibility to tune the bandgap in the POPOP process. Exemplary, we mix FAI and formamidinium bromide (FABr) precursors and adapt the deposition parameters for optimal conversion. As displayed in Figure 4.25, the photoluminescence peak position can be shifted controllably from 1.55 eV to 1.8 eV when varying the relative amounts of FAI : FABr.

The optical bandgap variation is cross-checked with changes in the lattice d-spacing to exclude optical effects. Introducing FABr accelerates the perovskite conversion and increases the optoelectronic quality (PLQY) of the films, Figure B.14. For example, the 2.67 FAI : 1 FABr mix, giving an optical bandgap of 1.63 eV, converts within 9 minutes, with good homogeneity and repeatability, Figure B.14b.

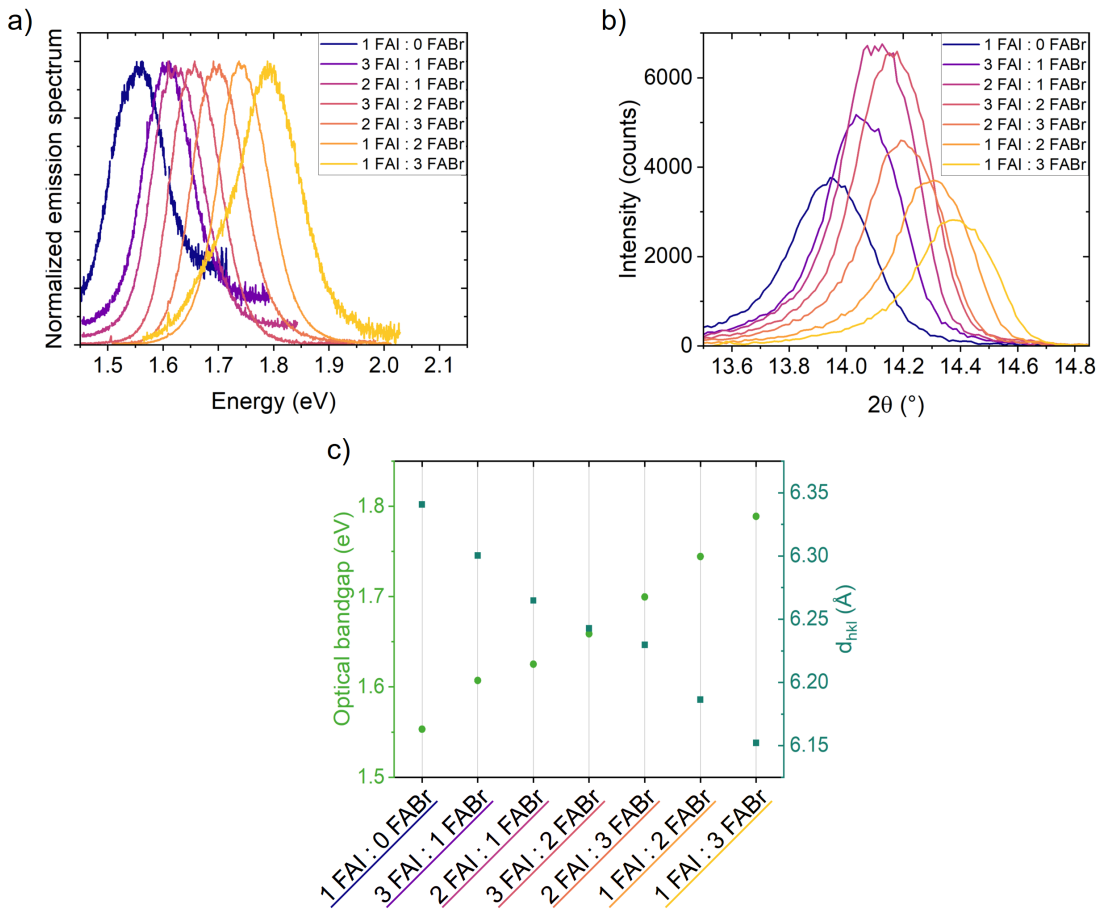

Figure 4.25: a) Bandgap tuning of the thin films, mixing FAI and FABr in precursors. Normalized emission spectra, b) perovskite (001) diffraction peak and c) corresponding optical bandgap and interplanar distance, respectively.

We chose the process parameters such that the reaction is in the self-limiting converging regime, as defined above. This increases the robustness: doubling the process time from 9 to 18 minutes does not lead to an oversaturation of the films. However, a decrease in PLQY is observed as the process time increases. Also, the bandgap decreases with a longer process time (from 1.63 eV at 9 minutes to 1.60 eV at 18 minutes of process), likely indicating a halide exchange (shift to more I-rich) proceeding after the complete conversion into perovskite.

One of the most common approaches to improve the performance of perovskite devices is to manipulate the growth via additives incorporation into the commonly solution-processed absorbers. For example, methylammonium chloride (MACl) is a popular choice for FA-based perovskites, allowing to tune perovskite crystallization to obtain large, passivated, and high-quality domains [222]. To demonstrate the feasibility of using MACl, we mixed it with our

2.67 FAI : 1 FABr baseline precursor composition (1.3 to 14% atomic MACl content relative to the total FAX organohalide). Figure B.15 displays XRD, PLQY, SEM, NMR and Time-of-Flight Secondary Ion Mass Spectrometry (ToF-SIMS) of the perovskite films grown with different amounts of MACl.

Notably, adding MACl did not result in drastic changes in the crystal structure, where the diffraction intensity is not notably impacted. The width of the (001) perovskite signal is mildly reduced, in line with the slight increase of the apparent domain size, reaching a maximum at 9.8% of MACl. We probed whether MA only impacts the film formation and thereafter evaporates or is incorporated into the perovskite. Indeed, we observe a signal from the methyl quadruplet in NMR, scaling with the relative amount of MACl in the precursor organohalide mix, up to a maximum at 9.8%. Analogously, we probed the presence of Cl^- in the film via ToF-SIMS and observed an increased signal with increasing amounts of MACl, however significantly higher than the signal changes in MA (as measured via NMR). This difference indicates that MA and Cl are not exclusively present as MACl. From the ToF-SIMS, we can deduce that the Cl appears to be distributed throughout the films and slightly more concentrated at the bottom interface.

We observe a reduction in the PLQY upon increasing MACl, suggesting non-radiative recombination. A possible explanation could be the decomposition of MACl into MA and HCl [166] when heated. This would rationalize the different amounts of MA and Cl and explain the lower optoelectronic quality, potentially due to deterioration upon uncontrolled HCl exposure. The report by Zhao *et al.* [223] suggests that when MACl is used in a post-processing step after the conversion as a vapor treatment, with dedicated process conditions, it can aid in promoting better optoelectronic performances.

Alternatively, we added formamidinium thiocyanate (FASCN) to the FAI/FABr baseline mix, inspired by recent demonstrations of vapor-assisted crystallization [145]. As displayed in Figure 4.26a, adding FASCN increases crystallinity (more pronounced diffraction intensity, reduced FWHM) and PLQY. At the same time, the domains appear larger and flatter, Figure 4.26b. Up to a ca. 7-8% FASCN, the morphology, crystallinity, and optoelectronic quality (measured through PLQY) improve unison, where a further increase beyond 9% results in the formation of pinholes in the thin film and a loss of crystallinity and PLQY. ToF-SIMS measurements in Figure B.16 reveal that the SCN^- ions are distributed throughout the perovskite film thickness in comparable quantities in all cases. This suggests that a self-limited amount of the additive is incorporated, while the 'excess' continues to influence the deposition without being absorbed by the growing film. Additionally, we observe a preferential accumulation at the bottom interface, suggesting that more additive is incorporated at the beginning of the conversion.

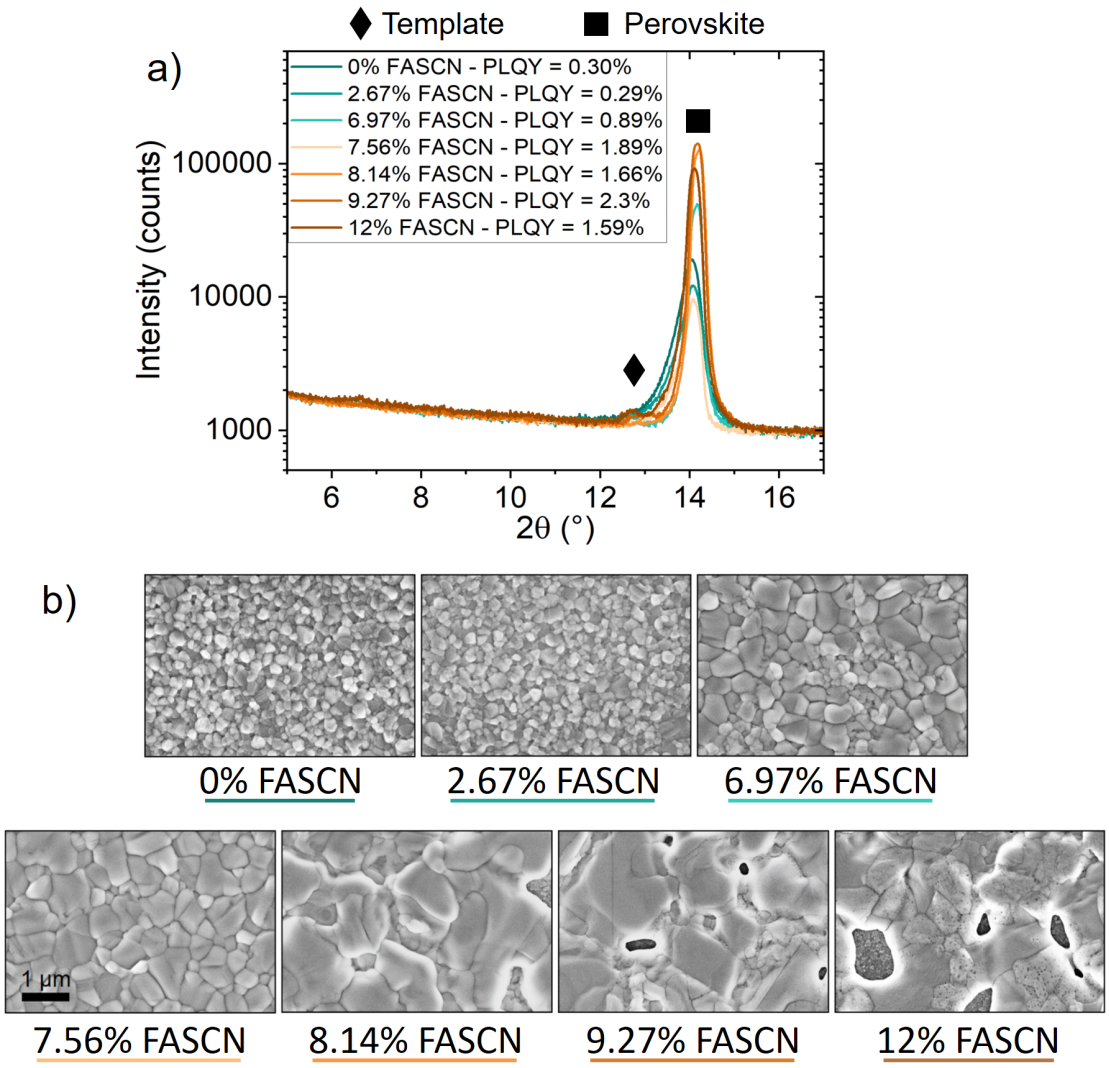

Figure 4.26: a) Effects of FASCN additive on PLQY and X-ray diffraction of the films. b) Top view SEM images of thin films with different amounts of FASCN. Scale is common to all images.

4.2.7 Photovoltaic devices

Photovoltaic devices are fabricated to investigate the potential of the presented process. For all devices, the structure is Glass/ITO/Meo-2PACz/Perovskite/C_{60}/SnO_2/Ag. Figure B.17 shows an optimisation of the process duration for the 2.67 FAI : 1 FABr baseline, an investigation of MACl and FASCN additives effect on devices. The latter results follow the trends of PLQY measurements: MACl as vapor additive consistently worsens photovoltaic performances, while the 7.56% FASCN is the optimal concentration for that second additive.

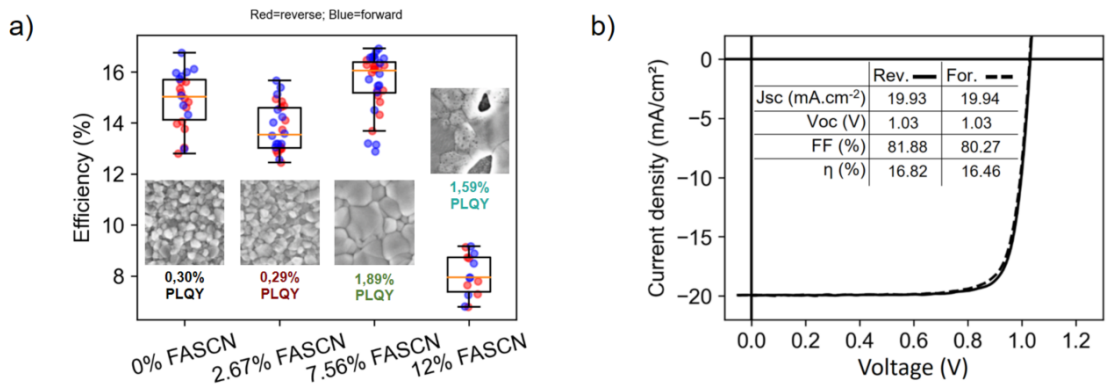

Figure 4.27: a) Photovoltaic devices with increasing FASCN content in the source. b) Current density – Voltage curve of the best-performing device (7.56% FASCN, 9 minutes baseline, 2.67 FAI : 1 FABr)

The best device, whose characteristics are displayed in Figure 4.27b, shows very low hysteresis at our standard scan speed of ~100 mV/s and a high fill factor exceeding 80%. Devices made from films grown with higher FASCN content exhibit substantially reduced open circuit voltages and fill factors, likely due to the formation of the above-mentioned pinholes. The statistics of FASCN cells, in Figure 4.27a, reveal that gains in PLQY are not directly translated in devices, where optimal FASCN content brings minor improvements compared to the six times higher PLQY. This suggests additional losses due to the transport layers and is confirmed by the losses study in Figure B.19 showing that the perovskite/C_{60} interface is causing losses. Moreover, other self-assembled monolayers such as Me-4PACz are known to have a higher hole transfer efficiency [224]. Using state-of-the-art charge transport layers, interlayers and improving the light-harvesting efficiency (cf. exemplary external quantum efficiency measurements in Figure B.18), e.g., through anti-reflective coatings, will enable significant efficiency improvements beyond the herein shown proof of concept.

4.2.8 Conclusion

An evolution of close space sublimation of organohalides for perovskite thin film deposition is proposed. The developed process is fast, simple, controllable, repeatable and upscalable. Halide tuning, as well as additive engineering, common in solution processing but rare in vapor depositions (or via post-treatment), are demonstrated and offer numerous possibilities. The process, consisting of four stages, is analysed both in and ex situ from a structural, optoelectronic and chemical point of view. Key insights regarding the influence of the chemical environment on thin film growth are provided, and the importance of mechanical design is discussed. Photovoltaic devices proving the repeatability and potential of the process are demonstrated.

5 Conclusion and perspectives

The objectives of this thesis were to pursue the perovskite vapor deposition activities of the group. Preliminary work featured interesting proofs of concept, but the home-built vapor deposition setup quickly appeared as limited for the next steps. From this point, analyzing the causes of the limitations and find, develop ways to deposit via vapor phase formamidinium-based perovskites were the starting guidelines of this PhD thesis work.

A deep analysis of literature on vapor deposition in general, along with various tests with homemade systems, allowed to develop an understanding on perovskite vapor deposition, from evaporation of the precursors to growth of the thin films. Conclusions drawn from this understanding were published in a review paper [42] and fed the development of the in-house process. Systematic and thorough characterization of the deposited thin films accompanied the development of the vapor deposition process, pushing further its comprehension.

The as-refined process is fast, versatile and compatible with high efficiency strategies (bandgap tuning, additive engineering). A research paper presenting this process along with complementary insights on its chemical, optoelectronic and structural aspects is to be submitted soon. One novelty introduced by this work is the exploration of the chemical environment, specifically how the materials surrounding the vapor deposition process influence thin film growth. This preliminary work provides new lines of thought and means to tune a perovskite vapor deposition process. Future work should investigate deeper the possibilities of such considerations, to further enhance key aspects of the process: thin film quality, speed of conversion, repeatability and robustness.

In parallel of the organohalide vapor deposition development, an alternative to the co-evaporation of the metal halide template has been investigated. Mechanical mixing of metal halide salts and their single source evaporation is still an underinvestigated yet promising topic for perovskite industrialisation. The results of this side project, unprecedented in literature, were published in a research article [43]. Follow-up investigations could study new

phases formation when ball milling precursors. Moreover, taking into account halide exchange between CsBr and PbI_2 during single source source evaporation and fine tuning the final composition of films adding new species to the mix (CsI, $PbBr_2$) is also a promising step towards an optimised, fast and controlled deposition of the metal halide template.

Now that the overall process is well understood and that many of its qualities were demonstrated (fast, robust, flexible), it is time to enter the race for high efficiencies. As explained in the introduction of this thesis, further increasing solar cells efficiency is of paramount importance for different reasons: lowering cost of electricity, space usage or environmental impact. Consequently, to validate the ability of the process to achieve high efficiency is the next important step of process development. The 17% efficiency with single junction device can easily be increased with the following strategies: single junction-specific optimization (slightly reducing the 1.63eV bandgap, increasing thickness), using more high efficiency compatible device structures (Me-4PACz instead of MeO-2PACz as hole transport layer, antireflective coating) or adding post-treatment step after perovskite conversion. Another critical aspect for potential industrialisation is the stability of perovskite solar cells. Although off-topic because of the framework of the thesis, this subject, common to all perovskite fabrication processes, must also be addressed in the view of further development of the technique.

The developed process is also now mature enough and well understood for upscaling and implementation in tandem devices. By design, upscaling of the process is made easy, yet will require slight optimisation of technical aspects to ensure homogeneity. Early tests for tandem implementation already started, very unfortunately slowed down due to machines failures. If conformal coating and conversion itself of the template into perovskite is easily achieved, some engineering is still required to protect the tandem devices (especially the back electrode) from the harsh conditions of perovskite vapor deposition. Several options (masking, taping, temporary encapsulation) are considered. Thanks to all the experience and knowledge gathered during this thesis, it is now just a matter of time and process engineering before proof of concept tandem devices on large areas are demonstrated with the presented techniques.

A Appendix A : experimental details

A.1 Processing of thin films and photovoltaic devices

A.1.1 Single source evaporation of metal halide powders

Precursors were mixed in a shaking mill at a frequency of 25 Hz for one hour with agate grinding balls. Powders were evaporated in a Lesker Mini SPECTROS evaporation system. 1g of each mix was loaded in a crucible, and the source was heated at setpoint as fast as possible, then the shutter was opened and the temperature was kept constant until the nominal thickness of 200 nanometers was reached. Evaporation rates ranged between 10 and 3 Å/s. The acoustic impedance, density and tooling factor used for CsBr and PbI_2 in our system are the following, resp. : [1.41, 4.456, 22.8], [0.11, 6.16, 19.9]. Accuracy of set, measured and effective deposition rate is ensured by dedicated tuning of the tooling factor of each source for each type of material. The tooling factor is adequately determined after a single material evaporation of a given compound by measuring the difference between the thickness measured by the QCM (with initial parameters of tooling factor, density etc) and the thickness of the film as determined by a combination of different tools : cross-section SEM, profilometer and ellipsometry. Conversion into perovskite was obtained by spin coating FAI:FABr (Greatcell) 1:2 dissolved in dry ethanol (Sigma-Aldrich) and then annealing the thin films at 150°C for 20 min in ambient air 30% RH. MeO-2PACz (TCI) was dissolved in dry ethanol to form a 1mg/mL solution, 100 microliters were dispersed on the static sample, then the sample was rotated to 3000 rpm, where 100 microliters were anew dispersed on the film. The sample was then annealed at 100°C for 10 minutes, then washed with dry ethanol. C_{60} (CreaPhys), bathocuproine and silver (Sigma-Aldrich) were thermally evaporated in high vacuum in a dedicated chamber with the following rates/thicknesses, respectively : 0.2 Å/s/20nm, 0.2 Å/s/5nm, 1.5 Å/s/130nm.

A.1.2 Vapor deposition of organohalides

Metal halide template is co-evaporated in a Lesker Mini SPECTROS evaporation system. PbI_2 and CsBr sources are tuned until reaching respectively 1 Å/s and 0.1 Å/s, then the shutter is opened. Maintained in rate control with PID controller, power is tuned to keep constant evaporation rate until reaching a total thickness of 200nm. Acoustic impedance, density and tooling factor used for CsBr and PbI_2 in our system are the following, resp. : [1.41, 4.456, 22.8], [0.11, 6.16, 19.9]. Precision of set, measured and effective deposition rate is ensured by dedicated tuning of the tooling factor of each source and each precursor. Tooling factor is adequately determined after a single material evaporation of a given compound by measuring the difference between the thickness measured by the QCM (with initial parameters of tooling factor, density etc) and the thickness of the film as determined by a combination of different tools : cross-section SEM, profilometer and ellipsometry.

For all measurements except photovoltaic devices, a 'half cell' structure is used : the same layer stack as the one used for devices is fabricated and stopped after perovskite deposition, in order to have the closest possible growth conditions. Photovoltaic devices stack is Soda Lime Glass/Indium Tin Oxide/MeO-2PACz/Perovskite/C_{60}/SnO_2/Ag. Consequently, 'half cells' are comprised of : Glass/Indium Tin Oxide/MeO-2PACz/Perovskite.

ITO-coated glass substrates, purchased from Kintec (Ω sheet = 15 ohm/sq), are sonicated in acetone and then IPA for 10 minutes and treated with UV-O3 before depositing self assembled monolayer.

MeO-2PACz (TCI) is dissolved in dry ethanol to form a 1mg/mL solution, 100 microliters are dispersed on the static sample, then the sample is rotated to 3000 rpm, where 100 μL are anew dispersed on the film. The sample is then annealed at 100°C for 10 minutes, then washed with dry ethanol (Sigma-Aldrich).

C_{60} (CreaPhys), and silver (Sigma-Aldrich) are thermally evaporated in high vacuum in a home-made, dedicated chamber with the following rates/thicknesses, respectively : 0.2 Å/s/25nm, 1.5 Å/s/130nm.

SnO_2 is deposited using an atomic layer deposition system Picosun R-200. Setup is set to 90°C, using 220 cycles of tetrakis(dimethylamino)tin (100 sccm, 0.3 s pulse, 6.0 s purge) and H2O (200 sccm, 0.1 s pulse, 6.0 s purge. Total thickness is approximately 20nm.

Organohalide evaporation is performed by either directly spreading the powders or dissolving the precursors/additives (FAI, FABr, MACl from Greatcell Solar and FASCN from TCI) in ethanol. Solution is then spread on the rough wafer then dried on a hotplate at 40°C, as described in Figure B.13. With mixed FAI/FABr or FAI/FABr + additives, the same total mass of salts is dissolved (50mg in 1 mL of ethanol). For the 2.67 FAI : 1 FABr + 7.56 at% of FASCN baseline optimum, 37.326 mg of FAI is dissolved in 0.67 mL of ethanol then mixed with 10.159 mg of FABr dissolved in 0.250 mL then 2.515 mg of FASCN in 0.08 mL of ethanol. For 2.17×10^{-4},

8.13×10^{-5} and 2.44×10^{-5} mol of FAI, FABr and FASCN respectively, final atomic percentages are 67.25% of FAI, 25.19% of FABr and 7.56% of FASCN. Between each run of organohalide vapor deposition, each part of holders is thoroughly washed with cleanroom tissue, acetone, isopropanol, deionized water then sonicated in isopropanol for dozen of minutes. Fresh precursors and solutions are used for each run. Temperature of the heating table is maintained at 191°C, chamber walls at 150°C and pressure is 0.3 mbar for all processes (except in the in situ chamber, pressure profiles provided in dedicated Figures). Polyimide foils used (for in situ holder windows, test in Figure 4.20 and Figure 4.21) are 50μm thick.

A.2 Characterization

A.2.1 Single source evaporation of metal halide powders

Synchrotron X-ray diffraction was performed at the BM01 diffraction beamline of the Swiss-Norvegian BeamLines (SNBL) of the European Synchrotron Radiation Facility (ESRF) in Grenoble, France. The wavelength during measurements was 0.694 Å. A Pilatus 2M2D detector was used [225]. For the in situ GIWAXS study of the powder evaporation, precursors were loaded in glass capillary tubes connected to a turbo pump, and a hot air blower was heating the capillary during the GIWAXS measurement. Different temperature ramps were tested from 6°C/min to 24°C/min without apparent changes in behavior. All data presented here were acquired using a 6°C/min ramp. Secondary electron SEM images were acquired with an in-lens detector in a Zeiss Gemini 2 microscope. EDX quantification of thin films was obtained with the same system by averaging data from 15 millimeter-sized areas taken over 3 substrates from the same evaporation. Pb, Cs, Br and I were fitted and Si, N, Mg, Ca, O, Na, B, C, In and Sn were deconvoluted (diverse backgrounds from glass substrate covered by indium tin oxide). The resulting standard deviations were in the few percent range. Current density voltage (J−V) measurements were performed using a two-lamp (halogen and xenon) class AAA WACOM sun simulator with an AM1.5G irradiance spectrum of 1000 $W.m^{-2}$. Shadow masks were used to define the illuminated area (0.1 cm^2), and the cells were measured with a scan rate of 100 $mV.s^{-1}$. External quantum efficiency (EQE) spectra were obtained using a custom-made spectral response setup with a lock-in amplifier using chopped light at a frequency of 232 Hz.

A.2.2 Vapor deposition of organohalides

^{1}H liquid NMR is performed with a Bruker AVANCE III HD 400 MHz spectrometer. Samples are dissolved in 600 μL of DMSO-d6 (99.8%, MagniSolv) and transferred to a NMR test tube. 1 μL of hydroiodic acid is added in each tube to increase acidity of the solution to hinder proton exchange and to provide highly resolved spectra [226].

X-ray diffractograms, if not specified to be acquired with the in situ setup, are collected with a Panalytical Empyrean diffractometer with a PIXcel-1D detector and a Cu-Kα radiation source.

FTIR spectra are obtained with a Bruker Vertex 80v spectrometer using a RT-DTGS detector and a KBr beamsplitter. The measurements are done in ambient air.

Absorbance is determined from reflectance and transmittance measurement obtained with a PerkinElmer Lambda 900 UV-Vis-NIR spectrophotometer fitted with an integrating sphere.

SEM images were acquired with an in-lens detector in a Zeiss Gemini 2 microscope, with an acceleration voltage of 5kV and a beam current of 500pA.

in situ GIWAXS & PL setup is a custom made system designed to simultaneously measure PL and GIWAXS. The reaction chamber is built out of beryllium allowing X-ray transparency. A X-ray Cu-Kα source with a tuned brilliance of 10^8 photons/s is used, incidence angle is set at 1°. Diffraction data are obtained with a Dectris Pilatus 200K. The PL illumination source is a 532nm laser diode, beam spot size 1mm^2 and power tuned to 90 μW. PL data is acquired via a vacuum compatible achromatic doublet lens, one focusing photoluminescence emission into multimode optical fiber. The latter is connected to Acton SpectraPro spectrometer, equipped with thermoelectrically cooled CCD camera (iDus 420BU, Andor).

PLQY is measured with a homemade system using a 514 nm laser shining on the sample in an integrating sphere. Sample emission is measured with an Ocean Optics USB2000 and excitation is measured by an Ocean Insight Maya2000 Pro. Both are connected to a bifurcated fiber from ThorLabs positioned to only collect directionally homogenized light. System is calibrated with a two-step procedure at different fixed integration times for either spectrometer (standard settings are 303 ms for the USB2000 and 1000ms for the Maya2000 Pro). First, multiple lasers (450 nm, 514 nm, 808 nm) are used, and calibrated photodiode (Newport 818UV/DB), and measured intensity is compared to the ones measured with the spectrometer. Then PLQY standard reference samples (Hamamatsu Photonics Inc.) are benchmarked. The results are consistent with minimal differences (<5% relative error). Laser intensity is set to reproduce 1-sun equivalent excitation conditions for the chosen bandgap (~55 mW/cm2, attenuation is obtained with continuous neutral-density filter wheel, Thorlabs), it is measured with another photodiode (Hamamatsu S13360) at the position of the sample before the start of each measurement. The fraction of absorbed photons is calculated by measuring the system without sample, then subtracting residual, reflected excitation when the sample is loaded. The laser spot is ~1 cm^2 and the luminescent yield is calculated with a setup-specific adaptation of the procedure suggested here : http://dx.doi.org/10.1002/adma.19970090308.

Current density voltage (J−V) measurements are realised with a two-lamp (halogen and xenon) class AAA WACOM sun simulator, an AM1.5G irradiance spectrum of 1000 W.m^{-2}. Shadow masks are used to define the illuminated area (0.1 cm^2), and the cells are measured at a scan rate of 100 mV.s^{-1}.

For ToF SIMS measurement, element depth profiles are obtained with a time of flight secondary ion mass spectrometer (ToF-SIMS V system, ION-TOF). The primary beam is 25 keV Bi^{3+} with a total current of 0.48 pA and a raster size of $50 \times 50\ \mu m^2$. Cs^+ ions are used with 1000 eV ion energy, 55 nA pulse current on a $300 \times 300\ \mu m^2$ raster size to bombard and etch the film. The data are plotted with the intensity for each signal normalized to the total counts of the signal.

B Appendix B : Supporting Information (SI)

B.1 SI : single source evaporation of metal halide powders

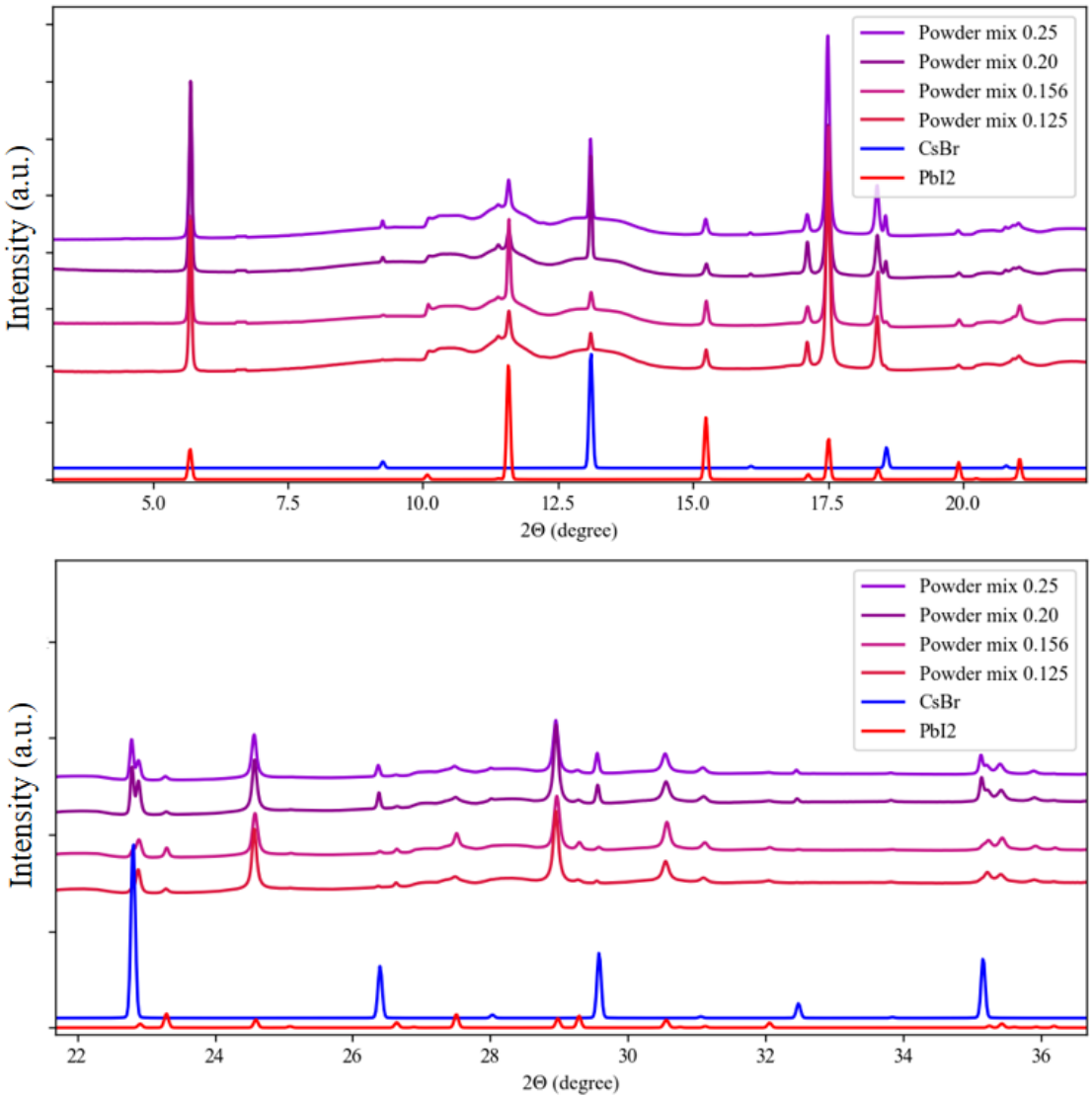

Figure B.1: Powder diffractograms of the mixtures obtained by ball milling. Notes : the patterns were collected via synchrotron X-ray diffraction with a beamline wavelength of 0.694 Å. The artifact at 6.6° is due to a gap between two modules of the detector.

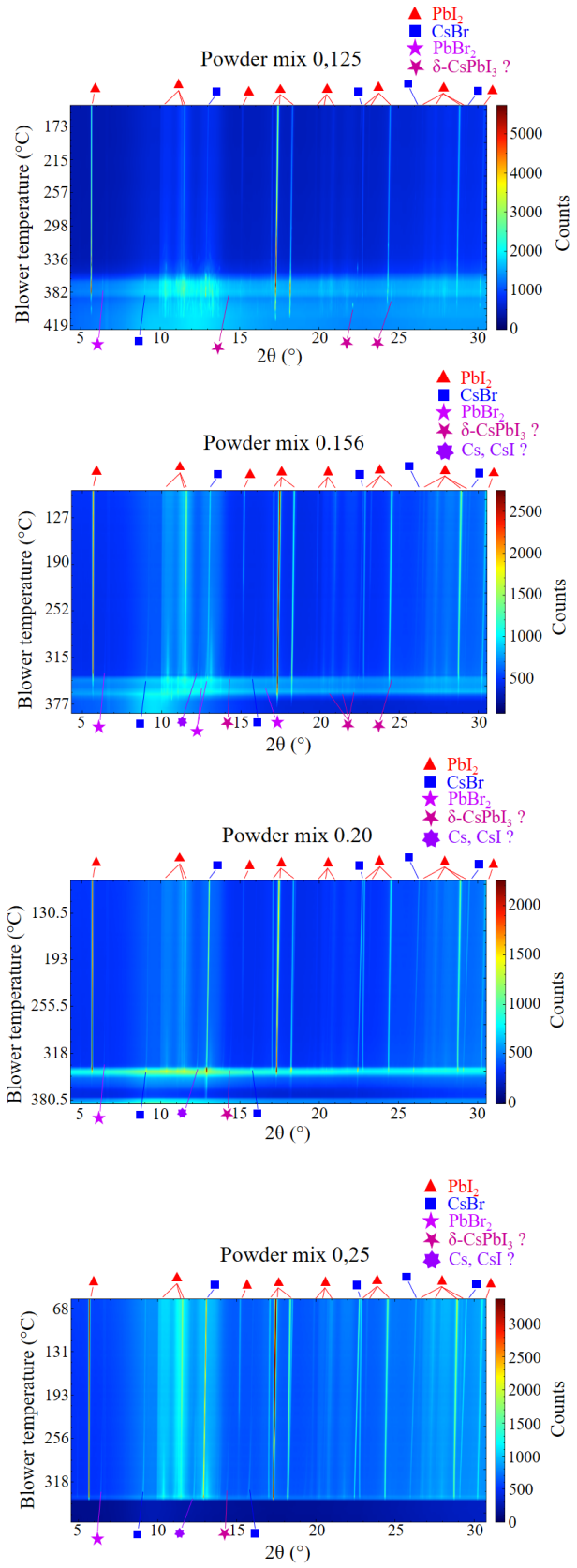

Figure B.2: Temperature evolution of the integrated 2D GIWAXS map from all powder mixes. Intriguingly, there is a weak but clear trend decreasing the coalescence/sublimation temperatures with an increasing CsBr fraction. This is counter-intuitive with respect to the sublimation temperatures of lead iodide and caesium bromide. Additionally, the detailed analysis of each diffractogram shows presence of lead iodide until the very end of the pre-sublimation stage for each composition.

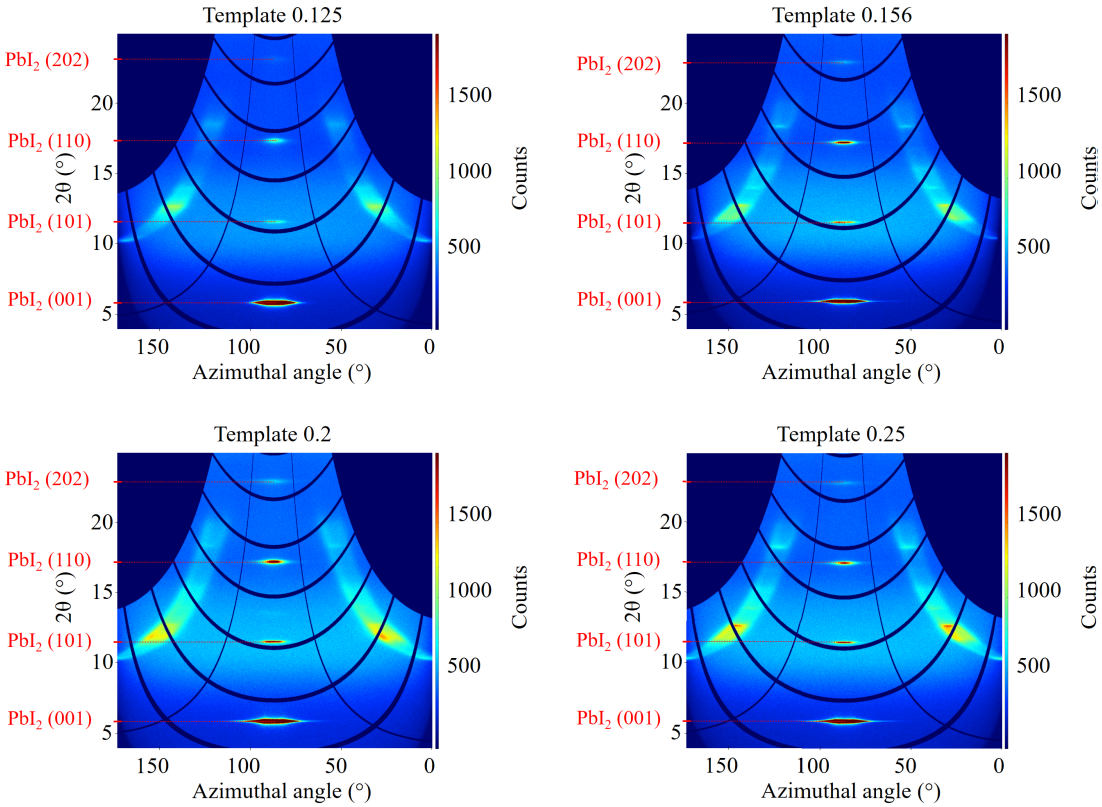

Figure B.3: Diffraction patterns as a function of the azimuthal angle, giving information on the orientation of each phase, for all evaporated metal halide templates. All single source evaporated powders give the same result, similar to thin films obtained by co-evaporation : a strongly oriented lead iodide signal, typical of these nanoplatelets oriented face up.

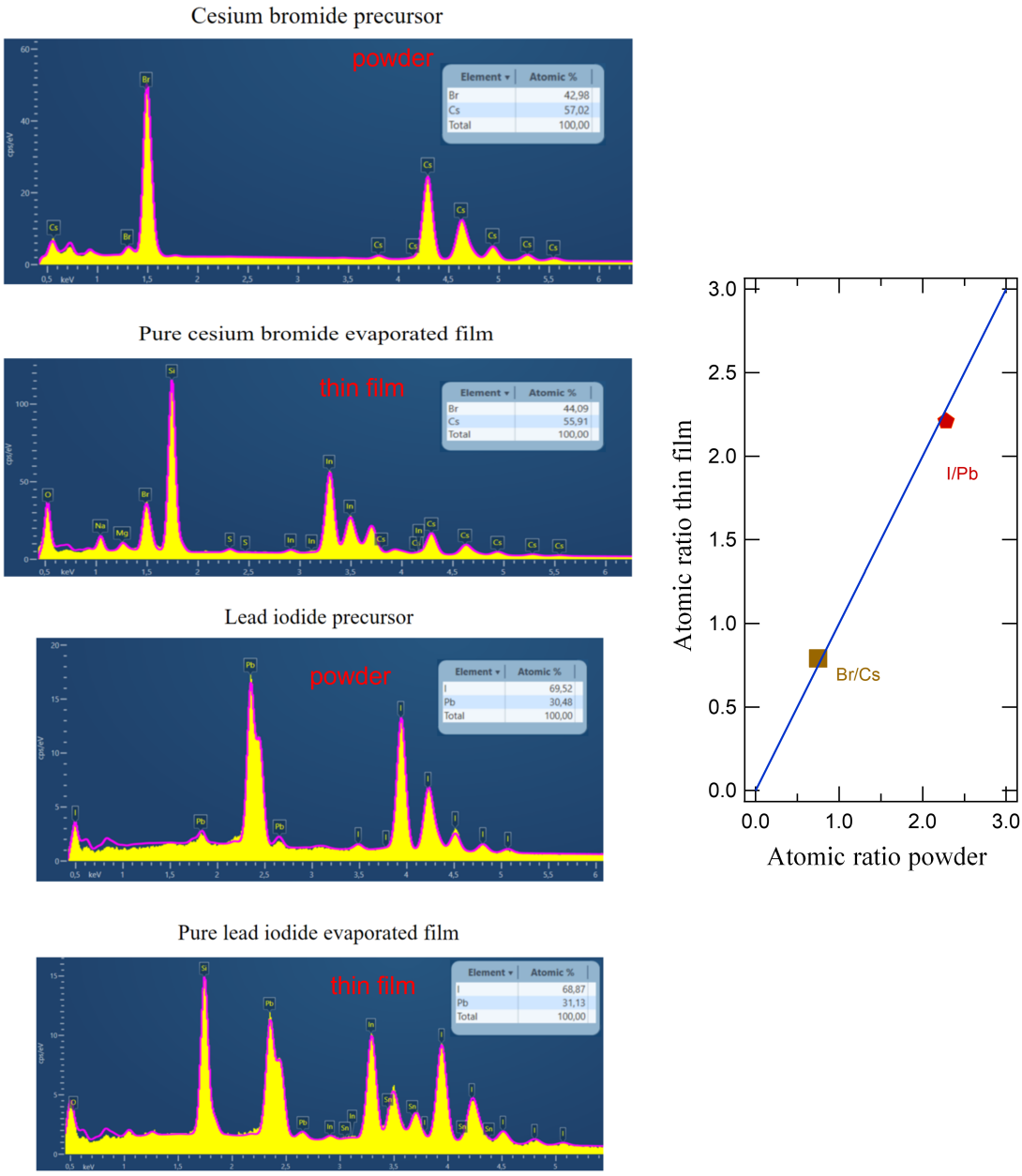

Figure B.4: EDX spectra of the CsBr and PbI_2 as powder and after evaporation as well as extracted atomic ratio before and after along a guide to the eye line (right panel).

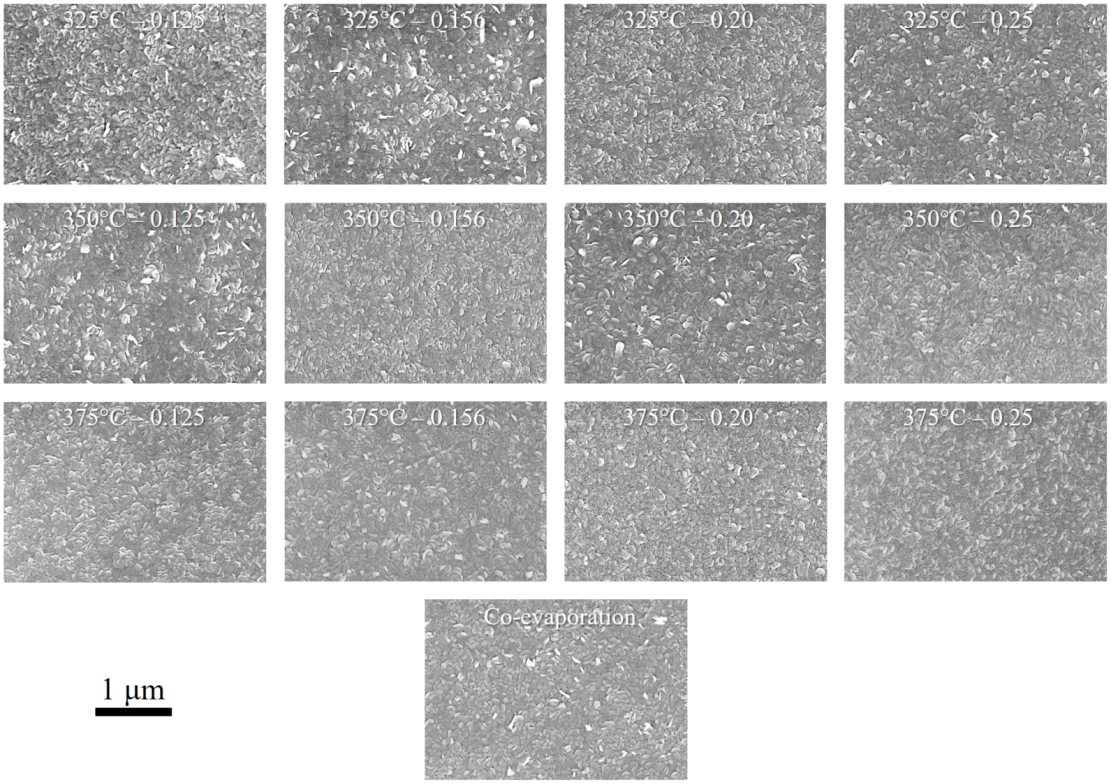

Figure B.5: Top view SEM images of single source and co-evaporated templates. Randomly chosen spots, same magnification.

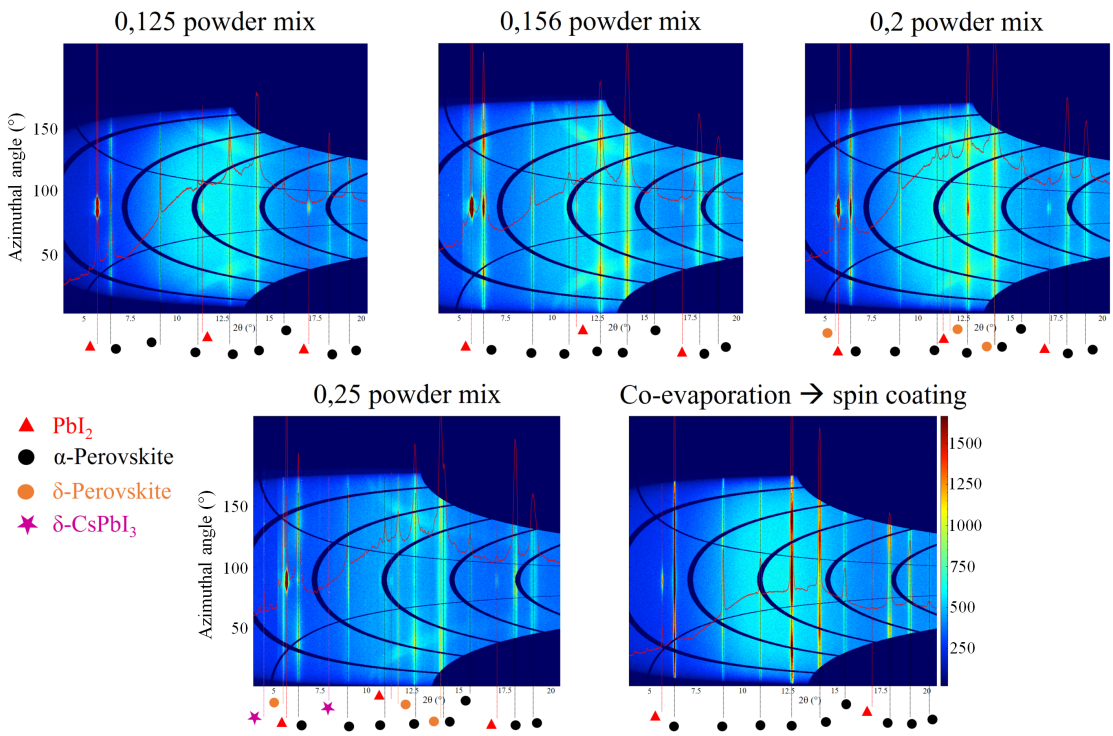

Figure B.6: Diffraction patterns as a function of the azimuthal angle, for all the converted templates into perovskite. Differences in conversion between the powder mix layers and the co-evaporated film are due to a thicker metal halide template caused by a tooling drift. This was corrected for all the other experiments of this study.

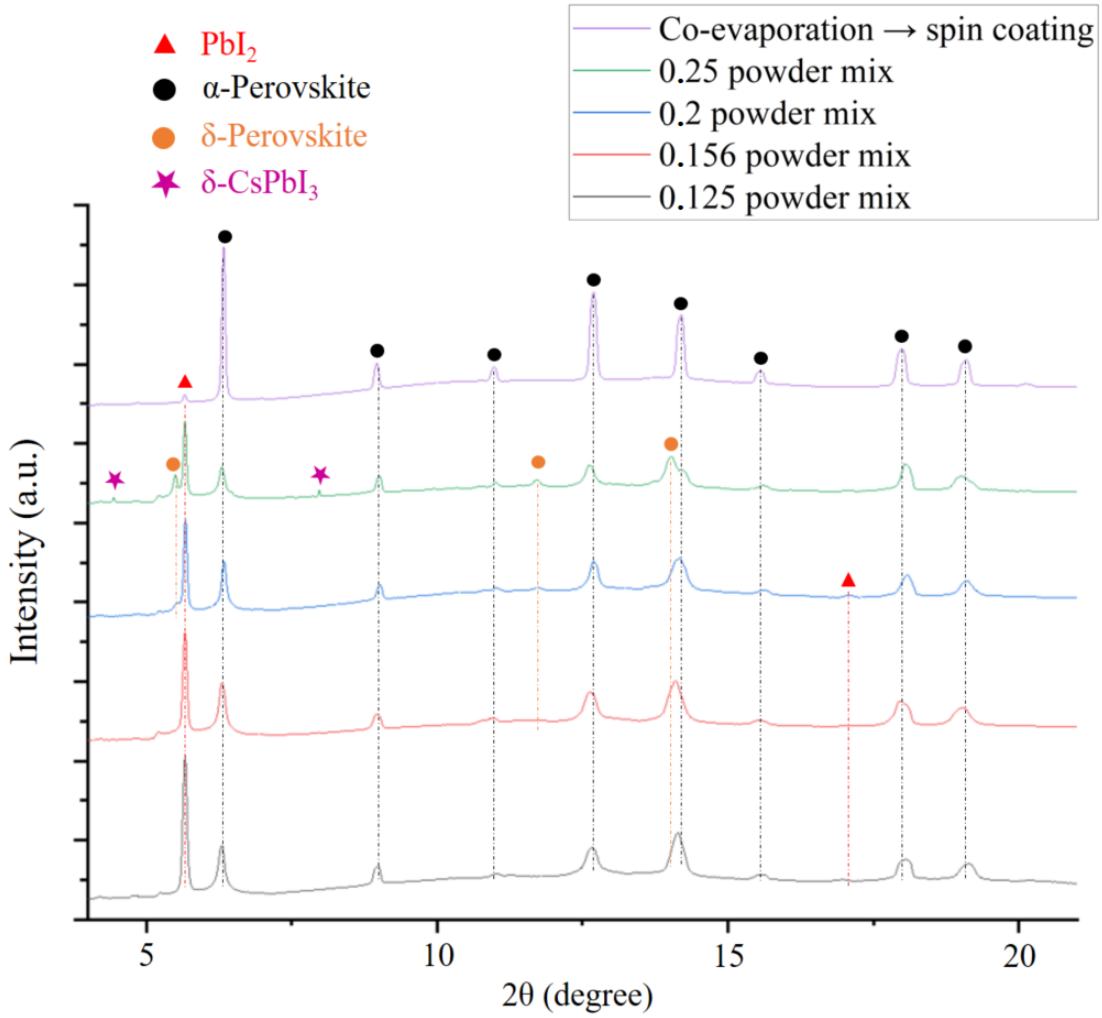

Figure B.7: Stacked diffractograms obtained from azimuthal integration of Figure B.6 2D maps.

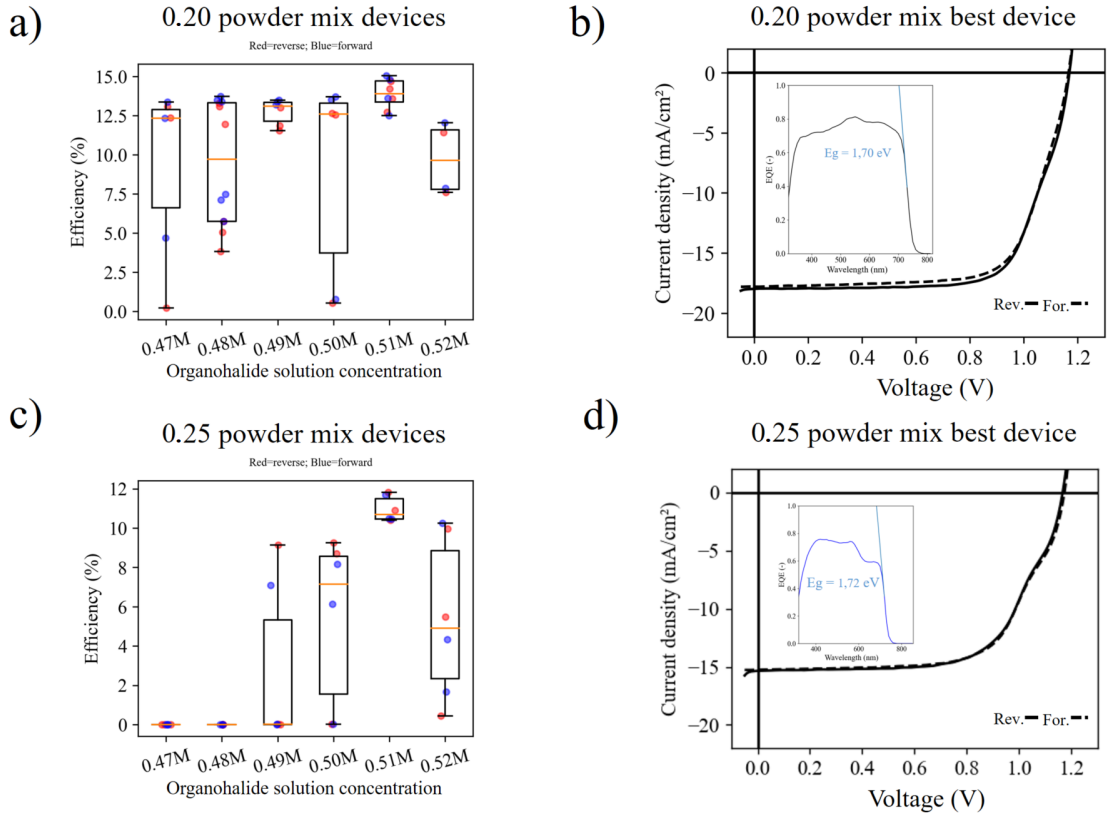

Figure B.8: (a) Statistics of 0.20 powder mix photovoltaic devices with (b) characteristics of best performing device. (c) Statistics of 0.25 powder mix photovoltaic devices with (d) characteristics of best performing device.

B.2 SI : vapor deposition of organohalides

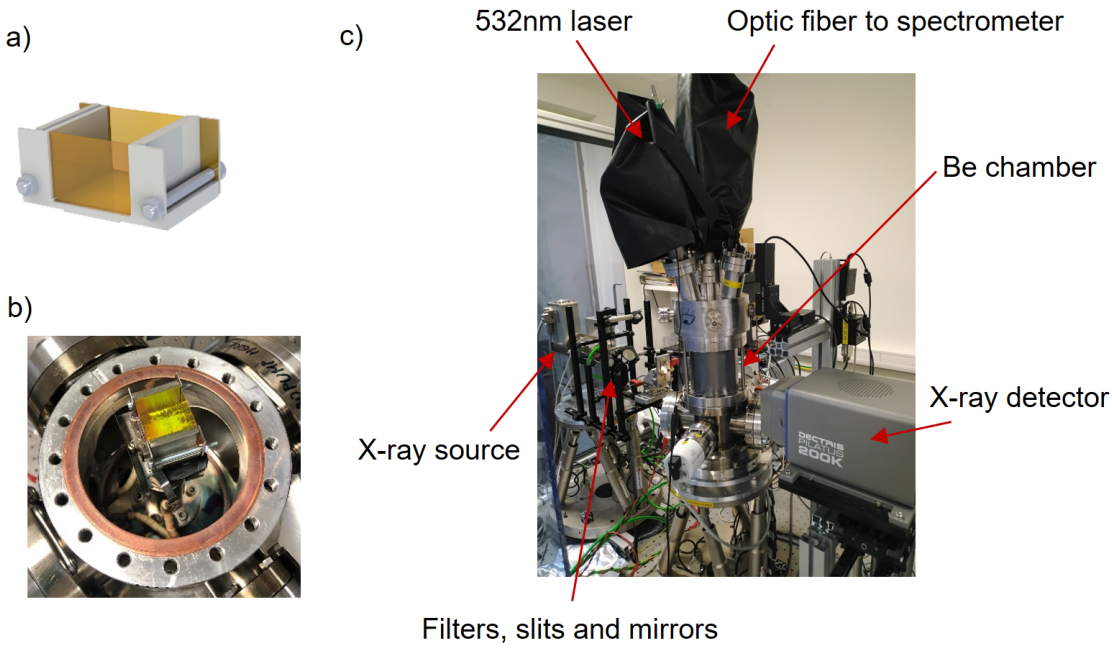

Figure B.9: a) Custom-made holder for simultaneous PhotoLuminescence (PL) and Grazing Incidence Wide Angle X-ray Scattering (GIWAXS) in situ experiments. In PTFE or stainless steel, a U-shaped central part holds a substrate facing down, with FAI powder at the bottom. Two polyimide windows 'close' the openings on the sides while letting X-rays pass, they are maintained by two flat U-shaped plates and bolts. b) Photograph of the stainless steel version of the holder ready to be processed : filled by FAI powder, with a metal halide template facing down, lying on the temperature-controlled stage. c) The top of the chamber (in Be, X-ray transparent) is then mounted and screwed on the bottom part, ready for beams check-up (intensity, alignement). An aluminium foil is positioned between the heating stage and the inside wall to prevent direct deposition on the Be walls.

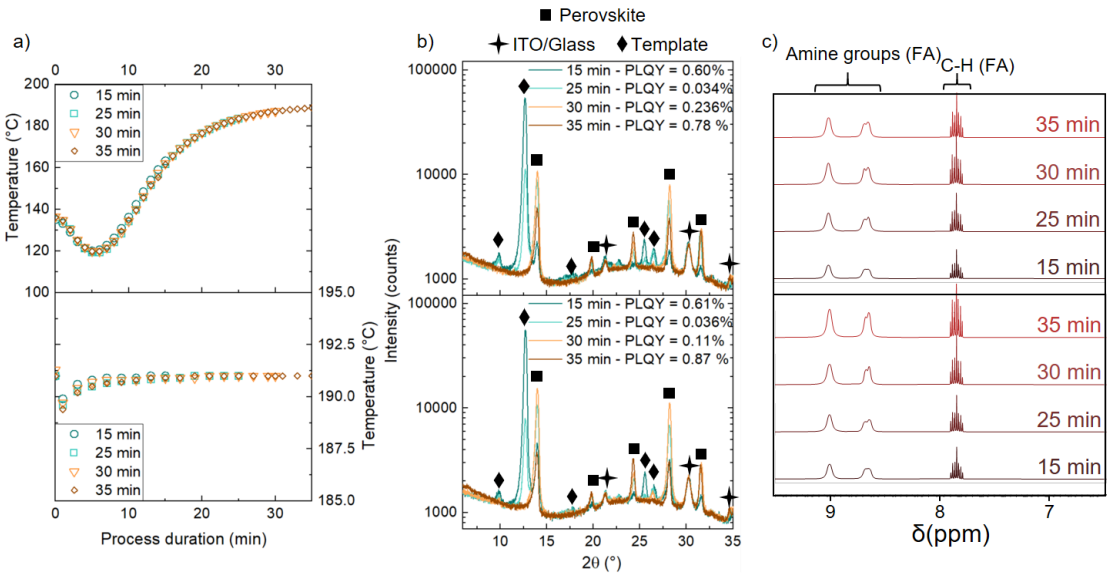

Figure B.10: Assessment of the impact of a 'regular' heating profile versus processing with temperature already at setpoint, in our homemade vapor deposition system (i.e. not the in situ one). a) Temperature profiles b) Diffractograms of thin films after different durations of the progressive heating profiles (up) and 'at setpoint' heating profiles (down), with corresponding PLQY and c) NMR spectra. The initial value and the first dip of the 'regular' heating profiles are explained by our setup : the walls are maintained at 150°C and the table is heated by a circulating calorific fluid. At the beginning of the process, the bath of calorific fluid is cold, thus the table is cooled until its temperature is surpassed by the oil's temperature. This profile is also a consequence of the temperature of the walls being kept at setpoint (150°C), necessary to reach 191°C with the heated table. A start from ambient temperature with the table would need the walls to be cold, and the high thermal inertia of these would prevent reaching high temperatures with the table before a long time. As a conclusion, we see that a more progressive heating of the FAI powders, in the investigated range, has very little impact on the process and the resulting films, all other parameters being equal.

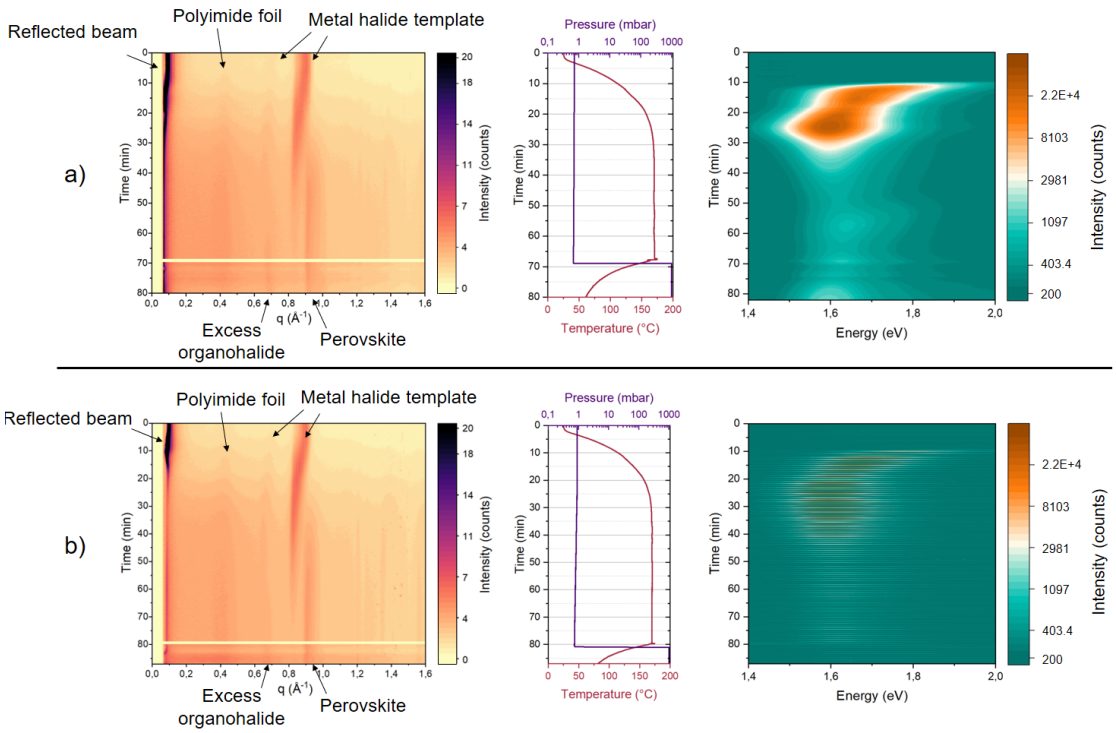

Figure B.11: Comparing two in situ experiments with a) continuous and b) discontinuous laser illumination. The 532 nm laser, set at 90 μW (as for all the other in situ measurements of this work) was blocked by a beam stop for 30 seconds every 5 seconds of illumination. Both the in situ GIWAXS and PL signals are equal in trends and magnitude.

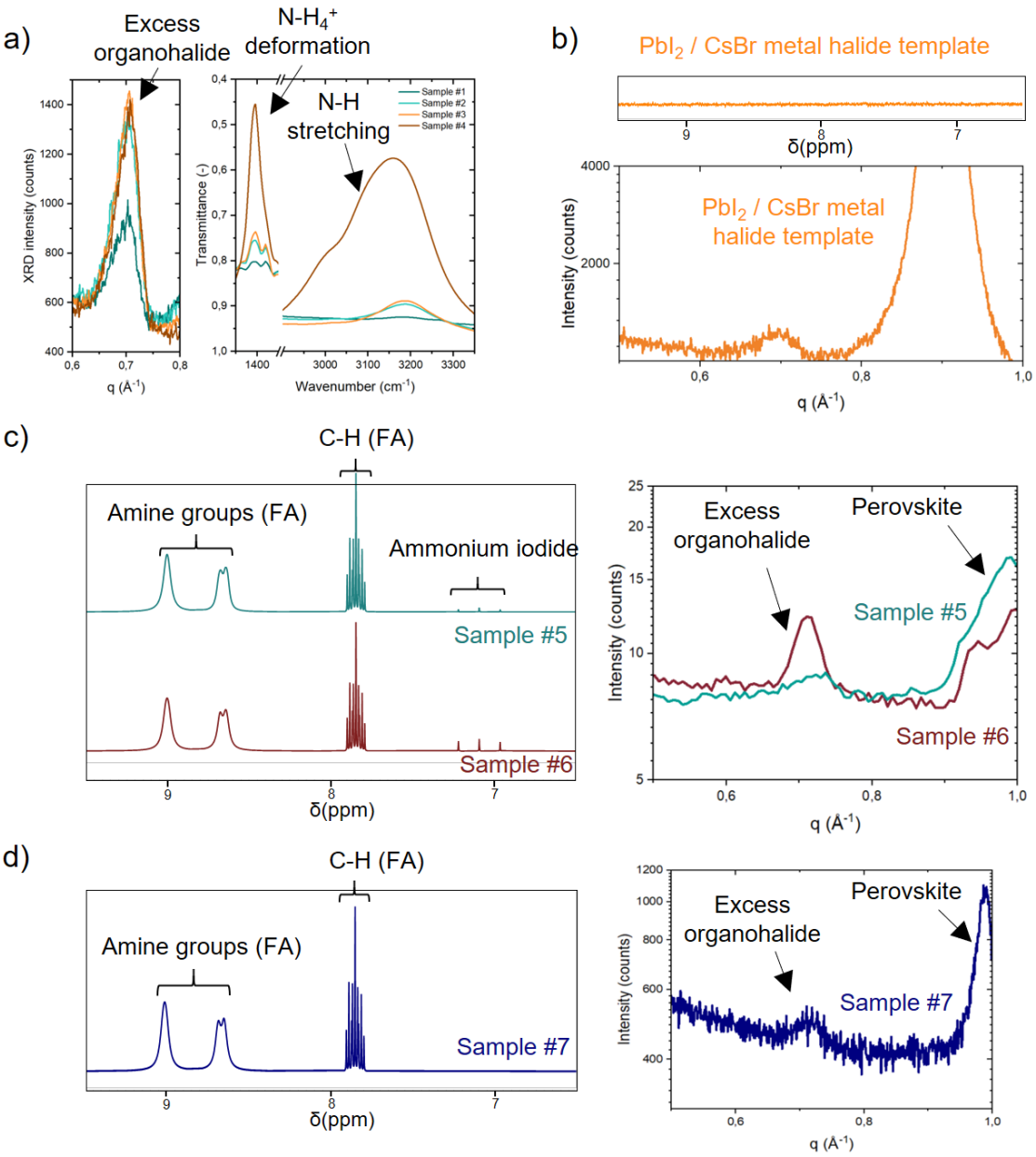

Figure B.12: Comparative analysis of the 0.7 $Å^{-1}$ peak. a) Correlation to some extent of the peak with NH_4I, as determined from FTIR. b) NMR and XRD spectrum of a metal halide template. c) Correlation of the peak with NH_4I, as determined by NMR. d) Counter-example of a perovskite thin film where the 0.7 $Å^{-1}$ peak is detected but without NH_4I detected in the film. Samples 1-4 where obtained with the old vapor deposition methods in the 'short pipes' configuration (cf. Figure 4.11). Samples 5 and 6 were obtained in the in situ setup presented in Figure B.9. Sample 7 was obtained at home in our setup, with the cubic PTFE prototype presented in Figure 4.14.

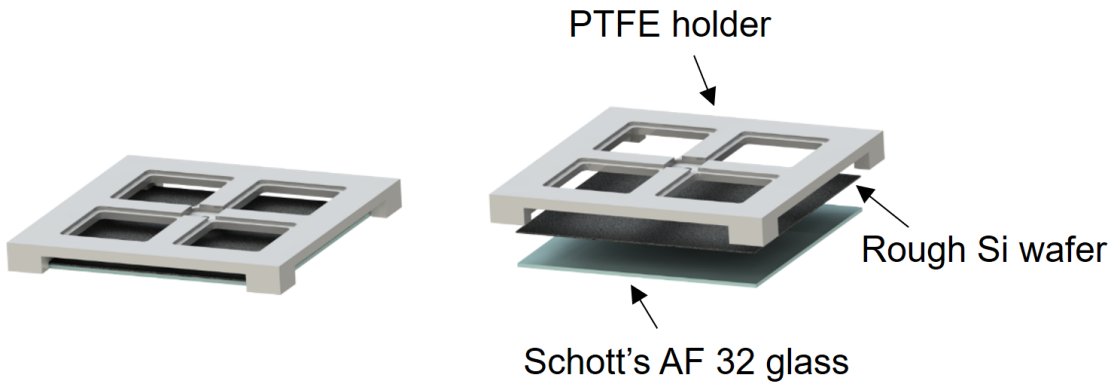

Figure B.13: Standard holder used as baseline. The upper part made out of PTFE is designed to fit four 25x25mm substrates. PTFE is used for its excellent chemical inertness, ease of machining and its good insulation properties (decorrelating to some extent the temperature of the substrates and the temperature of the precursor). The geometry of the PTFE holder is chosen to fit the axial symmetry of the vacuum chamber (and the heating table and pumping exhaust) developed in-house (cf. Figure 4.10). The openings on the sides of the PTFE holder are chosen to control and reduce the relative changes of the leaks of the holder: a PTFE holder tight at ambient temperature can already have millimeter-sized gaps from thermal deformation during the process. By imposing openings with non negligible area (at ambient T), the relative deformation when put at high temperature becomes negligible, hence greatly reducing design-induced inhomogeneities of the batch. A rough (as-cut) silicon wafer is used to dry the precursor solution in which the organohalide salts, additives are dissolved, usually 2-Propanol or ethanol. It has a very good thermal conductivity and also a good chemical inertness from the native silicon oxyde. The solution is dispersed through the openings of the holder via pipette. For larger area prototypes, spray coating / pipette manipulated by robotic arm (available from the automated perovskite fabrication/characterization activities of the lab) are considered. This solution dispersion is done with the full stack assembled on a hotplate at 40°C in ambient air, drying in approximately one minute. The 1.1 mm thick glass plate used to dampen the heating profile (AF 32 from Schott) has very good thermal and chemical resistances, and very low thermal dilatation coefficient, close to the value of a silicon wafer. Thus, even abrupt changes in temperature do not induce deformations of the ensemble. General principles for holder design based on our experience are summarized in the next sentences. First, different geometries lead to different temperature correlations between precursors and substrates. This obviously induces different evaporation/condensation/reevaporation schemes and consequently affects the process [121]. As described in previous section, the choice of material is not harmless. Process inhomogeneities can also arise from holder deformations, provoked by thermal expansion of the chosen materials and/or favored by design itself (thickness variations, machining/fabrication-induced residual stresses). Finally, the thermal conductivity of parts is another factor that greatly affects the effective heating profile applied to the precursors and the substrate, which makes it substantially influential in a short process.

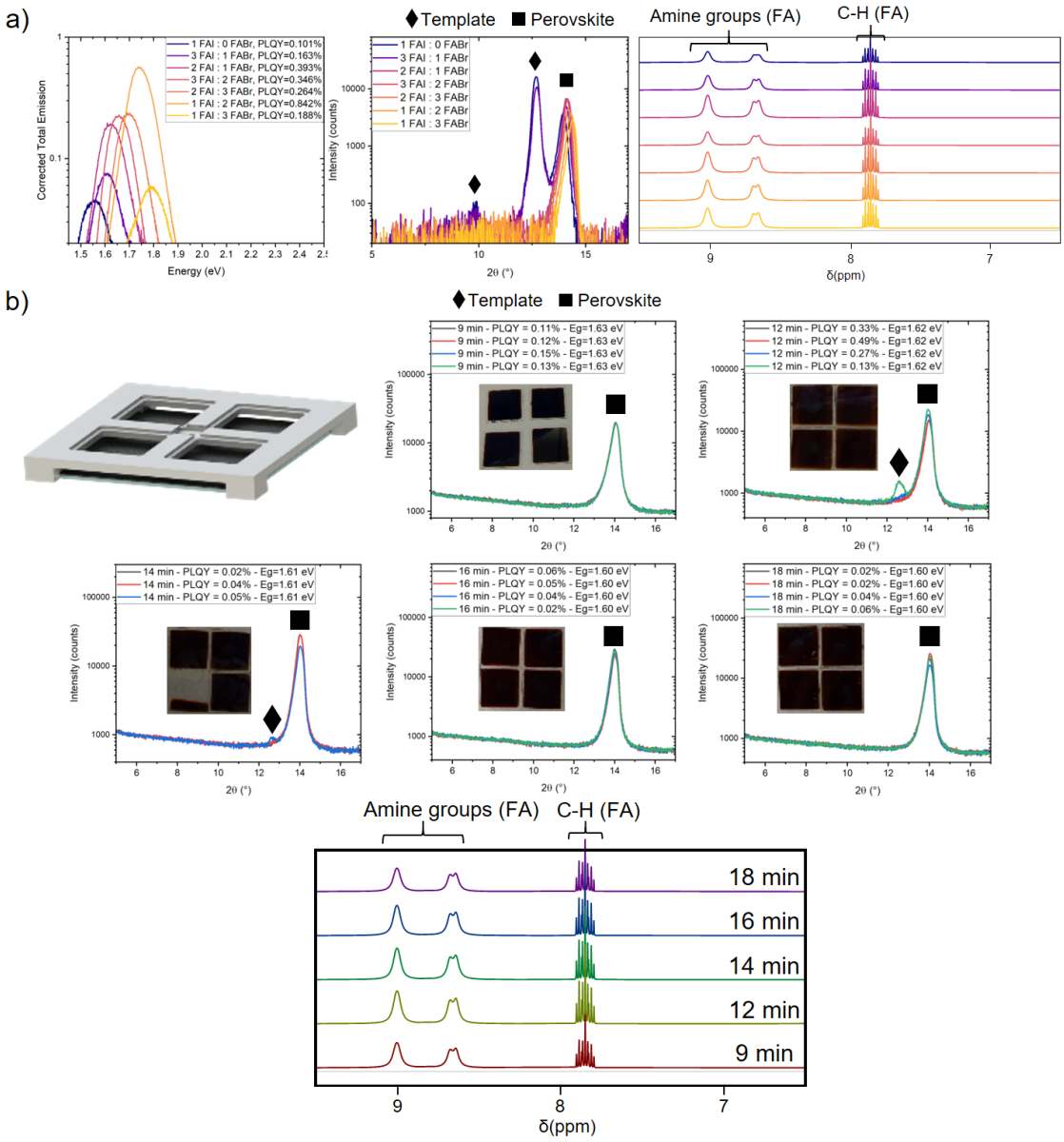

Figure B.14: a) Data complementary to Figure **??** a) et b), investigating bandgap tunability : non-normalized emission spectra, broader scope of XRD data and corresponding NMR spectra. b) XRD, PLQY and NMR of the baseline process converging regime : adding glass sheet and tuning precursor mass allows to reach converging regime, as defined in the conversion regimes section of the core text. Doubling the process duration after full conversion (from 9 to 18 minutes), the films do not show signs of oversaturation. PLQY tends to decrease with time, and the bandgap slightly shifts towards lower energy, showing halide exchange continuously happening. For the 14 minutes case, one of the four substrates moved during the evaporation of the metal halide template (bottom left corner of the picture), leading to a partial coverage of the susbtrate. Baseline without additive, 2.76 FAI : 1 FABr molar ratio, 50mg total mass dissolved and dispersed (cf Methods section and Figure B.13 for experimental details).

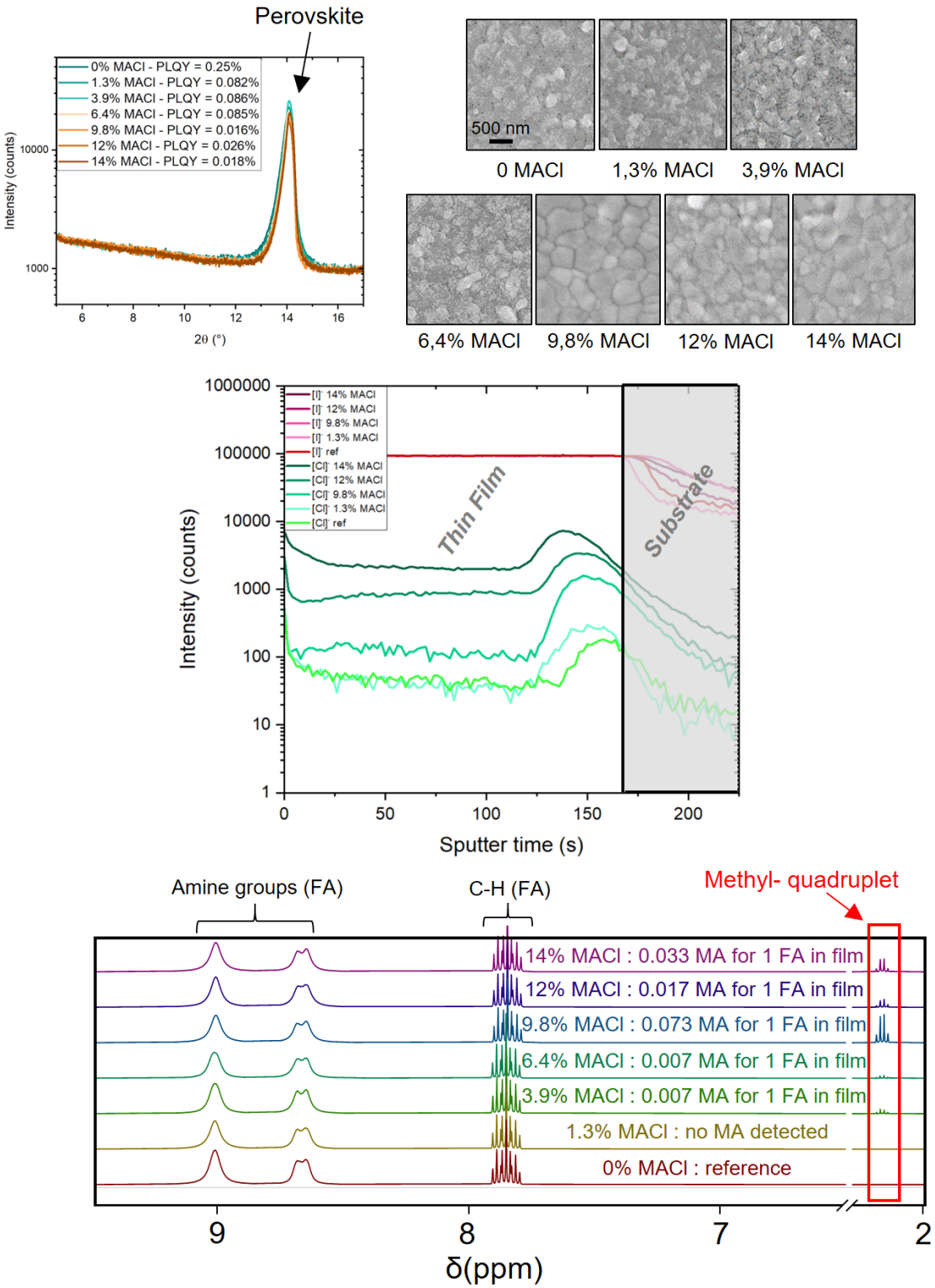

Figure B.15: MACl as additive in vapor deposition, added to the baseline presented Figure B.14b. Thin films are characterised by PLQY, XRD, top view SEM, NMR and Time of Flight Secondary Ions Mass Spectroscopy (ToF SIMS). Addition of MACl in the source systematically results in lower quality films, and little changes in crystallinity. MA and Cl ions are not incorporated the same way in the films : more MACl in the source results in more Cl in the films in the probed range (from ToF SIMS), but maximum amount of MA is attained for a content of MACl in the third quartile range (from NMR). From SEM images, MA content in the films seems correlated to domain size. Scale is common to all images.

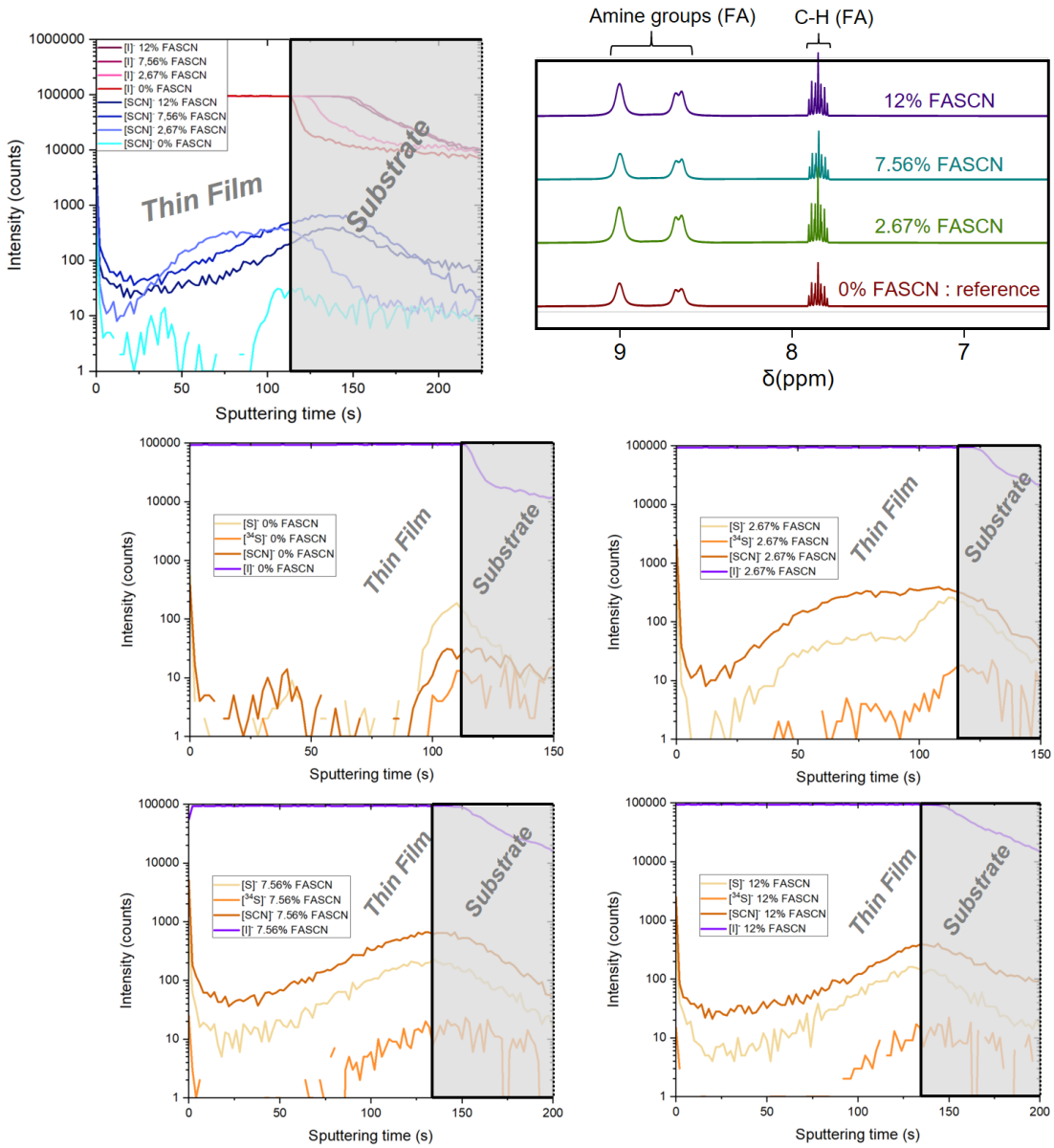

Figure B.16: NMR and ToF SIMS analysis of thin films fabricated with FASCN as additive. Since thiocynate only features poorly NMR-active elements (and not linked to a proton that would allow polarization transfer), its presence is investigated by ToF SIMS. The additive is found in low traces for all films, with similar content irrespective of the initial FASCN quantity. Thiocyanate presence is validated by comparing the as determined trends of S and ^{34}S signals. The differences in sputtering times to reach the substrate for the different cases is explained by differences in morphology and thickness of the different samples.

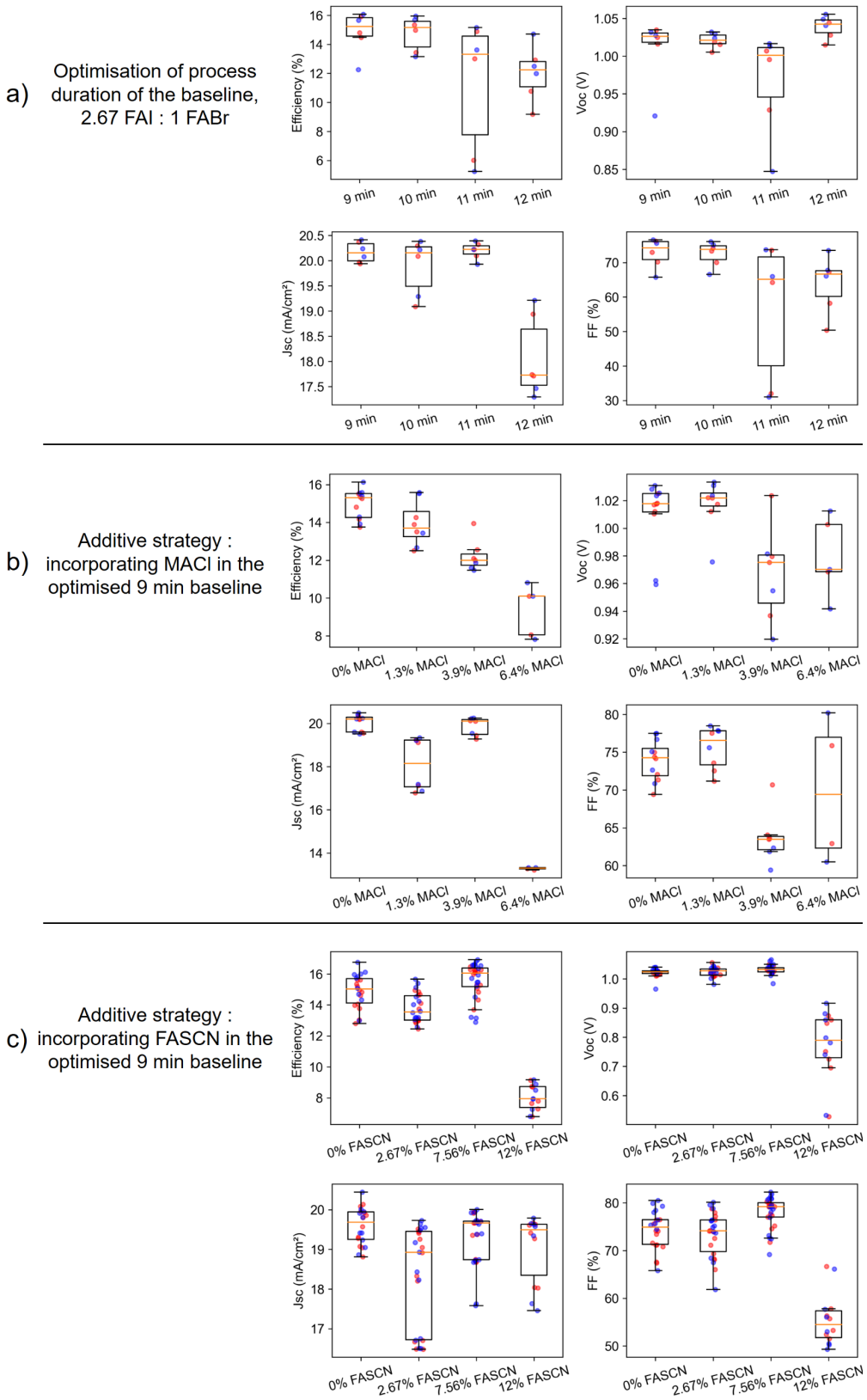

Figure B.17: Statistics of photovoltaic devices. Red and blue dots represent reverse and forward scans, respectively. a) Optimisation of the process duration, b) optimisation of MACl additive content, c) optimisation of FASCN additive content.

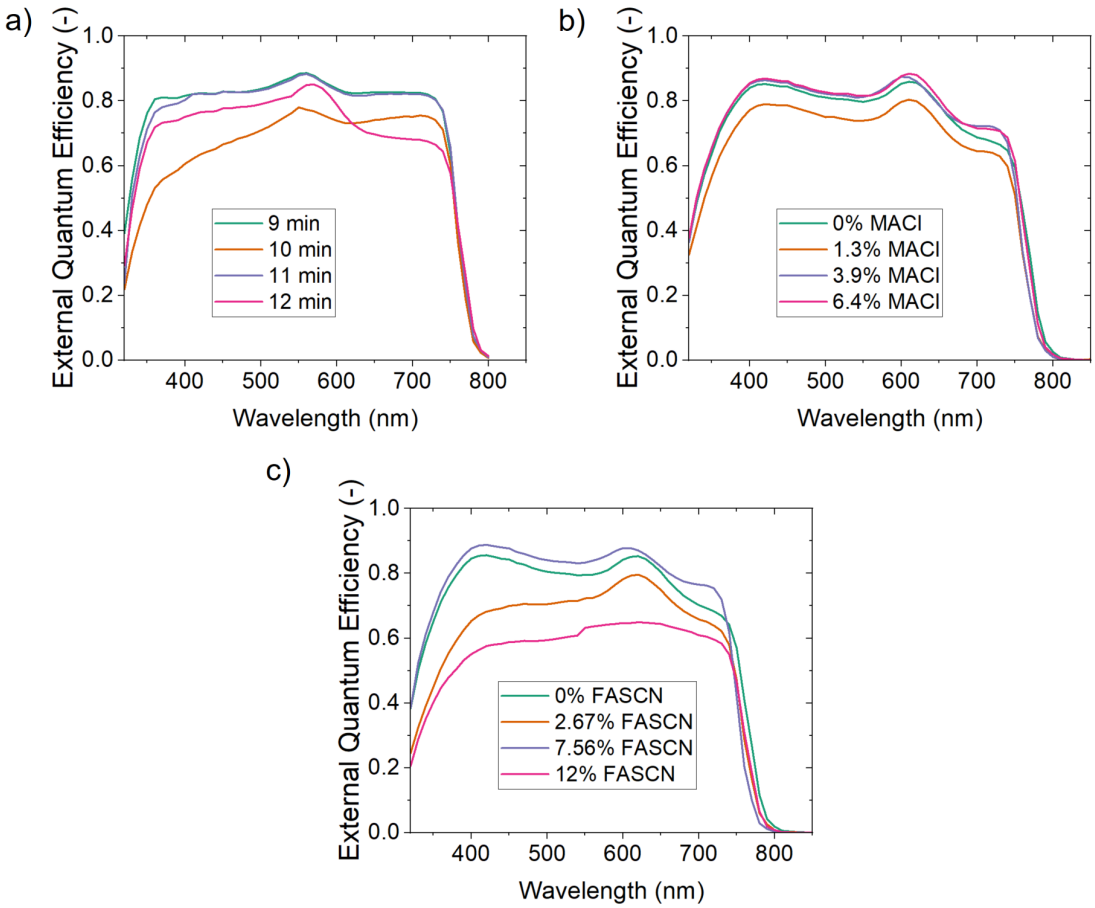

Figure B.18: Exemplary external quantum efficiency measurements of the conditions presented in Figure B.17.

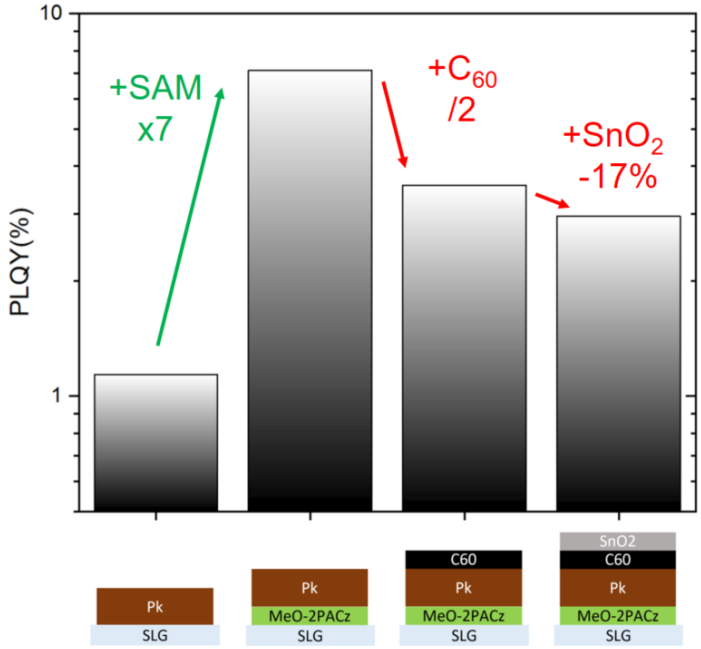

Figure B.19: Losses study of the different interfaces.

Bibliography

[1] IEA. *Trends 2022 in Photovoltaics Applications*. Tech. rep. 2022.

[2] Nancy M. Haegel et al. "Terawatt-scale photovoltaics: Transform global energy". In: *Science* 364.6443 (May 2019), pp. 836–838. ISSN: 0036-8075. DOI: 10.1126/science.aaw1845.

[3] A. Richter, M. Hermle, and S.W Glunz. "Crystalline Silicon Solar Cells Reassessment of the Limiting Efficiency for Crystalline Silicon Solar Cells". In: *IEEE Journal of Photovoltaics* 3.4 (2013), pp. 1184–1191. DOI: 10.1109/JPHOTOV.2013.2270351.

[4] National Renewable Energy Laboratory. *Best research-cell efficiency chart*. 2023. URL: https://www.nrel.gov/pv/cell-efficiency.html.

[5] Louise C. Hirst and Nicholas J. Ekins-Daukes. "Fundamental losses in solar cells". In: *Progress in Photovoltaics: Research and Applications* 19.3 (May 2011), pp. 286–293. ISSN: 10627995. DOI: 10.1002/pip.1024.

[6] Zhen Li et al. "Stabilizing Perovskite Structures by Tuning Tolerance Factor: Formation of Formamidinium and Cesium Lead Iodide Solid-State Alloys". In: *Chemistry of Materials* 28.1 (2016), pp. 284–292. ISSN: 15205002. DOI: 10.1021/acs.chemmater.5b04107.

[7] Jun Hong Noh et al. "Chemical management for colorful, efficient, and stable inorganic-organic hybrid nanostructured solar cells". In: *Nano Letters* 13.4 (2013), pp. 1764–1769. ISSN: 15306984. DOI: 10.1021/nl400349b.

[8] Wan-Jian Yin, Tingting Shi, and Yanfa Yan. "Unusual defect physics in CH3NH3PbI3 perovskite solar cell absorber". In: *Applied Physics Letters* 104.6 (Feb. 2014), p. 063903. ISSN: 0003-6951. DOI: 10.1063/1.4864778.

[9] Fan Fu et al. "Low-temperature-processed efficient semi-transparent planar perovskite solar cells for bifacial and tandem applications". In: *Nature Communications* 6.1 (Dec. 2015), p. 8932. ISSN: 2041-1723. DOI: 10.1038/ncomms9932.

[10] S. Albrecht et al. "Monolithic perovskite/silicon-heterojunction tandem solar cells processed at low temperature". In: *Energy Environ. Sci.* 9.1 (2016), pp. 81–88. ISSN: 1754-5692. DOI: 10.1039/C5EE02965A.

[11] Maximilian T. Hörantner et al. "The Potential of Multijunction Perovskite Solar Cells". In: *ACS Energy Letters* 2.10 (Oct. 2017), pp. 2506–2513. ISSN: 2380-8195. DOI: 10.1021/acsenergylett.7b00647. URL: https://pubs.acs.org/doi/10.1021/acsenergylett.7b00647.

[12] S. Altazin et al. “Design of perovskite/crystalline-silicon monolithic tandem solar cells”. In: *Optics Express* 26.10 (May 2018), A579. ISSN: 1094-4087. DOI: 10.1364/OE.26.00A579.

[13] Jérémie Werner, Bjoern Niesen, and Christophe Ballif. “Perovskite/Silicon Tandem Solar Cells: Marriage of Convenience or True Love Story? – An Overview”. In: *Advanced Materials Interfaces* 5.1 (2018), pp. 1–19. ISSN: 21967350. DOI: 10.1002/admi.201700731.

[14] Jonathan Lehr et al. “Energy yield modelling of perovskite/silicon two-terminal tandem PV modules with flat and textured interfaces”. In: *Sustainable Energy & Fuels* (2018). ISSN: 2398-4902. DOI: 10.1039/C8SE00465J.

[15] Zhengshan J. Yu, Joe V. Carpenter, and Zachary C. Holman. “Techno-economic viability of silicon-based tandem photovoltaic modules in the United States”. In: *Nature Energy* (2018). ISSN: 2058-7546. DOI: 10.1038/s41560-018-0201-5.

[16] K.A. Bush et al. “23.6%-efficient monolithic perovskite/silicon tandem solar cells with improved stability”. In: *Nature Energy* 2.4 (Feb. 2017), p. 17009. ISSN: 2058-7546. DOI: 10.1038/nenergy.2017.9.

[17] Yi Hou et al. “Efficient tandem solar cells with solution-processed perovskite on textured crystalline silicon”. In: *Science* 367.6482 (2020), pp. 1135–1140. ISSN: 0036-8075. DOI: 10.1126/science.aaz3691. URL: https://www.sciencemag.org/lookup/doi/10.1126/science.aaz3691.

[18] G. Nogay et al. “25.1%-Efficient monolithic perovskite/silicon tandem solar cell based on a p-type monocrystalline textured silicon wafer and high-temperature passivating contacts”. In: *ACS Energy Letters* 4.4 (2019), pp. 844–845. ISSN: 23808195. DOI: 10.1021/acsenergylett.9b00377.

[19] Julian Burschka et al. “Sequential deposition as a route to high-performance perovskite-sensitized solar cells”. In: *Nature* 499.7458 (2013), pp. 316–319. ISSN: 00280836. DOI: 10.1038/nature12340.

[20] Florent Sahli et al. “Fully textured monolithic perovskite/silicon tandem solar cells with 25.2% power conversion efficiency”. In: *Nature Materials* 17.9 (2018), pp. 820–826. ISSN: 14764660. DOI: 10.1038/s41563-018-0115-4.

[21] Jianghui Zheng et al. “Large area efficient interface layer free monolithic perovskite/homo-junction-silicon tandem solar cell with over 20% efficiency”. In: *Energy & Environmental Science* (2018), pp. 0–41. ISSN: 1754-5692. DOI: 10.1039/C8EE00689J.

[22] Jianghui Zheng et al. “21.8% Efficient Monolithic Perovskite/Homo-Junction-Silicon Tandem Solar Cell on 16 cm2”. In: *ACS Energy Letters* 3 (2018), acsenergylett.8b01382. ISSN: 2380-8195. DOI: 10.1021/acsenergylett.8b01382.

[23] Heping Shen et al. “In situ recombination junction between p-Si and TiO2 enables high-efficiency monolithic perovskite/Si tandem cells”. In: *Science Advances* 4.12 (Dec. 2018), eaau9711. ISSN: 2375-2548. DOI: 10.1126/sciadv.aau9711.

[24] Kevin A Bush et al. “Minimizing Current and Voltage Losses to Reach 25%-Efficient Monolithic Two-Terminal Perovskite-Silicon Tandem Solar Cells”. In: *ACS Energy Letters* (Aug. 2018), acsenergylett.8b01201. ISSN: 2380-8195. DOI: 10.1021/acsenergylett.8b01201.

[25] J. Werner et al. “Efficient Monolithic Perovskite/Silicon Tandem Solar Cell with Cell Area >1 cm 2”. In: *The Journal of Physical Chemistry Letters* 7.1 (Jan. 2016), pp. 161–166. ISSN: 1948-7185. DOI: 10.1021/acs.jpclett.5b02686.

[26] Marko Jošt et al. “Textured interfaces in monolithic perovskite/silicon tandem solar cells: Advanced light management for improved efficiency and energy yield”. In: *Energy & Environmental Science* (2019). ISSN: 1754-5692. DOI: 10.1039/C8EE02469C.

[27] Bo Chen et al. “Grain Engineering for Perovskite/Silicon Monolithic Tandem Solar Cells with Efficiency of 25.4%”. In: *Joule* (Oct. 2018), pp. 1–14. ISSN: 25424351. DOI: 10.1016/j.joule.2018.10.003.

[28] Luana Mazzarella et al. “Infrared Light Management Using a Nanocrystalline Silicon Oxide Interlayer in Monolithic Perovskite/Silicon Heterojunction Tandem Solar Cells with Efficiency above 25%”. In: *Advanced Energy Materials* 9.14 (2019), pp. 1–9. ISSN: 16146840. DOI: 10.1002/aenm.201803241.

[29] Florent Sahli et al. “Improved Optics in Monolithic Perovskite/Silicon Tandem Solar Cells with a Nanocrystalline Silicon Recombination Junction”. In: *Advanced Energy Materials* 8.6 (Feb. 2018), p. 1701609. ISSN: 16146832. DOI: 10.1002/aenm.201701609.

[30] YiLiang Wu et al. “Monolithic perovskite/silicon-homojunction tandem solar cell with over 22% efficiency”. In: *Energy & Environmental Science* 10.11 (2017), pp. 2472–2479. ISSN: 1754-5692. DOI: 10.1039/C7EE02288C.

[31] The Duong et al. “Rubidium Multication Perovskite with Optimized Bandgap for Perovskite-Silicon Tandem with over 26% Efficiency”. In: *Advanced Energy Materials* 7.14 (July 2017), p. 1700228. ISSN: 16146832. DOI: 10.1002/aenm.201700228.

[32] Bo Chen et al. “Blade-Coated Perovskites on Textured Silicon for 26%-Efficient Monolithic Perovskite/Silicon Tandem Solar Cells”. In: *Joule* (2020), pp. 1–15. ISSN: 25424351. DOI: 10.1016/j.joule.2020.01.008. URL: https://doi.org/10.1016/j.joule.2020.01.008.

[33] Anand Selvin Subbiah et al. “High-Performance Perovskite Single-Junction and Textured Perovskite/Silicon Tandem Solar Cells via Slot-Die-Coating”. In: *ACS Energy Letters* 5.9 (Sept. 2020), pp. 3034–3040. ISSN: 2380-8195. DOI: 10.1021/acsenergylett.0c01297.

[34] Jiangshan Feng et al. “High-throughput large-area vacuum deposition for high-performance formamidine-based perovskite solar cells”. In: *Energy & Environmental Science* 14.5 (Jan. 2021), pp. 3035–3043. ISSN: 1754-5692. DOI: 10.1039/D1EE00634G. URL: http://xlink.rsc.org/?DOI=D1EE00634G.

[35] Juliane Borchert et al. “Large-Area, Highly Uniform Evaporated Formamidinium Lead Triiodide Thin Films for Solar Cells”. In: *ACS Energy Letters* 2.12 (Dec. 2017), pp. 2799–2804. ISSN: 2380-8195. DOI: 10.1021/acsenergylett.7b00967. URL: https://pubs.acs.org/doi/10.1021/acsenergylett.7b00967.

[36] Long Luo et al. “Large-area perovskite solar cells with Cs x FA 1-x PbI 3-y Br y thin films deposited by a vapor–solid reaction method”. In: *Journal of Materials Chemistry A* 6.42 (2018), pp. 21143–21148. ISSN: 2050-7488. DOI: 10.1039/C8TA06557H. URL: http://xlink.rsc.org/?DOI=C8TA06557H.

[37] Longbin Qiu et al. “Hybrid Chemical Vapor Deposition Enables Scalable and Stable Cs-FA Mixed Cation Perovskite Solar Modules with a Designated Area of 91.8 cm2 Approaching 10% Efficiency”. In: *Journal of Materials Chemistry A* 7.12 (2019), pp. 6920–6929. ISSN: 20507496. DOI: 10.1039/C9TA00239A.

[38] Marcel Roß et al. “Co-Evaporated Formamidinium Lead Iodide Based Perovskites with 1000 h Constant Stability for Fully Textured Monolithic Perovskite/Silicon Tandem Solar Cells”. In: *Advanced Energy Materials* 11.35 (Sept. 2021), p. 2101460. ISSN: 1614-6832. DOI: 10.1002/aenm.202101460. URL: https://onlinelibrary.wiley.com/doi/10.1002/aenm.202101460.

[39] Emilio J. Juarez-Perez, Luis K. Ono, and Yabing Qi. “ Thermal degradation of formamidinium based lead halide perovskites into sym -triazine and hydrogen cyanide observed by coupled thermogravimetry-mass spectrometry analysis ”. In: *Journal of Materials Chemistry A* 7.28 (2019), pp. 16912–16919. ISSN: 2050-7488. DOI: 10.1039/c9ta06058h.

[40] Florent Sahli et al. “Ammonia-assisted vapour transport deposition of formamidinium salts for perovskite thin films”. In: *preprint* (2021). URL: http://infoscience.epfl.ch/record/288002.

[41] Florent Sahli et al. “Vapor Transport Deposition of Methylammonium Iodide for Perovskite Solar Cells”. In: *ACS Applied Energy Materials* (Apr. 2021), acsaem.0c02999. ISSN: 2574-0962. DOI: 10.1021/acsaem.0c02999.

[42] Quentin Guesnay et al. “Vapor deposition of metal halide perovskite thin films: Process control strategies to shape layer properties”. In: *APL Materials* 9.10 (2021), p. 100703. ISSN: 2166-532X. DOI: 10.1063/5.0060642. URL: https://doi.org/10.1063/5.0060642%0Ahttps://aip.scitation.org/doi/10.1063/5.0060642.

[43] Quentin Guesnay et al. “Substoichiometric Mixing of Metal Halide Powders and Their Single-Source Evaporation for Perovskite Photovoltaics”. In: *ACS Photonics* (Aug. 2023). ISSN: 2330-4022. DOI: 10.1021/acsphotonics.3c00438. URL: https://pubs.acs.org/doi/10.1021/acsphotonics.3c00438.

[44] Peter Würfel and Uli Würfel. *Physics of Solar Cells: From Basic Principles to Advanced Concepts*. Wiley-VCH, 2016, p. 288. ISBN: 978-3-527-41312-6.

[45] Tsutomu Miyasaka. *Perovskite Photovoltaics and Optoelectronics: From Fundamentals to Advanced Applications*. Vol. 6. August. Hoboken: Wiley-VCH, 2022, p. 480. ISBN: 3527347488,9783527347483.

[46] Peter Atkins, Julio de Paula, and James Keeler. *Atkins' Physical Chemistry*. Oxford University Press, 2023, p. 967. ISBN: 2022935397, 9780198847816.

[47] Jarla Thiesbrummel et al. "Universal Current Losses in Perovskite Solar Cells Due to Mobile Ions". In: *Advanced Energy Materials* 11.34 (Sept. 2021). ISSN: 1614-6832. DOI: 10.1002/aenm.202101447. URL: https://onlinelibrary.wiley.com/doi/10.1002/aenm.202101447.

[48] M. Era et al. "Self-organized growth of PbI-based layered perovskite quantum well by dual-source vapor deposition". In: *Chemistry of Materials* 9.16 (1997), pp. 8–10. ISSN: 0897-4756. DOI: 10.1021/cm960434m.

[49] Toshinori Matsushima et al. "Organic-inorganic field effect transistor with SnI-based perovskite channel layer using vapor phase deposition technique". In: *Organic Field Effect Transistors II* 5217.November 2003 (2003), p. 43. ISSN: 0277786X. DOI: 10.1117/12.505509.

[50] Toshinori Matsushima, Katsuhiko Fujita, and Tetsuo Tsutsui. "Preparation of conductive organic-inorganic cubic perovskite thin films by dual-source vacuum vapor deposition". In: *Japanese Journal of Applied Physics, Part 1: Regular Papers and Short Notes and Review Papers* 45.1 B (2006), pp. 523–525. ISSN: 00214922. DOI: 10.1143/JJAP.45.523.

[51] Mingzhen Liu, Michael B. Johnston, and Henry J. Snaith. "Efficient planar heterojunction perovskite solar cells by vapour deposition". In: *Nature* 501.7467 (Sept. 2013), pp. 395–398. ISSN: 0028-0836. DOI: 10.1038/nature12509. URL: http://www.nature.com/articles/nature12509.

[52] James M. Ball et al. "Dual-Source Coevaporation of Low-Bandgap FA1-xCsxSn1-yPbyI3 Perovskites for Photovoltaics". In: *ACS Energy Letters* 4.11 (2019), pp. 2748–2756. ISSN: 23808195. DOI: 10.1021/acsenergylett.9b01855.

[53] Olga Malinkiewicz et al. "Perovskite solar cells employing organic charge-transport layers". In: *Nature Photonics* 8.2 (Feb. 2014), pp. 128–132. ISSN: 1749-4885. DOI: 10.1038/nphoton.2013.341. URL: http://www.nature.com/articles/nphoton.2013.341.

[54] Dewei Zhao et al. "Annealing-free efficient vacuum-deposited planar perovskite solar cells with evaporated fullerenes as electron-selective layers". In: *Nano Energy* 19 (Jan. 2016), pp. 88–97. ISSN: 22112855. DOI: 10.1016/j.nanoen.2015.11.008. URL: http://dx.doi.org/10.1016/j.nanoen.2015.11.008%20https://linkinghub.elsevier.com/retrieve/pii/S2211285515004267.

[55] Shenghao Wang et al. "Smooth perovskite thin films and efficient perovskite solar cells prepared by the hybrid deposition method". In: *Journal of Materials Chemistry A* 3.28 (2015), pp. 14631–14641. ISSN: 20507496. DOI: 10.1039/c5ta03593g.

[56] Juliane Borchert et al. “Impurity Tracking Enables Enhanced Control and Reproducibility of Hybrid Perovskite Vapor Deposition”. In: *ACS Applied Materials and Interfaces* 11.32 (2019), pp. 28851–28857. ISSN: 19448252. DOI: 10.1021/acsami.9b07619.

[57] Tobias Abzieher et al. “Efficient All-Evaporated pin-Perovskite Solar Cells: A Promising Approach Toward Industrial Large-Scale Fabrication”. In: *IEEE Journal of Photovoltaics* 9.5 (2019), pp. 1249–1257. ISSN: 21563403. DOI: 10.1109/JPHOTOV.2019.2920727.

[58] Ranjith Kottokkaran et al. “Performance and stability of co-evaporated vapor deposited perovskite solar cells”. In: *Journal of Materials Science: Materials in Electronics* 30.6 (2019), pp. 5487–5494. ISSN: 1573482X. DOI: 10.1007/s10854-019-00842-y. URL: http://dx.doi.org/10.1007/s10854-019-00842-y.

[59] Luis K. Ono et al. “Fabrication of semi-transparent perovskite films with centimeter-scale superior uniformity by the hybrid deposition method”. In: *Energy and Environmental Science* 7.12 (2014), pp. 3989–3993. ISSN: 17545706. DOI: 10.1039/c4ee02539c.

[60] Marcel Roß et al. “Co-Evaporated p-i-n Perovskite Solar Cells beyond 20% Efficiency: Impact of Substrate Temperature and Hole-Transport Layer”. In: *ACS Applied Materials & Interfaces* 12.35 (Sept. 2020), pp. 39261–39272. ISSN: 1944-8244. DOI: 10.1021/acsami.0c10898.

[61] Cristina Momblona et al. “Efficient vacuum deposited p-i-n and n-i-p perovskite solar cells employing doped charge transport layers”. In: *Energy and Environmental Science* 9.11 (2016), pp. 3456–3463. ISSN: 17545706. DOI: 10.1039/c6ee02100j.

[62] Kilian B. Lohmann et al. “Control over Crystal Size in Vapor Deposited Metal-Halide Perovskite Films”. In: *ACS Energy Letters* (2020), pp. 710–717. ISSN: 2380-8195. DOI: 10.1021/acsenergylett.0c00183. URL: https://pubs.acs.org/doi/10.1021/acsenergylett.0c00183.

[63] Guijun Li et al. “Low cost, high throughput and centimeter-scale fabrication of efficient hybrid perovskite solar cells by closed space vapor transport”. In: *Physica Status Solidi - Rapid Research Letters* 10.2 (2016), pp. 153–157. ISSN: 18626270. DOI: 10.1002/pssr.201510386.

[64] Giulia Longo et al. “Fully Vacuum-Processed Wide Band Gap Mixed-Halide Perovskite Solar Cells”. In: *ACS Energy Letters* 3.1 (Jan. 2018), pp. 214–219. ISSN: 2380-8195. DOI: 10.1021/acsenergylett.7b01217.

[65] L. Gil-Escrig et al. “Vacuum Deposited Triple-Cation Mixed-Halide Perovskite Solar Cells”. In: *Advanced Energy Materials* 1703506 (2018), p. 1703506. ISSN: 16146832. DOI: 10.1002/aenm.201703506.

[66] Jérémie Werner et al. “Complex Refractive Indices of Cesium-Formamidinium-Based Mixed-Halide Perovskites with Optical Band Gaps from 1.5 to 1.8 eV”. In: *ACS Energy Letters* 3.3 (2018), pp. 742–747. ISSN: 23808195. DOI: 10.1021/acsenergylett.8b00089.

[67] J.-W. Lee et al. “Formamidinium and Cesium Hybridization for Photo- and Moisture-Stable Perovskite Solar Cell”. In: *Advanced Energy Materials* 5.20 (Oct. 2015), p. 1501310. ISSN: 16146832. DOI: 10.1002/aenm.201501310.

[68] Matthew R. Leyden, Yan Jiang, and Yabing Qi. “Chemical vapor deposition grown formamidinium perovskite solar modules with high steady state power and thermal stability”. In: *Journal of Materials Chemistry A* 4.34 (2016), pp. 13125–13132. ISSN: 2050-7488. DOI: 10.1039/C6TA04267H. URL: http://xlink.rsc.org/?DOI=C6TA04267H.

[69] Yicheng Zhao et al. “Perovskite seeding growth of formamidinium-lead-iodide-based perovskites for efficient and stable solar cells”. In: *Nature Communications* 9.1 (2018), pp. 1–10. ISSN: 20411723. DOI: 10.1038/s41467-018-04029-7. URL: http://dx.doi.org/10.1038/s41467-018-04029-7.

[70] Herlina Arianita Dewi et al. “Excellent Intrinsic Long-Term Thermal Stability of Co-Evaporated MAPbI3 Solar Cells at 85 °C”. In: *Advanced Functional Materials* 31.22 (2021), pp. 1–9. ISSN: 16163028. DOI: 10.1002/adfm.202100557.

[71] Jia Li et al. “Highly Efficient Thermally Co-evaporated Perovskite Solar Cells and Mini-modules”. In: *Joule* 4.5 (2020), pp. 1035–1053. ISSN: 25424351. DOI: 10.1016/j.joule.2020.03.005. URL: https://doi.org/10.1016/j.joule.2020.03.005.

[72] Tetsuhiko Miyadera et al. “Highly Controlled Codeposition Rate of Organolead Halide Perovskite by Laser Evaporation Method”. In: *ACS Applied Materials and Interfaces* 8.39 (2016), pp. 26013–26018. ISSN: 19448252. DOI: 10.1021/acsami.6b07837.

[73] Hao Hu et al. “Vapour-based processing of hole-conductor-free CH3NH 3PbI3 perovskite/C60 fullerene planar solar cells”. In: *RSC Advances* 4.55 (2014), pp. 28964–28967. ISSN: 20462069. DOI: 10.1039/c4ra03820g.

[74] Woojun Yoon et al. “Vapor deposition of organic-inorganic hybrid perovskite thin-films for photovoltaic applications”. In: *2014 IEEE 40th Photovoltaic Specialist Conference, PVSC 2014* (2014), pp. 1577–1580. DOI: 10.1109/PVSC.2014.6925219.

[75] Chang-Wen Chen et al. “Efficient and Uniform Planar-Type Perovskite Solar Cells by Simple Sequential Vacuum Deposition”. In: *Advanced Materials* 26.38 (2014), pp. 6647–6652. ISSN: 0935-9648. DOI: 10.1002/adma.201402461.

[76] Jay B. Patel et al. “Formation Dynamics of CH3NH3PbI3 Perovskite Following Two-Step Layer Deposition”. In: *Journal of Physical Chemistry Letters* 7.1 (2016), pp. 96–102. ISSN: 19487185. DOI: 10.1021/acs.jpclett.5b02495.

[77] Sheng-Yi Hsiao et al. “Efficient All-Vacuum Deposited Perovskite Solar Cells by Controlling Reagent Partial Pressure in High Vacuum”. In: *Advanced Materials* 28.32 (Aug. 2016), pp. 7013–7019. ISSN: 09359648. DOI: 10.1002/adma.201601505.

[78] Dong Yang et al. “Alternating precursor layer deposition for highly stable perovskite films towards efficient solar cells using vacuum deposition”. In: *Journal of Materials Chemistry A* 3.18 (2015), pp. 9401–9405. ISSN: 2050-7488. DOI: 10.1039/C5TA01824B.

[79] Annie Ng et al. “Efficiency enhancement by defect engineering in perovskite photovoltaic cells prepared using evaporated PbI 2 /CH 3 NH 3 I multilayers”. In: *Journal of Materials Chemistry A* 3.17 (2015), pp. 9223–9231. ISSN: 2050-7488. DOI: 10.1039/C4TA05070C.

[80] Qiang Guo et al. “The growth of a CH3NH3PbI3 thin film using simplified close space sublimation for efficient and large dimensional perovskite solar cells”. In: *Energy and Environmental Science* 9.4 (2016), pp. 1486–1494. ISSN: 17545706. DOI: 10.1039/c5ee03620h.

[81] M. Higgins et al. “Solvent-free and large area compatible deposition of methylammonium lead bromide perovskite by close space sublimation and its application in PIN diodes”. In: *Thin Solid Films* 692.November (2019), p. 137585. ISSN: 00406090. DOI: 10.1016/j.tsf.2019.137585. URL: https://doi.org/10.1016/j.tsf.2019.137585.

[82] Xiaomin Chen et al. “Large-area, high-quality organic–inorganic hybrid perovskite thin films via a controlled vapor–solid reaction”. In: *Journal of Materials Chemistry A* 4.23 (2016), pp. 9124–9132. ISSN: 2050-7488. DOI: 10.1039/C6TA03180C.

[83] Kejie Feng et al. “Preparation of CH3NH3PbI3 thin films for solar cells via Vapor Transfer Method”. In: *Journal of Energy Chemistry* 27.5 (2018), pp. 1386–1389. ISSN: 20954956. DOI: 10.1016/j.jechem.2018.01.007. URL: https://doi.org/10.1016/j.jechem.2018.01.007.

[84] Ranjith Kottokkaran et al. “Highly reproducible vapor deposition technique, device physics and structural instability of perovskite solar cells”. In: *2015 IEEE 42nd Photovoltaic Specialist Conference, PVSC 2015* (2015), pp. 1–4. DOI: 10.1109/PVSC.2015.7355612.

[85] Guoqing Tong et al. “Mixed cation perovskite solar cells by stack-sequence chemical vapor deposition with self-passivation and gradient absorption layer”. In: *Nano Energy* 48.March (2018), pp. 536–542. ISSN: 22112855. DOI: 10.1016/j.nanoen.2018.04.012. URL: https://doi.org/10.1016/j.nanoen.2018.04.012.

[86] Won Gyu Choi et al. “Organic-cation-mixed (FA,MA)PbI3 through sequential vapor growth for planar perovskite solar cells”. In: *Solar Energy* 178.December 2018 (2019), pp. 56–60. ISSN: 0038092X. DOI: 10.1016/j.solener.2018.11.061. URL: https://doi.org/10.1016/j.solener.2018.11.061.

[87] Xuejie Zhu et al. “Superior stability for perovskite solar cells with 20% efficiency using vacuum co-evaporation”. In: *Nanoscale* 9.34 (2017), pp. 12316–12323. ISSN: 2040-3364. DOI: 10.1039/C7NR04501H.

[88] D B Mitzi, M T Prikas, and K Chondroudis. “Thin Film Deposition of Organic-Inorganic Hybrid Materials Using a Single Source Thermal Ablation Technique”. In: *Chemistry of Materials* 11.3 (Mar. 1999), pp. 542–544. ISSN: 0897-4756. DOI: 10.1021/cm9811139.

[89] Giulia Longo et al. “Perovskite solar cells prepared by flash evaporation”. In: *Chemical Communications* 51.34 (2015), pp. 7376–7378. ISSN: 1359-7345. DOI: 10.1039/C5CC01103E.

[90] Yanglin Wu et al. “Grain growth study of perovskite thin films prepared by flash evaporation and its effect on solar cell performance”. In: *RSC Advances* 6.54 (2016), pp. 48851–48857. DOI: 10.1039/c6ra07549e.

[91] Ping Fan et al. “High-performance perovskite CH3 NH3 PbI3 thin films for solar cells prepared by single-source physical vapour deposition”. In: *Scientific Reports* 6.March (2016), pp. 1–9. ISSN: 20452322. DOI: 10.1038/srep29910.

[92] Huabin Lan et al. “Microstructural and optical properties of HC(NH2)2PbI3 thin films prepared by single source thermal evaporation”. In: *Journal of Materials Science: Materials in Electronics* 29.3 (2018), pp. 2267–2274. ISSN: 1573482X. DOI: 10.1007/s10854-017-8142-5. URL: http://dx.doi.org/10.1007/s10854-017-8142-5.

[93] Loredana Protesescu et al. “Low-Cost Synthesis of Highly Luminescent Colloidal Lead Halide Perovskite Nanocrystals by Wet Ball Milling”. In: *ACS Applied Nano Materials* 1.3 (2018), pp. 1300–1308. ISSN: 25740970. DOI: 10.1021/acsanm.8b00038.

[94] Haoming Wei et al. “Flash-evaporation printing methodology for perovskite thin films”. In: *NPG Asia Materials* 9.6 (2017), e395–e395. ISSN: 1884-4049. DOI: 10.1038/am.2017.91.

[95] Francisco Palazon et al. “Mechanochemical synthesis of inorganic halide perovskites: Evolution of phase-purity, morphology, and photoluminescence”. In: *Journal of Materials Chemistry C* 7.37 (2019), pp. 11406–11410. ISSN: 20507526. DOI: 10.1039/c9tc03778k.

[96] Carlos Alberto López et al. “Crystal structure features of CH3NH3PbI3-: XBrx hybrid perovskites prepared by ball milling: A route to more stable materials”. In: *CrystEngComm* 22.4 (2020), pp. 767–775. ISSN: 14668033. DOI: 10.1039/c9ce01461f.

[97] Yousra El Ajjouri et al. “Single-Source Vacuum Deposition of Mechanosynthesized Inorganic Halide Perovskites”. In: *Chemistry of Materials* 30.21 (2018), pp. 7423–7427. ISSN: 15205002. DOI: 10.1021/acs.chemmater.8b03352.

[98] Matthew J. Crane et al. “Single-Source Vapor Deposition of Quantum-Cutting Yb3+:CsPb(Cl1-xBrx)3 and Other Complex Metal-Halide Perovskites”. In: *ACS Applied Energy Materials* 2.6 (2019), pp. 4560–4565. ISSN: 25740962. DOI: 10.1021/acsaem.9b00910.

[99] Sara Bonomi et al. “Novel Physical Vapor Deposition Approach to Hybrid Perovskites: Growth of MAPbI3 Thin Films by RF-Magnetron Sputtering”. In: *Scientific Reports* 8.1 (2018), pp. 1–8. ISSN: 20452322. DOI: 10.1038/s41598-018-33760-w. URL: http://dx.doi.org/10.1038/s41598-018-33760-w.

[100] Claudia Borri et al. “First proof-of-principle of inorganic lead halide perovskites deposition by magnetron-sputtering”. In: *Nanomaterials* 10.1 (2020), pp. 1–11. ISSN: 20794991. DOI: 10.3390/nano10010060.

[101] Umesh Bansode and Satishchandra Ogale. “On-axis pulsed laser deposition of hybrid perovskite films for solar cell and broadband photo-sensor applications”. In: *Journal of Applied Physics* 121.13 (2017). ISSN: 10897550. DOI: 10.1063/1.4979865. URL: http://dx.doi.org/10.1063/1.4979865.

[102] Vivien M. Kiyek et al. “Single-Source, Solvent-Free, Room Temperature Deposition of Black γ-CsSnI 3 Films”. In: *Advanced Materials Interfaces* 7.11 (Apr. 2020), p. 2000162. ISSN: 2196-7350. DOI: 10.1002/admi.202000162.

[103] Tatiana Soto-Montero et al. “Single-Source Vapor-Deposition of MA 1–x FA x PbI 3 Perovskite Absorbers for Solar Cells”. In: *Advanced Functional Materials* (Mar. 2023). ISSN: 1616-301X. DOI: 10.1002/adfm.202300588. URL: https://onlinelibrary.wiley.com/doi/10.1002/adfm.202300588.

[104] Wiley A. Dunlap-Shohl et al. “MAPbI3 Solar Cells with Absorber Deposited by Resonant Infrared Matrix-Assisted Pulsed Laser Evaporation”. In: *ACS Energy Letters* 3.2 (2018), pp. 270–275. ISSN: 23808195. DOI: 10.1021/acsenergylett.7b01144.

[105] Meiqian Tai et al. “Efficient Inorganic Cesium Lead Mixed-Halide Perovskite Solar Cells Prepared by Flash-Evaporation Printing”. In: *Energy Technology* 7.8 (Mar. 2019), ente.201800986. ISSN: 2194-4288. DOI: 10.1002/ente.201800986.

[106] B.E. McCandless, R.W. Birkmire, and W.A. Buchanan. “Vapor transport deposition of cadmium telluride films”. In: *Conference Record of the Twenty-Ninth IEEE Photovoltaic Specialists Conference, 2002*. IEEE, 2002, pp. 547–550. ISBN: 0-7803-7471-1. DOI: 10.1109/PVSC.2002.1190623.

[107] L L C R.C. Powell: First Solar and Ohio Perrysburg. “Research Leading to High-Throughput Manufacturing of Thin-Film CdTe PV Modules: Annual Subcontract Report, September 2004–September 2005”. In: April (2006), pp. 1–29. URL: http://www.nrel.gov/docs/fy06osti/39669.pdf%5Cnpapers3://publication/uuid/34833AC1-BF82-4BFB-8953-34F65D3EAF37.

[108] Richard R. Lunt et al. “Organic vapor phase deposition for the growth of large area organic electronic devices”. In: *Applied Physics Letters* 95.23 (2009), pp. 2007–2010. ISSN: 00036951. DOI: 10.1063/1.3271797.

[109] Mohammad Mahdi Tavakoli et al. “Fabrication of efficient planar perovskite solar cells using a one-step chemical vapor deposition method”. In: *Scientific Reports* 5.1 (Sept. 2015), p. 14083. ISSN: 2045-2322. DOI: 10.1038/srep14083. URL: https://www.nature.com/articles/srep14083.

[110] Geemin Kim et al. “Perovskite Pattern Formation by Chemical Vapor Deposition Using Photolithographically Defined Templates”. In: *Chemistry of Materials* 31.19 (2019), pp. 8212–8221. ISSN: 15205002. DOI: 10.1021/acs.chemmater.9b03155.

[111] Siphelo Ngqoloda et al. “Air-Stable Hybrid Perovskite Solar Cell by Sequential Vapor Deposition in a Single Reactor”. In: *ACS Applied Energy Materials* (2020). ISSN: 25740962. DOI: 10.1021/acsaem.9b01925.

[112] Catherine P. Clark et al. “Carrier-gas assisted vapor deposition for highly tunable morphology of halide perovskite thin films”. In: *Sustainable Energy and Fuels* 3.9 (2019), pp. 2447–2455. ISSN: 23984902. DOI: 10.1039/c9se00200f.

[113] Max Shtein et al. “Material transport regimes and mechanisms for growth of molecular organic thin films using low-pressure organic vapor phase deposition”. In: *Journal of Applied Physics* 89.2 (2001), pp. 1470–1476. ISSN: 00218979. DOI: 10.1063/1.1332419.

[114] Maximilian T. Hoerantner et al. “High-Speed Vapor Transport Deposition of Perovskite Thin Films”. In: *ACS Applied Materials & Interfaces* 11.36 (2019), pp. 32928–32936. ISSN: 1944-8244. DOI: 10.1021/acsami.9b07651.

[115] S. Sanders et al. “Chemical Vapor Deposition of Organic-Inorganic Bismuth-Based Perovskite Films for Solar Cell Application”. In: *Scientific Reports* 9.1 (2019), pp. 1–8. ISSN: 20452322. DOI: 10.1038/s41598-019-46199-4.

[116] Kevin A. Bush, Maximilian Tobias Hoerantner, and Tomas Leijtens. *Patent Application Publication US 2020/0328077 A1*. 2020.

[117] A. Shah. *Thin-film silicon solar cells*. EPFL press, 2010.

[118] Hagen Klauk. *Organic Electronics: Materials, Manufacturing and Applications*. 2006, pp. 1–428. ISBN: 3527312641. DOI: 10.1002/3527608753.

[119] S. Sanders et al. “Showerhead-Assisted Chemical Vapor Deposition of Perovskite Films for Solar Cell Application”. In: *MRS Advances* (2020). DOI: 10.1557/adv.2020.126.

[120] M.R. Matthew R. Leyden et al. “High performance perovskite solar cells by hybrid chemical vapor deposition”. In: *Journal of Materials Chemistry A* 2.44 (2014), pp. 18742–18745. ISSN: 20507496. DOI: 10.1039/c4ta04385e.

[121] Thierry Moser et al. “Revealing the perovskite formation kinetics during chemical vapour deposition”. In: *Journal of Materials Chemistry A* (2020). ISSN: 2050-7488. DOI: 10.1039/d0ta04501b.

[122] Matthew R. Leyden et al. “Large formamidinium lead trihalide perovskite solar cells using chemical vapor deposition with high reproducibility and tunable chlorine concentrations”. In: *Journal of Materials Chemistry A* 3.31 (2015), pp. 16097–16103. ISSN: 20507496. DOI: 10.1039/c5ta03577e.

[123] Annie Ng et al. “Crystal Engineering for Low Defect Density and High Efficiency Hybrid Chemical Vapor Deposition Grown Perovskite Solar Cells”. In: *ACS Applied Materials and Interfaces* 8.48 (2016), pp. 32805–32814. ISSN: 19448252. DOI: 10.1021/acsami.6b07513.

[124] Jun Yin et al. “Vapor-assisted crystallization control toward high performance perovskite photovoltaics with over 18% efficiency in the ambient atmosphere”. In: *J. Mater. Chem. A* 4.34 (2016), pp. 13203–13210. ISSN: 20507496. DOI: 10.1039/c6ta04465d.

[125] Lidón Gil-Escrig et al. “Efficient Wide-Bandgap Mixed-Cation and Mixed-Halide Perovskite Solar Cells by Vacuum Deposition”. In: *ACS Energy Letters* 6.2 (Feb. 2021), pp. 827–836. ISSN: 2380-8195. DOI: 10.1021/acsenergylett.0c02445. URL: https://pubs.acs.org/doi/10.1021/acsenergylett.0c02445.

[126] Ivan Turkevych et al. “Strategic advantages of reactive polyiodide melts for scalable perovskite photovoltaics”. In: *Nature Nanotechnology* (2018). ISSN: 1748-3387. DOI: 10.1038/s41565-018-0304-y.

[127] Zhongmin Zhou et al. “Methylamine-Gas-Induced Defect-Healing Behavior of CH<inf>3</inf>NH<inf>3</inf> Thin Films for Perovskite Solar Cells”. In: *Angewandte Chemie - International Edition* 54.33 (2015), pp. 9705–9709. ISSN: 15213773. DOI: 10.1002/anie.201504379.

[128] Sonia R. Raga, Luis K. Ono, and Yabing Qi. “Rapid perovskite formation by CH3NH2 gas-induced intercalation and reaction of PbI2”. In: *Journal of Materials Chemistry A* 4.7 (2016), pp. 2494–2500. ISSN: 20507496. DOI: 10.1039/c5ta10055k.

[129] Brandon R. Sutherland et al. “Perovskite thin films via atomic layer deposition”. In: *Advanced Materials* 27.1 (2015), pp. 53–58. ISSN: 15214095. DOI: 10.1002/adma.201403965.

[130] Georgi Popov et al. “Atomic Layer Deposition of PbI 2 Thin Films”. In: *Chemistry of Materials* 31.3 (2019), pp. 1101–1109. ISSN: 15205002. DOI: 10.1021/acs.chemmater.8b04969.

[131] Hiroyuki Kanda et al. “Analysis of Sputtering Damage on I-V Curves for Perovskite Solar Cells and Simulation with Reversed Diode Model”. In: *Journal of Physical Chemistry C* 120.50 (2016), pp. 28441–28447. ISSN: 19327455. DOI: 10.1021/acs.jpcc.6b09219.

[132] José Maria Clemente Da Silva Filho, Viktor A. Ermakov, and Francisco Chagas Marques. “Perovskite Thin Film Synthesised from Sputtered Lead Sulphide”. In: *Scientific Reports* 8.1 (2018), pp. 1–8. ISSN: 20452322. DOI: 10.1038/s41598-018-19746-8.

[133] Jae Keun Hwang et al. “Conformal perovskite films on 100 cm2 textured silicon surface using two-step vacuum process”. In: *Thin Solid Films* 693.April 2019 (2020), p. 137694. ISSN: 00406090. DOI: 10.1016/j.tsf.2019.137694. URL: https://doi.org/10.1016/j.tsf.2019.137694.

[134] Chongwen Li et al. “Methylamine Gas Based Synthesis and Healing Process Toward Upscaling of Perovskite Solar Cells: Progress and Perspective”. In: *Solar RRL* 1.9 (2017), p. 1700076. ISSN: 2367198X. DOI: 10.1002/solr.201700076.

[135] Yuanyuan Zhou and Nitin P. Padture. “Gas-Induced Formation/Transformation of Organic–Inorganic Halide Perovskites”. In: *ACS Energy Letters* 2.9 (Sept. 2017), pp. 2166–2176. ISSN: 2380-8195. DOI: 10.1021/acsenergylett.7b00667.

[136] Sonia R. Raga et al. “Application of Methylamine Gas in Fabricating Organic–Inorganic Hybrid Perovskite Solar Cells”. In: *Energy Technology* 5.10 (2017), pp. 1750–1761. ISSN: 21944296. DOI: 10.1002/ente.201700423.

[137] Shuping Pang et al. “Transformative Evolution of Organolead Triiodide Perovskite Thin Films from Strong Room-Temperature Solid-Gas Interaction between HPbI3-CH3NH2Precursor Pair”. In: *Journal of the American Chemical Society* 138.3 (2016), pp. 750–753. ISSN: 15205126. DOI: 10.1021/jacs.5b11824.

[138] Yi Zhang et al. “Trash into Treasure: δ-FAPbI3 Polymorph Stabilized MAPbI3 Perovskite with Power Conversion Efficiency beyond 21%”. In: *Advanced Materials* 30.22 (2018), pp. 1–8. ISSN: 15214095. DOI: 10.1002/adma.201707143.

[139] Mingzhu Long et al. “Textured CH3NH3PbI3 thin film with enhanced stability for high performance perovskite solar cells”. In: *Nano Energy* 33.December 2016 (Mar. 2017), pp. 485–496. ISSN: 22112855. DOI: 10.1016/j.nanoen.2017.02.002.

[140] Weijun Ke et al. “Myths and reality of HPbI3 in halide perovskite solar cells”. In: *Nature Communications* 9.1 (2018), p. 4785. ISSN: 2041-1723. DOI: 10.1038/s41467-018-07204-y.

[141] Zonghao Liu et al. “Gas-solid reaction based over one-micrometer thick stable perovskite films for efficient solar cells and modules”. In: *Nature Communications* 9.1 (Dec. 2018), p. 3880. ISSN: 2041-1723. DOI: 10.1038/s41467-018-06317-8.

[142] Claudiu Mortan et al. “Preparation of methylammonium lead iodide (CH3NH3PbI3) thin film perovskite solar cells by chemical vapor deposition using methylamine gas (CH3NH2) and hydrogen iodide gas”. In: *Energy Science and Engineering* April (2020), pp. 1–9. ISSN: 20500505. DOI: 10.1002/ese3.734.

[143] Yuanyuan Zhou et al. “Exceptional Morphology-preserving evolution of formamidinium lead triiodide perovskite thin films via organic-cation displacement”. In: *Journal of the American Chemical Society* 138.17 (2016), pp. 5535–5538. ISSN: 15205126. DOI: 10.1021/jacs.6b02787.

[144] Guijun Li et al. “Reversible Anion Exchange Reaction in Solid Halide Perovskites and Its Implication in Photovoltaics”. In: *Journal of Physical Chemistry C* 119.48 (2015), pp. 26883–26888. ISSN: 19327455. DOI: 10.1021/acs.jpcc.5b09300.

[145] Haizhou Lu et al. “Vapor-assisted deposition of highly efficient, stable black-phase FAPbI 3 perovskite solar cells”. In: *Science* 370.6512 (Oct. 2020). ISSN: 0036-8075. DOI: 10.1126/science.abb8985. URL: http://www.ncbi.nlm.nih.gov/pubmed/33004488%20https://www.science.org/doi/10.1126/science.abb8985.

[146] Leon I. Maissel. *Handbook of thin film technology*. Ed. by New York [etc.] : McGraw-Hill. 1983.

[147] Brian Lewis and J C. Anderson. *Nucleation and growth of thin films*. Ed. by New York a.o. : Academic Press. 1978, p. 504.

[148] G. Zinsmeister. “Theory of thin film condensation. Part b: Solution of the simplified condensation equation”. In: *Thin Solid Films* 2.5-6 (1968), pp. 497–507. ISSN: 00406090. DOI: 10.1016/0040-6090(68)90063-1.

[149] D. Kashchiev. “Solution of the non-steady state problem in nucleation kinetics”. In: *Surface Science* 14.1 (1969), pp. 209–220. ISSN: 00396028. DOI: 10.1016/0039-6028(69)90055-7.

[150] K. F. Kelton, A. L. Greer, and C. V. Thompson. “Transient nucleation in condensed systems”. In: *The Journal of Chemical Physics* 79.12 (1983), pp. 6261–6276. ISSN: 00219606. DOI: 10.1063/1.445731.

[151] A. S. Edelstein and R. C. Cammaratra. “Nanomaterials: Synthesis, Properties, and Applications”. In: *Institute of Physics Publishing* (Oct. 1996). URL: http://doi.wiley.com/10.1002/adma.19970091219%20http://www.tandfonline.com/doi/abs/10.1080/10426914.2012.689458.

[152] Paramvir Ahlawat et al. “Atomistic Mechanism of the Nucleation of Methylammonium Lead Iodide Perovskite from Solution”. In: *Chemistry of Materials* 32.1 (2020), pp. 529–536. ISSN: 15205002. DOI: 10.1021/acs.chemmater.9b04259.

[153] Cao Zexian. *Thin Film Growth: Physics, Materials Science and Applications*. 2011. ISBN: 978-1-84569-736-5.

[154] John A. Thornton. “Structure-Zone Models Of Thin Films”. In: *Modeling of Optical Thin Films* 0821.February 1988 (1988), p. 95. DOI: 10.1117/12.941846.

[155] R. Messier, A.P. Giri, and R.A. Roy. “Revised structure zone model for thin film physical structure”. In: *Journal of Vacuum Science & Technology A: Vacuum, Surfaces, and Films* 2.2 (1984), p. 500. ISSN: 07342101. DOI: 10.1116/1.572604.

[156] I. Petrov et al. “Microstructural evolution during film growth”. In: *Journal of Vacuum Science & Technology A: Vacuum, Surfaces, and Films* 21.5 (2003), S117. ISSN: 07342101. DOI: 10.1116/1.1601610.

[157] L. Fanni et al. “Increasing Polycrystalline Zinc Oxide Grain Size by Control of Film Preferential Orientation”. In: *Crystal Growth and Design* 15.12 (2015), pp. 5886–5891. ISSN: 15287505. DOI: 10.1021/acs.cgd.5b01299.

[158] C.V. Thompson. “Structure Evolution During Processing of Polycrystalline Films”. In: *Annual Review of Materials Research* 30 (2000), pp. 159–190.

[159] Chongqiu Yang, Xiaobiao Shan, and Tao Xie. “Hysteresis Passivation in Planar Perovskite Solar Cells Utilizing Facile Chemical Vapor Deposition Process and PCBM Interlayer”. In: *Energies* 12.23 (Nov. 2019), p. 4508. ISSN: 1996-1073. DOI: 10.3390/en12234508. URL: https://www.mdpi.com/1996-1073/12/23/4508.

[160] Rui Zhu et al. “Numerical Simulation of Vapor Deposition Process of Perovskite Solar Cells: The Influence of Methylammonium Iodide Vapor Flow to Perovskite Growth”. In: *Journal of Solar Energy Engineering* 143.1 (2021), pp. 1–9. ISSN: 0199-6231. DOI: 10.1115/1.4047296.

[161] Chongqiu Yang, Terrence Simon, and Tianhong Cui. “Numerical simulation and analysis of hybrid physical-chemical vapor deposition to grow uniform perovskite MAPbI3”. In: *Journal of Applied Physics* 121.14 (2017). ISSN: 10897550. DOI: 10.1063/1.4980116. URL: http://dx.doi.org/10.1063/1.4980116.

[162] Beom Soo Kim et al. “Deposition Kinetics and Compositional Control of Vacuum-Processed CH3NH3PbI3Perovskite”. In: *Journal of Physical Chemistry Letters* 11.16 (2020), pp. 6852–6859. ISSN: 19487185. DOI: 10.1021/acs.jpclett.0c01995.

[163] Martin J. Bækbo et al. “Deposition of methylammonium iodide via evaporation – combined kinetic and mass spectrometric study”. In: *RSC Advances* 8.52 (2018), pp. 29899–29908. ISSN: 2046-2069. DOI: 10.1039/C8RA04851G.

[164] David P. Nenon et al. “Structural and chemical evolution of methylammonium lead halide perovskites during thermal processing from solution”. In: *Energy and Environmental Science* 9.6 (2016), pp. 2072–2082. ISSN: 17545706. DOI: 10.1039/c6ee01047d.

[165] Emilio J. Juarez-Perez et al. “Thermal degradation of CH3NH3PbI3perovskite into NH3 and CH3I gases observed by coupled thermogravimetry-mass spectrometry analysis”. In: *Energy and Environmental Science* 9.11 (2016), pp. 3406–3410. ISSN: 17545706. DOI: 10.1039/c6ee02016j.

[166] Alice E. Williams et al. “Perovskite processing for photovoltaics: A spectro-thermal evaluation”. In: *Journal of Materials Chemistry A* 2.45 (2014), pp. 19338–19346. ISSN: 20507496. DOI: 10.1039/c4ta04725g.

[167] Emilio J. Juarez-Perez, Luis K. Ono, and Yabing Qi. “Thermal degradation of formamidinium based lead halide perovskites into sym -triazine and hydrogen cyanide observed by coupled thermogravimetry-mass spectrometry analysis”. In: *Journal of Materials Chemistry A* 7.28 (2019), pp. 16912–16919. ISSN: 2050-7488. DOI: 10.1039/C9TA06058H. URL: http://xlink.rsc.org/?DOI=C9TA06058H.

[168] Sagar Motilal Jain et al. “Vapor phase conversion of PbI2 to CH3NH3PbI3: Spectroscopic evidence for formation of an intermediate phase”. In: *Journal of Materials Chemistry A* 4.7 (2016), pp. 2630–2642. ISSN: 20507496. DOI: 10.1039/c5ta08745g.

[169] Lijia Liu et al. “Tracking the formation of methylammonium lead triiodide perovskite”. In: *Applied Physics Letters* 107.6 (Aug. 2015). ISSN: 0003-6951. DOI: 10.1063/1.4928662. URL: http://dx.doi.org/10.1063/1.4928662%20https://pubs.aip.org/apl/article/107/6/061904/29336/Tracking-the-formation-of-methylammonium-lead.

[170] Weidong Xu et al. “Dissociation of methylammonium cations in hybrid organic-inorganic perovskite solar cells”. In: *Nano Letters* 16.7 (2016), pp. 4720–4725. ISSN: 15306992. DOI: 10.1021/acs.nanolett.6b02307.

[171] Selina Olthof and Klaus Meerholz. “Substrate-dependent electronic structure and film formation of MAPbI 3 perovskites”. In: *Scientific Reports* 7.December 2016 (2017), pp. 1–10. ISSN: 20452322. DOI: 10.1038/srep40267.

[172] Sampreetha Thampy et al. “Bulk and interfacial decomposition of formamidinium iodide (HC(NH 2) 2 I) in contact with metal oxide”. In: *Materials Advances* 1.9 (2020), pp. 3349–3357. ISSN: 2633-5409. DOI: 10.1039/D0MA00624F. URL: http://xlink.rsc.org/?DOI=D0MA00624F.

[173] Adrian Llanos, Emmanuel S. Thibau, and Zheng-Hong Lu. "Abnormal thin film structures in vapor-phase deposited methylammonium lead iodide perovskite". In: *Journal of Vacuum Science & Technology A: Vacuum, Surfaces, and Films* 34.6 (2016), p. 060601. ISSN: 0734-2101. DOI: 10.1116/1.4963071. URL: http://dx.doi.org/10.1116/1.4963071.

[174] Lidón Gil-Escrig et al. "Efficient Vacuum-Deposited Perovskite Solar Cells with Stable Cubic FA1–xMAxPbI3". In: *ACS Energy Letters* 7 (2020), pp. 3053–3061. ISSN: 2380-8195. DOI: 10.1021/acsenergylett.0c01473. URL: https://pubs.acs.org/doi/10.1021/acsenergylett.0c01473.

[175] Hong Zhang et al. "A Smooth CH3NH3PbI3 Film via a New Approach for Forming the PbI2 Nanostructure Together with Strategically High CH3NH3I Concentration for High Efficient Planar-Heterojunction Solar Cells". In: *Advanced Energy Materials* 5.23 (2015), pp. 1–10. ISSN: 16146840. DOI: 10.1002/aenm.201501354.

[176] Kai Sun et al. "Lewis Acid-Base Interaction-Induced Porous PbI 2 Film for Efficient Planar Perovskite Solar Cells". In: *ACS Applied Energy Materials* 1.5 (2018), pp. 2114–2122. ISSN: 25740962. DOI: 10.1021/acsaem.8b00160.

[177] Julian S.W. Godding et al. "Oxidative Passivation of Metal Halide Perovskites". In: *Joule* 3.11 (2019), pp. 1–16. ISSN: 25424351. DOI: 10.1016/j.joule.2019.08.006.

[178] Rodrigo Szostak et al. "Exploring the formation of formamidinium-based hybrid perovskites by antisolvent methods: In situ GIWAXS measurements during spin coating". In: *Sustainable Energy and Fuels* 3.9 (2019), pp. 2287–2297. ISSN: 23984902. DOI: 10.1039/c9se00306a.

[179] Jingbi You et al. "Moisture assisted perovskite film growth for high performance solar cells". In: *Applied Physics Letters* 105.18 (2014). ISSN: 00036951. DOI: 10.1063/1.4901510. URL: http://dx.doi.org/10.1063/1.4901510.

[180] Hao Gao et al. "Nucleation and crystal growth of organic-inorganic lead halide perovskites under different relative humidity". In: *ACS Applied Materials and Interfaces* 7.17 (2015), pp. 9110–9117. ISSN: 19448252. DOI: 10.1021/acsami.5b00895.

[181] Xueyan Wang et al. "Improving efficiency of planar hybrid CH 3 NH 3 PbI 3- x Cl x perovskite solar cells by isopropanol solvent treatment". In: *Organic Electronics* 24 (Sept. 2015), pp. 205–211. ISSN: 15661199. DOI: 10.1016/j.orgel.2015.05.043. URL: http://dx.doi.org/10.1016/j.orgel.2015.05.043%20https://linkinghub.elsevier.com/retrieve/pii/S1566119915002402.

[182] Atsushi Wakamiya et al. "Reproducible fabrication of efficient perovskite-based solar cells: X-ray crystallographic studies on the formation of CH3NH 3PbI3 layers". In: *Chemistry Letters* 43.5 (2014), pp. 711–713. ISSN: 13480715. DOI: 10.1246/cl.140074.

[183] Fan Fu et al. "I2 vapor-induced degradation of formamidinium lead iodide based perovskite solar cells under heat-light soaking conditions". In: *Energy and Environmental Science* 12.10 (2019), pp. 3074–3088. ISSN: 17545706. DOI: 10.1039/c9ee02043h.

[184] Paul Pistor et al. “Monitoring the phase formation of coevaporated lead halide perovskite thin films by in situ x-ray diffraction”. In: *Journal of Physical Chemistry Letters* 5.19 (2014), pp. 3308–3312. ISSN: 19487185. DOI: 10.1021/jz5017312.

[185] Vladimir Held et al. “Evolution of Structure and Optoelectronic Properties during Halide Perovskite Vapor Deposition”. In: *Journal of Physical Chemistry Letters* 13.51 (2022), pp. 11905–11912. ISSN: 19487185. DOI: 10.1021/acs.jpclett.2c03422.

[186] Minchao Qin, Pok Fung Chan, and Xinhui Lu. “A Systematic Review of Metal Halide Perovskite Crystallization and Film Formation Mechanism Unveiled by In Situ GIWAXS”. In: *Advanced Materials* 33.51 (Dec. 2021), p. 2105290. ISSN: 0935-9648. DOI: 10.1002/adma.202105290. URL: https://onlinelibrary.wiley.com/doi/10.1002/adma.202105290.

[187] Florent Sahli et al. “Fully textured monolithic perovskite/silicon tandem solar cells with 25.2% power conversion efficiency”. In: *Nature Materials* 17.9 (2018), pp. 820–826. ISSN: 14764660. DOI: 10.1038/s41563-018-0115-4.

[188] Ana M. Igual-Muñoz et al. “Room-Temperature Vacuum Deposition of CsPbI2Br Perovskite Films from Multiple Sources and Mixed Halide Precursors”. In: *Chemistry of Materials* 32.19 (2020), pp. 8641–8652. ISSN: 15205002. DOI: 10.1021/acs.chemmater.0c03038.

[189] Nathan Rodkey et al. “Pulsed Laser Deposition of Cs2AgBiBr6: From Mechanochemically Synthesized Powders to Dry, Single-Step Deposition”. In: *Chemistry of Materials* 33.18 (2021), pp. 7417–7422. ISSN: 15205002. DOI: 10.1021/acs.chemmater.1c02054.

[190] Loredana Protesescu et al. “Low-Cost Synthesis of Highly Luminescent Colloidal Lead Halide Perovskite Nanocrystals by Wet Ball Milling”. In: *ACS Applied Nano Materials* 1.3 (2018), pp. 1300–1308. ISSN: 25740970. DOI: 10.1021/acsanm.8b00038.

[191] Yousra El Ajjouri et al. “Tunable Wide-Bandgap Monohalide Perovskites”. In: *Advanced Optical Materials* 8.17 (2020), pp. 1–5. ISSN: 21951071. DOI: 10.1002/adom.202000423.

[192] Sheng Tang et al. “Mechanochemical synthesis of pure phase mixed-cation/anion (FAPbI3)x(MAPbBr3)1-xhybrid perovskite materials: compositional engineering and photovoltaic performance”. In: *RSC Advances* 11.11 (2021), pp. 5874–5884. ISSN: 20462069. DOI: 10.1039/d0ra10751d.

[193] Carlos Alberto López et al. “Crystal structure features of CH3NH3PbI3-: XBrx hybrid perovskites prepared by ball milling: A route to more stable materials”. In: *CrystEngComm* 22.4 (2020), pp. 767–775. ISSN: 14668033. DOI: 10.1039/c9ce01461f.

[194] Francisco Palazon et al. “Mechanochemical synthesis of inorganic halide perovskites: Evolution of phase-purity, morphology, and photoluminescence”. In: *Journal of Materials Chemistry C* 7.37 (2019), pp. 11406–11410. ISSN: 20507526. DOI: 10.1039/c9tc03778k.

[195] Sebastian Bette et al. “Solution of the heavily stacking faulted crystal structure of the honeycomb iridate H3LiIr2O6”. In: *Dalton Transactions* 46.44 (2017), pp. 15216–15227. ISSN: 14779234. DOI: 10.1039/c7dt02978k.

[196] B. Palosz. “The structure of PbI2 polytypes 2H and 4H: A study of the 2H-4H transition”. In: *Journal of Physics: Condensed Matter* 2.24 (1990), pp. 5285–5295. ISSN: 09538984. DOI: 10.1088/0953-8984/2/24/001.

[197] P. A. Beckmann. “A review of polytypism in lead iodide”. In: *Crystal Research and Technology* 45.5 (May 2010), pp. 455–460. ISSN: 02321300. DOI: 10.1002/crat.201000066. URL: https://onlinelibrary.wiley.com/doi/10.1002/crat.201000066.

[198] Hang Li et al. “Molten Salt Strategy for Reproducible Evaporation of Efficient Perovskite Solar Cells”. In: *Advanced Functional Materials* (2022). ISSN: 16163028. DOI: 10.1002/adfm.202211232.

[199] Matthew P. Hautzinger et al. “Metal Halide Perovskite Heterostructures: Blocking Anion Diffusion with Single-Layer Graphene”. In: *Journal of the American Chemical Society* (2023). ISSN: 15205126. DOI: 10.1021/jacs.2c12441.

[200] Fan Fu et al. “Controlled growth of PbI2 nanoplates for rapid preparation of CH3NH3PbI3 in planar perovskite solar cells”. In: *Physica Status Solidi (A) Applications and Materials Science* 212.12 (2015), pp. 2708–2717. ISSN: 18626319. DOI: 10.1002/pssa.201532442.

[201] Alejandro Koffman-Frischknecht et al. “Tuning morphological features of lead iodide by low pressure vapor phase deposition”. In: *Thin Solid Films* 653.February (2018), pp. 249–257. ISSN: 00406090. DOI: 10.1016/j.tsf.2018.03.040.

[202] T. Moser et al. “Understanding the Formation Process of Perovskite Layers Grown by Chemical Vapour Deposition”. In: *Frontiers in Energy Research* 10.June (June 2022), pp. 1–11. ISSN: 2296-598X. DOI: 10.3389/fenrg.2022.883882. URL: https://www.frontiersin.org/articles/10.3389/fenrg.2022.883882/full.

[203] Lukas Oesinghaus et al. “Toward Tailored Film Morphologies: The Origin of Crystal Orientation in Hybrid Perovskite Thin Films”. In: *Advanced Materials Interfaces* 3.19 (Oct. 2016), p. 1600403. ISSN: 21967350. DOI: 10.1002/admi.201600403. URL: https://onlinelibrary.wiley.com/doi/10.1002/admi.201600403.

[204] Luyao Wang et al. “Favorable grain growth of thermally stable formamidinium-methylammonium perovskite solar cells by hydrazine chloride”. In: *Chemical Engineering Journal* 430.P1 (2022), p. 132730. ISSN: 13858947. DOI: 10.1016/j.cej.2021.132730. URL: https://doi.org/10.1016/j.cej.2021.132730.

[205] Bart G. H. M. Groeneveld et al. “Stable Cesium Formamidinium Lead Halide Perovskites: A Comparison of Photophysics and Phase Purity in Thin Films and Single Crystals”. In: *Energy Technology* 8.4 (Apr. 2020), p. 1901041. ISSN: 2194-4288. DOI: 10.1002/ente.201901041. URL: https://onlinelibrary.wiley.com/doi/10.1002/ente.201901041.

[206] Richard R. Lunt et al. “Organic vapor phase deposition for the growth of large area organic electronic devices”. In: *Applied Physics Letters* 95.23 (2009), pp. 2007–2010. ISSN: 00036951. DOI: 10.1063/1.3271797.

[207] Nada Mrkyvkova et al. “Combined in Situ Photoluminescence and X-ray Scattering Reveals Defect Formation in Lead-Halide Perovskite Films”. In: *The Journal of Physical Chemistry Letters* 12.41 (Oct. 2021), pp. 10156–10162. ISSN: 1948-7185. DOI: 10.1021/acs.jpclett.1c02869. URL: https://pubs.acs.org/doi/10.1021/acs.jpclett.1c02869.

[208] Sebastian Svanström et al. “X-ray stability and degradation mechanism of lead halide perovskites and lead halides”. In: *Physical Chemistry Chemical Physics* 23.21 (2021), pp. 12479–12489. ISSN: 14639076. DOI: 10.1039/d1cp01443a.

[209] Klara Suchan et al. “Optical in situ monitoring during the synthesis of halide perovskite solar cells reveals formation kinetics and evolution of optoelectronic properties”. In: *Journal of Materials Chemistry A* 8.20 (2020), pp. 10439–10449. ISSN: 2050-7488. DOI: 10.1039/D0TA01237H. URL: http://xlink.rsc.org/?DOI=D0TA01237H.

[210] Lukas Wagner et al. “Distinguishing crystallization stages and their influence on quantum efficiency during perovskite solar cell formation in real-time”. In: *Scientific Reports* 7.1 (2017), pp. 1–6. ISSN: 20452322. DOI: 10.1038/s41598-017-13855-6.

[211] Elizabeth S. Parrott et al. “Growth modes and quantum confinement in ultrathin vapour-deposited MAPbI3 films”. In: *Nanoscale* 11.30 (2019), pp. 14276–14284. ISSN: 20403372. DOI: 10.1039/c9nr04104d.

[212] Gede W.P. Adhyaksa et al. “Understanding Detrimental and Beneficial Grain Boundary Effects in Halide Perovskites”. In: *Advanced Materials* 30.52 (2018). ISSN: 15214095. DOI: 10.1002/adma.201804792.

[213] Adam D. Wright et al. “Intrinsic quantum confinement in formamidinium lead triiodide perovskite”. In: *Nature Materials* 19.11 (Nov. 2020), pp. 1201–1206. ISSN: 1476-1122. DOI: 10.1038/s41563-020-0774-9. URL: http://dx.doi.org/10.1038/s41563-020-0774-9%20https://www.nature.com/articles/s41563-020-0774-9.

[214] Mingzhu Long et al. “Large-Grain Formamidinium PbI 3- x Br x for High-Performance Perovskite Solar Cells via Intermediate Halide Exchange”. In: *Advanced Energy Materials* 7.12 (June 2017), p. 1601882. ISSN: 16146832. DOI: 10.1002/aenm.201601882. URL: https://onlinelibrary.wiley.com/doi/10.1002/aenm.201601882.

[215] Hongge Zheng et al. “Temperature-dependent photoluminescence properties of mixed-cation methylammonium–formamidium lead iodide [HC(NH 2) 2] x [CH 3 NH 3] 1-x PbI 3 perovskite nanostructures”. In: *Journal of Materials Chemistry C* 5.46 (May 2017), pp. 12057–12061. DOI: 10.1039/C7TC04146B. URL: http://xlink.rsc.org/?DOI=C7TC04146B.

[216] Adam D. Wright et al. “Electron–phonon coupling in hybrid lead halide perovskites”. In: *Nature Communications* 7.1 (May 2016), p. 11755. ISSN: 2041-1723. DOI: 10.1038/ncomms11755. URL: https://www.nature.com/articles/ncomms11755.

[217] Jae Keun Nam et al. “Unveiling the Crystal Formation of Cesium Lead Mixed-Halide Perovskites for Efficient and Stable Solar Cells”. In: *The Journal of Physical Chemistry Letters* 8.13 (July 2017), pp. 2936–2940. ISSN: 1948-7185. DOI: 10.1021/acs.jpclett.7b01067. URL: https://pubs.acs.org/doi/10.1021/acs.jpclett.7b01067.

[218] Chong Liu et al. “All-Inorganic CsPbI2Br Perovskite Solar Cells with High Efficiency Exceeding 13%”. In: *Journal of the American Chemical Society* 140.11 (2018), pp. 3825–3828. ISSN: 15205126. DOI: 10.1021/jacs.7b13229.

[219] Xuejie Zhu et al. “Vapor-fumigation for record efficiency two-dimensional perovskite solar cells with superior stability”. In: *Energy and Environmental Science* 11.12 (2018), pp. 3349–3357. ISSN: 17545706. DOI: 10.1039/c8ee02284d.

[220] Thierry Alain Moser. “Development and investigation of chemical vapour deposition for perovskite solar cells”. In: 28549 (2022). URL: https://doi.org/10.3929/ethz-b-000577809.

[221] Wenjing Qi et al. “Manipulated Crystallization and Passivated Defects for Efficient Perovskite Solar Cells via Addition of Ammonium Iodide”. In: *ACS Applied Materials & Interfaces* 13.29 (July 2021), pp. 34053–34063. ISSN: 1944-8244. DOI: 10.1021/acsami.1c05903. URL: https://pubs.acs.org/doi/10.1021/acsami.1c05903.

[222] Kyro Odysseas Kosmatos et al. “Methylammonium Chloride: A Key Additive for Highly Efficient, Stable, and Up-Scalable Perovskite Solar Cells”. In: *ENERGY & ENVIRONMENTAL MATERIALS* 2.2 (June 2019), pp. 79–92. ISSN: 2575-0356. DOI: 10.1002/eem2.12040. URL: https://onlinelibrary.wiley.com/doi/10.1002/eem2.12040.

[223] Fuping Zhao et al. “Two-Step Vapor-Solid Reaction for the Growth of High-Quality CsFA-Based Lead Halide Perovskite Thin Films”. In: *Solar RRL* 7.11 (June 2023). ISSN: 2367-198X. DOI: 10.1002/solr.202300062. URL: https://onlinelibrary.wiley.com/doi/10.1002/solr.202300062.

[224] Igal Levine et al. “Charge transfer rates and electron trapping at buried interfaces of perovskite solar cells”. In: *Joule* 5.11 (Nov. 2021), pp. 2915–2933. ISSN: 25424351. DOI: 10.1016/j.joule.2021.07.016. URL: https://doi.org/10.1016/j.joule.2021.07.016%20https://linkinghub.elsevier.com/retrieve/pii/S2542435121003548.

[225] Vadim Dyadkin et al. “A new multipurpose diffractometer PILATUS@SNBL”. In: *Journal of Synchrotron Radiation* 23.3 (May 2016), pp. 825–829. ISSN: 1600-5775. DOI: 10.1107/S1600577516002411. URL: https://scripts.iucr.org/cgi-bin/paper?S1600577516002411.

[226] Wouter T. M. Van Gompel et al. “Degradation of the Formamidinium Cation and the Quantification of the Formamidinium–Methylammonium Ratio in Lead Iodide Hybrid Perovskites by Nuclear Magnetic Resonance Spectroscopy”. In: *The Journal of Physical Chemistry C* 122.8 (Mar. 2018), pp. 4117–4124. ISSN: 1932-7447. DOI: 10.1021/acs.jpcc.7b09805. URL: https://pubs.acs.org/doi/10.1021/acs.jpcc.7b09805.

Acronyms and abbreviations

ALD : Atomic Layer Deposition

c-Si : Crystalline silicon

CR : Conversion Ratio

CNT : Classical Nucleation Theory

CVD : Chemical Vapor Deposition

DFT : Density Functional Theory

DMA : Dimethylamine

DMF : N,N-dimethylformamide

EDX : Energy-dispersive X-ray spectroscopy

EQE : External Quantum Efficiency

FA : Formamidine

FAI, FABr, FASCN : Formamidinium iodide, bromide, thiocyanate

FAPI : Formamidinium lead triiodide

FTIR : Fourier-Transform InfraRed spectroscopy

FTO : Fluorine-doped Tin Oxide

GIWAXS : Grazing Incidence Wide-Angle X-ray Scattering

GW : Gigawatt

HI : Hydroiodic acid

ITO : Indium Tin Oxide

IQE : Internal Quantum Efficiency

KOH : Potassium hydroxide

LCOE : Levelized Cost Of Electricity

MA : Methylamine

MAI, MABr, MACl : Methylammonium iodide, bromide, chloride

MAPI : Methylammonium lead triiodide

MPP : Maximum Power Point

NMR : Nuclear Magnetic Resonance

PCE : Power Conversion Efficiency

PI : Polyimide

PL : PhotoLuminescence

PLQY : PhotoLuminescence Quantum Yield

POPOP : Pizza Oven Processing of Organohalide Perovskites

PV : Photovoltaics

PTFE : PolyTetraFluoroEthylene

PVD : Physical Vapor Deposition

QCM : Quartz Crystal Microbalance

QFLS : Quasi-Fermi Level Splitting

RH : Relative Humidity

RIR-MAPLE : Resonant Infrared, Matrix-Assisted Pulsed Laser Evaporation

SCN : Thiocyanate

SEM : Scanning Electron Miscroscopy

SXRD : Synchrotron X-Ray Diffraction

TCO : Transparent Conductive Oxide

ToF SIMS : Time of Flight Secondary Ion Mass Spectroscopy

UPS : Ultraviolet Photoelectron Spectroscopy

UV-Vis-NIR : Ultraviolet - Visible - Near InfraRed

XPS : X-Ray Photoelectron Spectroscopy

XRD : X-Ray Diffraction

Publications

- Guesnay Q., Sahli F., Jeangros Q. and Ballif C., *'Vapor deposition of metal halide perovskite thin films: Process control strategies to shape layer properties'*, APL Materials, (2021).
  DOI : https://doi.org/10.1063/5.0060642

- Guesnay Q., McMonagle C.J., Chernyshov D., Zia W., Wieczorek A., Siol S., Saliba M., Ballif C. and Wolff C.M., *'Sub-stoichiometric mixing of metal halide powders and their single source evaporation for perovskite photovoltaics'*, ACS Photonics, (2023).
  DOI : https://doi.org/10.1021/acsphotonics.3c00438

- Guesnay Q., Sahli F., Artuk K., Turkay D., Kuba A.G., Mrkývková N., Végsö K., Šiffalovič P., Ledinský M., Lai H., Fu F., Fürst N., Schafflützel A., Bucher C., Jeangros Q., Ballif C. and Wolff C.M., *'Pizza Oven Processing of Organohalide Perovskites (POPOP) : a simple, versatile and efficient vapor deposition method.'*, manuscript to be submitted.

- Ginies P., Even Y. and Guesnay Q., *'Concentration measurement of refrigerant/lubricant mixture by capacitive sensor'*, Proceedings of 24th International Compressor Engineering Conference, (2018).
  DOI : https://docs.lib.purdue.edu/icec/2554/

- Sahli F., Miaz N., Salsi N., Bucher C., Schafflützel A, Guesnay Q., Duchêne L., Niesen B., Ballif C. and Jeangros Q., *'Vapor Transport Deposition of Methylammonium Iodide for Perovskite Solar Cells'*, ACS Appl. Energy Mater., (2021).
  DOI : https://doi.org/10.1021/acsaem.0c02999

- Chin X.Y., Turkay D., Steele J.A., Tabean S., Eswara S., Mensi M., Fiala P., Wolff C.M., Paracchino A., Artuk K., Jacobs D., Guesnay Q., Sahli F., Andreatta G., Boccard M., Jeangros Q. and Ballif C., *'Interface passivation for 31.25%-efficient perovskite/silicon tandem solar cells'*, Science, (2023).
  DOI : https://doi.org/10.1126/science.adg0091

Oral Presentations

- Guesnay Q., Bloch L., Holweger J., Ballif C. and Wyrsch N., *'Smart Control of Heat Pump for Grid-tied Photovoltaic System'*, SCCER - FURIES, October 2018. Lausanne, Switzerland.

- Guesnay Q., Sahli F., Salsi N., Duchêne L., Niesen B., Ballif C. and Jeangros Q., *3AO.4.2 'Hybrid PVD/VTD Vapor Deposition Processing for Perovskite Tandem Solar Cell Upscaling'*, European Photovoltaic Solar Energy Conference (EU PVSEC), September 2021. Online event

- Guesnay Q., Sahli F., Jeangros Q., Ballif C. and Wolff C.M., *2CO.3.3 'Hybrid PVD/VTD Vapor Deposition Processing for Perovskite Tandem Solar Cell Upscaling'*, World Conference of Photovoltaic Energy Conversion (WCPEC), September 2022. Milano, Italy.

Quentin Guesnay

R&D Engineer

https://www.linkedin.com/in/quentin-guesnay-05494414b

SUMMARY

Engineer and scientist always looking for discovering new fields and taking inspiration from his diverse background to solve problems.
As passionate about scientific and technical topics as he is about designing the best ways to communicate about them.

SKILLS

- Abilities : Research & Development, Material Characterization (Structural, Chemical, Optoelectronic), Project Management, Process Engineering, Laboratory Experimental Work.
- Langages : Fluent in French and English, Notions of Spanish.
- Coding/Data Analysis : Python, Matlab, Java, C, VBA, Excel.
- CAD : CATIA, SolidWorks, PTC Creo.
- Simulation : Simulink, ADAMS, Abaqus, ANSYS, Cast3M.
- Communication : Powerpoint, Word, LaTeX, Blender, Prezi.

EXPERIENCE

PhD Researcher, EPFL PV-lab

Neuchâtel, Suisse — 2019-2023
Development of a new vapor deposition process of perovskite thin films for photovoltaic application. Process engineering (homemade CVD, Thermal Evaporation, ALD, Sputtering, Solution Processing) and in depth characterization (GIWAXS, XRD, PL, NMR, FTIR, ToF SIMS, SEM – EDX, EQE – IV, UV-Vis-NIR). Innovative results presented in multiple publications and conference talks.

R&D intern, Indeotec

Neuchâtel, Suisse — 2019
Participation in R&D activities of the company: PECVD deposition of amorphous silicon, coding GUI software for Raman spectra quantitative analysis, developing automated bench determining samples thickness (UV-Vis measurement, Tauc-Lorentz fit), characterization of films : FTIR, PL, Ellipsometry.

R&D intern, PASAN

Neuchâtel, Suisse — 2018
Development of a Python tool for IV measurement of highly capacitive Solar Cells.

Master Student, EPFL PV-lab

Neuchâtel, Suisse — 2018
Development of a control algorithm finding optimal control of the following system : {Photovoltaic panels + Inverter + Grid Connection + House Loads + Heat Pump + Domestic Water Tank + Domestic Hot Water demand}. Work presented in conference talk and poster.

R&D intern, Danfoss Commercial Compressors

Reyrieux, France — 2017
Design of a capacitive sensor monitoring refrigerant by measuring relative permittivity, study of discharge valve's wear and thermodynamic studies (frigorific cycle). Results on capacitive sensor published in 24th International Compressor Engineering Conference.

R&D intern, ONERA – The French Aerospace Lab

Modane, France — 2016
Modelisation and improvement of heat exchangers, calculations for implementation of brakes for rotating shafts of wind tunnels.

EDUCATION

ECOLE POLYTECHNIQUE, FRANCE

Renewable Energies Science and Technology, M2 (2017-2018)
Main courses : Photovoltaics, Chemical Storage of Energy, Renewable Thermal Energy, Hydro Wind and Maritime Renewable Energies, Smart Grids for Renewable Energy.
Recipient of the 'Science & Enseignement – EDF – Institut de France – Académie des Sciences' Scholarship.

INSA RENNES, FRANCE

Mechanical and Control System engineering, MEng (2012-2017)
Main courses : Design and Processes, Mechanical Engineering and Materials, Automation and Model-building.

REFERENCES

Available upon request.